



D 2022



# DEVELOPMENT OF MULTI-FUNCTIONALIZED TRIBOCORROSION RESISTANT BIO-MMCS

**LUÍS SOUSA**

TESE DE DOUTORAMENTO APRESENTADA  
À FACULDADE DE ENGENHARIA DA UNIVERSIDADE DO PORTO EM  
PROGRAMA DOUTORAL EM MATERIAIS E PROCESSAMENTO AVANÇADOS



## **Acknowledgements**

To my supervisor, Prof. Sónia Simões, for always being supportive and being always available to discuss my work.

To my co-supervisor, Prof. Fatih Toptan, for his guidance and countless hours discussing results.

To Prof. Manuel Vieira from FEUP for all his help during this PhD.

To Alexandra Alves for the helpful discussions about my experimental results and many suggestions.

To Prof. Ana Maria Pinto for her insights and providing experimental conditions for the development of this work.

To Prof. Aníbal Guedes for his insights and sharing his knowledge.

To Prof. Maria Helena Fernandes and Liliana Grenho for receiving me at Faculdade de Medicina Dentária da Universidade do Porto and introducing me to biological experiments.

To Dr. Ana Ribeiro and Prof. Luís Rocha for the opportunity to develop work in CBPF in Brasil.

To Natália Costa, Prof. André Rossi and Sara Gemini Piperni from CBPF, for their help in experimental work and receiving me in Brasil.

To Prof. João Salvador for his valuable insights and discussion about electrochemistry.

To all the people who helped me in my practical work and made it easier: Eng. Filipe, Dr. Edith Ariza, Miguel Abreu and Leonor Carneiro.

To my colleagues in lab, which accompanied me in this journey, Ana Costa and Ishan Çaha, for their friendship and always being available to help me.

To my colleagues in FEUP: Bruno, Aida and Clarissa for their help and hours spent together.

Lastly, to my family and friends, who helped me along the way.

This work was supported by Portuguese FCT, under UIDB/04436/2020 and M-ERA-NET/0001/2015 projects. L. Sousa is grateful for the PhD grant through NORTE-08-5369-FSE-000051 project.





## Abstract

Titanium and its alloys are widely used in load bearing biomedical implants owing to their adequate mechanical properties, corrosion resistance and biocompatibility. However, some concerns remain such as poor tribocorrosion resistance (combined action of wear and corrosion) and lack of bioactivity. By adding hard ceramic reinforcement particles into a Ti matrix, by producing titanium matrix composites (TMCs), it is possible to improve the tribocorrosion behaviour of Ti through direct and indirect strengthening mechanisms. In order to enhance the bioactivity, simple techniques such as micro-arc oxidation (MAO) or thermal oxidation (TO) treatments can be used to biofunctionalize the Ti-based surfaces by forming thick TiO<sub>2</sub> layers with improved biological properties.

This PhD work aimed to produce biofunctionalized TMCs, to improve both the tribocorrosion and biological behaviour of Ti. The effect of distinct reinforcement phases (Al<sub>2</sub>O<sub>3</sub>, B<sub>4</sub>C, and *in-situ* TiB and TiC reinforcement phases) and processing methods and parameters on the corrosion and tribocorrosion behaviour of Ti were studied in physiological solutions at body temperature. TMCs were processed by conventional powder metallurgy or hot-pressing, followed by MAO or TO treatments on Ti-Al<sub>2</sub>O<sub>3</sub>, Ti-B<sub>4</sub>C, and Ti-TiB-TiC composite surfaces. Electrochemical characterization was performed by potentiodynamic polarization and electrochemical impedance spectroscopy tests. Tribocorrosion tests were carried out in tribometer with a reciprocating ball-on-plate configuration where open circuit potential or current evolution were monitored before, during and after sliding.

Compared to unreinforced Ti, TMCs reinforced with a relatively low percentage of reinforcement phases (3 – 10 %vol.), presented considerably lower wear volume losses after tribocorrosion tests, also tended to show reduced tendency to corrosion as well as reduced corrosion kinetics during sliding action. Biofunctionalized composites presented improved corrosion and tribocorrosion behaviour compared to untreated composites. On the other hand, biofunctionalized TMCs also presented improved tribocorrosion behaviour under harsher conditions compared to biofunctionalized unreinforced Ti surfaces. *In-situ* Ti-TiB-TiC composites showed promising results regarding biological

behaviour, since reinforcement phases did not jeopardize the biocompatibility of Ti, where the results also hinted at improved bioactivity.

Thus, within the limitations of this work, it can be concluded that biofunctionalized TMCs may have the potential for load bearing biomedical implants.

**Keywords:** Titanium matrix composites, Corrosion, Tribocorrosion, Biofunctionalization

## Resumo

O titânio e as suas ligas são amplamente usados em implantes biomédicos, uma vez que possuem propriedades mecânicas adequadas, excelente resistência à corrosão e biocompatibilidade. No entanto, ainda existem algumas preocupações, tais como a baixa resistência à tribocorrosão (ação combinada entre desgaste e corrosão) e a baixa bioatividade. Através da introdução de partículas cerâmicas duras numa matriz de Ti, para produzir compósitos de matriz de titânio (CMT), é possível aumentar a resistência à tribocorrosão devido a mecanismos de reforço diretos e indiretos. De modo a melhorar a bioatividade, técnicas relativamente simples como a oxidação por micro-arco ou oxidação térmica podem ser usadas para biofuncionalizar superfícies de Ti, através da formação de camadas espessas de  $\text{TiO}_2$  com melhores propriedades biológicas.

Esta tese de doutoramento teve como objetivo a produção de CMT com superfícies biofuncionalizadas com o intuito de melhorar a resistência à tribocorrosão e o comportamento biológico do Ti. O efeito da adição de fases de reforço distintas ( $\text{Al}_2\text{O}_3$ ,  $\text{B}_4\text{C}$  ou fases TiB e TiC formadas *in-situ*), assim como o método e parâmetros de processamento no comportamento à corrosão e à tribocorrosão do Ti foram estudados em soluções fisiológicas à temperatura corporal. Os compósitos foram processados ou por metalurgia dos pós convencional ou por hot-pressing, de seguida as superfícies dos compósitos foram biofuncionalizadas por oxidação por micro-arco ou por oxidação térmica. Os testes de corrosão consistiram em testes de polarização potenciodinâmica e espectroscopia de impedância eletroquímica, enquanto os testes de tribocorrosão foram realizados num tribómetro com uma configuração bola-placa com movimento recíproco, onde tanto o potencial de circuito aberto ou corrente foram monitorizados antes, durante e após o deslizamento.

Em comparação com o Ti não reforçado, compósitos reforçados com uma percentagem de reforço relativamente baixa (3 – 10 %vol.), apresentaram volumes de desgaste consideravelmente mais baixos. Para além disso, os CMT também tendiam a apresentar menor tendência e taxa de corrosão durante o deslizamento. Já os compósitos biofuncionalizados apresentaram uma resistência à corrosão e à tribocorrosão superiores aos compósitos não tratados, assim como um melhor comportamento à tribocorrosão em condições mais

extremas (cargas superiores) quando comparado com o Ti tratados nas mesmas condições. Os compósitos *in-situ* apresentaram resultados promissores no que toca ao comportamento biológico, para além da biocompatibilidade não ter sido comprometida, os resultados sugerem que os compósitos apresentam uma maior bioatividade em relação ao Ti não reforçado.

Assim, e tendo em conta as limitações deste trabalho, é possível concluir que CMT com superfícies biofuncionalizadas apresentam potencial para a produção de implantes biomédicos.

**Palavras-Chave:** Compósitos de matriz de titânio, Corrosão, Tribocorrosão, Biofuncionalização.

## Table of contents

---

Acknowledgements.....	i
Abstract .....	iii
Resumo .....	v
List of Acronyms .....	xi
List of Figures .....	xiii
List of Tables .....	xvii
<b>Structure of the Thesis.....</b>	<b>xix</b>
<b>Chapter 1.....</b>	<b>1</b>
<b>Introduction, motivation, and objectives .....</b>	<b>1</b>
<b>References .....</b>	<b>7</b>
<b>Chapter 2.....</b>	<b>11</b>
<b>State of the art.....</b>	<b>11</b>
<b>2.1. Total Hip Replacement (THR).....</b>	<b>11</b>
2.1.1. <i>Biomaterials for hip implants</i> .....	13
2.1.2. <i>Failure of hip implants</i> .....	20
2.1.3. <i>Corrosion and tribocorrosion in hip implants</i> .....	22
<b>2.2. Titanium matrix composites for improved tribocorrosion resistance.....</b>	<b>26</b>
2.2.1. <i>Ti-B<sub>4</sub>C and Ti-TiB-TiC composites</i> .....	26
2.2.2. <i>Ti-Al<sub>2</sub>O<sub>3</sub> composites</i> .....	30
<b>2.3. Micro-arc and thermal oxidation treatment for improvement of bioactivity</b>	<b>33</b>
<b>Chapter 3.....</b>	<b>51</b>
<b>Influence of Ti-Al intermetallic phases on the corrosion and tribocorrosion behavior of Ti-Al<sub>2</sub>O<sub>3</sub> composites.....</b>	<b>51</b>
<b>Abstract.....</b>	<b>53</b>
<b>3.1. Introduction .....</b>	<b>53</b>
<b>3.2. Experimental .....</b>	<b>55</b>
3.2.1. <i>Materials and methods</i> .....	55
3.2.2. <i>Corrosion tests</i> .....	56
3.2.3. <i>Tribocorrosion tests</i> .....	56
3.2.4. <i>Characterization</i> .....	57
<b>3.3. Results and discussion .....</b>	<b>58</b>
3.3.1. <i>Microstructural characterization</i> .....	58
3.3.2. <i>Corrosion behaviour</i> .....	60
3.3.3. <i>Tribocorrosion behaviour</i> .....	66
<b>3.4. Conclusions .....</b>	<b>73</b>
<b>References .....</b>	<b>75</b>
<b>Chapter 4.....</b>	<b>79</b>
<b>Corrosion and tribocorrosion behaviour of Ti-B<sub>4</sub>C composites processed by conventional sintering and hot-pressing technique .....</b>	<b>79</b>
<b>Abstract.....</b>	<b>81</b>
<b>4.1. Introduction .....</b>	<b>81</b>
<b>4.2. Experimental .....</b>	<b>83</b>
4.2.1. <i>Materials and methods</i> .....	83
4.2.2. <i>Electrochemical tests</i> .....	85

4.2.3.	<i>Tribocorrosion tests</i> .....	85
4.2.4.	<i>Characterization</i> .....	86
<b>4.3.</b>	<b>Results</b> .....	87
4.3.1.	<i>Microstructure</i> .....	87
4.3.2.	<i>Electrochemical behaviour</i> .....	88
4.3.3.	<i>Tribocorrosion behaviour</i> .....	91
<b>4.4.</b>	<b>Discussion</b> .....	97
<b>4.5.</b>	<b>Conclusions</b> .....	102
	<b>References</b> .....	105
<b>Chapter 5</b> .....		109
<b>Preliminary tribo-electrochemical and biological responses of the Ti-TiB-TiC<sub>x</sub> <i>in-situ</i> composites intended for load-bearing biomedical implants</b> .....		
	<b>Abstract</b> .....	111
<b>5.1.</b>	<b>Introduction</b> .....	111
<b>5.2.</b>	<b>Materials and methods</b> .....	114
5.2.1.	<i>Processing</i> .....	114
5.2.2.	<i>Electrochemical tests</i> .....	115
5.2.3.	<i>Tribocorrosion tests</i> .....	115
5.2.4.	<i>Osteoblasts viability</i> .....	116
5.2.5.	<i>Characterization</i> .....	116
<b>5.3.</b>	<b>Results and discussion</b> .....	117
5.3.1.	<i>Composite microstructures</i> .....	117
5.3.2.	<i>Electrochemical behaviour</i> .....	118
5.3.3.	<i>Tribocorrosion behaviour</i> .....	121
5.3.4.	<i>Biological behaviour</i> .....	126
<b>5.4.</b>	<b>Conclusions</b> .....	127
	<b>References</b> .....	129
<b>Chapter 6</b> .....		133
<b>Tribocorrosion behaviour of bio-functionalized porous Ti surfaces obtained by two-step anodic treatment</b> .....		
	<b>Abstract</b> .....	135
<b>6.1.</b>	<b>Introduction</b> .....	135
<b>6.2.</b>	<b>Materials and methods</b> .....	137
6.2.1.	<i>First-step anodic treatment</i> .....	137
6.2.2.	<i>Second-step anodic treatment under MAO regime</i> .....	138
6.2.3.	<i>Wettability</i> .....	139
6.2.4.	<i>Corrosion tests</i> .....	139
6.2.5.	<i>Tribocorrosion tests</i> .....	139
<b>6.3.</b>	<b>Results and discussion</b> .....	140
6.3.1.	<i>First-step anodic treatment</i> .....	140
6.3.2.	<i>Second-step anodic treatment under MAO regime</i> .....	143
6.3.3.	<i>Roughness</i> .....	145
6.3.4.	<i>Wettability</i> .....	146
6.3.5.	<i>Corrosion behaviour</i> .....	147
6.3.6.	<i>Tribocorrosion behaviour</i> .....	148
6.3.7.	<i>Tribocorrosion mechanisms</i> .....	154
<b>6.4.</b>	<b>Conclusions</b> .....	155
	<b>References</b> .....	157
<b>Chapter 7</b> .....		161
<b>Tribocorrosion-resistant biofunctionalized Ti-Al<sub>2</sub>O<sub>3</sub> composites</b> .....		
		161

<b>Abstract</b> .....	163
<b>7.1. Introduction</b> .....	163
<b>7.2. Materials and methods</b> .....	165
7.2.1. <i>Processing</i> .....	165
7.2.2. <i>Biofunctionalization</i> .....	166
7.2.3. <i>Electrochemical tests</i> .....	166
7.2.4. <i>Tribocorrosion tests</i> .....	167
7.2.5. <i>Characterization</i> .....	168
<b>7.3. Results</b> .....	168
7.3.1. <i>Characterization</i> .....	168
7.3.2. <i>Corrosion behaviour</i> .....	170
7.3.3. <i>Tribocorrosion behaviour</i> .....	172
<b>7.4. Conclusions</b> .....	179
<b>References</b> .....	181
<b>Chapter 8</b> .....	185
<b>Effect of micro-arc oxidation and thermal oxidation treatments on Ti-B<sub>4</sub>C composite surfaces intended for biomedical applications</b> .....	185
<b>Abstract</b> .....	187
<b>8.1. Introduction</b> .....	187
<b>8.2. Materials and methods</b> .....	189
8.2.1. <i>Processing</i> .....	189
8.2.2. <i>Electrochemical tests</i> .....	189
8.2.3. <i>Tribocorrosion tests</i> .....	190
8.2.4. <i>Characterization</i> .....	190
<b>8.3. Results and discussion</b> .....	191
8.3.1. <i>Microstructure</i> .....	191
8.3.2. <i>Electrochemical behaviour</i> .....	196
8.3.3. <i>Tribocorrosion behaviour</i> .....	199
<b>8.4. Conclusions</b> .....	205
<b>References</b> .....	207
<b>Chapter 9</b> .....	209
<b>Micro-arc and Thermal oxidation treated <i>in-situ</i> Ti composites intended for load-bearing biomedical implants</b> .....	209
<b>Abstract</b> .....	211
<b>9.1. Introduction</b> .....	211
<b>9.2. Materials and methods</b> .....	213
9.2.1. <i>Processing</i> .....	213
9.2.2. <i>Electrochemical tests</i> .....	214
9.2.3. <i>Tribocorrosion tests</i> .....	214
9.2.4. <i>Characterization</i> .....	215
<b>9.3. Results and discussion</b> .....	215
9.3.1. <i>Microstructure</i> .....	215
9.3.2. <i>Electrochemical behaviour</i> .....	219
9.3.3. <i>Tribocorrosion behaviour</i> .....	220
<b>9.4. Conclusions</b> .....	226
<b>References</b> .....	229
<b>Chapter 10</b> .....	233
<b>General discussion, conclusions, and future work</b> .....	233
<b>10.1. General discussion</b> .....	233
<b>10.2. Conclusions</b> .....	239

<b>10.3. Future works</b> .....	241
<b>References</b> .....	243



## List of Acronyms

---

ALTR – Adverse local tissue reaction  
AM – Additive manufacturing  
ANOVA – One-way analysis of variance  
AP – Anodic potential  
AT – Anodic treatment  
BMI – Body mass index  
BSE – Back scattering electron  
CA – Calcium acetate  
CE – Counter electrode  
CoC – Ceramic-on Ceramic  
COF – Coefficient of friction  
CoM – Ceramic on metal  
CoP – Ceramic on Polyethylene  
CP – Cathodic potential  
CP Ti – Commercially pure titanium  
CSTi – Cancellous-structured titanium  
CTE – Coefficient of thermal expansion  
DMEM - Dulbecco's modified Eagle's medium  
EBM – Electron beam melting  
EDS – Energy dispersive spectroscopy  
EEC – Electrochemical equivalent circuit  
EIS – Electrochemical impedance spectroscopy  
FBS – fetal bovine serum  
FEG-SEM – Field emission gun – scanning electron microscope  
HA – Hydroxyapatite  
HP – Hot-pressing  
ICP-AES – inductively coupled plasma-atomic emission spectrometer  
LENS – laser engineered net shaping  
LMD – Laser melting deposition  
MAC – Mechanically-assisted corrosion  
MACC – Mechanically-assisted crevice corrosion  
MAO – Micro-arc oxidation

MMC – Metal matrix composite  
MoM – Metal on metal  
MoP – Metal on polymer  
OA – Osteoarthritis  
OCP – Open Circuit Potential  
ODZ – Oxygen diffusion zone  
OM – Optical Microscope  
PBS – Phosphate-buffered saline  
PM – Powder metallurgy  
PVA – Poly (vinyl alcohol)  
RE – Reference electrode  
SAED – Selected area electron diffraction  
SCE – Saturated calomel electrode  
SE – Secondary electron  
SLM – Selective laser melting  
SPS – Spark plasma sintering  
TEM – Transmission electron microscope  
THA – Total hip arthroplasty  
THR – Total hip replacement  
TMC – Titanium matrix composite  
TO – Thermal oxidation  
UHMWPE – Ultra-high molecular weight polyethylene  
WE – Working electrode  
XLPE – High crosslinked polyethylene  
XRD – X-ray diffraction  
 $\beta$ -GP –  $\beta$ -glycerophosphate disodium salt pentahydrate

## List of Figures

---

<b>Figure 1.</b> Outline of the thesis. ....	xxii
<b>Figure 2.1.</b> Main components of a traditional hip implant (adapted from [9]).....	13
<b>Figure 2.2.</b> Changes in (a) Gibbs free energy ( $\Delta G$ ) and (b) reaction enthalpy ( $\Delta H$ ) for reactions in the Ti-B-C system [105]. ....	27
<b>Figure 2.3.</b> Ternary phase diagram of Ti-B-C system at 1400 °C [127].....	28
<b>Figure 2.4.</b> Schematic diagram of the microstructure evolution in the Ti-B <sub>4</sub> C system [111]. ....	29
<b>Figure 2.5.</b> Ternary phase diagram of Ti-Al-O system at 1100 °C [151].....	31
<b>Figure 3.1.</b> Low magnification OM images of (a) Ti, (b) Ti-5Al <sub>2</sub> O <sub>3</sub> composites and (c) Ti-10Al <sub>2</sub> O <sub>3</sub> composite, together with low magnification SE/BSE SEM image of (d) Ti-10Al <sub>2</sub> O <sub>3</sub> composite, higher magnification BSE and SE images of (e,f) Ti-5Al <sub>2</sub> O <sub>3</sub> composite, (g) EDS spectra taken from Z1 and Z2 and (h) nano-indentations and hardness values taken from the reaction zone (h).....	60
<b>Figure 3.2.</b> a) Bode and b) Nyquist diagrams obtained for Ti and composite groups; c) EEC used for Ti and d) for composite groups; e) potentiodynamic polarization curves obtained for Ti and composites in 9 wt.% NaCl at 37 °C. ....	61
<b>Figure 3.3.</b> Evolution of OCP before, during, and after sliding, together with the evolution of COF during sliding. ....	67
<b>Figure 3.4.</b> Lower magnification SE and BSE images of the wear tracks taken from Ti, Ti-5Al <sub>2</sub> O <sub>3</sub> and Ti-10Al <sub>2</sub> O <sub>3</sub> under C1 and C2 conditions, respectively, together with the corresponding EDS spectra taken from the counter-body. ....	68
<b>Figure 3.5.</b> a) Wear volume loss values and representative wear track profiles for b) C1 and c) C2 condition. ....	69
<b>Figure 3.6.</b> Higher magnification SE and BSE SEM images of wear tracks from Ti, Ti-5Al <sub>2</sub> O <sub>3</sub> , and Ti-10Al <sub>2</sub> O <sub>3</sub> composites under C1 and C2, respectively, together with the evolution of OCP and COF during sliding.....	72
<b>Figure 3.7.</b> Proposed wear mechanisms for Ti and Ti-Al <sub>2</sub> O <sub>3</sub> composites. ....	73
<b>Figure 4.1.</b> Particle size distribution for Ti and B <sub>4</sub> C powders. ....	85
<b>Figure 4.2.</b> Back-scattered electron (BSE) SEM images of the composites processed by PM and HP, together with EDS spectra taken from the B <sub>4</sub> C particles, reaction zone and Ti matrix.....	88
<b>Figure 4.3.</b> XRD spectra obtained from a Ti-24 %vol. B <sub>4</sub> C composite processed under the same PM conditions.....	88
<b>Figure 4.4.</b> Corrosion results: a) Representative potentiodynamic polarization curves, b) Bode diagrams, c) Nyquist diagrams, and EECs used for d) Ti_PM, Ti_HP and Ti-3B <sub>4</sub> C_HP groups and for e) Ti-3B <sub>4</sub> C_PM group. ....	90
<b>Figure 4.5.</b> Evolution of a) OCP and b) anodic current density before, during and after sliding together with the corresponding evolution of COF during sliding.....	93

<b>Figure 4.6.</b> SE/BSE SEM images of the wear tracks and respective counter-bodies for tribocorrosion tests performed under OCP.....	94
<b>Figure 4.7.</b> SE/BSE SEM images of the wear tracks and respective counter-bodies for tribocorrosion tests performed under 500 mV (anodic regime).....	95
<b>Figure 4.8.</b> SE/BSE SEM images of the wear tracks and respective counter-bodies for tribocorrosion tests performed under -750 mV (cathodic regime).....	96
<b>Figure 4.9.</b> a) Representative wear profiles for all the testes groups and tribocorrosion conditions together with b) average wear volume loss values calculated from wear profiles.....	97
<b>Figure 5.1.</b> Characterization after processing: a) BSE SEM image of as-processed composite, b) SE (secondary electron) SEM image and EDS elemental distribution maps of an over-etched composite surface, c) dark-field STEM image of the composite with a higher magnification of the reinforcement phase. The insert shows a selectred area electron diffraction pattern (SAED). The diffraction pattern could be indexed in [6 10 1] direction of the $TiC_{0.59}$ phase, and d) XRD pattern of the composite showing the presence of TiB and TiC phases. ....	118
<b>Figure 5.2.</b> Electrochemical behaviour: a) Representative potentiodynamic polarization curves for Ti and its composites, b) Nyquist diagrams, c) Bode diagrams and EEC used to fit EIS data. ....	121
<b>Figure 5.3.</b> Evolution of OCP before, during and after sliding together with the evolution of COF during sliding for both conditions and groups.....	122
<b>Figure 5.4.</b> BSE/SE SEM images of the worn surfaces and SE SEM images of the $Al_2O_3$ balls used as counter-body with respective EDS analysis.....	125
<b>Figure 5.5.</b> Wear volume loss values calculated from wear profiles.....	125
<b>Figure 5.6.</b> Biological behaviour: a) Cell survival (%), b) fluorescence micrography of MG-63 cells cultured 24 h on control Ti surfaces and Ti-TiB-TiC composites (green represents live cells and red represents dead cells) and c) SEM images of MG-63 cells attached Ti surfaces and Ti-TiB-TiC composites surfaces for 24 h.....	127
<b>Figure 6.1.</b> a) and b) OM images of the cross-sections after first step of anodic treatment before and after etching, respectively and c) secondary electron (SE) and backscattered electron (BSE) SEM images of the porous surface after etching. ....	141
<b>Figure 6.2.</b> OM images after the first-step anodic treatment performed for a) 1, b) 2, c) 3, d) 4 and e) 5 minutes. ....	141
<b>Figure 6.3.</b> Pore size distribution after the first-step anodic treatment for Ti_1 to Ti_5 groups, respectively .....	142
<b>Figure 6.4.</b> Representative SE-SEM images obtained after the second-step anodic treatment for Ti_MAO (a and d), Ti_1MAO (b and e), and Ti_3MAO (c and f).....	143
<b>Figure 6.5.</b> Cross-sectional OM images of a) Ti_MAO, b) Ti_1MAO, and c) Ti_3MAO, and d) respective current evolution during MAO treatment.....	144
<b>Figure 6.6.</b> a) EDS and b) XRD spectra after the two-step anodic treatment. ....	145

<b>Figure 6.7.</b> Contact angle values for each group and the respective representative images (*Significant difference within the first-step group ( $p < 0.05$ )).	147
<b>Figure 6.8.</b> Potentiodynamic polarization curves before (Ti_1 and Ti_3) and after (Ti_1MAO and Ti_3MAO) the second-step anodic treatments, in comparison with their control groups (Ti and Ti_MAO, respectively).	148
<b>Figure 6.9.</b> OM and SEM images of the worn sample surfaces, together with the SEM images and the respective EDS spectra taken from the worn counter-body surfaces after the first- and the second-step anodic treatments.	150
<b>Figure 6.10.</b> Higher magnification SEM images of the worn surfaces after the second-step anodic treatment (a and b), together with EDS spectra taken from the marked zones (c and d).	151
<b>Figure 6.11.</b> Evolution of OCP before, during and after sliding on the samples before (a) and after the second-step anodic treatments (b), with the respective COF values.	153
<b>Figure 6.12.</b> Schematic draws of the suggested tribocorrosion mechanisms for a) Ti, b) Ti after the first-step, c) Ti after the second-step, and d) Ti after two-step anodic treatments.	155
<b>Figure 7.1.</b> SE SEM images of the raw Ti and Al <sub>2</sub> O <sub>3</sub> powders.	166
<b>Figure 7.2.</b> General setup used in MAO treatments, together with corrosion and tribocorrosion tests.	167
<b>Figure 7.3.</b> Overall microstructure of the a,b) as-processed and b,c) biofunctionalized composites, e) XRD spectra for MAO treated groups, and f) cross section BSE images from Ti-Al <sub>2</sub> O <sub>3</sub> _1100C group.	170
<b>Figure 7.4.</b> Potentiodynamic polarization curves for all the conditions.	172
<b>Figure 7.5.</b> Evolution of OCP before, during and after sliding, together with the respective COF values registered during sliding.	174
<b>Figure 7.6.</b> BSE and SE SEM images of the worn surfaces for untreated groups after tribocorrosion tests together with SE SEM images of the Al <sub>2</sub> O <sub>3</sub> balls used as counter-body and respective overall chemical composition of these surfaces.	176
<b>Figure 7.7.</b> BSE and SE SEM images of the worn surfaces for MAO treated groups after tribocorrosion tests.	177
<b>Figure 7.8.</b> Representative optical microscope (OM) images of Vickers indentations for each composite group.	177
<b>Figure 7.9.</b> a) Representative wear track profiles and b) average wear volume loss values calculated from wear profiles.	178
<b>Figure 8.1.</b> a and b) Backscattered electron (BSE) SEM images of the untreated composite, c) dark-field TEM image of the B <sub>4</sub> C and reaction zone together with line EDS scan, and diffraction pattern for TiB and TiC phase.	193
<b>Figure 8.2.</b> a) BSE and secondary electron (SE) SEM images of the composite surfaces after MAO treatment, and b) cross-section optical microscope (OM) images of composites after MAO treatment.	193
<b>Figure 8.3.</b> XRD patterns for untreated, MAO and TO treated Ti-B <sub>4</sub> C composites.	194

<b>Figure 8.4.</b> a,b) BSE and SE SEM images of composite surfaces after TO treatment and c,d,e,f) BSE SEM images of cross-sections obtained for TO treated Ti-B <sub>4</sub> C composites. ....	194
<b>Figure 8.5.</b> Proposed mechanism for the oxidation behaviour of Ti-B <sub>4</sub> C composites.	196
<b>Figure 8.6.</b> Potentiodynamic polarization curves for all tested groups together with a CP scan for the untreated composite. ....	198
<b>Figure 8.7.</b> a) Evolution of current density during potentiostatic tests for the untreated composites; optical microscope (OM) images of composite surfaces b) before and c) after potentiostatic tests at 1 V; and OM images of composite surfaces d) before and e) after potentiostatic tests at 1.4 V. ....	198
<b>Figure 8.8.</b> OCP evolution before, during and after sliding, together with the evolution of COF during sliding. ....	200
<b>Figure 8.9.</b> SE SEM images of the worn surfaces together with SE SEM images and EDS analysis of the Al <sub>2</sub> O <sub>3</sub> balls used as counter-body for 0.5 N. ....	201
<b>Figure 8.10.</b> BSE/SE SEM images of the worn surfaces together with SE SEM images and EDS spectra of the Al <sub>2</sub> O <sub>3</sub> balls used as counter-body for 10 N. ....	202
<b>Figure 8.11.</b> a) Representative 2D wear profiles for all the groups together with b) wear volume values estimated from wear profiles. ....	203
<b>Figure 9.1.</b> Representative SE SEM image of MAO and TO treated Ti and composite groups .....	217
<b>Figure 9.2.</b> a) BSE/SE SEM image of a representative cross-section of MAO treated composite, b and c) BSE SEM image of a representative cross-section of TO treated Ti and composite, respectively, and d) XRD patterns for untreated composite and MAO and TO treated Ti and composite groups. ....	218
<b>Figure 9.3.</b> Representative potentiodynamic polarization curves for all the groups...	220
<b>Figure 9.4.</b> OCP evolution before, during, and after sliding for both conditions under 0.5 and 10 N, together with the evolution of COF during sliding. ....	222
<b>Figure 9.5.</b> Worn surfaces for all the groups tested under 0.5 N condition. ....	224
<b>Figure 9.6.</b> SEM images of the worn surfaces and Al <sub>2</sub> O <sub>3</sub> balls together with EDS analysis from Al <sub>2</sub> O <sub>3</sub> balls for 10 N. ....	225
<b>Figure 9.7.</b> Wear profiles and average wear volume loss for 10 N applied load. ....	226

## List of Tables

---

<b>Table 3.1.</b> Particle size distribution of Ti and Al <sub>2</sub> O <sub>3</sub> powders.....	56
<b>Table 3.2.</b> Parameters used in tribocorrosion tests, where C1 and C2 represent lighter and harsher conditions, respectively. ....	57
<b>Table 3.3.</b> Hardness and fracture toughness values estimated from eq. (3.1).....	59
<b>Table 3.4.</b> Fitted parameters obtained from EIS data for Ti and composite groups.....	63
<b>Table 3.5.</b> Passivation current density ( $i_{pass}$ ), corrosion current density ( $i_{corr}$ ), and corrosion potential ( $E_{(i=0)}$ ) values for Ti and Ti-Al <sub>2</sub> O <sub>3</sub> composites.....	63
<b>Table 4.1.</b> Hardness values obtained for both Ti and Ti-B <sub>4</sub> C groups.....	88
<b>Table 4.2.</b> Corrosion potential ( $E_{(i=0)}$ ), open circuit potential ( $E_{OCP}$ ) and passivation current density ( $i_{pass}$ ) values. ....	90
<b>Table 4.3.</b> EEC parameters obtained from EIS data. ....	90
<b>Table 5.1.</b> EEC parameters obtained from EIS data. ....	120
<b>Table 6.1.</b> Groupings of samples after the first- and the second-step anodic treatment. ....	137
<b>Table 6.2.</b> Open circuit potential ( $E_{OCP}$ ), corrosion potential ( $E_{(i=0)}$ ), and passivation current density ( $i_{pass}$ ) values for all testing groups. ....	148
<b>Table 7.1.</b> Particle size distribution for Ti and Al <sub>2</sub> O <sub>3</sub> powders.....	166
<b>Table 7.2.</b> $E_{corr}$ , $E_{(i=0)}$ and $i_{pass}$ values for all tested groups.....	172
<b>Table 9.1.</b> Average values of $E_{(i=0)}$ and $i_{pass}$ values for all the groups. ....	220





## Structure of the Thesis

---

For a better understanding of this thesis, a brief outline of the document will be given in this section. This document is divided in 10 different chapters, as briefly described below.

In **Chapter 1**, the main motivation for the development of this work is given. A brief introduction about the total hip replacement (THR) market is provided, where a connection is made between this topic and the main objectives of this work.

The state-of-art of the most relevant topics for this thesis is given in **Chapter 2**. These include a contextualization of THR surgery, the main characteristics of the materials used in the fabrication of hip implants, and the main challenges that these materials face in real conditions. Emphasis on corrosion and tribocorrosion properties of titanium matrix composites (TMCs), specifically Ti-B<sub>4</sub>C and Ti-Al<sub>2</sub>O<sub>3</sub> composites, was given as they were one of the main focuses of this work. B<sub>4</sub>C and *in-situ* TiB and TiC reinforcement phases (obtained by reacting Ti and B<sub>4</sub>C powders) were chosen once it is reported that these phases are one of the best options to produce TMCs. On the other hand, Al<sub>2</sub>O<sub>3</sub> was selected since it is a well-known material used in hip implants (femoral head) due to its high wear resistance and biocompatibility. In addition, specific emphasis was given to micro-arc oxidation (MAO) and thermal oxidation (TO) treatments as these were the surface treatments studied in this work.

The main results and conclusions of this work will be given through chapters 3 to 9 in the form of scientific papers (some published, and others submitted or to be submitted in peer-reviewed journals). The outline of these works can be seen in Figure 1.

***“Influence of Ti-Al intermetallic phases on the corrosion and tribocorrosion behaviour of Ti-Al<sub>2</sub>O<sub>3</sub> composites”*** is presented in **Chapter 3**. The overall corrosion and tribocorrosion behaviour of TMCs is heavily influenced by the interface between the reinforcement phases and metal matrix. The role of Ti-Al intermetallic phases formed due to Ti + Al<sub>2</sub>O<sub>3</sub> reaction on the corrosion and tribocorrosion behaviour of Ti-Al<sub>2</sub>O<sub>3</sub> composites was studied. On the tribocorrosion behaviour, the effect of parameters such as contact pressure, frequency and sliding time was also evaluated.

In **Chapter 4** the **“Corrosion and tribocorrosion behaviour of Ti-B<sub>4</sub>C composites processed by conventional sintering and hot-pressing technique”** is given. In order to obtain TMCs with the desired properties, it is essential to choose an adequate processing technique. At the same time, other factors such as the overall complexity and cost of the selected processing method should also be considered. This chapter compares the overall properties of Ti-B<sub>4</sub>C composites processed by a relatively simple technique (conventional sintering) and a more advanced processing technique (hot-pressing). The influence of both processing methods on the corrosion and tribocorrosion behaviour of TMCs was studied. Additionally, unreinforced titanium processed under the same conditions was used as control groups in order to understand the role of B<sub>4</sub>C reinforcement phases.

**“Preliminary tribo-electrochemical and biological responses of the Ti-TiB-TiC<sub>x</sub> in-situ composites intended for load-bearing biomedical implants”** is presented in **Chapter 5**. *In-situ* TiB and TiC reinforcements have been considered one of the best options to produce TMCs, mainly due to the strong interfacial bonding of the reinforcement phases with the Ti matrix. Over the years, several studies reported the mechanical properties of Ti-TiB-TiC composites. However very few studies have reported their corrosion and tribocorrosion behaviour. In this work, *in-situ* Ti-TiB-TiC composites were produced by reactive hot-pressing. The reinforcement phases were constituted by clusters of small grains of TiB and TiC<sub>x</sub> phases. The corrosion and tribocorrosion response of this system was evaluated together with a preliminary approach on its biological response.

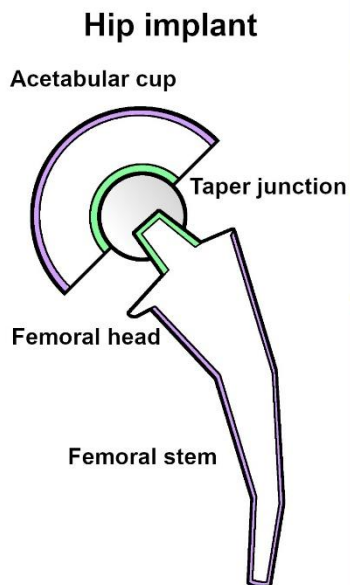
Anodic treatment, more specifically MAO treatment, was first studied in **Chapter 6**, **“Tribocorrosion behaviour of bio-functionalized porous Ti surfaces obtained by two-step anodic treatment”**. A bio-functionalized porous surface was obtained on CP (commercially pure) Ti by a two-step anodic treatment. While the first-step provided macro-porosity, the second-step, a bio-functionalization process by MAO, led to micro-pores and bio-active surface. The corrosion and tribocorrosion behaviour of bio-functionalized hierarchical porous surfaces were evaluated in this chapter.

The effect of MAO treatment on Ti-Al<sub>2</sub>O<sub>3</sub> composite surfaces was studied in **Chapter 7, “Tribocorrosion-resistant biofunctionalized Ti-Al<sub>2</sub>O<sub>3</sub> composites”**. The main goal was to investigate the influence of this treatment on these composite surfaces. Firstly, Ti-Al<sub>2</sub>O<sub>3</sub> composites were processed under two different processing temperatures in order to obtain distinct amounts of Ti-Al intermetallic phases, followed by MAO treatment. The influence of the extension of the reaction zone formed due to Ti and Al<sub>2</sub>O<sub>3</sub> reaction on corrosion and tribocorrosion behaviour of the as processed composites was described together with the influence of MAO treatment on Ti-Al<sub>2</sub>O<sub>3</sub> composites.

In **Chapter 8**, the “**Effect of Micro-arc oxidation and thermal oxidation treatments on Ti-B<sub>4</sub>C composite surfaces intended for biomedical applications**” was studied. Due to the different nature of the reinforcement phases, the mechanisms of oxide layer growth and the final structures were quite different depending on the surface treatment. The roles of the MAO and TO layers on the corrosion and tribocorrosion behaviour were also accessed.

The final study is presented in **Chapter 9: “Micro-arc and thermal oxidation treated in-situ Ti composites intended for load-bearing biomedical implants”**. The objective of this study was to investigate the influence of both MAO and TO treatments on *in-situ* composites developed in chapter 5. The effect of both treatments on corrosion and tribocorrosion behaviour of *in-situ* Ti-TiB-TiC<sub>x</sub> composites was described.

Finally, in **Chapter 10**, a general discussion and link of all results, from Chapter 3 to Chapter 9, is given. The main and most relevant conclusions of this work are also presented in this chapter. As a final point, some future works that could be of interest for further development of biofunctionalized composites for biomedical applications are suggested.



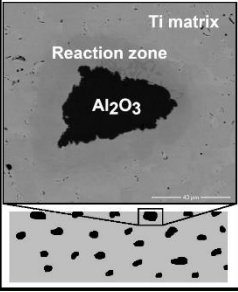
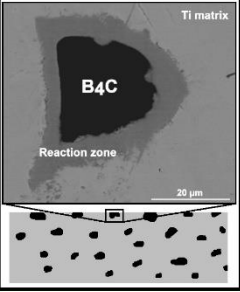
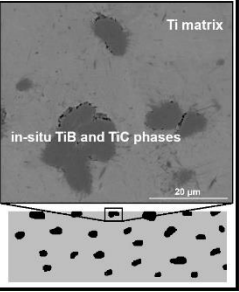
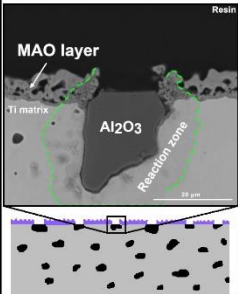
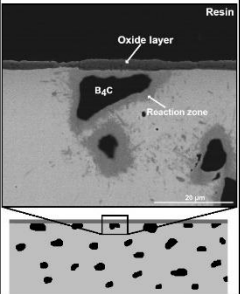
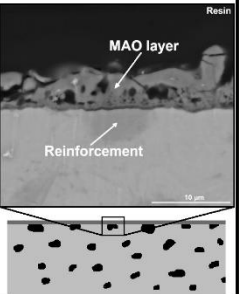
<b>TMCs for improved tribocorrosion resistance</b>		
<b>Chapter 3</b>	<b>Chapter 4</b>	<b>Chapter 5</b>
<p><b>Ti-Al<sub>2</sub>O<sub>3</sub> composites</b>            Role of Ti-Al intermetallic phases on corrosion and tribocorrosion behaviour of Ti-Al<sub>2</sub>O<sub>3</sub> composites. Emphasis on the role of tribocorrosion parameters: time, load and frequency.</p> 	<p><b>Ti-B<sub>4</sub>C composites</b>            Effect of two distinct processing methods (conventional sintering vs hot-pressing) on the corrosion and tribocorrosion behaviour of Ti-B<sub>4</sub>C composites.</p> 	<p><b>Ti-TiB-TiC composites</b>            Corrosion and tribocorrosion behaviour of in-situ Ti-TiB-TiC composites produced by Ti+B<sub>4</sub>C reaction, with a preliminary study on biological behaviour.</p> 
<b>Biofunctionalized TMCs for improved tribocorrosion resistance and bioactivity</b>		
<b>Chapter 6</b>		
<p><b>Bio-functionalized porous Ti surfaces obtained by two-step anodic treatment</b>            Introductory chapter about anodic and MAO treatment on Ti surfaces. Corrosion and tribocorrosion behaviour of hierarchical porous structures obtained by combining anodic and MAO treatments.</p>		
<b>Chapter 7</b>	<b>Chapter 8</b>	<b>Chapter 9</b>
<p><b>Biofunctionalized Ti-Al<sub>2</sub>O<sub>3</sub> composites</b>            Effect of MAO treatment on Ti-Al<sub>2</sub>O<sub>3</sub> composite surfaces, with emphasis on corrosion and tribocorrosion behaviour.</p> 	<p><b>Biofunctionalized Ti-B<sub>4</sub>C composites</b>            Effect of MAO and TO treatments on Ti-B<sub>4</sub>C composite surfaces. Mechanisms of oxide layer growth, corrosion and tribocorrosion behaviour.</p> 	<p><b>Biofunctionalized Ti-TiB-TiC composites</b>            Effect of MAO and TO treatments on Ti-TiB-TiC composite surfaces and their effects on corrosion and tribocorrosion behaviour.</p> 

Figure 1. Outline of the thesis.

# Chapter 1

## Introduction, motivation, and objectives

---

Global life expectancy has been improving each year. In the last two decades alone, life expectancy increased by more than 6 years [1]. By 2030, persons with or older than 60 years old are projected to account for one in six people worldwide [1,2]. However, with age, there are also increasing incidences of chronic diseases including cardiovascular, osteoporosis, and osteoarthritis (OA) related problems, among many others. OA is one of the most common diseases and it is expected to rise in the following years. Clinically, this disease is mainly characterized by joint pain, stiffness and limitation of motion [3].

Since there is no known cure for OA, medical implants such as hip-replacements are considered as one of the best options for end-stage OA. Increased awareness of the benefits of hip-replacement surgery, technological development, improved healthcare infrastructures, and increased global acceptance of medical implants are also responsible for the orthopaedic implant market growth [4]. From 2018 alone, revenue from the sale of orthopaedic implants was estimated as 46 billion euros [5].

Hip replacements are used when the hip joint of the patient is damaged or diseased to restore the strength and motion of the hip and to relieve pain [6]. Total hip replacement (THR) is considered as one of the most successful orthopaedic surgery, with around 90% survivorship at 15 years follow-up [7], and considered by some as the “orthopaedic operation of the century” [8]. However, these implants do not last indefinitely, and given enough time *in-situ*, they will eventually fail due to numerous reasons including problems related to corrosion, wear, lack of bonding between the implant and the bone, inflammations, among others [9]. It was estimated that a hip implant would last 25 years in 58% of the patients [10].

Naturally, the lifespan of such an implant will also depend on several factors such as the design of the implant, surgeon expertise and factors related to the patient itself, including age, weight, level of activity, and the overall health.

Once implant failure occurs, a revision surgery is needed, which not only is an expensive surgery, but its success rate is also less when compared with the first implementation [11]. As it would be expected, if the patient received THR at a young age, the chance for revision surgery is higher. For example, the probability for revision surgery is about 5% for patients with age above 70 years old. However, if they are between 50 to 54 years old, this probability increases to around 29% [12]. If younger patients are considered, this chance will be even higher. Considering the economic impact and more importantly, the patient wellbeing, the chance for revision surgery should be reduced. Postponing this surgery as much as possible is an option, however, until there, the quality of life of the patient will also be severely reduced. In this way, efforts must be made to achieve more lasting implants.

Two critical aspects of implant success reside on the tribocorrosion resistance (combined action of wear and corrosion) and bioactivity needed to achieve a good fixation with the adjacent bone. In hip implants, the femoral component (stem) and the bone are fixed to each other. However, it is known that micromotions (small amplitude displacement or vibrations) occur at the interface, leading to a particular form of tribocorrosion known as fretting corrosion. Small amplitude oscillations also occur at the interface between different components of the implant such as the interface between the femoral head and femoral stem [13]. The consequences of tribocorrosion can be devastating since they can lead to implant loosening and its adverse biological response from wear debris and metallic ion release, including allergies, inflammations and even carcinomas [14–16].

Regarding the fixation of the implant, there are two options: cemented or cementless fixation. Cemented fixation, where cement is used to fix the implant to the adjacent bone, is usually used in older patients and less active people [17]. This method has the advantage of providing rapid fixation after implementation, providing a better short-term clinical outcome. However, it is not satisfactory in the long run, especially for a young and active person [18]. Due to poor mechanical properties, the cement is considered a weak point in a cemented

implant, as eventually the cement will also wear out and revision surgery will be needed [17]. To achieve better long-term properties, cementless fixation was developed. In this method, the prosthesis is directly fixated to the bone by osteointegration. Bone ingrowth at the bone/implant interface is obtained with porous and bioactive surfaces [16,17,19].

Ti and its alloys found their use in biomedical implants in 1940, in virtue of its outstanding properties such as high corrosion resistance, high strength, low density, relatively low Young's modulus, and high biocompatibility [16,20,21]. When compared to their main competitors as stainless steel and cobalt-chromium alloys, Ti and its alloys have the advantage of possessing overall lower Young's modulus (110 to 55 GPa for Ti alloys), against 210 GPa and 240 GPa for stainless steel (316L) and cobalt-chromium alloys, respectively. Young's modulus is one of the key properties for these kinds of implants, as Young's modulus closer to the bone (between 15 and 30 GPa) are preferred to avoid stress shielding problems. While titanium has strength very close to cobalt alloys and stainless steels, it possesses lower density and thus higher strength to density ratio [9,16]. Despite being frequently used in hip implants, low tribocorrosion resistance and lack of bioactivity are still concerns regarding Ti-based hip implants.

Regarding tribocorrosion resistance, it is well known that the addition of hard ceramic particles into a metallic matrix can significantly improve the wear resistance of the base material [22]. For that reason, metal matrix composites (MMCs) have found many applications in the automotive and aerospace sectors. However, they are yet to be considered for load bearing biomedical implants in the biomedical implant market.

$\text{Al}_2\text{O}_3$  could be an interesting choice to produce titanium matrix composites (TMCs), as it is already used in this type of implants. In the last years, femoral heads made of alumina composites have been increasing due to higher wear resistance and very low risk of osteolysis in the long term. The risk of ceramic composite femoral head failure was found to be very low in the last years, and are often related to displacements, geometric mismatch between the femoral head and the acetabular cup and/or severe traumatic conditions but not to the mechanical failure of the material itself [23–25].

On the other hand, boron carbide ( $\text{B}_4\text{C}$ ) or reaction products due to reaction with Ti, being TiC and TiB phases, could also be potential reinforcement

candidates to produce TMCs for biomedical applications. Nowadays, TiB and TiC reinforcements are considered one of the best options to produce TMCs. They possess several advantages such as high hardness, high wear resistance, good biocompatibility, good corrosion resistance, and similar density and thermal expansion coefficients to titanium [26–30]. Furthermore, *in-situ* TMCs reinforced with TiC and TiB can be easily processed by combining Ti and B<sub>4</sub>C powders.

In order to improve the integration of the implanted material with the surrounding bone and tissue, a range of surface modification techniques can be used. Commercially used techniques such as arc deposition, plasma spray, and sintered metal beads are used to improve the osteointegration of hip-implants by the formation of a porous surface to induce bone ingrowth and thus mechanical interlocking of the implant. In addition, hydroxyapatite (HA) coatings are often combined with porous structures to improve osteointegration further. Despite being relatively successful in improving osteointegration, these techniques do not provide adequate wear resistance [31–34].

Micro-arc oxidation (MAO) is a type of anodic treatment (AT), where several hundreds of volts are applied to the desired surface to produce a porous, crystalline, and thick titanium oxide layer that is recognized for having good osteointegration capabilities [35,36]. It has been widely reported that these structures can improve the bioactivity of titanium [37–39]. Besides increasing bioactivity, this type of layers also presents other advantages that are of extreme importance for biomedical devices, such as high corrosion and wear resistance [40–42].

On the other hand, thermal oxidation (TO) is also a simple and cost-effective technique that can be used to improve the bioactivity of Ti. This technique takes advantage of the high reactivity of Ti with air and/or water, to promote the growth of the native TiO<sub>2</sub> passive layer and alter its properties, such as crystal structure, topography, and chemical composition in a way to improve bioactivity [43–46].

Considering these problems associated with hip implant failure, this PhD work hypothesized that TMCs with biofunctionalized surfaces can improve both tribocorrosion resistance and bioactivity of titanium. Thus, this PhD work aimed to develop tribocorrosion-resistant, bio-functionalized MMCs for hip implants. The objective was to produce distinct TMCs, being *ex-situ* Ti-Al<sub>2</sub>O<sub>3</sub> composites,



*ex-situ* Ti-B<sub>4</sub>C composites and *in-situ* Ti-TiB-TiC composites and then to biofunctionalize the composite surfaces through MAO and TO treatments.

The main innovative objectives are given below:

- To process, characterize and study the effect of reinforcement particles and *in-situ* phases on the corrosion and tribocorrosion behaviour of three distinct TMCs: Ti-Al<sub>2</sub>O<sub>3</sub>, Ti-B<sub>4</sub>C and Ti-TiB-TiC composites;
- to biofunctionalize the composite surfaces by MAO (with incorporation of bioactive elements such as Ca and P) and/or by TO;
- to study the effect of MAO and TO treatments on the corrosion and tribocorrosion behaviour of composites;
- to assess the bioactivity of the composite surfaces by understanding the *in vitro* biological phenomena and mechanisms that regulate cell adhesion and proliferation.



## References

- [1] Sonny Eli Zaluchu, *World Health Statistics 2021: monitoring health for the SDGs, sustainable development goals*, Geneva: World Health Organization, 2021.
- [2] Department of Economic and Social Affairs, *World Population Ageing 2015*, United Nations, 2015.
- [3] D. Pereira, E. Ramos, J. Branco, Osteoarthritis, *Acta Med Port.* 27 (2014) 1–8.
- [4] S. Shihde, A. Srivastava, O. Sumant, *Medical Implant Market By Product Type (Orthopedic Implants, Cardiovascular Implants, Spinal Implant, Neurostimulators, Ophthalmic Implants, Dental Implants, Facial Implants, and Breast Implants) and Biomaterial Type (Metallic Biomaterials, Ceramic Biomaterials, Polymers Biomaterials, and Natural Biomaterials): Global Opportunity Analysis and Industry Forecast, 2020–2027*, 2020.
- [5] C. Cheng, X. Wang, Y. Luan, N. Zhang, B. Liu, X. Ma, M. Nie, Challenges of pre-clinical testing in orthopedic implant development, *Med. Eng. Phys.* 72 (2019) 49–54.
- [6] F. Stuart J., *100 Questions & Answers About Hip Replacement*, Jones and Bartlett Publishers, 2010.
- [7] N. Sodhi, M.A. Mont, Survival of total hip replacements, *Lancet.* 393 (2019) 613.
- [8] I.D. Learmonth, C. Young, C. Rorabeck, B. Bs, The operation of the century: total hip replacement, *Lancet.* 370 (2007) 1508–1519.
- [9] M. Geetha, A.K. Singh, R. Asokamani, A.K. Gogia, Ti based biomaterials, the ultimate choice for orthopaedic implants - A review, *Prog. Mater. Sci.* 54 (2009) 397–425.
- [10] J.T. Evans, J.P. Evans, R.W. Walker, A.W. Blom, M.R. Whitehouse, A. Sayers, How long does a hip replacement last? A systematic review and meta-analysis of case series and national registry reports with more than 15 years of follow-up, *Lancet.* 393 (2016) 647–654.
- [11] P. Jayakumar, S.U. Islam, A financial analysis of revision hip arthroplasty, *J. Bone Jt. Surg.* 94 (2012) 619–623.
- [12] A.C. McFarlane, Total joint arthroplasty in younger patients: heading for trouble?, *Lancet.* 389 (2017) 1374–1375.
- [13] N. Diomidis, S. Mischler, N.S. More, M. Roy, Tribo-electrochemical characterization of metallic biomaterials for total joint replacement, *Acta Biomater.* 8 (2012) 852–859.
- [14] H. Matusiewicz, Potential release of in vivo trace metals from metallic medical implants in the human body: From ions to nanoparticles - A systematic analytical review, *Acta Biomater.* 10 (2014) 2379–2403.
- [15] J.C.M. Souza, S.L. Barbosa, E. Ariza, J.P. Celis, L.A. Rocha, Simultaneous degradation by corrosion and wear of titanium in artificial saliva containing fluorides, *Wear.* 292–293 (2012) 82–88.
- [16] S. Affatato, D. Brando, Introduction to wear phenomena of orthopaedic implants, in: S. Affatato (Ed.), *Wear Orthop. Implant. Artif. Joints*, 1st ed., Woodhead, 2012: pp. 3–26.
- [17] X. Liu, P.K. Chu, C. Ding, Surface modification of titanium, titanium alloys, and related materials for biomedical applications, *Mater. Sci. Eng. R Reports.* 47 (2004) 49–121.
- [18] A. Abdulkarim, P. Ellanti, N. Motterlini, T. Fahey, J.M. O’Byrne, Cemented versus uncemented fixation in total hip replacement: a systematic review and meta-analysis of randomized controlled trials, *Orthop. Rev. (Pavia).* 5 (2013) 8.
- [19] S. Morshed, K.J. Bozic, M.D. Ries, H. Malchau, J.M. Colford, Comparison of cemented and uncemented fixation in total hip replacement: A meta-analysis, *Acta Orthop.* 78 (2007) 315–326.
- [20] R. Kossowsky, N. Kossovsky, *Materials Sciences and Implant Orthopedic Surgery*, 1st ed., Springer Netherlands, 1986.

- [21] G.G. de Lima, G.B. de Souza, C.M. Lepienski, N.K. Kuromoto, Mechanical properties of anodic titanium films containing ions of Ca and P submitted to heat and hydrothermal treatment, *J. Mech. Behav. Biomed. Mater.* 64 (2016) 18–30.
- [22] N. Chawla, Y.L. Shen, Mechanical behavior of particle reinforced metal matrix composites, *Adv. Eng. Mater.* 3 (2001) 357–370.
- [23] G.C. Lee, R.H. Kim, Incidence of Modern Alumina Ceramic and Alumina Matrix Composite Femoral Head Failures in Nearly 6 Million Hip Implants, *J. Arthroplasty.* 32 (2017) 546–551.
- [24] S. Affatato, E. Modena, A. Toni, P. Taddei, Retrieval analysis of three generations of BioloX® femoral heads: Spectroscopic and SEM characterisation, *J. Mech. Behav. Biomed. Mater.* 13 (2012) 118–128.
- [25] D. Hannouche, M. Zingg, H. Miozzari, R. Nizard, A. Lübbecke, Third-generation pure alumina and alumina matrix composites in total hip arthroplasty, *EFORT Open Rev.* 3 (2018) 7–14.
- [26] L. Jia, X. Wang, B. Chen, H. Imai, S. Li, Z. Lu, K. Kondoh, Microstructural evolution and competitive reaction behavior of Ti-B<sub>4</sub>C system under solid-state sintering, *J. Alloys Compd.* 687 (2016) 1004–1011.
- [27] Y. Chen, J. Zhang, N. Dai, P. Qin, H. Attar, L.-C. Zhang, Corrosion Behaviour of Selective Laser Melted Ti-TiB Biocomposite in Simulated Body Fluid, *Electrochim. Acta.* 232 (2017) 89–97.
- [28] A. Miklaszewski, M.U. Jurczyk, K. Jurczyk, M. Jurczyk, Plasma surface modification of titanium by TiB precipitation for biomedical applications, *Surf. Coatings Technol.* 206 (2011) 330–337.
- [29] M. Brama, N. Rhodes, J. Hunt, A. Ricci, R. Teghil, S. Migliaccio, C. Della Rocca, S. Leccisotti, A. Lioi, M. Scandurra, G. De Maria, D. Ferro, F. Pu, G. Panzini, L. Politi, R. Scandurra, Effect of titanium carbide coating on the osseointegration response in vitro and in vivo, *Biomaterials.* 28 (2007) 595–608.
- [30] Y. Diao, K. Zhang, Microstructure and corrosion resistance of TC2 Ti alloy by laser cladding with Ti/TiC/TiB<sub>2</sub> powders, *Appl. Surf. Sci.* 352 (2015) 163–168.
- [31] M. Gottlieb, O. Rahbek, P.F. Ottosen, K. Søballe, M. Stilling, Superior 11-year survival but higher polyethylene wear of hydroxyapatite-coated Mallory-Head cups, *HIP Int.* 22 (2012) 35–40.
- [32] S. Lazarinis, K.T. Mäkelä, A. Eskelinen, L. Havelin, G. Hallan, S. Overgaard, A.B. Pedersen, J. Kärrholm, N.P. Hailer, Does hydroxyapatite coating of uncemented cups improve long-term survival? An analysis of 28,605 primary total hip arthroplasty procedures from the Nordic Arthroplasty Register Association (NARA), *Osteoarthr. Cartil.* 25 (2017) 1980–1987.
- [33] E.W. Morscher, A. Hefti, U. Aebi, Severe osteolysis after third-body wear due to hydroxyapatite particles from acetabular cup coating, *J. Bone Jt. Surg.* 80 (1998) 267–272.
- [34] M. Green, P. Howard, M. Porter, A. Price, M. Wilkinson, N. Wishart, National Joint Registry 13th Annual report, 2016.
- [35] M. Tsai, Y. Chang, H. Huang, Y. Wu, T. Shieh, Micro-arc oxidation treatment enhanced the biological performance of human osteosarcoma cell line and human skin fibroblasts cultured on titanium – zirconium films, *Surf. Coat. Technol.* 303 (2016) 268–276.
- [36] C. Chang, X. Huang, Y. Liu, L. Bai, X. Yang, R. Hang, B. Tang, P.K. Chu, High-current anodization: A novel strategy to functionalize titanium-based biomaterials, *Electrochim. Acta.* 173 (2015) 345–353.
- [37] Y. Zhao, T.-Y. Xiong, Formation of bioactive titania films under specific anodisation conditions, *Surf. Eng.* 28 (2012) 371–376.

- [38] B. Yang, M. Uchida, H.M. Kim, X. Zhang, T. Kokubo, Preparation of bioactive titanium metal via anodic oxidation treatment, *Biomaterials*. 25 (2004) 1003–1010.
- [39] Y. Li, B. Li, X. Fu, J. Li, C. Li, H. Li, H. Li, C. Liang, H. Wang, L. Zhou, S. Xin, Anodic Oxidation Modification Improve Bioactivity and Biocompatibility of Titanium Implant Surface, *J. Hard Tissue Biol.* 22 (2013) 351–358.
- [40] G. Ryan, A. Pandit, D.P. Apatsidis, Fabrication methods of porous metals for use in orthopaedic applications, *Biomaterials*. 27 (2006) 2651–2670.
- [41] A.C. Alves, F. Wenger, P. Ponthiaux, J.P. Celis, A.M. Pinto, L.A. Rocha, J.C.S. Fernandes, Corrosion mechanisms in titanium oxide-based films produced by anodic treatment, *Electrochim. Acta*. 234 (2017) 16–27.
- [42] F. Toptan, A.C. Alves, A.M.P. Pinto, P. Ponthiaux, Tribocorrosion behavior of bio-functionalized highly porous titanium, *J. Mech. Behav. Biomed. Mater.* 69 (2017) 144–152.
- [43] P.S. Vanzillotta, M.S. Sader, I.N. Bastos, G. De Almeida, Improvement of in vitro titanium bioactivity by three different surface treatments, *Dent. Mater.* 22 (2006) 275–282.
- [44] Y. Park, H.-J. Song, I. Kim, H. Yang, Surface characteristics and bioactivity of oxide film on titanium metal formed by thermal oxidation, *J. Mater. Sci.* 18 (2007) 565–575.
- [45] G. Wang, J. Li, K. Lv, W. Zhang, X. Ding, G. Yang, Surface thermal oxidation on titanium implants to enhance osteogenic activity and in vivo osseointegration, *Sci. Rep.* 6 (2016) 1–13.
- [46] S. El-hadad, Optimizing the Surface Treatment Processes to Enhance the Bioactivity of Ti–6Al–7Nb Alloy, *Trans. Indian Inst. Met.* 73 (2020) 2727–2738.



## Chapter 2

### State of the art

---

#### 2.1. Total Hip Replacement (THR)

The natural hip joint can be considered one of the most weight bearing joints in the human body, playing a major role in the static and dynamic physiology of the locomotor system. The synovial hip joint is mainly consisted of two distinct parts: the femoral head, sitting on the top of the femur, and the acetabulum, a cup-like depression present in the pelvis. The femoral head has a hemispherical shape and is fitted completely in the concavity of the acetabulum. In addition, both are covered by cartilage, which is thicker at the places of weight bearing. Due to several factors such as diseases like rheumatoid arthritis and osteoarthritis, fractures, dislocations and accidents, the hip joint can be permanently damaged [1–4].

THR or total hip arthroplasty (THA) is a medical procedure where the diseased cartilage, the femoral head and the acetabulum are surgically replaced with artificial materials (hip implant). When the hip joint of the patient is severely damaged or diseased, THR may be considered the best option to relieve pain and restore the strength and motion of the hip [4–6].

There are various types of hip implants on the market, which can be divided in five major categories: metal on metal (MoM), metal on polyethylene (MoP), ceramic on metal (CoM), ceramic on ceramic (CoC) and ceramic on polyethylene (CoP) [7]. Traditional hip implants are composed of four distinct parts: the stem, the femoral head, the acetabular cup and the liner, as shown in Fig. 2.1 [8,9]. The stem (femoral component) is the part of the implant inserted on the medullary canal of the femur. Its purpose is it to fix the femoral side of the hip prosthesis to

the femoral bone and ensure a uniform load transfer from the prosthesis to the lower limb [9]. The highest mechanical stresses are observed in this component, thus high mechanical strength and fatigue resistance are required. The fixation of the stem to the bone can be done by two different ways: cemented or cementless fixation. Each method has its advantages and disadvantages and nowadays there is still controversy about the best approach [10,11]. In general, cemented fixation is clinically better in the short-term and it can be used when the bone has a poor quality for a cementless fixation [10,12]. However, it can present problems in long-term once the cement can wear out, leading to implant loosening and/or adverse biological reactions from wear debris [12].

In order to avoid these problems cementless fixation was developed. In this method, the prosthesis is directly fixated to the bone by osteointegration. Bone ingrowth at the bone–implant interface is obtained with porous and bioactive surfaces [8,11,12]. This fixation method has the advantage of providing better long-term fixation. However, it is hard to achieve a good initial fixation which can result in implant loosening and pain [13].

The femoral head is responsible for articular coupling between the stem and the acetabular cup. This component is attached to the stem's neck by a taper junction and to the inner part of the acetabular cup. The critical parameters for this component include the mechanical resistance of the material, roughness, and diameter. The surface roughness must be as low as possible to reduce friction and wear rates. The diameter plays an important role in determining the full range of motion achievable by the prosthesis. Higher diameters allows higher range of motion and improved stability, however, higher diameters also result in higher wear rates [14].

The liner or insert fits into the acetabular cup and its purpose is to allow the femoral head to move smoothly in the acetabular socket. This component can be made of polymeric, metallic or ceramic materials, each with advantages and disadvantages. The material choice depends on the minimum thickness of the acetabular cup to ensure mechanical stability, which differs on the size of the iliac bone present in the pelvis, where the acetabular cup is inserted [9].

The acetabular cup is fixed to the pelvis and its purpose is to provide mechanical stability for the liner. Similar to the stem, the acetabular cup can be either fixed by cemented or cementless fixation. In addition, screws can also be



used to improve the fixation. In the case of cementless fixations, the external surface of the acetabular cup must provide adequate osteointegration, which is usually achieved by porous structures and/or hydroxyapatite (HA) coatings. In MoM pairs, the acetabular cup can also act as a liner, however, this configuration presents a major disadvantage. If the inner part of the acetabular cup is worn-out and revision surgery is needed, replacing the whole acetabular cup, even if it shows good osteointegration is necessary. Therefore, the modularity liner/acetabular cup is usually preferred [9].

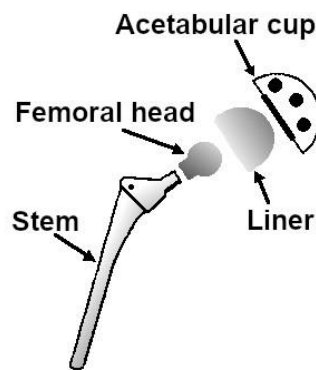


**Figure 2.1.** Main components of a traditional hip implant (adapted from [9]).

### 2.1.1. Biomaterials for hip implants

Materials used in orthopaedic implants, especially in load bearing applications, should possess an adequate combination of properties to achieve a long-lasting implant. These include mechanical properties such as strength and Young's modulus, biocompatibility, corrosion and tribocorrosion resistance, and bioactivity in the case of cementless implants [8,15]. The supporting components of the implant (stem and acetabular cup) are usually made of stainless steel, cobalt-chromium (CoCr) alloys or Ti alloys, mainly due to their biocompatibility, adequate mechanical properties and high corrosion resistance, owing to the spontaneous formation of a protective passive film on the surface when in contact with the body environment [16]. Naturally, it is expected that these materials will not cause any adverse biological reactions after implantation. In general terms, a material can be considered biocompatible if it does not cause any harm to surround tissues in the long-term.[17].

Adequate mechanical properties including tensile strength, hardness, fatigue strength and Young's modulus also make these materials suitable for these applications. Young's modulus is particularly important since a mismatch

in Young's modulus between the implant and the surrounding bone can lead to stress-shielding effect. If insufficient stress is transferred to the bone, its mineral density will decrease leading to bone resorption and eventually to implant loosening after some years. Bone structures (cortical bone) usually present Young's modulus between 10 and 30 GPa. Since the implant is subjected to repeated cyclic loads during its life cycle, fatigue strength is also of high importance.

Corrosion and tribocorrosion resistance are also important, since wear debris and/or metallic ions released to the surrounding tissue can lead to adverse local tissue reactions (ALTRs). In addition, mechanical failure and implant loosening can also be a consequence of corrosion and wear. For cementless implants, materials should also possess good osteointegration capabilities to achieve an adequate fixation with the adjacent bone.

Stainless steels (iron-carbon based alloys) containing Cr, Ni, Mo, Mn and C alloying elements were the first used materials in the fabrication of hip-implants in 1948 [18]. Relative ease of machining, forming, and hardening made stainless steel a strong candidate to produce hip implants. Compared to CoCr and Ti alloys, stainless steels present superior fatigue strength, ductility, are easier to machine and are cheaper. Despite this, stainless steels are sensitive to crevice and pitting corrosion, which limits their use in porous structures and narrow down their applications. The main austenitic steels used in implant materials are low carbon stainless steels such as ASTM F138/139 316 L (21Cr-10Ni-3Mn-2.5Mo), nitrogen-strengthened stainless steels such as ASTM 1314 (22Cr-12.5Ni-5Mn-2.5Mo-0.30N), and Nickel free stainless steels such as ASTM 1314 F2229 (23Mn-21Cr-1Mo-0.95N). Nickel free stainless steels were also developed, once it has been reported that Nickel ions can act as allergens and thus have an harmful effect on the human body [8,19,20].

CoCr alloys are among the most used materials in the fabrication of hip implants owing to their high corrosion and wear resistance [21]. These alloys typical contain 30 to 60 % Co and 20 to 30 % Cr, being CoCrMo and CoNiCrMo alloys the most used. The main CoCr alloys used in hip implants include: ASTM F75 (Co-28Cr-6Mo) alloy, ASTM F90 (Co-20Cr-15W-10Ni) alloy and ASTM F562 (Co-35Ni-20Cr-10Mo) alloy, among others [19]. The high corrosion resistance of CoCr is due to the high reactivity of Co and Cr, which oxidize rapidly under the

biological medium, leading to the formation of a protective oxide film such as  $\text{Cr}_2\text{O}_3$  [22]. Cr is added to improve the corrosion resistance, while Co is added to enhance the mechanical properties of the alloy [8]. Compared to stainless steels and titanium alloys, CoCr alloys have the advantage of having superior wear resistance [23].

Amongst various metallic materials, Ti and Ti alloys have been widely used for a wide range of biomedical applications. These materials were first used in mid-1940s and after that have been receiving great attention due to their unique properties [24]. When compared to stainless steels and CoCr alloys, Ti and Ti alloys have the advantage of possessing relatively lower Young's modulus (110 to 55, 210, and 240 GPa for Ti or Ti alloys, stainless steel 316L and CoCr alloys, respectively). While Ti has tensile strength very close to that of Co alloys and stainless steels (550–1000, 450–650 and 450–950 MPa for Ti alloys, stainless steel and CoCr alloys, respectively [25]), it possesses lower density. Therefore when comparing strength to density ratio, Ti outperforms the other two materials [8,15]. CoCr alloys and stainless steels may also cause adverse biological effects in the human body due to the release of elements such as Ni, Cr, and Co to the surrounding tissue. Commercially,  $\alpha + \beta$  Ti alloys, have been the most commonly used to produce hip implants, with Ti-6Al-4V alloy being by far the most common even today [26–28]. This alloy was introduced in 1946 for aeroplane applications and soon became an exceptional alloy for biomedical applications due to its comparatively higher mechanical performance than CP (commercially pure) Ti [19,27,29]. After some years, new alloys were introduced to further decrease Young's modulus and to gradually decrease or even eliminate the amount of Al and V from the alloy composition, due to concerns regarding Al and V ions leading to long-term health problems [15]. Considering these aspects, Ti-6Al-7Nb and Ti-6Al-2.5Fe alloys were developed to substitute V. These alloys are also known as  $\alpha + \beta$  microstructure and present very similar properties to Ti-6Al-4V alloy [30,31]. Other  $\alpha + \beta$  alloys were also developed such as Ti-5Al-2.5Fe, Ti-15Zr-4Nb-2Ta-0.2Pd, Ti-5Al-3Mo-4Zr and Ti-15Sn-4Nb-2Ta. Low Young's modulus  $\beta$  type Ti alloys containing compatible alloying elements, such as Nb, Zr and Ta have also been developed, once Nb and Zr elements are not released to the biological environment as metallic ions and instead are incorporated into the passive layer. Additionally, these alloys

present good formability and ductility. The most known  $\beta$  type alloys are Ti-29Nb-13Ta-4.6Zr, Ti-12Mo-6Zr-2Fe (TMZF) and Ti-35Nb-7Zr-5Ta (TiOsteum) [29].  $\beta$  type alloys also show corrosion behaviour comparable to CP Ti or other known Ti alloys such as Ti-6Al-4V [29,32,33].

To achieve more lasting implants through cementless implantation, there was also the need to improve the osteointegration with the surrounding bone. Thus, the use of rough and porous surfaces in femoral stems were developed and increased in the last years [27,34]. These surfaces promote bone ingrowth (firm fixation through bone growth into a porous structure) and bone ongrowth (fixation between the implant and the bone through bone growth on rough surfaces) [35].

Rough surfaces are used for bone ongrowth and are characterized by their macro- and micro- structures with average roughness values ( $R_a$ ) between 4 and 15  $\mu\text{m}$ . Surfaces for bone ongrowth can be achieved by different methods including blasted surfaces, where Ti or the Ti alloy is bombarded by hard and wear resistant particles, such as  $\text{Al}_2\text{O}_3$ , to obtain average  $R_a$  values ranging from 4 to 10  $\mu\text{m}$ . Other methods include etching, where chemical and electrochemical processes are used to generate rough surfaces, as well as machining, drilling and milling operations, which are also usually followed by blasting operation [36].

Porous surfaces for bone ingrowth can be obtained through several methods. Commercially, the most used include cancellous-structured titanium (CSTi), diffusion bonding, sintered metal beads, mesh structures, and porous coatings through the thermal plasma spray technique.

The goal of CSTi structures is to mimic the overall structure of the cancellous bone, characterized by interconnected pores. Generally, these structures present between 50 and 60% porosity and average pore sizes of 500  $\mu\text{m}$ . To obtain these structures, Ti powders are mixed with a polymer pore former. In this way, during sintering the polymer is evaporated and the porous Ti structure is left behind [37].

Mesh structures consist of Ti wires welded in such a way to achieve a porous structure of about 50 to 60 % porosity and pore sizes ranging from 100  $\mu\text{m}$  up to 400  $\mu\text{m}$ . These structures are obtained through diffusion bonding process where the wires are attached to a Ti or Ti alloy substrate [37].

Spherical metal beads with diameters ranging from a few microns to 1 mm in diameter are used to produce porous beaded surfaces. In this process the beads are glued together to the stem or acetabular cup substrate by means of a soluble binder. Afterwards, the beaded-coated implant is sintered at high temperatures leading to binder removal (evaporation) and solid-state diffusion between the bead and the substrate. This process can also be repeated multiple times to obtain coating with higher thickness. Porosity between 30 to 50% and pore sizes ranging from 100 to 500  $\mu\text{m}$  can be obtained through this process [37,38].

Nowadays, plasma spray coating is widely used to obtain porous structures. This technique not only is cost effective, but it is also very versatile since it is readily applicable to all implant designs. In 1984, cementless implants coated with HA through plasma spraying were introduced by Ronald Furlong. Synthetic HA has similar properties to the inorganic component of bone and has been found to have osteoinductive properties (induce bone formation). Many of today's brands that produce cementless hip implants incorporate a HA coating with very good results in terms of implant fixation in the long run [39–44]. Despite being an effective method by itself, HA coatings produced by plasma spray still present some concerns such as delamination, the disintegration of the coating, brittleness and HA wear particles, all of which can lead to third body wear, inflammations, and implant loosening [45,46]. In order to avoid these issues, today many manufacturers combine porous structures with HA coatings. These implants have a double layer structure that consists of a porous Ti layer coated with HA layer. HA coatings in a porous structure show improved bonding, thus reduced risk of delamination, as well as improved implant fixation to the bone since the increased osteoconductivity of HA promotes bone ingrowth into the porous structure. The plasma spray technique also has the capability and advantage of producing both structures (Ti porous layer and HA layer) [44–46].

Despite the large number of techniques that can be used to produce porous surfaces, the Ti core of these implants is still mostly obtained through machining operations of Ti blanks. Due to low thermal conductivity and high reactivity of Ti and its alloys, machining is incredibly difficult and thus time and cost intensive. Due to the nature of machining operations, a large amount of raw material is also lost during the process [47].

In the last years, additive manufacturing (AM) techniques have been gaining traction. AM techniques can produce complex geometries with tailored porous structures and with much more design freedom. Additionally, complex designs, result in lighter components and at the same time reduce material waste due to near net-shape implants. The main AM techniques used to produce porous Ti structures include selective laser melting (SLM), laser metal deposition (LMD) and electron beam melting (EBM). These techniques function on a layer-by-layer basis where a high energy beam/laser is used to melt the Ti powders and form the desired geometry. AM techniques offer several advantages over the more traditional methods however some shortcomings still need to be solved for a more widespread adoption. These include the high cost of AM technologies, processing scalability, poor surface finish, residual stresses, among others [48–51]

Bearing surfaces in hip implants, i. e. the liner and femoral head, must have low coefficient of friction (COF), high surface hardness, wear resistance, biocompatibility, and bioinertness. Currently, the gold standard is still a metal on polymer bearing couple, where a femoral head made of CoCr alloy slides on an ultra-high molecular weight polyethylene (UHMWPE) liner [52,53]. UHMWPE was first used as liner in 1958 and is characterized by its long chains of ethylene monomers. Compared to other polymers, UHMWPE offers superior wear resistance, high fracture toughness and biocompatibility [54]. Similar to other materials, UHMWPE polymers also faced some problems earlier on, mainly degradation of the mechanical properties due to sterilization, inadequate implant geometry, low shelf life, and oxidative degradation, all of which resulted in increased wear rates. UHMWPE wear particles were found to cause osteolysis and eventually failure of the implant. In order to improve the wear resistance, high crosslinked polyethylene (XLPE) was developed and introduced in orthopaedics in the late 1970s. In orthopaedic applications, crosslinking of UHMWPE is obtained through high-energy irradiation through either gamma or electron beam radiation, to obtain polymer chains with stable C-C bonds and thus higher molecular weight. After crosslinking, the polymer is heat treated and finally sterilized. Studies showed an improvement in wear resistance over the base UHMWPE [55]. However, due to heat treatment, XLPE tends to present inferior tensile strength, Young's modulus, elongation-to-break and fatigue resistance to

UHMWPE, nonetheless, mechanical properties are still above the ones required [54]. Currently, research is being made to improve the drawbacks of XLPE, such as the addition of antioxidants like vitamin E and surface treatments [27].

Ceramic on ceramic bearings (CoC), including the femoral head and the liner, were introduced in the late 1960s and since then have been subjected to a few iterations, mainly to reduce the risk of fracture. Ceramic materials are promising when it comes to the higher life-span of hip implants. Compared to other bearing couples, CoC bearings show higher wear resistance and lower COF values. In addition, wear particles from these bearing are relatively inert with very low risk of osteolysis [56]. Alumina ( $\text{Al}_2\text{O}_3$ ) was the first ceramic to be used in THR, due to its biocompatibility and high wear resistance. Despite early studies showing significantly lower wear volume losses, there was still significant implant failure due to fracture. In the following years after its first use, considerable efforts were made, mainly on the manufacturing process, to improve the fracture toughness of alumina. The second generation of alumina bearings contained small amounts of magnesium oxide (MgO) to prevent grain growth during processing. Later, alumina bearings were processed by hot isostatic pressing (HIP), which allowed denser microstructures and improved mechanical properties [57]. Along the years, the risk of fracture for alumina bearings has decreased considerably [56]. In the early years of CoC bearings, zirconia was also used. Zirconia ( $\text{ZrO}_2$ ) and yttria-stabilized zirconia (YSZ) were used in femoral heads instead of  $\text{Al}_2\text{O}_3$ , due to increased fracture toughness and bending strength. However, after some years, it was found that under the environmental conditions of the human body (moisture and stress),  $\text{ZrO}_2$  could undergo a phase transition, which could lead to catastrophic failure due to increased risk of fracture and wear [58]. Despite being used in hundreds of thousands of implants, over the years, the use of  $\text{ZrO}_2$  in hip implants has been decreasing [59]. In order to prevent the drawbacks of both  $\text{Al}_2\text{O}_3$  and  $\text{ZrO}_2$  bearings,  $\text{Al}_2\text{O}_3$ - $\text{ZrO}_2$  composites were developed around the year 2000 and are now widely used.  $\text{ZrO}_2$ -toughened  $\text{Al}_2\text{O}_3$  (ZTA) is a very successful and common composite. In these composites, up to 25 wt% of YSZ is added to fine grained  $\text{Al}_2\text{O}_3$  (0.5 to 0.6  $\mu\text{m}$ ), to obtain composites with high wear resistance and improved fracture toughness and flexural strength. In recent years, these composites are being further improved.

During processing, strontium oxide crystals can be added to the powder mixtures, to form strontium aluminate platelets ( $\text{SrAl}_{12}\text{-Cr}_x\text{O}_{19}$ ), which reduce crack propagation by neutralizing the crack energy, i. e. when the crack reaches these platelets, extra energy is required to go around them. Otherwise, the crack does not propagate further. Additives such as chromium oxide can also be added, which have been reported to improve toughness without jeopardizing the hardness [27,57]. More advanced materials have also been developed. In 2003, Smith & Nephew, introduced a ceramic/metal hybrid material (Oxium™), which can have the advantages of both a ceramic and metal. This material is a zirconium alloy (Zr-2.5Nb) that, when heated in an oxygen environment, the surface (about 4 to 5  $\mu\text{m}$  depth) transforms in a black zirconium oxide with high wear resistance, while the core maintains the increased fracture toughness and fatigue strength of the base alloy [60,61].

### *2.1.2. Failure of hip implants*

Despite THA being one of the most successful orthopaedic surgeries, with very high survival rates, implant failure still occurs and revision surgery is needed [62,63]. Several factors can lead to implant failure, and these can be divided in three groups: patient-related factors, implant-related factors, and surgery-related factors [64,65]. Patient-related factors include bone quality for acetabular and femoral stem survival [66], as well as other variables that may lead to higher probability of infections and dislocations [64]. Over the years, many studies have been conducted to determine other outside factors such as BMI (Body Mass Index), smoking, use of anti-inflammatory drugs, psychological factors, age, sex, social factors, socioeconomic factors, among others. Despite this, most of the time, contradictory results are obtained and thus an apparent effect of such factors is still subjected to controversy [64,65,67–71]. For surgery-related factors, the surgical approach to THA surgery is important. There are three distinct approaches to THA surgery: lateral, posterior and anterior approach and each one has advantages and disadvantages [72]. Some studies have reported that the posterior approach is associated with higher percentage of revision surgery due to increased risk of dislocation and infection [72–75]. Surgeon experience and expertise also play an important role in early implant failure and there are



reports showing that THA surgery performed by less experienced doctors lead to higher risk of revision surgery [76].

The most common implant-related factors include aseptic loosening, bioinertness, and osteolysis due to wear and corrosion products. Aseptic loosening is mainly associated with wear debris and stress-shielding effects. Upon implantation, the structure of the bone surrounding the hip implant will change once its load distribution heavily influences it. Basically, the bone adjusts its mineral density and structure to accommodate the new load demand. However, if the bone does not receive enough mechanical stimulus, since the implant supports most of the load. In that case, its mineral density will decrease leading to bone resorption around the implant and ultimately implant loosening [77,78].

Wear and corrosion are associated with osteolysis and aseptic loosening processes since osteolysis is one of the main consequences of wear and corrosion. In general terms, osteolysis can be described as a cascade of biological responses that start from the release of wear and corrosion products from the implant to the surrounding bone. The released debris will be phagocytosed (absorbed) by macrophages, which in response will release cytokines (proteins), enzymes and other biological compounds that trigger a complex biological response by osteoclasts, which are the organisms responsible for bone resorption [79,80]. Along with this process, other biological responses such as infections can also be present and most of the time implant removal is necessary to eradicate the problem. Infections occur due to bacterial adhesion and proliferation on the implant surface, and the most convenient way to prevent infections is to inhibit bacterial adhesion and proliferation. Surface chemistry and roughness play an important role in bacterial inhibition [81,82]

Bioinertness can also be a problem concerning implants made of Ti and its alloys. The inability of an implant surface to integrate with the adjacent bone and other tissues lead to poor osteointegration, which is necessary to have a lasting implant and avoid implant loosening [83]. Hence, materials with an appropriate surface are highly essential for the implant to integrate well with the adjacent bone. Surface chemistry, surface roughness and surface topography play a major role in the development of effective osteointegration [15].

### 2.1.3. Corrosion and tribocorrosion in hip implants

Even though Ti and Ti alloys based biomedical implants are recognized for having good corrosion behaviour in the human body, corrosion processes may still occur. In hip implants, corrosion processes are usually associated to a tribocorrosion process. Severe corrosion problems have often been related to modular implants, such as crevice and mechanically assisted corrosion (MAC). Although modular hip offers several advantages, mainly because they allow to tailor the implant for each individual, the interface between different parts of the implant has revealed to be quite problematic when it comes to corrosion [84]. The most common interfaces include the neck/stem and neck/femoral head interface, which have been reported to be quite susceptible to a combination of crevice and fretting corrosion, described as mechanically assisted crevice corrosion (MACC) [85].

As described by Gilbert et al. in 1993 [86], MACC can be considered as classic crevice corrosion with some minor modifications. At these interfaces, it is expected that narrow gaps will exist. Gaps may arise from machining marks, surface irregularities, errors during implantation, the mismatch between components, overall design of the components, among others. These gaps will result in the formation of small crevices, where body fluids can penetrate. Due to physical activity, shear stresses, and micromovements (fretting), the native oxide film will be damaged leading to exposure of fresh metallic area to the surrounding environment. Due to oxidation of the metal surfaces, oxygen is consumed from the environment and consequently the concentration of free metal ions increases. With time, metal ions will attract chloride ions to form metal-chlorides which will react with water to form hydroxide and hydrochloric acids leading to very low pH levels. Regardless of the fact that Ti can repassivate (regenerate the passive oxide film), if this repassivation rate is lower than the degradation process, Ti will act as an active metal under this environment. In the last years, studies have reported implant failure due to MACC, in both Ti and CoCr based implants [87–89].

It is also known that tribocorrosion processes may also occur at the implant/bone interface (stem/bone and acetabular cup/bone interface). In addition, if screws are used to fix the acetabular component, tribocorrosion

processes may also take place at the screw/bone interface. Despite the fact that these interfaces are fixated to each other, with physical activity, some degree of motion between these interfaces is bound to happen [16].

Another important factor to be taken into consideration is that the surrounding environment may also change and influence the corrosion behaviour of the implant. Both articulating surfaces and junctions of the implant are surrounded by the synovial fluid (buffered solution with pH 7.4 at around 37 °C), however, this environment is prone to change. The presence of ions such as Cl<sup>-</sup>, Ca<sup>2+</sup>, and K<sup>+</sup>, may change the overall corrosion behaviour of the implant. Chloride ions are highly aggressive to metal surfaces, as they can easily penetrate the passive film due to high diffusivity, and it has been reported that high levels of chloride ions may induce localized corrosion. Ions such as Ca<sup>2+</sup> and K<sup>+</sup> are responsible for maintaining body pH. If there are drastic alterations in their concentration, body pH may drastically change, increasing the probability of corrosion processes taking place [90]. The presence of proteins at the implant surface may also lead to significant changes in the corrosion behaviour. In fact, they can have beneficial or detrimental effects on both corrosion and tribocorrosion behaviour. Proteins may present a shielding effect and/or lubrication effect, which may protect the material from corrosion and wear. However, these proteins can also have a negative effect: by trapping wear debris at the implant interface, the material can be more susceptible to third body wear. Additionally, the corrosion behaviour can also be significantly jeopardized, as proteins can bind to the metal and consequently cause degradation of the native oxide film [91].

Adverse Local Tissue Reactions (ALTRs) are one of the main causes of tribocorrosion processes taking place within the implant and is one of the main causes of hip implant failure. ALTRs are caused by the interaction of body proteins and wear debris leading to the growth of cystic and fibrotic masses. A simple explanation is that the immune system has a stronger reaction than it should have and consequently, it leads to the dysregulation of the expected biological behaviour at these zones [92]. A significant amount of studies reported hip implant failure due to ALTRs throughout the years [93–98].

The effect of material properties and environment on the tribocorrosion behaviour of Ti and its alloys have been thoroughly researched. Several Ti alloys

have been studied regarding the tribocorrosion behaviour under simulated body fluids. Correa et al. [99] studied the effect of molybdenum (Mo) content on the tribocorrosion behaviour of Ti-Zr-based alloys. The authors reported that the addition of Mo lead to an improvement in tribocorrosion resistance compared to CP Ti, mainly attributed to changes in the overall microstructure of the alloys. In addition, the authors also reported that higher amount of Mo led to lower overall Young's modulus, to values closer to the bone. However, the authors also reported that a substantial amount of Mo could also lead to overall lower hardness values, which could reduce the overall tribocorrosion resistance of the alloy. Pina et al. [100] studied the effect of tin (Sn) content on the tribocorrosion behaviour of  $\beta$ -type Ti-30Nb alloys, once Sn functions as a  $\beta$ -phase stabilizer to decrease Young's modulus. The authors concluded that up to 2 wt% of Sn content, improved tribocorrosion behaviour, as the alloys presented reduced corrosion kinetics during sliding action, attributed to higher quality of the passive oxide film. However, higher amounts of Sn led to a decrease in the overall hardness of the alloys, which translated into lower wear resistance and thus higher corrosion kinetics during sliding action. Çaha et al. [101] studied the tribocorrosion behaviour of Ti-40Nb and Ti-25Nb-5Fe alloys and reported significant differences in the overall tribocorrosion behaviour. Ti-25Nb-5Fe alloy presented similar tribocorrosion behaviour under open circuit potential (OCP) and under anodic and cathodic applied potentials, indicating that the tribocorrosion behaviour was mainly influenced by mechanical wear. However, Ti-40Nb alloy presented considerably lower wear volume loss under the anodic domain which was attributed to the antagonistic effect between wear and corrosion, due to formation of dense tribolayers during mechanical action, which gave limited protection against wear. Hacisalihoglu et al. [102] studied the tribocorrosion behaviour of  $\alpha$  (CP Ti),  $\alpha+\beta$  (Ti-6Al-4V) and  $\beta$ -type (Ti13Nb13Zr, Ti15Mo and Ti-45Nb) alloys. While the corrosion behaviour under static conditions was mostly very similar for all alloys, differences could be observed in the tribocorrosion behaviour. Under OCP, CP Ti presented a nobler behaviour than the other alloys, while Ti-6Al-4V presented the more active behaviour despite presenting the lowest wear volume loss. On the other hand, Ti-15Mo and Ti-45Nb alloys, presented considerably higher wear volume losses compared to the other alloys due to higher reactivity. Differences were also observed on the morphology of the

wear track and wear debris. The wear tracks of Ti-6Al-4V and Ti-13Nb-13Zr alloys showed practically the same morphology yet the wear debris were quite different. Wear debris from Ti-6Al-4V alloy were smaller and grainy-shaped and wear debris from Ti-13Nb-13Zr alloy were larger and flaky-type. CP Ti presented more smearing effect and large plastic deformation while Ti-15Mo and Ti-45Nb alloys presented considerably higher COF values that may indicate a much stronger abrasive effect from wear products.

Besides the overall composition of the alloy, the processing method may also influence the tribocorrosion behaviour of the material. Buciumeanu et al. [103] compared the tribocorrosion behaviour of commercial Ti-6Al-4V alloy and the same alloy processed by hot-pressing and by laser engineered net shaping (LENS). The authors reported that the alloy processed by LENS presented better tribocorrosion resistance, as it presented less tendency to corrosion under sliding as well as lower wear volume loss, which was explained by the fact that this technique allowed to obtain finer microstructures due to the formation of acicular  $\alpha$ -phase. In addition, the authors also reported that the improved behaviour could also be related to the fact that the alloy presented higher percentage of  $\alpha$  phases than the alloys produced by casting and hot-pressing. Toptan et al. [104] also studied the tribocorrosion behaviour of Ti-6Al-4V alloy processed by different processing techniques, being hot-pressing, cast and selective laser melting (SLM). In this study, the authors did not find significant differences on the tribocorrosion behaviour, however, under static condition, the alloy processed by SLM showed reduced corrosion resistance, which was attributed to the overall lower quality of the passive film, probably due to formation of more  $\alpha'$  martensite phase.

The effect of the environment on the tribocorrosion behaviour of Ti and its alloys has also been studied. Wang et al. [105] studied the effect of particle concentration (third body wear) and applied load on the tribocorrosion behaviour of Ti-25Nb-3Mo-3Zr-2Sn biomedical alloy by adding hard SiC particles into the electrolyte (Ringer's solution). The authors reported that higher concentration of particles led to higher wear volumes, however, some differences were observed. For lower concentrations, the worn surfaces tended to present severe plastic deformation explained by the increased load per particle and thus higher penetration. Nevertheless, for higher concentrations, the particles could only roll

and remove material. In fact, due to the rolling effect, higher particle concentration led to lower average COF values. Runa et al. [106] studied the effect that proteins have on the tribocorrosion behaviour of Ti-6Al-4V alloys by adding proteins (albumin fraction V) to PBS (phosphate-buffered saline solution) electrolyte. Under static condition, the presence of proteins did not significantly affect the corrosion behaviour of the alloy, however, differences were observed under sliding. The authors found that under certain conditions, proteins might present a detrimental effect as they can slow down the repassivation of the worn surface during sliding, however, it was also noticed that after some time, these proteins could also act as a tribolayer and therefore have a protective effect.

## **2.2. Titanium matrix composites for improved tribocorrosion resistance**

In order to improve the tribocorrosion resistance of Ti and its alloys, a variety of surface modification techniques can be used to produce wear resistant surfaces [107–113]. The addition of hard ceramic particles to produce TMCs has also been an effective method in enhancing tribocorrosion resistance of titanium [107,114]. These reinforcement particles can improve the wear resistance through direct strengthening since they carry the applied load when in contact with another material. Furthermore, they also enhance the strength of the metallic matrix by inducing an increase in dislocation density, Orowan strengthening, and grain size refinement [114]. Although Ti composites are an effective method to increase the wear resistance of titanium, most of hip implants, that currently exist on the market, do not yet take advantage of TMCs.

### *2.2.1. Ti-B<sub>4</sub>C and Ti-TiB-TiC composites*

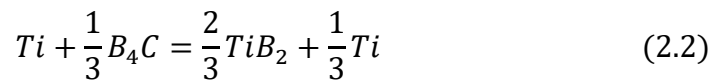
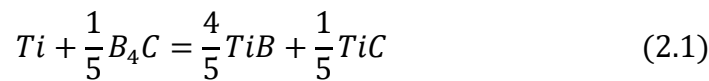
B<sub>4</sub>C, known for being the third hardest material after diamond and cubic boron nitride, is widely used to produce TMCs. B<sub>4</sub>C particles can fully react with titanium to produce TiB, TiC, and/or TiB<sub>2</sub> reinforcements (*in-situ* TMCs) and it can also be used as ex-situ reinforcement to improve the tribocorrosion resistance of Ti [114].

TiB whiskers and TiC particles are recognized for being excellent reinforcements for TMCs. Strong interfacial bonding with Ti as well as similar coefficients of thermal expansion (CTEs), being  $8.2 \times 10^{-6}/^{\circ}\text{C}$  for Ti,  $7.2 \times 10^{-6}/^{\circ}\text{C}$  for TiB, and  $7.9 \times 10^{-6}/^{\circ}\text{C}$  for TiC, make these phases highly suitable to produce

TMCs. Furthermore, these reinforcements also possess desirable mechanical and electrochemical properties such as high hardness, low density and good corrosion resistance [115–117].

It is well reported that the addition of these reinforcements can improve the mechanical properties of Ti, however, studies on corrosion and tribocorrosion are still very limited. Another advantage of these composites resides in the fact that they can be easily and economically processed by a mixture of Ti and B<sub>4</sub>C powders using powder metallurgy based techniques [118–121].

The Ti-B<sub>4</sub>C system is characterized by the formation of TiB, TiB<sub>2</sub>, and TiC phases. When Ti reacts with B<sub>4</sub>C, two potential reactions can occur (reactions 2.1 and 2.2) [122,123].



These reaction products belong to the Ti-B-C system. Because of lower Gibbs free energy ( $\Delta G$ ) and enthalpy ( $\Delta H$ ), TiB<sub>2</sub> is more likely to form in preference of TiB. However, due to limited mass transport rate in solid-state sintering, the main products of Ti-B<sub>4</sub>C reaction are almost always TiC and TiB [123]. In fact, several studies show that the main products of Ti + B<sub>4</sub>C reaction are TiB whiskers TiC particles [116,117,123–126].

Changes in  $\Delta G$  and  $\Delta H$  reaction of the Ti-B-C system are shown in Fig. 2.2.

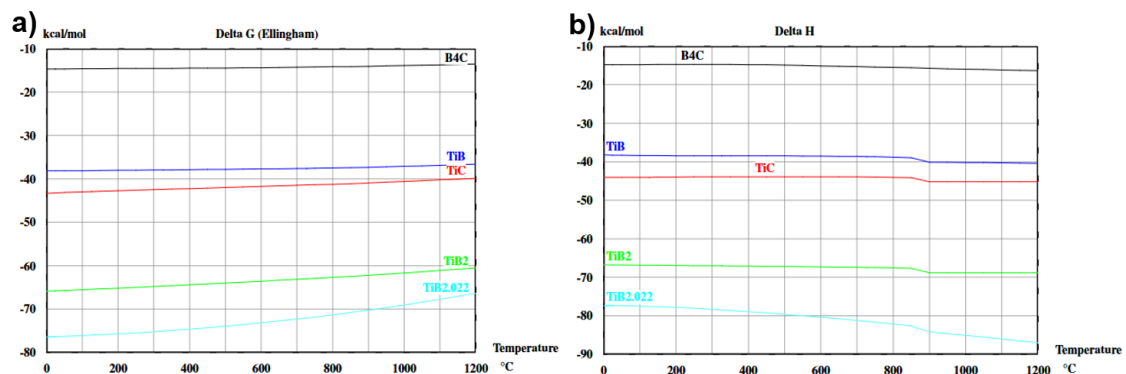


**Figure 2.2.** Changes in (a) Gibbs free energy ( $\Delta G$ ) and (b) reaction enthalpy ( $\Delta H$ ) for reactions in the Ti-B-C system [105].

The ternary phase diagram of the Ti-B-C system is shown in Fig. 2.3. As can be seen, the formation of TiB and/or TiB<sub>2</sub> is possible, depending on the percentage of B and C. TiB<sub>2</sub> is more likely to form near the B<sub>4</sub>C particles, since

the concentration of B is higher. Meanwhile, TiB is more likely to form near the Ti matrix due to the lower amount of B.

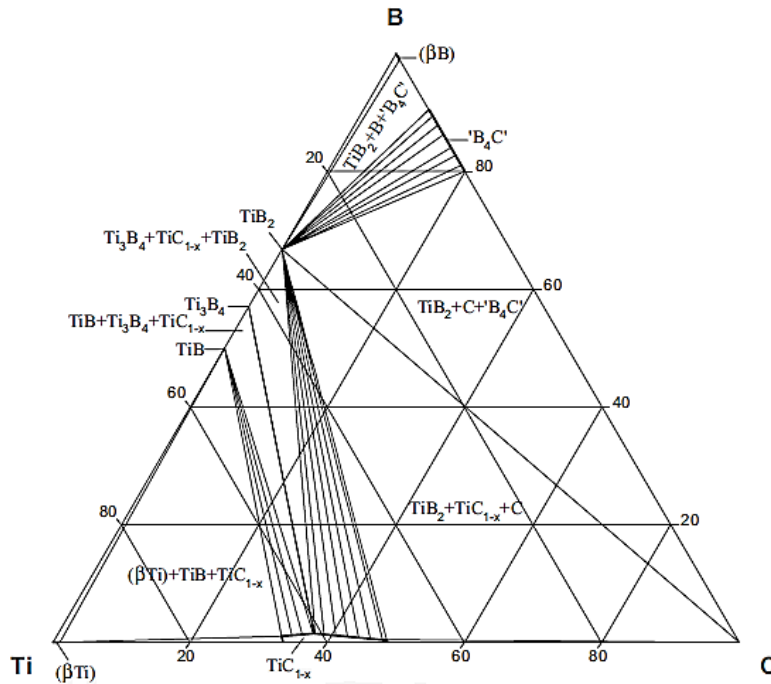


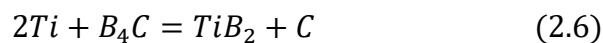
**Figure 2.3.** Ternary phase diagram of Ti-B-C system at 1400 °C [127].

A schematic diagram of the microstructure evolution at the interface between  $B_4C$  and Ti is given in Fig. 2.4. In the first stage, dissolution of  $B_4C$  starts to occur and consequently B and C atoms begin to diffuse into the Ti matrix. Because of the vacancies left behind, Ti atoms from the matrix start to diffuse into the  $B_4C$  particle.

Because of the B and C atoms present in the Ti matrix, reactions (2.3) -(2.5) can happen:



Since the concentration of B is higher at the interface, TiB whiskers are the first to form, and after some time TiC particles also form. In the  $B_4C$  particle, the presence of Ti can give origin to reaction (2.6), and a  $TiB_2$  layer starts to form between the previous layer and the  $B_4C$  particle.





As the  $\text{TiB}_2$  layer grows, the diffusion of C is inhibited, giving origin to a C layer. Currently, most studies focus on *in-situ* TMCs, where the reaction products ( $\text{TiB}$ ,  $\text{TiC}$  and  $\text{TiB}_2$ ) act as reinforcement [115–117,128].



**Figure 2.4.** Schematic diagram of the microstructure evolution in the Ti-B<sub>4</sub>C system [111].

The mechanical properties of TMCs reinforced with either TiB or TiC or both are widely reported. TiB whiskers are reported to improve several mechanical properties, such as yield strength [129,130], ultimate compressive strength [130], tensile strength and creep resistance once these phases can undertake higher stresses than the titanium matrix [115,126,131]. TiC particles are reported to prevent crack nucleation and propagation [115,116], improve yield strength and ultimate tensile strength [132]. TMCs reinforced by both TiB and TiC are also reported to have improved ultimate tensile strength and yield strength [133]. Furthermore, synergistic effects between TiB and TiC on ultimate tensile strength have also been reported, meaning that TMCs reinforced by both TiB and TiC can exhibit better mechanical behaviour over sole TiB or sole TiC reinforced TMCs [134].

The effect of TiC and TiB reinforcements on wear resistance of titanium has also been reported: However, literature is still very limited regarding this topic. TMCs reinforced with TiC and TiB show a decreased wear loss under dry sliding and fretting conditions compared with unreinforced Ti. Furthermore, wear resistance is also reported to increase with reinforcement content [107,128,135]. In these studies, the increase in wear resistance is explained by the increase in overall hardness due to reinforcement phases. To the best of the author's knowledge, there are no studies on tribocorrosion behaviour of Ti-TiB-TiC composites, there are, however, some studies regarding similar composites. Toptan et al. [114] studied the tribocorrosion behaviour of *ex-situ* Ti-B<sub>4</sub>C composites processed by hot-pressing. The authors observed the formation of a reaction zone between the B<sub>4</sub>C particles and the titanium matrix which was

identified to be a mixture of TiB and TiC phases. Composites presented less tendency to corrosion as well as reduced corrosion kinetics during sliding action in addition to a significant reduction and wear volume loss values, attributed to the ability of reinforcement particles to carry the applied load and protect the Ti matrix. Silva et al. [136] studied the tribocorrosion behaviour of *in-situ* Ti-TiB-TiN<sub>x</sub> composites processed by reactive hot-pressing and also reported reduced tendency to corrosion under sliding in addition to significantly reduced wear volume loss values compared to unreinforced Ti.

Literature regarding the effect of both TiB and TiC phases on the corrosion behaviour of Ti is also still very limited. Diao et al. [137] studied the corrosion behaviour of a Ti alloy by laser cladding with Ti/TiC/TiB<sub>2</sub> powders and reported an increase in OCP and a decrease in corrosion kinetics due to grain refinement and increased corrosion resistance of TiC and TiB<sub>2</sub> phases. Chen et al. [138] studied the corrosion behaviour of Ti-TiB composites processed by SLM and obtained favourable results. Ti-TiB composites showed increased corrosion resistance, which was attributed to the presence of TiB<sub>2</sub> and TiB particles. These particles acted as a micro-cathode during corrosion process, facilitating the anodic dissolution of Ti and consequently accelerating the formation of the protective passive film.

Regarding the biological response of these two phases, literature is also very limited. TiB phases have been reported to have similar cytocompatibility to that of Ti [139], while TiC coatings have been reported to improve the bioactivity of titanium once these coatings stimulate osteoblast proliferation, adhesion, and differentiation [140].

### 2.2.2. *Ti-Al<sub>2</sub>O<sub>3</sub> composites*

Alumina has been widely used in biomedical implants, being first used in 1971 in France and more generally in Europe in 1974. Alumina was first used to replace the typical metallic femoral head of hip implants and today it is still used together with UHMWPE, which is a part of the acetabular component [141–143]. In a total hip replacement, alumina-alumina bearings are known to be one of the most resistant to wear. Furthermore, a low rate of osteolysis has also been reported due to alumina's exceptional wear resistance and low surface

roughness [144–147]. Similar CTE with Ti matrix and excellent compressive strength also make alumina a potential candidate for TMCs [148,149].

Similar to other TMCs, the reaction products that form at the interface also plays an essential role in the final composite properties, therefore, understanding of the phase transformations is important. As can be seen in the ternary diagram of this system, Ti-Al intermetallic compounds, such as  $Ti_3Al$ ,  $TiAl$ ,  $TiAl_2$  and  $TiAl_3$  can be formed at the interface (Fig. 2.5). Furthermore, Ti oxides, such as  $TiO$  and  $TiO_2$ , are also likely to form [150].

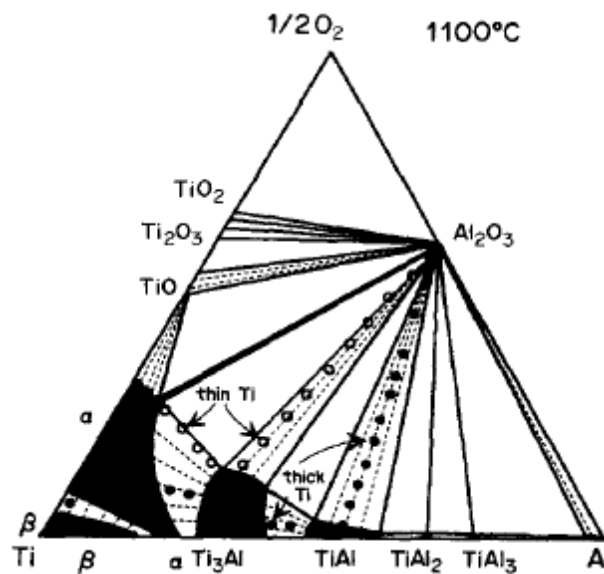


**Figure 2.5.** Ternary phase diagram of Ti-Al-O system at 1100 °C [151].

Regarding these oxides, it has been reported that due to the limited diffusion capability of oxygen,  $TiO$  and  $TiO_2$  oxides are harder to be detected in the reaction zone. Since Al has higher diffusion capability, Ti-Al intermetallic are more likely to form at the interface. According to some researchers [152,153],  $TiAl_2$ ,  $TiAl_5$ , and  $TiAl_3$  have lower  $\Delta G$ , meaning that they are more prone to form at the interface. However, it has been reported that at higher temperatures, these compounds are unstable and  $TiAl_3$  easily reacts with Ti to form  $TiAl$  and  $Ti_3Al$  [150].

It has been widely reported in the literature that  $TiAl$  and  $Ti_3Al$  are the main reaction products of  $Ti-Al_2O_3$  reaction system [149,154,155] where the reaction sequence at 1100 °C is  $Al_2O_3/TiAl/Ti_3Al/Ti$  [149,154].  $TiAl$  and  $Ti_3Al$  are the main intermetallic compounds found in the Ti-Al-O system, and are characterized for

having low density and high melting point, but they also present high Young's modulus [155].

The formation of these reaction products depends on the local oxygen activity and temperature. Under low oxygen pressure, dissolution of both oxygen and Al take place in  $\text{Al}_2\text{O}_3$ . For this reason, near the Ti matrix,  $\text{Ti}_3\text{Al}$  starts to form and further Al diffusion gives origin to TiAl. Diffusion of oxygen can result in the transformation of  $\beta$ -Ti in  $\alpha$ -Ti. It has also been reported that  $\text{Ti}_3\text{Al}$  is the first to form and after Al enrichment the formation of TiAl can occur. With low residence time and lower temperature, the formation of TiAl can be reduced or avoided [150,156].

Similar to Ti-TiB-TiC composites, literature is also very limited on the corrosion and tribocorrosion behaviour of these composites. Gordo et al. [157] studied the corrosion and tribocorrosion behaviour of Ti + 1 wt. %  $\text{Al}_2\text{O}_3$  composites processed by pressureless sintering. It was observed that the corrosion behaviour of both Ti and Ti- $\text{Al}_2\text{O}_3$  were similar, meaning that the introduction of the ceramic phase did not jeopardize the corrosion resistance of CP Ti. However, in this study, the  $\text{Al}_2\text{O}_3$  particles were fully dissolved in the matrix and were not used directly as reinforcement particles. It has been reported that the presence of TiAl can negatively affect the corrosion resistance of Ti- $\text{Al}_2\text{O}_3$  interfaces. Rocha et al. [154] studied the corrosion behaviour of Ti- $\text{Al}_2\text{O}_3$  interfaces produced by diffusion bonding of titanium substrates and alumina. It was observed that both TiAl and  $\text{Ti}_3\text{Al}$  formed at the interface. Regarding the corrosion tests, it was reported that the chemical degradation of the interface was dictated by the presence of TiAl while  $\text{Ti}_3\text{Al}$  was found to be electrochemical compatible with titanium.

More recent studies by Bahraminasab et al. [158,159] reported that the addition of  $\text{Al}_2\text{O}_3$  particles into a Ti matrix, may have a dual effect on the corrosion behaviour of the composites.  $\text{Al}_2\text{O}_3$  particles may lead to an improvement in corrosion resistance when compared with unreinforced Ti, due to the formation of a higher quality native oxide film, however, higher percentage of reinforcement phase may lead to reduced corrosion behaviour compared to Ti, probably due to higher amount of TiAl phases which may have increased susceptibility to corrosion.

There are also limited number of published works on the tribocorrosion behaviour of Ti-Al<sub>2</sub>O<sub>3</sub> composites. Oliveira et al. [160] studied the wear behaviour of Ti-Al<sub>2</sub>O<sub>3</sub> composites processed by conventional powder metallurgy. Depending on the wear parameters, composites could present reduced or increased wear volume losses compared to unreinforced Ti. Under harsher sliding conditions (higher contact pressure and sliding frequency), Al<sub>2</sub>O<sub>3</sub> particles could break and be released as third body wear debris, which resulted in considerably higher wear volume loss after the tests.

There are some studies regarding metallic matrixes reinforced with Al<sub>2</sub>O<sub>3</sub>. Ribeiro et al. [161] studied the synergism between corrosion and wear on hot-pressed CoCrMo alloys reinforced by 10% (vol.) Al<sub>2</sub>O<sub>3</sub>. The authors concluded that the introduction of reinforcement particles did not jeopardize the corrosion resistance of the base alloy. Furthermore, the authors also concluded that the composites presented lower wear volume loss due to the increased wear resistance provided by the presence of alumina particles. The wear resistance of aluminium matrix composites with alumina particles has also been extensively studied and similar results were obtained: the introduction of alumina particles leads to an increase in wear resistance when compared with the base material [162–165]. Still, it is important to note that for Ti-Al<sub>2</sub>O<sub>3</sub> systems, results may be different once distinct reaction products form at the interface, which play an important role in corrosion, tribocorrosion, and mechanical behaviour.

### **2.3. Micro-arc and thermal oxidation treatment for improvement of bioactivity**

Bioactivity, which determines the osteointegratability of the implant, is a requirement to produce a lasting implant [12]. Unfortunately, Ti cannot bond directly to the bone due to lack of bioactivity. Surface modification techniques such as thermal spraying, physical vapor deposition, cold gas spraying, sand blasting, etching, anodization, thermal oxidation, among other techniques are being used in order to solve these issues [166–174]. These techniques aim to modify the surface of the implant in terms of topography and chemistry to improve osteointegration.

Topography plays an essential role in producing a lasting implant. Porous structures, in the macro scale ranging from 50 to 400 μm, are known to improve

implant fixation [175]. Bone growth into a porous structure is known to produce a mechanical interlocking between the bone and implant. On the other hand, porosity in the micro-scale has proven to be beneficial in osteoblast adhesion and proliferation, mainly due to increased contact area between the cells and the implant material [176–178]. Surface chemistry also plays an important role. Wettability is directly related to the degree of contact between the implant and the surrounding biologic environment, thus, increased wettability enhances the contact between the implant surface and the biological environment [179]. Bioactive agents, such as Ca and P, can also be used to improve bioactivity. While Ca ions are known to stimulate osteoblastic cell differentiation, increase bone-implant contact, and the ability to attract proteins resulting in a faster osteointegration, phosphate ions show increased bone-implant contact [180–183].

AT has good potential when it comes to producing implants with adequate topography and chemistry. Depending on the parameters (mainly electrolyte composition and voltage) it is possible to obtain pores in both macro, micro and even nano-range. Another advantage resides in the fact that multiple ATs can be combined to produce a hierarchical porous structure. Generally, in the first treatment, the objective is to obtain porosity in the macroscale range for bone ingrowth. Then, in the next step, the aim is to produce micro- or/and nano-porosity on top of the macro-pores formed before, to promote cell adhesion and proliferation [178,184–186].

Micro-arc oxidation (MAO) treatment is one type of AT treatment, where several hundreds of volts are used to produce a micro-porous, crystalline, and thick TiO<sub>2</sub> layer that is recognized for having good osteointegration capabilities [167,187–190]. The distribution, size and morphology of the pores can be controlled by changing parameters, such as electrolyte composition, applied voltage or current and time. Another advantage of this technique is that it is also possible to incorporate bioactive elements in these layers, such as Ca and P, using an electrolyte rich in these elements. The amount and ratio of these elements can also be adjusted, changing electrolyte composition/concentration [191,192].

Implant associated infections are also a problem and once infection occurs, conventional antibiotic therapy is generally ineffective. Therefore, bacterial

adhesion must be avoided [82]. Surface modification together with antimicrobial agents, such as Mg and Zn elements, have been found to be an effective way to reduce or inhibit the occurrence of implant associated infections [193]. Mg and Zn elements can also be directly added to the TiO<sub>2</sub> layer during MAO treatment [81,194]. Zn is an attractive element since in addition to antibacterial properties, it also has the advantage of improving bioactivity once it is a structural component of some enzymes, proteins and bone. [195]. Incorporation of Zn into TiO<sub>2</sub> layers produced by MAO can be done by adding zinc acetate into the electrolyte [196]. Mg is also an interesting choice once it has been reported that the corrosion products of Mg prevent the growth of bacteria [197].

Thermal oxidation (TO) is a simple and cost effective technique that takes advantage of the high reactivity of Ti with air and/or water, in order to promote the growth of the native TiO<sub>2</sub> passive layer and alter its properties, such as crystal structure, topography, and chemical composition in a way to improve bioactivity [198–201]. This technique generally consists in heating up the Ti or Ti alloy to temperatures ranging from 400 to 1000 °C in open or oxygen-rich atmospheres, with stage times ranging from a few minutes to several hours. Depending on these parameters, it is possible to control the structure of the TiO<sub>2</sub> layer. In general, higher temperatures and longer stage times lead to the formation of TiO<sub>2</sub> layers with higher thickness and increased roughness. In addition, these also tend to present a higher amount of crystalline phases, such as anatase and rutile phases [202–204]. The structure of these layers can have an impact on the biological response. For example, Wang et al. [200] studied the effect of thermal oxidation time (2, 4 and 6 h) on the biological response of TO treated Ti at 450 °C. The authors observed that samples treated for 6 h presented higher cell adhesion and osteogenic activity (responsible for bone formation) than the other groups, attributed to the higher thickness and higher rutile ratio on these layers. Park et al. [199] studied the effect of TO temperature (530, 600, 700, 800, 900 and 1000 °C) on the biological response of TO treated Ti. The temperature had a significant impact on the phase composition of these layers, as the rutile phase was only observed for TO treatments above 700 °C. Chemical composition was also influenced by the time, mainly the amount of hydroxyl groups which also had an impact on the biological response. TO layers formed at 800 and 900 °C presented the best biological response in terms of calcium phosphate formation

due to higher amount of hydroxyl groups. However, it is important to note that prolonged cycles at high temperatures may lead to problems such as spallation [203].

Besides increasing bioactivity, TiO<sub>2</sub> layers of MAO and TO treatments also present other advantages that are of extreme importance for biomedical devices. In addition to reducing stiffness mismatches [205], these layers also provide additional corrosion and wear resistance due to their higher hardness and overall higher wear resistance. Alves et al. [191] studied the corrosion mechanisms in titanium oxide-based films produced by anodic treatment together with incorporating bioactive elements (Ca and P). It was observed that the samples with anodic treatment showed two orders of magnitude drop in the corrosion current density as compared to CP Ti. On the other hand, Felgueiras et al. [182] also studied the bio-tribocorrosion behaviour of MAO treated Ti containing Ca and P, before and after osteoblastic cell culture. The authors demonstrated that the anodized surfaces granted superior resistance to repetitive sliding solicitation and ability to induce cell attachment even after degradation. Cao et al. [109] studied the tribocorrosion behaviour of TO treated Ti (700 °C during 5 h) and reported an improvement in corrosion and tribocorrosion behaviour. TO treated surfaces presented considerably lower corrosion kinetics as well as less tendency to corrosion under static and sliding conditions. In addition, a significant decrease in wear volume loss was also observed compared to untreated Ti. Similar improvements in corrosion and tribocorrosion behaviour have also been reported by other authors. Kumar et al [204] studied the effect of treatment time (8, 16, 24 and 48 h) on the corrosion resistance of thermal treated Ti at 650 °C. Samples treated for 48h presented the highest corrosion resistance which was explained by increased treatment time due to increased thickness of the oxide layers and higher amount of rutile phases. Bailey et al. [206] studied the tribocorrosion behaviour of thermal treated CP Ti (650 °C, 20 h) and reported that the rutile oxide layer presented lower friction and considerable higher wear resistance compared to untreated Ti. The authors also reported that under applied anodic potentials the durability of the oxide layer was higher.

To the best of the author knowledge, the effect of MAO or TO treatments on TMC surfaces is yet to be understood, at least from a corrosion and tribocorrosion standpoint. For the first time, the effect of these treatments on Ti-Al<sub>2</sub>O<sub>3</sub>, Ti-B<sub>4</sub>C



and *in-situ* Ti-TiB-TiC composite surfaces will be evaluated on the research papers presented through chapters 7 to 9. More detailed corrosion and tribocorrosion studies on the base composites will be first presented in chapters 3 to 5.



## References

- [1] D.P. Byrne, K.J. Mulhall, J.F. Baker, *Anatomy & Biomechanics of the Hip*, *Open Sport Med. J.* 4 (2014) 51–57.
- [2] D. Manganaro, K. Alsayouri, *Anatomy, Bony Pelvis and Lower Limb*, *Ankle Joint*, StatPearls. (2019).
- [3] J. Pfeil, *Anatomy of the hip joint*, *Minim. Invasive Surg. Total Hip Arthroplast.* (2010) 7–19.
- [4] M.L. Wolford, K. Palso, A. Bercovitz, P.D. Monica L. Wolford, M.A.; Kathleen Palso, M.A.; and Anita Bercovitz, M.P.H., *Hospitalization for Total Hip Replacement Among Inpatients Aged 45 and Over: United States, 2000–2010*, *Nchs.* (2015) 8. <http://www.cdc.gov/nchs/data/databriefs/db186.htm%5Chttp://www.ncbi.nlm.nih.gov/pubmed/25714040>.
- [5] F. Stuart J., *100 Questions & Answers About Hip Replacement*, Jones and Bartlett Publishers, 2010.
- [6] G.C. Lee, R.H. Kim, *Incidence of Modern Alumina Ceramic and Alumina Matrix Composite Femoral Head Failures in Nearly 6 Million Hip Implants*, *J. Arthroplasty.* 32 (2017) 546–551.
- [7] C. Centeno, *Replacement Materials – A Complete Guide to the Best and Worst*, (2015). <https://www.regenexx.com/hip-replacement-materials-best-worst/> (accessed September 15, 2017).
- [8] S. Affatato, D. Brando, *Introduction to wear phenomena of orthopaedic implants*, in: S. Affatato (Ed.), *Wear Orthop. Implant. Artif. Joints*, 1st ed., Woodhead, 2012: pp. 3–26.
- [9] U. Holzwarth, G. Cotogno, *Total Hip Arthroplasty*, 2012.
- [10] A. Abdulkarim, P. Ellanti, N. Motterlini, T. Fahey, J.M. O’Byrne, *Cemented versus uncemented fixation in total hip replacement: a systematic review and meta-analysis of randomized controlled trials*, *Orthop. Rev. (Pavia).* 5 (2013) 8.
- [11] S. Morshed, K.J. Bozic, M.D. Ries, H. Malchau, J.M. Colford, *Comparison of cemented and uncemented fixation in total hip replacement: A meta-analysis*, *Acta Orthop.* 78 (2007) 315–326.
- [12] X. Liu, P.K. Chu, C. Ding, *Surface modification of titanium, titanium alloys, and related materials for biomedical applications*, *Mater. Sci. Eng. R Reports.* 47 (2004) 49–121.
- [13] G.A. Schmale, P.F. Lachiewicz, S.S. Kelley, *Early failure of revision total hip arthroplasty with cemented precoated femoral components: comparison with uncemented components at 2 to 8 years*, *J Arthroplast.* 15 (2000) 718–729.
- [14] M. Ali, M. Al-Hajjar, L.M. Jennings, *Tribology of UHMWPE in the Hip*, Third Edit, Elsevier Inc., 2016.
- [15] M. Geetha, A.K. Singh, R. Asokamani, A.K. Gogia, *Ti based biomaterials, the ultimate choice for orthopaedic implants - A review*, *Prog. Mater. Sci.* 54 (2009) 397–425.
- [16] N. Diomidis, S. Mischler, N.S. More, M. Roy, *Tribo-electrochemical characterization of metallic biomaterials for total joint replacement*, *Acta Biomater.* 8 (2012) 852–859.
- [17] D.F. Williams, *On the mechanisms of biocompatibility*, *Biomaterials.* 29 (2008) 2941–2953.
- [18] M. Merola, S. Affatato, *Materials for hip prostheses: A review of wear and loading considerations*, *Materials (Basel).* 12 (2019).
- [19] S. Affatato, D. Brando, M.R. Choroszyński, M.R. Choroszyński, S.J. Skrzypek, *Biomaterials for hip implants - Important considerations relating to the choice of materials*, *Bio-Algorithms and Med-Systems.* 13 (2017) 133–145.
- [20] K. Yang, Y. Ren, *Nickel-free austenitic stainless steels for medical applications*, *Sci. Technol. Adv. Mater.* 11 (2010) 014105.

- [21] M.J. Runa, L.A. Rocha, M.T. Mathew, Corrosion and tribocorrosion behavior of CoCrMo alloys used as hip joint implant materials under simulated body fluids: Effect of proteins and normal load, 1st Port. Meet. Biomed. Eng. ENBENG 2011. (2011).
- [22] M. Bull, CoCrMo Metal-on-Metal Hip Replacements, *Bone*. 23 (2008) 1–7.
- [23] M.A. Hussein, A.S. Mohammed, N. Al-aqeeli, S. Arabia, Wear Characteristics of Metallic Biomaterials: A Review, *Materials (Basel)*. 8 (2015) 2749–2768.
- [24] F. Matassi, A. Botti, L. Sirleo, C. Carulli, M. Innocenti, Porous metal for orthopedics implants, *Clin. Cases Miner. Bone Metab.* 10 (2013) 111–115.
- [25] G. Eddy Jai Poinern, S. Brundavanam, D. Fawcett, Biomedical Magnesium Alloys: A Review of Material Properties, Surface Modifications and Potential as a Biodegradable Orthopaedic Implant, *Am. J. Biomed. Eng.* 2 (2013) 218–240.
- [26] T. McTighe, D. Brazil, W. Bruce, Metallic Alloys in Total Hip Arthroplasty, *Hip Preserv. Replace. Revis.* (2015) 1–12.
- [27] C.Y. Hu, T.R. Yoon, Recent updates for biomaterials used in total hip arthroplasty, *Biomater. Res.* 22 (2018) 1–12.
- [28] J. Quinn, R. Mcfadden, C. Chan, L. Carson, Titanium for Orthopedic Applications : An Overview of Surface Modification to Improve Biocompatibility and Prevent Bacterial Biofilm Formation, *ISCIENCE*. 23 (2020) 101745.
- [29] H.J. Rack, J.I. Qazi, Titanium alloys for biomedical applications, *Mater. Sci. Eng. C*. 26 (2006) 1269–1277.
- [30] M.F. Semlitsch, H. Weber, R.M. Streicher, R. Schön, Joint replacement components made of hot-forged and surface-treated Ti-6Al-7Nb alloy, *Biomaterials*. 13 (1992) 781–788.
- [31] M. Long, H.J. Rack, Titanium alloys in total joint replacement--a materials science perspective., *Biomaterials*. 19 (1998) 1621–1639.
- [32] Y. Okazaki, Corrosion resistance and corrosion fatigue strength of new titanium alloys for medical implants without V and Al, *Mater. Sci. Eng. A*. 213 (1996) 138–147.
- [33] M. Atapour, A.L. Pilchak, G.S. Frankel, J.C. Williams, Corrosion behavior of  $\beta$  titanium alloys for biomedical applications, *Mater. Sci. Eng. C*. 31 (2011) 885–891.
- [34] M. Windler, R. Klabunde, Titanium for Hip and Knee Prostheses, (2001) 703–746.
- [35] J.T. Kim, J.J. Yoo, Implant Design in Cementless Hip Arthroplasty, *Hip Pelvis*. 28 (2016) 65–75.
- [36] K.E. Tanner, Titanium in Medicine, in: *Proc. Inst. Mech. Eng. Part H J. Eng. Med.*, 2002: pp. 215–215.
- [37] B.R. Levine, D.W. Fabi, Porous metals in orthopedic applications - A review., *Materwiss. Werksttech*. 41 (2010) 1001–1010.
- [38] J. Muth, M. Poggie, G. Kulesha, R. Michael Meneghini, Novel highly porous metal technology in artificial hip and knee replacement: Processing methodologies and clinical applications, *Jom*. 65 (2013) 318–325.
- [39] S. Singh, S.P. Trikha, A.J. Edge, Hydroxyapatite ceramic-coated femoral stems in young patients. A prospective ten-year study, *J. Bone Jt. Surg. - Ser. B*. 86 (2004) 1118–1123.
- [40] A.V.L. Jr, K.R. Berend, T.H. Mallory, M.D.S. Do, J.B.A. Bfa, Survivorship of 2000 Tapered Titanium Porous Plasma-sprayed Femoral Components, *HIP Soc. Meet.* 2008. (2009) 146–154.
- [41] I. Castellini, L. Andreani, P.D. Parchi, E. Bonicoli, N. Piolanti, F. Risoli, M. Lisanti, W. Score, Hydroxyapatite in total hip arthroplasty. Our experience with a plasma spray porous titanium alloy/hydroxyapatite double-coated cementless stem, *Clin. Cases Miner. Bone Metab.* 13 (2016) 221–227.

- [42] F. Schönweger, C.M. Sprecher, S. Milz, C. Dommann-scherrer, C. Meier, A. Dommann, A. Neels, P. Wahl, New Insights into Osteointegration and Delamination from a Multidisciplinary Investigation of a Failed Hydroxyapatite-Coated Hip Joint Replacement, *Materials (Basel)*. 13 (2020) 4713.
- [43] S. Solanke, V. Gaval, Most commonly used metallic biomaterials for plasma sprayed hydroxyapatite coatings, in: *IOP Conf. Ser. Mater. Sci. Eng.*, 2021.
- [44] B. Beig, U. Liaqat, M. Farooq, K. Niazi, I. Douna, Current Challenges and Innovative Developments in Hydroxyapatite-Based Coatings on Metallic Materials for Bone Implantation: A Review, *Coatings*. 10 (2020) 1249.
- [45] I. Landor, P. Vavrik, A. Sosna, D. Jahoda, H. Hahn, M. Daniel, Hydroxyapatite porous coating and the osteointegration of the total hip replacement, *Arch. Orthop. Trauma Surg.* 127 (2007) 81–89.
- [46] K.A. Gross, W. Walsh, E. Swarts, Analysis of retrieved hydroxyapatite-coated hip prostheses, *J. Therm. Spray Technol.* 13 (2004) 190–199.
- [47] M. Qian, W. Xu, M. Brandt, H.P. Tang, Additive manufacturing and postprocessing of Ti-6Al-4V for superior mechanical properties, *Mater. Res. Soc.* 41 (2016) 775–783.
- [48] M. Dabić, R & D Management in the Knowledge Era Challenges of Emerging Technologies, in: *Addit. Manuf. Technol. Assess. Titan. Hip Implant Fabr.*, Springer, 2019: pp. 237–259.
- [49] S.P. Narra, P.N. Mittwede, S.D. Wolf, K.L. Urish, A.D. Group, M. Hospital, Additive Manufacturing in Total Joint Arthroplasty Sneha, *Orthop. Clin. North Am.* 50 (2020) 13–20.
- [50] A. Rodriguez-contreras, M. Punset, J.A. Calero, F. Javier, E. Ruperez, J. María, Powder metallurgy with space holder for porous titanium implants: A review, *J. Mater. Sci. Technol.* 76 (2021) 129–149.
- [51] O. Okolie, I. Stachurek, B. Kandasubramanian, 3D Printing for Hip Implant Applications: A Review, *Polymers (Basel)*. 12 (2020) 2682.
- [52] N. Kumar, N.C. Arora, B. Datta, Bearing surfaces in hip replacement - Evolution and likely future, *Med. J. Armed Forces India.* 70 (2014) 371–376.
- [53] E.H. Schemitsch, J.P. Waddell, A. Atrey, F. Tr, Wear Rates of XLPE Nearly 50% Lower Than Previously Thought After Adjusting for Initial Creep, *J. Bone Jt. Surg.* (2020) e0066.
- [54] E.M. Brach del Prever, A. Bistolfi, P. Bracco, L. Costa, UHMWPE for arthroplasty: Past or future?, *J. Orthop. Traumatol.* 10 (2009) 1–8.
- [55] D.W. Manning, P.P. Chiang, J.M. Martell, J.O. Galante, W.H. Harris, In vivo comparative wear study of traditional and highly cross-linked polyethylene in total hip arthroplasty, *J. Arthroplasty.* 20 (2005) 880–886.
- [56] J.R.T. Jeffers, W.L. Walter, Ceramic-on-ceramic bearings in hip arthroplasty: State of the art and the future, *J. Bone Jt. Surg. - Ser. B.* 94 B (2012) 735–745.
- [57] V. Gopal, G. Manivasagam, Zirconia-alumina composite for orthopedic implant application, in: *Appl. Nanocomposite Mater. Orthop.*, Elsevier Inc., 2018: pp. 201–219..
- [58] I.C. Clarke, M. Manaka, D.D. Green, P. Williams, G. Pezzotti, Y.H. Kim, M. Ries, N. Sugano, L. Sedel, C. Delauney, B. Ben Nissan, T. Donaldson, G.A. Gustafson, Current status of zirconia used in total hip implants, *J. Bone Jt. Surg. - Ser. A.* 85 (2003) 73–84.
- [59] J. Chevalier, What future for zirconia as a biomaterial?, *Biomaterials.* 27 (2006) 535–543.
- [60] H. Tribe, S. Malek, J. Stammers, V. Ranawat, J.A. Skinner, Advanced wear of an Oxinium™ femoral head implant following polyethylene liner dislocation., *Ann. R. Coll. Surg. Engl.* 95 (2013) 4–6.

- [61] P. Hernigou, G. Mathieu, A. Poignard, O. Manicom, P. Filippini, A. Demoura, Oxinium, a new alternative femoral bearing surface option for hip replacement, *Eur. J. Orthop. Surg. Traumatol.* 17 (2007) 243–246.
- [62] A. Ashkanfar, D.J. Langton, T.J. Joyce, A large taper mismatch is one of the key factors behind high wear rates and failure at the taper junction of total hip replacements : A finite element wear analysis, *J. Mech. Behav. Biomed. Mater.* 69 (2017) 257–266.
- [63] S. Leuridan, Q. Goossens, J. Roosen, L. Pastrav, K. Denis, M. Mulier, W. Desmet, J. Vander, A biomechanical testing system to determine micromotion between hip implant and femur accounting for deformation of the hip implant : Assessment of the influence of rigid body assumptions on micromotions measurements, *Clin. Biomech.* 42 (2017) 70–78.
- [64] S.D. Ulrich, T.M. Seyler, D. Bennett, R.E. Delanois, K.J. Saleh, I. Thongtrangan, M. Kuskowski, E.Y. Cheng, P.F. Sharkey, J. Parvizi, J.B. Stiehl, M.A. Mont, Total hip arthroplasties: What are the reasons for revision?, *Int. Orthop.* 32 (2008) 597–604.
- [65] R.W. Crawford, D.W. Murray, Total hip replacement: Indications for surgery and risk factors for failure, *Ann. Rheum. Dis.* 56 (1997) 455–457.
- [66] S. Kobayashi, N. Saito, H. Horiuchi, R. Iorio, K. Takaoka, Poor bone quality or hip structure as risk factors affecting survival of total-hip arthroplasty, *Lancet.* 355 (2000) 1499–1504.
- [67] M. Mathew, Failure Causes in Total Hip Replacements: A Review, *Austin J. Orthop. Rheumatol.* 5 (2018) 1–7.
- [68] P. Münger, C. Röder, U. Ackermann-Liebrich, A. Busato, Patient-related risk factors leading to aseptic stem loosening in total hip arthroplasty: A case-control study of 5,035 patients, *Acta Orthop.* 77 (2006) 567–574.
- [69] T. Kawai, M. Kataoka, K. Goto, Y. Kuroda, K. So, S. Matsuda, Patient- and Surgery-Related Factors that Affect Patient-Reported Outcomes after Total Hip Arthroplasty, *J. Clin. Med.* 7 (2018) 358.
- [70] T. Ibrahim, S. Hobson, A. Beiri, C.N. Esler, No influence of body mass index on early outcome following total hip arthroplasty, *Int. Orthop.* 29 (2005) 359–361.
- [71] M.H.A. Malik, J. Gray, P.R. Kay, Early aseptic loosening of cemented total hip, arthroplasty: The influence of non-steroidal anti-inflammatory drugs and smoking, *Int. Orthop.* 28 (2004) 211–213.
- [72] S. Petis, J. Howard, B. Lanting, I. Jones, T. Birmingham, E. Vasarhelyi, Comparing the anterior, posterior and lateral approach: gait analysis in total hip arthroplasty, *Can. J. Surg.* 60 (2017) 3217.
- [73] J.M. Roberts, F.H. Fu, E.J. McClain, A.B. Ferguson, A Comparison of the Posterolateral and Anterolateral Approaches to Total Hip Arthroplasty, *Clin. Orthop. Relat. Res.* (1984) 205–210.
- [74] G. Triantafyllopoulos, O. Stundner, S. Memtsoudis, L.A. Poultsides, Patient, surgery, and hospital related risk factors for surgical site infections following total hip arthroplasty, *Sci. World J.* 2015 (2015).
- [75] L.E. Miller, J.S. Gondusky, A.F. Kamath, F. Boettner, J. Wright, S. Bhattacharyya, Influence of surgical approach on complication risk in primary total hip arthroplasty: Systematic review and meta-analysis, *Acta Orthop.* 89 (2018) 289–294.
- [76] E. Losina, J. Barrett, N.N. Mahomed, J.A. Baron, J.N. Katz, Early Failures of Total Hip Replacement: Effect of Surgeon Volume, *Arthritis Rheum.* 50 (2004) 1338–1343.
- [77] M. Sundfeldt, L. V Carlsson, C.B. Johansson, P. Thomsen, M. Sundfeldt, L. V Carlsson, C.B. Johansson, P. Thomsen, Aseptic loosening , not only a question of wear : A review of different theories, *Acta Orthop.* 77 (2006) 177–197.
- [78] M. Bahraminasab, B.B. Sahari, K.L. Edwards, F. Farahmand, M. Arumugam, Aseptic loosening of femoral components – A review of current and future trends in materials used, *Mater. Des.* 42 (2012) 459–470.

- [79] B. Ollivere, J.A. Wimhurst, I.M. Clark, S.T. Donell, Current concepts in osteolysis, *Curr. Concepts Osteolysis*. 94 (2012) 10–15.
- [80] R. Dattani, Femoral osteolysis following total hip replacement, *Postgr. Med J.* 83 (2007) 312–316.
- [81] C. Della Valle, L. Visai, M. Santin, L. Cigada, G. Candiani, D. Pezzoli, C.R. Arciola, M. Imbriani, R. Chiesa, A novel antibacterial modification treatment of titanium capable to improve osseointegration, *Int. J. Artif. Organs*. 35 (2012) 864–875.
- [82] C. Yue, B. Yang, Bioactive Titanium Surfaces with the Effect of Inhibiting Biofilm Formation, *J. Bionic Eng.* 11 (2014) 589–599.
- [83] R. Zhang, Y. Wan, A. Xing, T. Wang, B. Men, Preparation of micro-nanostructure on titanium implants and its bioactivity, *Trans. Nonferrous Met. Soc. China*. 26 (2016) 1019–1024.
- [84] S.K. Fokter, A. Moli, R. Kavalari, P. Pelicon, R. Rudolf, Why do some titanium-alloy total hip arthroplasty modular necks fail ?, *J. Mech. Behav. Biomed. Mater.* 69 (2017) 107–114.
- [85] J.J. Jacobs, Corrosion at the Head-Neck Junction: Why Is This Happening Now?, *J. Arthroplasty*. 31 (2016) 1378–1380.
- [86] J.L. Gilbert, C.A. Buckley, J.J. Jacobs, G.E.T. Al, In vivo corrosion of modular hip prosthesis components in mixed and similar metal combinations. The effect of crevice, stress, motion, and alloy coupling, *J. Biomed. Mater. Res.* 27 (1993) 1533–1544.
- [87] C.D. Canham, P.I. Muradov, J.B. Simpson, S.J. Incavo, Corrosion and adverse local tissue reaction after total hip arthroplasty with a modular titanium alloy femoral neck, *Arthroplast. Today*. 3 (2017) 211–214.
- [88] D.O. Molloy, M.B. Bch, F. Tr, S. Munir, C.M. Jack, M.B. Bch, F. Tr, M.B. Cross, W.L. Walter, W.K.W. Sr, Fretting and Corrosion in Modular-Neck Total Hip Arthroplasty Femoral Stems, *J. Bone Jt. Surg.* (2014) 488–493.
- [89] S.A. Atwood, E.W. Patten, K.J. Bozic, L.A. Pruitt, M.D. Ries, Corrosion-Induced Fracture of a Double-Modular Hip Prosthesis A Case Report, 2010.
- [90] M. Talha, Y. Ma, P. Kumar, Y. Lin, A. Singh, Role of protein adsorption in the bio corrosion of metallic implants – A review, *Colloids Surfaces B Biointerfaces*. 176 (2019) 494–506.
- [91] Y.S. Hedberg, Role of proteins in the degradation of relatively inert alloys in the human body, *Npj Mater. Degrad.* 2 (2018) 1–5.
- [92] F. Eltit, Q. Wang, R. Wang, Mechanisms of Adverse Local Tissue Reactions to Hip Implants, *Front. Bioeng. Biotechnol.* 7 (2019) 1–17.
- [93] R.B. Cook, B.J.R.F. Bolland, J.A. Wharton, S. Tilley, J.M. Latham, R.J.K. Wood, Pseudotumour Formation Due to Tribocorrosion at the Taper Interface of Large Diameter Metal on Polymer Modular Total Hip Replacements, *J. Arthroplasty*. 28 (2013) 1430–1436.
- [94] H.J. Cooper, R.M. Urban, R.L. Wixson, R.M. Meneghini, J.J. Jacobs, Adverse Local Tissue Reaction Arising from Corrosion at the Femoral Neck-Body Junction in a Dual-Taper Stem with a Cobalt-Chromium Modular Neck, *J. Bone Jt. Surg. Inc.* (2013) 865–872.
- [95] H.J. Cooper, C.J. Della Valle, R.A. Berger, M. Tetreault, W.G. Paprosky, S.M. Sporer, J.J. Jacobs, Corrosion at the Head-Neck Taper as a Cause for Adverse Local Tissue Reaction After Total Hip Arthroplasty, *J. Bone Jt. Surgery, Inc.* (2012) 1655–1661.
- [96] A. Charles, H. Ho, Metal-on-Metal Hip Arthroplasty Does Early Clinical Outcome Justify the Chance of an Adverse Local Tissue Reaction?, *Clin. Orthop. Relat. Res.* (2010) 406–412.
- [97] I. Antoniac, M. Negrusoiu, M. Mardare, C. Socoliuc, M. Niculescu, Adverse local tissue reaction after 2 revision hip replacements for ceramic liner fracture A case report, *Medicine (Baltimore)*. 96 (2017) p e6687.

- [98] M.R. Whitehouse, M. Endo, B.A. Masri, Adverse Local Tissue Reaction Associated With a Modular Hip Hemiarthroplasty, *Clin Orthop Relat Res.* 471 (2013) 4082–4086.
- [99] D.R.N. Correa, P.A.B. Kuroda, C.R. Grandini, L.A. Rocha, F.G.M. Oliveira, Tribocorrosion behavior of  $\beta$ -type Ti-15Zr-based alloys, *Mater. Lett.* 179 (2016) 118–121.
- [100] V.G. Pina, A. Dalmau, F. Devesa, V. Amigó, A.I. Muñoz, Tribocorrosion behavior of beta titanium biomedical alloys in phosphate buffer saline solution, *J. Mech. Behav. Biomed. Mater.* 46 (2015) 59–68.
- [101] I. Çaha, A. Alves, C. Caterina, A. Pinto, S. Tsipas, E. Gordo, F. Toptan, Corrosion and Tribocorrosion Behavior of Ti-40Nb and Ti-25Nb-5Fe Alloys Processed by Powder Metallurgy, *Met. Mater Trans A.* (2020) 3256–3267.
- [102] I. Hacisalihoglu, A. Samancioglu, F. Yildiz, G. Purcek, A. Alsaran, Tribocorrosion properties of different type titanium alloys in simulated body fluid, *Wear.* 333 (2015) 679–686.
- [103] M. Buciumeanu, A. Bagheri, N. Shamsaei, S.M. Thompson, F.S. Silva, B. Henriques, Tribocorrosion behavior of additive manufactured Ti-6Al-4V biomedical alloy, *Tribol. Int.* 119 (2018) 381–388.
- [104] F. Toptan, A.C. Alves, Ó. Carvalho, F. Bartolomeu, A.M.P. Pinto, F. Silva, G. Miranda, Corrosion and tribocorrosion behaviour of Ti6Al4V produced by selective laser melting and hot pressing in comparison with the commercial alloy, *J. Mater. Process. Tech.* 266 (2019) 239–245.
- [105] Z. Wang, W. Huang, Y. Li, H. He, Y. Zhou, Z. Zheng, Tribocorrosion behaviour of a biomedical Ti-25Nb-3Mo-3Zr-2Sn alloy in Ringer's solution, *Mater. Sci. Eng. C.* 76 (2017) 1094–1102.
- [106] M.J. Runa, M.T. Mathew, L.A. Rocha, Tribocorrosion response of the Ti6Al4V alloys commonly used in femoral stems, *Tribology Int.* 68 (2013) 85–93.
- [107] J.-S. Kim, K.-M. Lee, D.-H. Cho, Y.-Z. Lee, Fretting wear characteristics of titanium matrix composites reinforced by titanium boride and titanium carbide particulates, *Wear.* 301 (2013) 562–568.
- [108] M.K. Harman, S.A. Banks, W. Andrew Hodge, Wear analysis of a retrieved hip implant with titanium nitride coating, *J. Arthroplasty.* 12 (1997) 938–945.
- [109] L. Cao, Y. Wan, S. Yang, J. Pu, The Tribocorrosion and Corrosion Properties of Thermally Oxidized Ti6Al4V Alloy in 0.9 wt.% NaCl Physiological Saline, *Coatings.* 8 (2018) 285.
- [110] Y. Fu, F. Zhou, Q. Wang, M. Zhang, Z. Zhou, Electrochemical and tribocorrosion performances of CrMoSiCN coating on Ti-6Al-4V titanium alloy in artificial seawater, *Corros. Sci.* 165 (2020) 108385.
- [111] W. Cui, F. Niu, Y. Tan, G. Qin, Microstructure and tribocorrosion performance of nanocrystalline TiN graded coating on biomedical titanium alloy, *Trans. Nonferrous Met. Soc. China.* 29 (2019) 1026–1035.
- [112] J. Grabarczyk, J. Gaj, B. Pazik, W. Kaczorowski, Tribology International Tribocorrosion behavior of Ti6Al4V alloy after thermo-chemical treatment and DLC deposition for biomedical applications, *Tribol. Int.* 153 (2021) 106560.
- [113] L.D. Trino, E.S. Bronze-uhle, A. Ramachandran, P.N. Lisboa-filho, M.T. Mathew, A. George, Titanium surface bio-functionalization using osteogenic peptides: Surface chemistry, biocompatibility, corrosion and tribocorrosion aspects, *J. Mech. Behav. Biomed. Mater.* 81 (2018) 26–38.
- [114] F. Toptan, A. Rego, A.C. Alves, A. Guedes, Corrosion and tribocorrosion behavior of Ti–B4C composite intended for orthopaedic implants, *J. Mech. Behav. Biomed. Mater.* 61 (2016) 152–163.
- [115] V.S. Balaji, S. Kumaran, Densification and microstructural studies of titanium–boron carbide (B4C) powder mixture during spark plasma sintering, *Powder Technol.* 264 (2014) 536–540.



- [116] S. Li, K. Kondoh, H. Imai, B. Chen, L. Jia, J. Umeda, Y. Fu, Strengthening behavior of *in situ*-synthesized (TiC–TiB)/Ti composites by powder metallurgy and hot extrusion, *Mater. Des.* 95 (2016) 127–132.
- [117] S. LI, K. Kondoh, H. Imai, B. Chen, L. Jia, J. Umeda, Microstructure and mechanical properties of P/M titanium matrix composites reinforced by in-situ synthesized TiC–TiB, *Mater. Sci. Eng. A.* 628 (2015) 75–83.
- [118] L. Geng, D.R. Ni, J. Zhang, Z.Z. Zheng, Hybrid effect of TiBw and TiCp on tensile properties of *in situ* titanium matrix composites, *J. Alloys Compd.* 463 (2008) 488–492.
- [119] D.R. Ni, L. Geng, J. Zhang, Z.Z. Zheng, Effect of B4C particle size on microstructure of *in situ* titanium matrix composites prepared by reactive processing of Ti-B4C system, *Scr. Mater.* 55 (2006) 429–432.
- [120] B. V. Radhakrishna Bhat, J. Subramanyam, V. V. Bhanu Prasad, Preparation of Ti-TiB-TiC & Ti-TiB composites by in-situ reaction hot processing, *Mater. Sci. Eng. A.* 325 (2002) 126–130.
- [121] D.R. Ni, L. Geng, J. Zhang, Z.Z. Zheng, TEM characterization of symbiosis structure of *in situ* TiC and TiB prepared by reactive processing of Ti-B4C, *Mater. Lett.* 62 (2008) 686–688.
- [122] X. Zhang, W. Lu, D. Zhang, R. Wu, *In Situ* Technique for synthesizing (TiB+TiC)/Ti composites, *Scr. Mater.* 41 (1999) 39–46.
- [123] L. Jia, S.F. Li, H. Imai, B. Chen, K. Kondoh, Size effect of B4C powders on metallurgical reaction and resulting tensile properties of Ti matrix composites by in-situ reaction from Ti-B4C system under a relatively low temperature, *Mater. Sci. Eng. A.* 614 (2014) 129–135.
- [124] Y. Qin, W. Lu, D. Xu, D. Zhang, High-temperature OM investigation of the early stage of (TiC+TiB)/Ti oxidation, *J. Mater. Sci.* 40 (2005) 687–692.
- [125] X. Shen, Z. Zhang, S. Wei, F. Wang, S. Lee, Microstructures and mechanical properties of the *in situ* TiB–Ti metal–matrix composites synthesized by spark plasma sintering process, *J. Alloys Compd.* 509 (2011) 7692–7696.
- [126] J. Wang, X. Guo, J. Qin, D. Zhang, W. Lu, Microstructure and mechanical properties of investment casted titanium matrix composites with B4C additions, *Mater. Sci. Eng. A.* 628 (2015) 366–373.
- [127] P. Rogl, H. Bittermann, H. Duschanek, Ternary Alloy Systems: Phase Diagrams, Crystallographic and Thermodynamic Data critically evaluated by MSIT® · Light Metal Systems. Part 4, 2006.
- [128] B. Choi, I.-Y. Kim, Y. Lee, Y. Kim, Microstructure and friction/wear behavior of (TiB+TiC) particulate-reinforced titanium matrix composites, *Wear.* 318 (2014) 68–77.
- [129] H.T. Tsang, C.G. Chao, C.Y. Ma, Effects of volume fraction of reinforcement on tensile and creep properties of in-situ TiB/Ti MMC, *Acta Metall.* 37 (1997) 1359–1365.
- [130] H. Attar, M. Bonisch, M. Calin, L. Zhang, S. Scudino, J. Eckert, Selective laser melting of *in situ* titanium–titanium boride composites: Processing, microstructure and mechanical properties, *Acta Mater.* 76 (2014) 13–22.
- [131] H.K.S. Rahoma, Y.Y. Chen, X.P. Wang, S.L. Xiao, Influence of (TiC+TiB) on the microstructure and tensile properties of Ti-B20 matrix alloy, *J. Alloys Compd.* 627 (2015) 415–422.
- [132] M.H. Loretto, D.G. Konitzer, The effect of matrix reinforcement reaction on fracture in Ti-6Al-4V-base composites, *Metall. Trans. A.* 21 (1990) 1579–1587.
- [133] C.J. Zhang, F.T. Kong, S.L. Xiao, E.T. Zhao, L.J. Xu, Y.Y. Chen, Evolution of microstructure and tensile properties of *in situ* titanium matrix composites with volume fraction of (TiB and TiC) reinforcements, *Mater. Sci. Eng. A.* 548 (2012) 152–160.

- [134] D.R. Ni, L. Geng, J. Zhang, Z.Z. Zheng, Fabrication and tensile properties of *in situ* TiBw and TiCp hybrid-reinforced titanium matrix composites based on Ti-B4C-C, *Mater. Sci. Eng. A*. 478 (2008) 291–296.
- [135] I.Y. Kim, B.J. Choi, Y.J. Kim, Y.Z. Lee, Friction and wear behavior of titanium matrix (TiB+TiC) composites, *Wear*. 271 (2011) 1962–1965.
- [136] J.I. Silva, A.C. Alves, A.M. Pinto, F. Toptan, Corrosion and tribocorrosion behavior of Ti-TiB-TiNx *in-situ* hybrid composite synthesized by reactive hot pressing, *J. Mech. Behav. Biomed. Mater.* 74 (2017) 195–203.
- [137] Y. Diao, K. Zhang, Microstructure and corrosion resistance of TC2 Ti alloy by laser cladding with Ti/TiC/TiB<sub>2</sub> powders, *Appl. Surf. Sci.* 352 (2015) 163–168.
- [138] Y. Chen, J. Zhang, N. Dai, P. Qin, H. Attar, L.-C. Zhang, Corrosion Behaviour of Selective Laser Melted Ti-TiB Biocomposite in Simulated Body Fluid, *Electrochim. Acta*. 232 (2017) 89–97.
- [139] A. Miklaszewski, M.U. Jurczyk, K. Jurczyk, M. Jurczyk, Plasma surface modification of titanium by TiB precipitation for biomedical applications, *Surf. Coatings Technol.* 206 (2011) 330–337.
- [140] M. Brama, N. Rhodes, J. Hunt, A. Ricci, R. Teghil, S. Migliaccio, C. Della Rocca, S. Leccisotti, A. Lioi, M. Scandurra, G. De Maria, D. Ferro, F. Pu, G. Panzini, L. Politi, R. Scandurra, Effect of titanium carbide coating on the osseointegration response *in vitro* and *in vivo*, *Biomaterials*. 28 (2007) 595–608.
- [141] J.A. M Navarro, A Michiardi, O Castaño, Planell, Biomaterials in orthopaedics, *J. Chem. Technol. Biotechnol.* (2008) 1137–1158.
- [142] Y.H. Kim, J.W. Park, Eighteen-Year Results of Cementless THA with Alumina-on-HXLPE Bearings in Patients <30 Years Old: A Concise Follow-up of a Previous Report\*, *J. Bone Jt. Surg. - Am. Vol.* 102 (2020) 1255–1259.
- [143] J. Langlois, M. Hamadouche, Recent update on crosslinked polyethylene in total hip arthroplasty, *Sicot-J.* 6 (2020) 0–6.
- [144] S. Affatato, F. Traina, M. De Fine, S. Carmignato, A. Toni, Alumina-on-alumina hip implants: A wear study of retrieved components, *J. Bone Jt. Surg. - Br. Vol.* 94–B (2012) 37–42.
- [145] S. Affatato, F. Traina, A. Toni, Microseparation and stripe wear in alumina-on- alumina hip implants, *Int J Artif Organs*. 34 (2011) 506–512.
- [146] P. Boyer, D. Hutten, P. Loriaut, V. Lestrat, C. Jeanrot, P. Massin, Is alumina-on-alumina ceramic bearings total hip replacement the right choice in patients younger than 50 years of age? A 7 to 15 year follow-up study, *Orthop. Traumatol. Surg. Res.* 96 (2010) 616–622.
- [147] B. Masson, Emergence of the alumina matrix composite in total hip arthroplasty, *Int. Orthop.* 33 (2009) 359–363.
- [148] M. Liu, Z. Wang, J. Wu, Q. Li, Effects of Nd<sub>2</sub>O<sub>3</sub> on the mechanical properties and oxidation behavior of Ti/Al<sub>2</sub>O<sub>3</sub> composites by vacuum hot pressing sintering, *J. Alloys Compd.* 648 (2015) 116–121.
- [149] K. Girish, A.H. Carim, Phase Equilibria in the Ti-Al-O system at 945°C and Analysis of Ti/Al<sub>2</sub>O<sub>3</sub> reactions, *J. Am. Ceram. Soc.* 3 (1995) 572–573.
- [150] M. Liu, Z. Wang, J. Wu, Q. Li, Ti/Al<sub>2</sub>O<sub>3</sub> interfacial diffusion: Kinetic equation for growth of reaction layer and formation mechanism, *J. Alloys Compd.* 652 (2015) 260–265.
- [151] X.L. Li, R. Hillel, F. Teyssandier, S.K. Choi, F.J.J. Van Loo, Reactions and phase relations in the TiAlO system, *Acta Metall. Mater.* 40 (1992) 3149–3157.
- [152] Y. Wei, W. Aiping, Z. Guisheng, R. Jialie, Formation process of the bonding joint in Ti/Al diffusion bonding, *Mater. Sci. Eng. A*. 480 (2008) 456–463.
- [153] R. Jiangwei, L. Yajiang, F. Tao, Microstructure characteristics in the interface zone of Ti/Al diffusion bonding, *Mater. Lett.* 56 (2002) 647–652.

- [154] L. A. Rocha, E. Ariza, A. Maria, Electrochemical Behavior of Ti/ Al<sub>2</sub>O<sub>3</sub> Interfaces Produced by Diffusion Bonding, *Mater. Res.* 6 (2003) 439–444.
- [155] L.E. Karkina, L.I. Yakovenkova, Dislocation core structure and deformation behavior of Ti<sub>3</sub>Al, *Model. Simul. Mater. Sci. Eng.* 20 (2012) 065003.
- [156] A.M. Kliauga, M. Ferrante, Interface compounds formed during the diffusion bonding of Al<sub>2</sub>O<sub>3</sub> to Ti, *J. Mater. Sci.* 35 (2000) 4243–4249.
- [157] E. Gordo, R.G. das Neves, B. Ferrari, A. Jimenez-Morales, A. Lima, A.C. Alves, A.M. Pinto, F. Toptan, Corrosion and tribocorrosion behavior of Ti-Alumina composites, *Key Eng. Mater.* 704 (2016) 28–37.
- [158] M. Bahraminasab, M. Bozorg, S. Ghaffari, F. Kavakebian, Electrochemical corrosion of Ti-Al<sub>2</sub>O<sub>3</sub> biocomposites in Ringer's solution, *J. Alloys Compd.* 777 (2019) 34–43.
- [159] M. Bahraminasab, M. Bozorg, S. Ghaffari, F. Kavakebian, Corrosion of Al<sub>2</sub>O<sub>3</sub>-Ti composites under inflammatory condition in simulated physiological solution, *Mater. Sci. Eng. C.* 102 (2019) 200–211.
- [160] A. Oliveira, F. Toptan, Wear Behavior of Ti-Al<sub>2</sub>O<sub>3</sub> Biocomposites in 9 g/L NaCl Solution, *J. Mater. Eng. Perform.* 28 (2019) 6000–6010.
- [161] A.M. Ribeiro, A.C. Alves, L.A. Rocha, F.S. Silva, F. Toptan, Tribology International Synergism between corrosion and wear on CoCrMo on Al<sub>2</sub>O<sub>3</sub> biocomposites in a physiological solution, *Tribol. Int.* (2015) 1–8.
- [162] M. Rahimian, N. Parvin, N. Ehsani, The effect of production parameters on microstructure and wear resistance of powder metallurgy Al–Al<sub>2</sub>O<sub>3</sub> composite, *Mater. Des.* 32 (2011) 1031–1038.
- [163] A. Baradeswaran, A. Elayaperumal, R.F. Issac, A Statistical Analysis of Optimization of Wear Behaviour of Al-Al<sub>2</sub>O<sub>3</sub> Composites Using Taguchi Technique, *Procedia Eng.* 64 (2013) 973–982.
- [164] R. Purohit, M.M.U. Qureshi, R.S. Rana, The Effect of Hot Forging and Heat Treatment on Wear Properties of Al6061-Al<sub>2</sub>O<sub>3</sub> Nano Composites, *Mater. Today Proc.* 4 (2017) 4042–4048.
- [165] M. Nagral, Effect of Al<sub>2</sub>O<sub>3</sub> Particles on Mechanical and Wear Properties of 6061al Alloy Metal Matrix Composites, *J. Mater. Sci. Eng.* 02 (2013) 2–5.
- [166] Y. Wang, H. Yu, C. Chen, Z. Zhao, Review of the biocompatibility of micro-arc oxidation coated titanium alloys, *Mater. Des.* 85 (2015) 640–652.
- [167] C. Chang, X. Huang, Y. Liu, L. Bai, X. Yang, R. Hang, B. Tang, P.K. Chu, High-current anodization : A novel strategy to functionalize titanium-based biomaterials, *Electrochim. Acta.* 173 (2015) 345–353.
- [168] K. Alagarsamy, V. Vishwakarma, G.S. Kaliaraj, Synthesis and Characterization of bioactive composite coating on Titanium by PVD for biomedical application, in: *Conf. Ser. Mater. Sci. Eng.*, 2019.
- [169] S. Durdu, Characterization, Bioactivity and Antibacterial Properties of Copper-Based TiO<sub>2</sub> Bioceramic Coatings Fabricated on Titanium, *Coatings.* 9 (2019) 0–19.
- [170] J. Guillem-marti, N. Cinca, M. Punset, I. García, F. Javier, J. Maria, S. Dosta, Porous titanium-hydroxyapatite composite coating obtained on titanium by cold gas spray with high bond strength for biomedical applications, *Colloids Surfaces B Biointerfaces.* 180 (2019) 245–253.
- [171] J. Huang, X. Zhang, W. Yan, Z. Chen, X. Shuai, A. Wang, Y. Wang, Nanotubular topography enhances the bioactivity of titanium implants, *Nanomedicine Nanotechnology, Biol. Med.* 13 (2017) 1913–1923.
- [172] X. Liu, Y. Niu, W. Xie, D. Wei, Q. Du, Comparative investigations of in vitro and in vivo bioactivity of titanium vs. Ti–24Nb–4Zr–8Sn alloy before and after sandblasting and acid etching, *R. Soc. Chem.* 10 (2020) 23582–23591.

- [173] B. Ren, Y. Wan, G. Wang, Z. Liu, Y. Huang, H. Wang, Biomaterials Morphologically modified surface with hierarchical micro-/nano-structures for enhanced bioactivity of titanium implants, *J. Mater. Sci.* 53 (2018) 12679–12691.
- [174] W. He, X. Yin, L. Xie, Z. Liu, J. Li, S. Zou, J. Chen, Enhancing osseointegration of titanium implants through large-grit sandblasting combined with micro-arc oxidation surface modification, *J. Mater. Sci. Mater. Med.* 30 (2019).
- [175] J.D. BOBYN, R.M. PILLIAR, H.U. CAMERON, G.C. WEATHERLY, The Optimum Pore Size for the Fixation of Porous-Surfaced Metal Implants by the Ingrowth of Bone, *Clin. Orthop. Relat. Res.* (1980) 263–270.
- [176] R.A. Gittens, T. McLachlan, R. Olivares-Navarrete, Y. Cai, S. Berner, R. Tannenbaum, Z. Schwartz, K.H. Sandhage, B.D. Boyan, The effects of combined micron-/submicron-scale surface roughness and nanoscale features on cell proliferation and differentiation, *Biomaterials.* 32 (2011) 3395–3403.
- [177] A.L. Raines, R. Olivares-Navarrete, M. Wieland, D.L. Cochran, Z. Schwartz, B.D. Boyan, Regulation of angiogenesis during osseointegration by titanium surface microstructure and energy, *Biomaterials.* 31 (2010) 4909–4917.
- [178] R. Zhou, D. Wei, J. Cao, W. Feng, S. Cheng, Q. Du, B. Li, Y. Wang, D. Jia, Y. Zhou, Conformal coating containing Ca, P, Si and Na with double-level porous surface structure on titanium formed by a three-step microarc oxidation, *RSC Adv.* 5 (2015) 28908–28920.
- [179] D. Buser, N. Broggini, M. Wieland, R.K. Schenk, A.J. Denzer, D.L. Cochran, B. Hoffmann, A. Lussi, S.G. Steinemann, Enhanced Bone Apposition to a Chemically Modified SLA Titanium Surface, *J. Dent. Res.* 83 (2004) 529–533.
- [180] J.W. Park, Y.J. Kim, J.H. Jang, Enhanced osteoblast response to hydrophilic strontium and/or phosphate ions-incorporated titanium oxide surfaces, *Clin. Oral Implants Res.* 21 (2010) 398–408.
- [181] C.A.H. Laurindo, R.D. Torres, S.A. Mali, J.L. Gilbert, P. Soares, Incorporation of Ca and P on anodized titanium surface: Effect of high current density, *Mater. Sci. Eng. C* 37 (2014) 223–231.
- [182] H.P. Felgueiras, L. Castanheira, S. Changotade, F. Poirier, S. Oughlis, M. Henriques, C. Chakar, N. Naaman, R. Younes, V. Migonney, J.P. Celis, P. Ponthiaux, L.A. Rocha, D. Lutomski, Biotribocorrosion (tribo-electrochemical) characterization of anodized titanium biomaterial containing calcium and phosphorus before and after osteoblastic cell culture, *J. Biomed. Mater. Res. - Part B Appl. Biomater.* 103 (2015) 661–669.
- [183] N.C.M. Oliveira, C.C.G. Moura, D.Z. Barbosa, D.B.S. Mendonça, G. Mendonça, P. Dechichi,, Effects of titanium surface anodization with CaP incorporation on human osteoblastic response, *Mater. Sci. Eng. C* 33 (2015) 1958–1962.
- [184] L. Xie, X. Liao, G. Yin, Z. Huang, D. Yan, Y. Yao, W. Liu, X. Chen, J. Gu, Preparation, characterization, in vitro bioactivity, and osteoblast adhesion of multi-level porous titania layer on titanium by two-step anodization treatment, *J. Biomed. Mater. Res. - Part A.* 98 A (2011) 312–320.
- [185] L. Xie, X. Liao, H. Xu, G. Yin, Z. Huang, Y. Yao, X. Chen, J. Gu, A facile one-step anodization treatment to prepare multi-level porous titania layer on titanium, *Mater. Lett.* 72 (2012) 141–144.
- [186] Y. Li, W. Wang, J. Duan, M. Qi, A super-hydrophilic coating with a macro/micro/nano triple hierarchical structure on titanium by two-step micro-arc oxidation treatment for biomedical applications, *Surf. Coatings Technol.* 311 (2017) 1–9.
- [187] M. Tsai, Y. Chang, H. Huang, Y. Wu, T. Shieh, Micro-arc oxidation treatment enhanced the biological performance of human osteosarcoma cell line and human skin fibroblasts cultured on titanium – zirconium films, *Surf. Coat. Technol.* 303 (2016) 268–276.
- [188] Y. Zhao, T.-Y. Xiong, Formation of bioactive titania films under specific anodisation conditions, *Surf. Eng.* 28 (2012) 371–376.

- [189] B. Yang, M. Uchida, H.M. Kim, X. Zhang, T. Kokubo, Preparation of bioactive titanium metal via anodic oxidation treatment, *Biomaterials*. 25 (2004) 1003–1010.
- [190] Y. Li, B. Li, X. Fu, J. Li, C. Li, H. Li, H. Li, C. Liang, H. Wang, L. Zhou, S. Xin, Anodic Oxidation Modification Improve Bioactivity and Biocompatibility of Titanium Implant Surface, *J. Hard Tissue Biol.* 22 (2013) 351–358.
- [191] A.C. Alves, F. Wenger, P. Ponthiaux, J.P. Celis, A.M. Pinto, L.A. Rocha, J.C.S. Fernandes, Corrosion mechanisms in titanium oxide-based films produced by anodic treatment, *Electrochim. Acta*. 234 (2017) 16–27.
- [192] G.G. de Lima, G.B. de Souza, C.M. Lepienski, N.K. Kuromoto, Mechanical properties of anodic titanium films containing ions of Ca and P submitted to heat and hydrothermal treatment, *J. Mech. Behav. Biomed. Mater.* 64 (2016) 18–30.
- [193] G. Li, Q. Zhao, H. Yang, L. Cheng, J. Province, Antibacterial and Microstructure Properties of Titanium Surfaces Modified with Ag-Incorporated Nanotube Arrays, *Mater. Res.* 19 (2016) 735–740.
- [194] F.G. Oliveira, A.R. Ribeiro, G. Perez, B.S. Archanjo, C.P. Gouvea, J.R. Araújo, A.P.C. Campos, A. Kuznetsov, C.M. Almeida, M.M. Maru, C.A. Achete, P. Ponthiaux, J.P. Celis, L.A. Rocha, Understanding growth mechanisms and tribocorrosion behaviour of porous TiO<sub>2</sub> anodic films containing calcium, phosphorous and magnesium, *Appl. Surf. Sci.* 341 (2015) 1–12.
- [195] A. Arunachalam, S. Dhanapandian, C. Manoharan, G. Sivakumar, Physical properties of Zn doped TiO<sub>2</sub> thin films with spray pyrolysis technique and its effects in antibacterial activity, *Spectrochim. Acta Part A Mol. Biomol. Spectrosc.* 138 (2015) 105–112.
- [196] H. Hu, W. Zhang, Y. Qiao, X. Jiang, X. Liu, C. Ding, Antibacterial activity and increased bone marrow stem cell functions of Zn-incorporated TiO<sub>2</sub> coatings on titanium, *Acta Biomater.* 8 (2012) 904–915.
- [197] D.A. Robinson, R.W. Griffith, D. Shechtman, R.B. Evans, M.G. Conzemius, In vitro antibacterial properties of magnesium metal against *Escherichia coli*, *Pseudomonas aeruginosa* and *Staphylococcus aureus*, *Acta Biomater.* 6 (2010) 1869–1877.
- [198] P.S. Vanzillotta, M.S. Sader, I.N. Bastos, G. De Almeida, Improvement of in vitro titanium bioactivity by three different surface treatments, *Dent. Mater.* 22 (2006) 275–282.
- [199] Y. Park, H.-J. Song, I. Kim, H. Yang, Surface characteristics and bioactivity of oxide film on titanium metal formed by thermal oxidation, *J. Mater. Sci.* 18 (2007) 565–575.
- [200] G. Wang, J. Li, K. Lv, W. Zhang, X. Ding, G. Yang, Surface thermal oxidation on titanium implants to enhance osteogenic activity and in vivo osseointegration, *Sci. Rep.* 6 (2016) 1–13.
- [201] S. El-hadad, Optimizing the Surface Treatment Processes to Enhance the Bioactivity of Ti-6Al-7Nb Alloy, *Trans. Indian Inst. Met.* 73 (2020) 2727–2738.
- [202] H. Gülerüüz, H. Çimenoğlu, Effect of thermal oxidation on corrosion and corrosion-wear behaviour of a Ti-6Al-4V alloy, *Biomaterials*. 25 (2004) 3325–3333.
- [203] M. Jamesh, T.S.N.S. Narayanan, P.K. Chu, Thermal oxidation of titanium : Evaluation of corrosion resistance as a function of cooling rate, *Mater. Chem. Phys.* 138 (2013) 565–572.
- [204] S. Kumar, T.S.N.S. Narayanan, S.G. Sundara, S.K. Seshadri, Thermal oxidation of CP-Ti : Evaluation of characteristics and corrosion resistance as a function of treatment time, *Mater. Sci. Eng. C*. 29 (2009) 1942–1949.
- [205] G. Ryan, A. Pandit, D.P. Apatsidis, Fabrication methods of porous metals for use in orthopaedic applications, *Biomaterials*. 27 (2006) 2651–2670.
- [206] R. Bailey, Y. Sun, Corrosion and Tribocorrosion Performance of Thermally Oxidized Commercially Pure Titanium in a 0.9 % NaCl Solution, *J. Mater. Eng. Perform.* 24 (2015) 1669–1678.



## Chapter 3

### Influence of Ti-Al intermetallic phases on the corrosion and tribocorrosion behavior of Ti-Al<sub>2</sub>O<sub>3</sub> composites

*To be submitted*

---

**L. Sousa<sup>a,b</sup>**, R.D.M Antunes<sup>c</sup>, J.C.S. Fernandes<sup>d,e</sup>, A.C. Alves<sup>a,f</sup>, F. Toptan <sup>a,f,g</sup>

<sup>a</sup> CMEMS-UMinho – Center of MicroElectroMechanical Systems – Universidade Minho, Campus de Azurém, Guimarães, Portugal

<sup>b</sup> DEMM – Department of Metallurgical and Materials Engineering – Faculdade de Engenharia da Universidade do Porto, Porto, Portugal

<sup>c</sup> Center of Physics, University of Minho, Campus of Azurém, Guimarães, Portugal

<sup>d</sup> Department of Chemical Engineering – Instituto Superior Técnico, Lisboa, Portugal

<sup>e</sup> CQE – Instituto Superior Técnico, Lisboa, Portugal

<sup>f</sup> IBTN/Euro – European Branch of the Institute of Biomaterials, Tribocorrosion and Nanomedicine, Dept. Eng. Mecânica, Universidade do Minho, Azurém, 4800-058 Guimarães, Portugal

<sup>g</sup> Department of Materials Science and Engineering, Izmir Institute of Technology, 35430, Urla, Izmir, Turkey





## Abstract

Ti and Ti alloys are among the most used materials in the fabrication of orthopaedic implants owing to their high corrosion resistance, biocompatibility, and lower Young's modulus compared to CoCr alloys and stainless steels. However, some concerns remain such as the poor tribocorrosion resistance. Recently, some research is being made on Ti-Al<sub>2</sub>O<sub>3</sub> composites, as these materials show promising properties for load-bearing biomedical implants, however, the effect of alumina reinforcement particles on the tribo-electrochemical response of Ti is still poorly understood. Thus, in the present work, the corrosion and tribocorrosion behaviour of Ti-Al<sub>2</sub>O<sub>3</sub> composites processed by conventional powder metallurgy was investigated in 0.9 wt.% NaCl solution at body temperature. Results showed that the incorporation of Al<sub>2</sub>O<sub>3</sub> particles had a negative effect on the corrosion behaviour of Ti due to the presence of Ti-Al intermetallic phases formed due to reaction between Ti and Al<sub>2</sub>O<sub>3</sub>. However, although composites presented reduced fracture toughness, the tribocorrosion behaviour was drastically improved, evidenced by less tendency to corrosion under sliding as well as significantly reduced wear loss mainly due to the load-carrying effect of the reinforcement particles.

### 3.1. Introduction

Titanium (Ti) and its alloys are one of the most used materials in hip-implants, owing to their good properties such as high corrosion resistance, high strength, low density, relatively low Young's modulus, and biocompatibility [1,2]. However, some concerns remain such as low tribocorrosion resistance. Wear is one of the most common problem found in hip-implants. In addition to large amplitude oscillations that occur between the femoral head and the acetabular cup, it is also known that micromovements (small amplitude displacement or vibrations) occur at the interface between the bone, and the implant and between different parts of the prosthesis, in the case of modular implants [3]. Moreover, these implants are also in contact with corrosive fluids, being under the simultaneous action of corrosion and wear defined as tribocorrosion. In such cases, material loss due to tribocorrosion cannot be separately evaluated by corrosion and wear experiments since synergistic or antagonistic effects may

occur [4]. Besides mechanical failure of the implant, poor wear resistance will result in the release of metal ions and wear debris into the surrounding tissue, that may lead to adverse biological reactions [5]. In order to improve the tribocorrosion resistance of Ti and its alloys, a variety of techniques can be used, such as coatings or surface modification techniques [6–9]. On the other hand, the incorporation of hard ceramic particles into a Ti matrix has been found to be a cost-effective method to enhance the tribocorrosion resistance of Ti [10,11]. The incorporation of the reinforcement particles can improve the wear resistance through direct or indirect strengthening mechanisms. The reinforcement particles may carry the applied load when in contact with another material. On the other hand, when ceramic particles are incorporated into a metallic matrix, the strength of the metallic matrix increases due to induced dislocation, Orowan strengthening mechanism and grain size refinement [10].

Al<sub>2</sub>O<sub>3</sub> is a widely known biomaterial and it can be considered as an interesting choice to produce titanium matrix composites (TMCs) for biomedical applications. Alumina has been widely used in the femoral head of hip implants due to its extremely high wear resistance and very low risk of osteolysis in long term [12–14]. Similar coefficient of thermal expansion (CTE) between Ti matrix and Al<sub>2</sub>O<sub>3</sub> particles together with excellent compressive strength also make Al<sub>2</sub>O<sub>3</sub> a potential candidate for TMCs [15,16]. The reaction products formed at the interface between the matrix and reinforcement phases play an important role in the final composite properties, therefore, understanding of the phase transformations is important.

In literature, it has been widely reported that TiAl and Ti<sub>3</sub>Al are the main reaction products of Ti-Al<sub>2</sub>O<sub>3</sub> system [16–18] and that the reaction sequence at 1100 °C is Al<sub>2</sub>O<sub>3</sub>/TiAl/Ti<sub>3</sub>Al/Ti [16,17]. However, it has also been reported that the presence of TiAl can negatively affect the corrosion resistance of Ti-Al<sub>2</sub>O<sub>3</sub> interfaces. Rocha et al. [17] studied the corrosion behavior of Ti-Al<sub>2</sub>O<sub>3</sub> interfaces produced by diffusion bonding of Ti substrates and Al<sub>2</sub>O<sub>3</sub>. The authors observed that both TiAl and Ti<sub>3</sub>Al were formed at the interface. Moreover, chemical degradation of the interface was dictated by the presence of TiAl while Ti<sub>3</sub>Al was found to have electrochemical behavior closer to Ti.

Literature on the tribocorrosion behavior of Ti-Al<sub>2</sub>O<sub>3</sub> composites is very limited. Gordo et al. [19] studied the corrosion and tribocorrosion behavior of Ti

reinforced with 1 wt.% Al<sub>2</sub>O<sub>3</sub>, processed by a combination of colloidal techniques and pressureless sintering. The authors observed that the corrosion behavior of both Ti and Ti-Al<sub>2</sub>O<sub>3</sub> composites were similar, meaning that the incorporation of the ceramic phase did not deteriorate the corrosion resistance of Ti. Additionally, the composites showed less wear volume loss. However, it is important to note that in this study Al<sub>2</sub>O<sub>3</sub> was not used as a direct reinforcement but as an additive to control the microstructure of Ti. More recently, a study by one of the present authors [20] showed promising results regarding wear behavior of Ti-Al<sub>2</sub>O<sub>3</sub> composites processed by powder metallurgy. Depending on the testing conditions, composites showed four-times decrease in wear volume loss. However, for more demanding conditions, the authors reported that fragmentation of Al<sub>2</sub>O<sub>3</sub> particles (average particle size of 63 μm) may take place during sliding and act as third-body abrasive. When this fragmentation happened, composites tended to present elevated wear volume loss compared to unreinforced Ti hence it was concluded that optimization of reinforcement particle size may be necessary. Accordingly, in the present work, Ti-Al<sub>2</sub>O<sub>3</sub> composites were produced using smaller reinforcement particles, and the effect of reinforcement and intermetallic phases on the corrosion and tribocorrosion behavior was explored.

## **3.2. Experimental**

### *3.2.1. Materials and methods*

Ti and Ti-Al<sub>2</sub>O<sub>3</sub> composites were synthesized by using Grade 2 Ti (Alfa Aesar) and Al<sub>2</sub>O<sub>3</sub> (Siladent) powders, both with irregular shapes. Particle size distribution was determined by laser diffraction (Malvern Series 2600), and the results are given in Table 3.1. Raw powders, Ti and Al<sub>2</sub>O<sub>3</sub>, were weighted to produce 5% and 10% vol. Al<sub>2</sub>O<sub>3</sub> reinforced TMCs together with 0.4 vol.% of PVA (Sigma Aldrich, Mowiol 8-88) that was used as binder. Before mixing, powders were kept at 105°C for 30 min to evaporate the water used in PVA solution. The powders were then mixed in a ball mill (with 10 mm diameter Al<sub>2</sub>O<sub>3</sub> balls) operating at 120 rpm for 8 h and under an Ar atmosphere. Afterwards, powders were cold compacted in a steel die (lubricated with zinc stearate) for 2 min under uniaxial pressure of 350 MPa. Binder was then removed in a tubular furnace set at 450 °C for 3 h and under an Ar atmosphere, with heating and cooling rates of

5 °C/min. Samples were then sintered at 1100 °C for 3 h under high vacuum (<10<sup>-5</sup> mbar), where 5°C/min was set as heating and cooling rates. Prior to all tests and characterization, samples were ground down to 4000 mesh size SiC paper and then polished with colloidal silica suspension (Struers) to 0.04 µm. Afterwards, samples were ultrasonically cleaned in propanol for 10 min followed by 5 min in distilled water and dried with harm air. In order to obtain similar surface conditions, samples were kept in a desiccator for 24 h prior to each corrosion or tribocorrosion test.

**Table 3.1.** Particle size distribution of Ti and Al<sub>2</sub>O<sub>3</sub> powders.

	D[v,0.1] (µm)	D[v,0.5] (µm)	D[v,0.9] (µm)
Ti	10	25	44
Al <sub>2</sub> O <sub>3</sub>	17	42	71

### 3.2.2. Corrosion tests

Corrosion tests were performed in an electrochemical cell containing 200 mL of 0.9 wt.% NaCl solution at body temperature (37 ± 2 °C) using a three-electrode setup, where the sample was connected as working electrode (WE, exposed area of 0.38 cm<sup>2</sup>), a Pt wire was used as counter-electrode and a saturated calomel electrode (SCE) was plugged as reference electrode (all the potential values are given versus SCE). The corrosion tests consisted in monitoring open circuit potential (OCP), followed by electrochemical impedance spectroscopy (EIS) and finally by potentiodynamic polarization. All the tests were performed using a Gamry Potentiostat/Galvanostat/ZRA (model Referece-600). The OCP measurements were performed until stabilization, and the system was considered stable when the potential drift was below 60 mV/h. EIS measurements were carried out at OCP and the data acquisition was performed by scanning a range of frequencies from 10<sup>5</sup> to 10<sup>-2</sup> Hz, with 7 points per frequency decade and an amplitude of the sinusoidal signal of 10 mV. Potentiodynamic polarization scans were performed in the anodic direction, starting at 0.2 V below OCP values up to 1.5 V<sub>SCE</sub>, with a scanning rate of 1 mV/s.

### 3.2.3. Tribocorrosion tests

Tribocorrosion tests were performed in a tribo-electrochemical cell placed in a tribometer (CETR-UMT-2) with a reciprocating ball-on-plate configuration. A

10 mm diameter alumina ball (Ceratec) was used as counter-body. All the tests were performed in 30 mL of 0.9 wt.% NaCl solution at body temperature ( $37 \pm 2$  °C). OCP was measured before, during, and after sliding using a two-electrode setup (SCE as reference electrode and sample as working electrode) connected to a Gamry Potentiostat/Galvanostat/ZRA (model Referece-600). Two different tribological parameters were used as presented in Table 3.2. The conditions were chosen based on the previous study of the one of the present authors [20] where 2<sup>4</sup> full factorial experimental design was performed in order to study the effect of reinforcement volume fraction, applied normal load, sliding frequency, and time on wear behavior of Ti-Al<sub>2</sub>O<sub>3</sub> composites. The authors determined that the most important factors in wear volume loss were normal load, frequency, and sliding time [20]. In the present study, lightest (C1) and harshest (C2) conditions of the previous work were chosen to study the tribocorrosion behavior of Ti-Al<sub>2</sub>O<sub>3</sub> composites. All the tests were repeated at least 3 times in order to assure repeatability of the results. After tribocorrosion tests, the samples were cleaned as described previously.

**Table 3.2.** Parameters used in tribocorrosion tests, where C1 and C2 represent lighter and harsher conditions, respectively.

Condition	Load (N)	Frequency (Hz)	Amplitude (mm)	Time (s)	Initial Hertzian contact pressure for CP Ti (MPa)
C1	1	1	5	1800	420
C2	2	2	5	3600	530

#### 3.2.4. Characterization

The microstructure and chemical composition were evaluated by FEI Nova 200 field emission gun scanning electron microscope (FEG-SEM), equipped with EDAX energy dispersive X-ray spectroscopy (EDS). Hardness was evaluated by Vickers macro-hardness tests performed on an Officine Galileo Mod. D200 tester under 30 kgf of load during 15 s, where 5 indentations were made per sample to calculate the average hardness values in at least on three different samples. The worn surfaces were characterized by using FEG-SEM/EDS, where all the images were taken parallel to the sliding direction. The wear track profiles were obtained by a surface profilometer (Veeco, Dektak 150). The wear volume calculations followed the same procedure given elsewhere [21].

### 3.3. Results and discussion

#### 3.3.1. Microstructural characterization

The overall microstructure of the as-sintered composites is shown in Fig. 3.1. As can be seen on the optical microscope (OM) images, Fig 3.1b and 3.1c, and more clearly on the back-scattered electron (BSE) and secondary electron (SE) SEM images presented in Fig. 3.1d, residual porosity was observed in all groups, which is commonly obtained in conventional powder metallurgy-based routes. Ti-10Al<sub>2</sub>O<sub>3</sub> composites presented higher porosity compared to Ti-5Al<sub>2</sub>O<sub>3</sub> composite, which can be rationalized by the increased amount of reinforcement phases. Hence, Oksiuta et al. [22] reported that as the amount of reinforcement increases, it leads to an increase in internal friction and consequent bridging effects which hinder consolidation of the material. On the other hand, porosity may also be caused due to pulling out and/or fragmentation of reinforcement particles during sample preparation. The microstructure of both composites can be seen in more detail in Fig. 3.1e. Both composites are composed by dark reinforcement particles (Al<sub>2</sub>O<sub>3</sub>), a light grey matrix (Ti) and a dark grey reaction zone surrounding the Al<sub>2</sub>O<sub>3</sub> particles. SE images showed a clean interface between the reinforcement and the reaction zone without any defects such as porosity. The reaction zone itself was composed by two distinct zones: Z1 and Z2, as shown in Fig. 3.1f. EDS analysis suggested that Z1 and Z2 were mainly constituted by Ti<sub>3</sub>Al and TiAl, respectively (Fig. 3.1g). These results are in accordance with a recent published work by one of the present authors, where Ti-Al<sub>2</sub>O<sub>3</sub> composites were processed under identical processing parameters [20]. In the literature, it has been reported that TiAl and Ti<sub>3</sub>Al are the main reaction products of Ti-Al<sub>2</sub>O<sub>3</sub> reaction system [16–18]. The formation of these reaction products depends on the local oxygen activity and temperature. Under low oxygen pressure, dissolution of both oxygen and aluminum take place in Al<sub>2</sub>O<sub>3</sub>. Thus, near the Ti matrix, Ti<sub>3</sub>Al starts to form and further Al diffusion gives origin to TiAl, while oxygen tends to be diffusion into the Ti matrix [23,24].

The effect of reinforcement content on macro-hardness and fracture toughness values are shown in Table 3.3. Ti-5Al<sub>2</sub>O<sub>3</sub> group presented 44 % higher hardness than pure Ti, while Ti-10Al<sub>2</sub>O<sub>3</sub> group only presented an 8% increase. These values can be due to several factors, such as amount of porosity or increased brittleness, that can be expected to be correlated with volume fraction

of reinforcement. The Vickers indentations were also used to estimate the fracture toughness ( $K_C$ ) of the composites by taking in consideration the cracks that were formed on the tips of the indentation. As reported by Meir et al. [25], Ti-Al<sub>2</sub>O<sub>3</sub> composites present a Palmqvist crack system, where  $K_C$  values can be calculated following Eq. (3.1).

$$K_C = 0,0264(HVa) \left( \frac{E}{HV} \right)^{0,4} l^{-0,5} \quad (3.1)$$

Where HV is the Vickers hardness, E is the Young's modulus, ( $a$ ) is the half of the diagonal of the Vickers indentation and ( $l$ ) is the crack length starting from the tip of the indentation. For the purpose of this work, the Young's modulus values of the processed composites were estimated using rule of mixtures by taking in consideration reported values for CP Ti and alumina (around 120 GPa for CP grade 2 Ti and around 380 GPa for alumina [25]). In this way,  $E$  values were estimated as 133 and 146 GPa for Ti-5Al<sub>2</sub>O<sub>3</sub> and Ti-10Al<sub>2</sub>O<sub>3</sub>, respectively. As can be seen in Table 3.3, both composites presented significantly reduced fracture toughness compared to the ones usually reported for Ti. Similar results were also reported in literature [25]. Marjan et al. [26] reported that the formation of TiAl and Ti<sub>3</sub>Al intermetallics on Ti-Al<sub>2</sub>O<sub>3</sub> composites may have a detrimental effect on the mechanical properties due to high brittleness of these phases. In the same study, the authors also observed Al<sub>2</sub>O<sub>3</sub> particle de-bonding, which may indicate a weak ceramic-matrix interface, possibly due to formation of these phases. Nano-indentation tests were performed on the reaction zone of Ti-5Al<sub>2</sub>O<sub>3</sub> composites by applying a 50 mN load during 5 s. The results revealed a highly heterogeneous reaction zone, at least from a hardness standpoint (Fig. 3.1h).

**Table 3.3.** Hardness and fracture toughness values estimated from eq. (3.1).

	Ti	Ti-5Al <sub>2</sub> O <sub>3</sub>	Ti-10Al <sub>2</sub> O <sub>3</sub>
Hardness (HV <sub>30</sub> )	192 ± 11	277 ± 9	208 ± 17
Fracture Toughness (K <sub>c</sub> )	55 – 66 [43]	5.0 ± 0.2	3.9 ± 0.3

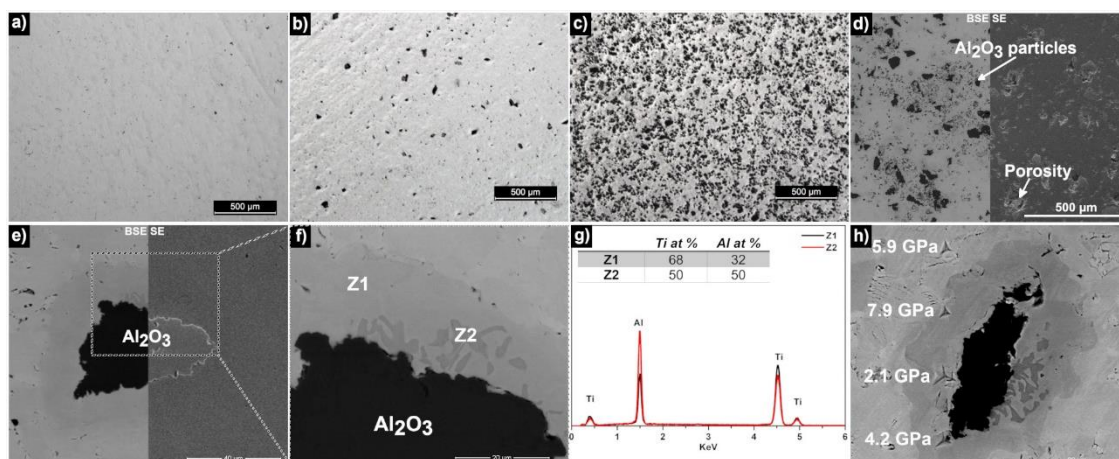


**Figure 3.1.** Low magnification OM images of (a) Ti, (b) Ti-5Al<sub>2</sub>O<sub>3</sub> composites and (c) Ti-10Al<sub>2</sub>O<sub>3</sub> composite, together with low magnification SE/BSE SEM image of (d) Ti-10Al<sub>2</sub>O<sub>3</sub> composite, higher magnification BSE and SE images of (e,f) Ti-5Al<sub>2</sub>O<sub>3</sub> composite, (g) EDS spectra taken from Z1 and Z2 and (h) nano-indentations and hardness values taken from the reaction zone (h).

### 3.3.2. Corrosion behaviour

Representative EIS spectra in the form of Bode and Nyquist diagrams are shown in Fig. 3.2a and 3.2b, respectively. Based on these results, the corrosion behavior can be divided in two different groups: unreinforced Ti and composite (Ti-5Al<sub>2</sub>O<sub>3</sub> and Ti-10Al<sub>2</sub>O<sub>3</sub>) groups. The schematic representations of the equivalent electric circuits (EEC) used to fit the EIS results for Ti and composites groups can be seen in Figs. 3.2c and 3.2d, respectively. Traditionally, Ti samples are usually represented by a simple EEC R(RQ). However, in the present study the obtained  $\chi^2$  values were considerably high (c.a.  $10^{-3}$ ). Moreover, after a detailed analysis, evidence of two-time constants could be seen, one at high frequency range and the second one at low frequency range. Thus, it is more adequate to use a ladder ECC consisting as R(Q[R(RQ)]). The use of this EEC can be explained based on the residual porosity observed on Ti originating from the processing method. Therefore, R0 represents the electrolyte resistance, CPE-T represents the capacitance of the native oxide film formed at the surface (which could be in parallel with a resistance of the oxide, however, it was removed from the EEC due to its extremely high value, thus, it acts as an open circuit), R1 is an additional resistance of the electrolyte inside the pores and the pair R2/CPE2 represents the resistance and the capacitance of the oxide formed inside the pores. Thus, all the Ti surface is covered by an oxide film, but with different thickness and, so, different responses at the surface and inside the pores. The fitted parameters obtained from EIS data for all groups of samples are



presented in Table 3.4. R<sub>0</sub> values are not presented since these values are a function of the electrolyte resistivity, electrochemical cell geometry, and the distance between working electrode and reference electrode. All these factors were kept constant during the corrosion tests, hence the R<sub>0</sub> values do not bring any relevant information on the studied system.

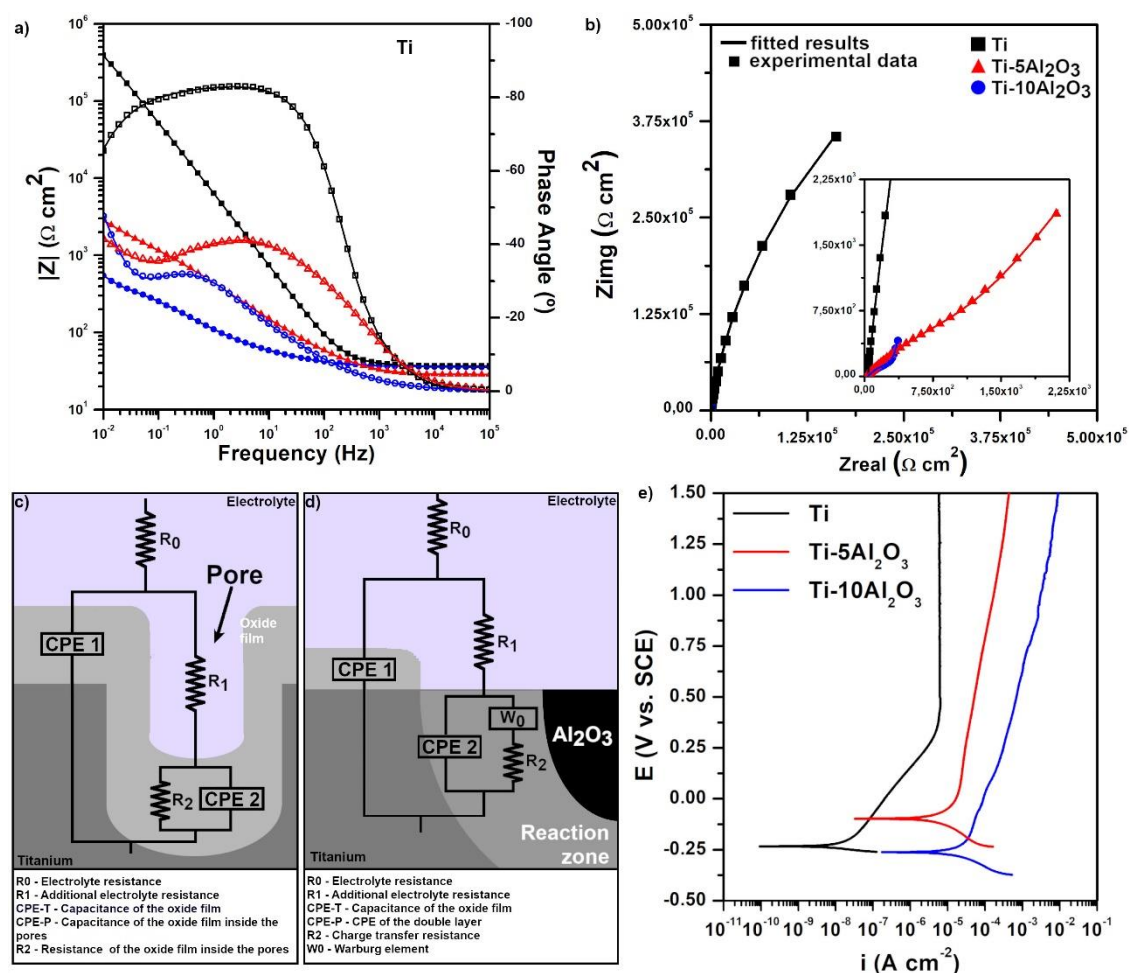


**Figure 3.2.** a) Bode and b) Nyquist diagrams obtained for Ti and composite groups; c) EEC used for Ti and d) for composite groups; e) potentiodynamic polarization curves obtained for Ti and composites in 9 wt.% NaCl at 37 °C.

Both composites presented considerable differences when compared with unreinforced Ti, however, there is an evolution according with the reinforcement volume fraction. In fact, there is an abrupt decrease on the total impedance of the system. It is even impossible to observe simultaneously the spectra of Ti and of the composites on the same Nyquist diagram. The obtained results indicate that there is an active phase that probably is not covered by an oxide film and thus it was corroding. Although the EEC used in this case only shows the addition of a diffusion element, it is worth to note that R<sub>2</sub> and CPE2 correspond to an active

surface and, therefore, have a different physical meaning when compared with EEC used for unreinforced Ti.

In fact, in addition to the oxide film formed at the Ti matrix surface, there was the presence of the reaction zone, composed of TiAl and Ti<sub>3</sub>Al, where the electrochemical activity was probably concentrated. Thus, the pair R2/CPE2 represents the charge transfer resistance and the double layer capacitance, respectively, of an active material. Due to the high reaction rate, the process became controlled by the species diffusion in these regions, so a diffusional element is added in series with the charge transfer resistance. These faradaic processes are limited by the charge transfer resistance and by the diffusion resistance, which is represented by a generalized finite Warburg element and it is an extension of another more common element, the finite-length Warburg W0. This element is characterized by a resistance value (W0-R), a parameter related with the thickness of the diffusion film (W0-T) and an exponent (W0-P). Moreover, the unreacted Al<sub>2</sub>O<sub>3</sub> particles were not considered in this EEC due to its extremely high insulating characteristics, which do not contribute to the EIS spectra. However, the presence of these insulating particles may have an impact on the EIS response of the system, once they may influence either the general porosity or the percentage of TiAl and/or Ti<sub>3</sub>Al phases depending on the reinforcement volume fraction.

CPE1 values for Ti-5Al<sub>2</sub>O<sub>3</sub> composites increased about 8 times compared to Ti, while for Ti-10Al<sub>2</sub>O<sub>3</sub> composites these values increased by almost 2 decades. Comparing the  $n_1$  values, Ti presented values equal to 1, while composites presented values around 0.82 and 0.53 for Ti-5Al<sub>2</sub>O<sub>3</sub> and Ti-10Al<sub>2</sub>O<sub>3</sub> composites, respectively. Comparing the R2 values of Ti and its composites, it is possible to observe that the composites presented much lower values. In the case of the unreinforced Ti, R2 values represented the electronic resistance on an oxide, while in the case of the composites these values represented the charge transfer resistance that occurred on the active material (mostly on the reaction zone). However, the reaction that occurs on the active material might be an anodic reaction of the products present at the reaction zone, a cathodic reaction promoted by the presence of TiAl and/or Ti<sub>3</sub>Al phases, or both anodic and cathodic reactions occurring at this zone. When a charge transfer resistance is considered in a general corrosion process, this resistance is considered as the

resistance of two processes (anodic or cathodic), but if the resistance of each individual process is significantly different, the reaction of the slowest process is the dominant. Thus, in this study, in order to obtain additional information, it would be necessary to perform EIS at potentials that promote the anodic reaction (above the OCP values) and at potentials where the cathodic reaction will be promoted (under OCP values). In this way, it would be possible to notice the influence of those potentials on R2 values. Furthermore, as the reinforcement volume fraction increased, R2 values decreased. Wo-R values give insight about the areas where corrosion took place i.e. where there was no formation of the native oxide film. As can be seen, these values also decreased with reinforcement content, which are in accordance with the experimental data.

**Table 3.4.** Fitted parameters obtained from EIS data for Ti and composite groups.

	Ti	Ti-5Al <sub>2</sub> O <sub>3</sub>	Ti-10Al <sub>2</sub> O <sub>3</sub>
<b>CPE1-T (x 10<sup>-5</sup>S<sup>n</sup>/Ωcm<sup>-2</sup>)</b>	(1.2 ± 0.7) x 10 <sup>-5</sup>	(8.2 ± 2.9) x 10 <sup>-5</sup>	(2.8 ± 1.4) x 10 <sup>-3</sup>
<b>n<sub>1</sub></b>	1.0 ± 0.1	0.8 ± 0.1	0.56 ± 0.01
<b>CPE2-T (x 10<sup>-5</sup>S<sup>n</sup>/Ωcm<sup>-2</sup>)</b>	(1.4 ± 0.9) x 10 <sup>-5</sup>	(5.6 ± 1.6) x 10 <sup>-4</sup>	(1.3 ± 0.3) x 10 <sup>-3</sup>
<b>n<sub>2</sub></b>	0.89 ± 0.03	0.57 ± 0.05	0.7 ± 0.1
<b>R<sub>2</sub> (Ω.cm<sup>-2</sup>)</b>	(1.1 ± 0.4) x 10 <sup>5</sup>	(2.6 ± 1.7) x 10 <sup>3</sup>	(4.2 ± 0.9) x 10 <sup>2</sup>
<b>W<sub>0</sub>- R (Ω.cm<sup>-2</sup>)</b>	–	(2.0 ± 1.3) x 10 <sup>3</sup>	(2.2 ± 0.9) x 10 <sup>2</sup>
<b>W<sub>0</sub>- T</b>	–	11.8 ± 14.1	4.9 ± 2.0
<b>W<sub>0</sub>- P</b>	–	0.3 ± 0.1	0.5 ± 0.0
<b>χ<sup>2</sup></b>	< 10 <sup>-4</sup>	< 10 <sup>-5</sup>	< 10 <sup>-5</sup>

Representative potentiodynamic polarization (PD) curves for unreinforced Ti and composite groups are presented in Fig. 3.2e and corrosion potential (E<sub>(i=0)</sub>), corrosion current density (i<sub>corr</sub>) and passivation current density (i<sub>pass</sub>) values obtained from the potentiodynamic polarization curves are given in Table 3.5. It is important to note that for Ti group, i<sub>pass</sub> is given instead of i<sub>corr</sub> due to formation of the passive oxide film. Unreinforced Ti samples presented a cathodic domain for potentials below -0.25 V and a passive plateau starting at 0.40 V due to formation of the passive oxide film presenting a passivation current density of 5.5 μA cm<sup>-2</sup>.

**Table 3.5.** Passivation current density (i<sub>pass</sub>), corrosion current density (i<sub>corr</sub>), and corrosion potential (E<sub>(i=0)</sub>) values for Ti and Ti-Al<sub>2</sub>O<sub>3</sub> composites.

	Ti	Ti-5Al <sub>2</sub> O <sub>3</sub>	Ti-10Al <sub>2</sub> O <sub>3</sub>
<b>i<sub>pass</sub> (μA cm<sup>-2</sup>)</b>	5.53 ± 0.67	–	–
<b>i<sub>corr</sub> (μA cm<sup>-2</sup>)</b>	–	11.96 ± 4.99	38.86 ± 1.99
<b>E<sub>(i=0)</sub> (V)</b>	- 289 ± 90	- 0.12 ± 0.02	- 0.28 ± 0.02

Composites presented a different behavior, where the well-defined passivation plateau observed on Ti was lost. Instead, an increase of current density values with the applied potential was noticed. In addition, it is important to note that the curves were also shifted to the right side of the graph, with Ti-5Al<sub>2</sub>O<sub>3</sub> and Ti-10Al<sub>2</sub>O<sub>3</sub> composites showing an overall one decade and two decades increase, respectively, in corrosion current density values. Although no passivation plateau was observed, the increase in corrosion current density with potential was relatively small. This behavior suggests that a passive film was forming on the surface, although a passivation plateau was not reached. Considering the overall microstructure of the composite surfaces, it is reasonable to assume that the Ti matrix still had the ability to form the native oxide film. However, the high CPE1-T values suggest that this oxide film presented higher level of heterogeneities and overall, less quality. The presence of Al<sub>2</sub>O<sub>3</sub> particles, reaction zones and overall porosity are probably the cause. These not only disrupted the continuity of the passive layer but there was also the fact of the presence of TiAl and Ti<sub>3</sub>Al phases that can contribute to an active corrosion mechanism, as shown by the EIS results.

It is well-known that the incorporation of inert ceramic particles can affect the overall corrosion resistance of the base material. If both reinforcement particles and possible reaction zones are electrochemically neutral, no significant change on corrosion behavior may be expected to occur [27]. However, the changes in microstructure and/or chemical composition may happen, such as residual stresses, porosity, micro-crevices, formation of second phase, and interfacial products, which may influence the electrochemical behavior. Porosity and micro-crevices may lead to a different state of the passive film inside the pores, leading to a decrease in the overall corrosion resistance of the material [10]. Moreover, from a general point of view the presence of the ceramic reinforcement particles may also affect the integrity and continuity of the passive film. The second phases and interfacial products may change the corrosion resistance, depending on their nature, which may lead to a more electrochemical active behavior or act as an inert barrier against corrosion. The reinforcement itself may improve the overall corrosion resistance of the base material by acting as an inert physical barrier. Moreover, reinforcement particles may also lead to the formation of micro-galvanic cells, acting as cathode and thus leading to

increased oxidation kinetics on the base material, accelerating the formation of the native oxide film [28].

Recent studies by Marjan et. al. [29,30] on the corrosion behavior of Ti-Al<sub>2</sub>O<sub>3</sub> composites processed by spark plasma sintering (SPS) showed that, depending on the reinforcement volume fraction, the composites may or may not have similar behavior to that of Ti. The authors reported that higher amount of reinforcement led to the formation of a native oxide layer with overall less quality as evidenced by the lower  $R_{ox}$  and higher  $C_{dl}$  values. The authors justified these values by the presence of more TiAl and Ti<sub>3</sub>Al reaction products, which are more corrosion susceptible. Nevertheless, in those studies, the corrosion behavior of the composites was still close to that of the unreinforced Ti. However, it is important to note that in those studies, very fine Al<sub>2</sub>O<sub>3</sub> particles (0,1-3  $\mu$ m) were used, and consequently the overall microstructure was quite different from the one obtained in the present work. Similar results were also reported by Gordo. et al. [19], where Ti-Al<sub>2</sub>O<sub>3</sub> composites were also processed with very fine Al<sub>2</sub>O<sub>3</sub> particles (0.5  $\mu$ m) and presented corrosion behavior very close to that of Ti.

It has been reported that the corrosion behavior of binary TiAl and Ti<sub>3</sub>Al intermetallic phases can be placed between the corrosion behavior of pure Ti and pure Al, with the corrosion behavior of Ti<sub>3</sub>Al being closer to that of Ti due to higher percentage of Ti [31]. Rocha et al. [17] studied the electrochemical behavior of Ti/Al<sub>2</sub>O<sub>3</sub> interfaces. Results obtained by potentiodynamic tests, galvanic corrosion studies, and EIS showed that the chemical degradation of the interface was dictated by the presence of TiAl. The authors reported that TiAl had a strong detrimental influence on the corrosion resistance of the interface. On the other hand, Ti<sub>3</sub>Al was found to have corrosion behavior similar to that of Ti. Saffarin et al. [31] reported that TiAl was susceptible to pitting under environments containing chloride (Cl<sup>-</sup>), such as NaCl based solutions, where pitting started at potentials close to 0  $V_{SCE}$  depending on pH of the solution and Cl<sup>-</sup> concentration. Under the same conditions, pitting on Ti<sub>3</sub>Al was only observed at potentials above 1.5  $V_{SCE}$ , however, the presence of cracks or small defects may lower this potential to values close to 0.6  $V_{SCE}$ .

Considering the obtained results, corrosion behavior of the composites can be explained by the formation of a heterogeneous oxide film, with lower overall quality, on the Ti matrix, together with increased susceptibility to corrosion

introduced by the presence of Ti<sub>3</sub>Al and TiAl intermetallic phases at the matrix/reinforcement interface, that may have been amplified by the presence of microstructural defects due to processing as well as sample preparation.

### 3.3.3. Tribocorrosion behaviour

The representative evolution of OCP before, during, and after sliding together with the evolution of coefficient of friction (COF) during sliding for all groups and testing conditions are given in Fig. 3.3. Before sliding, Ti presented stable OCP values due to growth of the passive film. Independently of the testing conditions, a sharp cathodic shift in OCP values was observed for Ti as soon as the load was applied and sliding started. This behavior is due to destruction of the passive film and consequent formation of active zones leading to an increase in susceptibility to corrosion under the mechanical action. OCP values for Ti dropped down to values in the range of  $-0.6$  V and  $-0.8$  V for C1 and C2 conditions, respectively, indicating an increase in susceptibility to corrosion for harsher conditions as compared to the lighter ones. Under sliding, after some time, sudden increases in OCP and COF values were observed for Ti tested under C1 condition, which were not observed on C2 condition. After sliding, OCP values increased to more positive values and tended to reach the similar values recorded before sliding, due to repassivation of the worn area.

Composites presented a different behavior compared to unreinforced Ti. Before sliding, composites presented stable OCP values. Under C1 condition, the values remained almost unaffected after sliding started and only after a very short run-in period (around 2 min), a very small drop on OCP (around 50 mV) was observed. Regarding the evolution of COF, both composites presented similar behaviors under C1 condition. Similar to OCP evolution, a run-in period was also observed on COF values during the same time, where COF values started at around 0.1 and increased to around 0.6 for Ti-5Al<sub>2</sub>O<sub>3</sub> and around 0.7 for Ti-10Al<sub>2</sub>O<sub>3</sub> group, then followed a relatively horizontal course until the end of sliding. Under C2 condition, a run-in period could also be observed in OCP and COF values, although with some differences. OCP values presented a very slow decrease immediately after sliding started, however this decrease was very small as compared to Ti. COF values also presented a run-in period during the same

period, however, compared to C1 condition, COF values were significantly higher at the start of sliding.

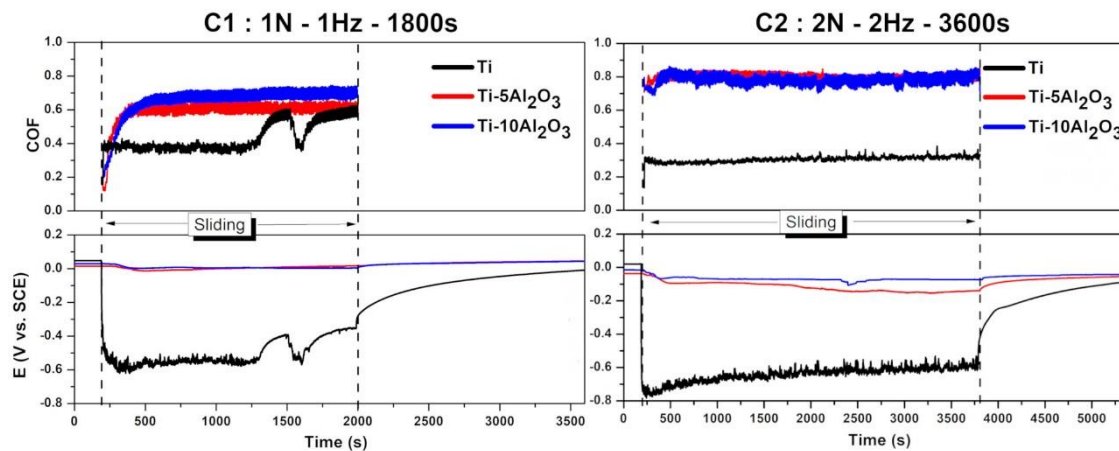


**Figure 3.3.** Evolution of OCP before, during, and after sliding, together with the evolution of COF during sliding.

Fig 3.4. presents lower magnification BSE and SE SEM images of the wear tracks after tribocorrosion tests, together with EDS spectra taken from the corresponding counter-body surfaces. The damage observed on the unreinforced Ti surfaces was more severe to what was observed on both composites, especially under C2 condition. Comparing both composite groups, wider wear tracks were obtained for Ti-10Al<sub>2</sub>O<sub>3</sub> composites under both conditions. In the same way, the counter-body surfaces that slid against the composite surfaces also presented considerably less wear damage than the ones that slid against Ti, specially under C2 condition. Regardless of the testing conditions, Ti peaks were observed in all the groups, confirming the transference of Ti from the worn surfaces to the counter-body (adhesive wear).



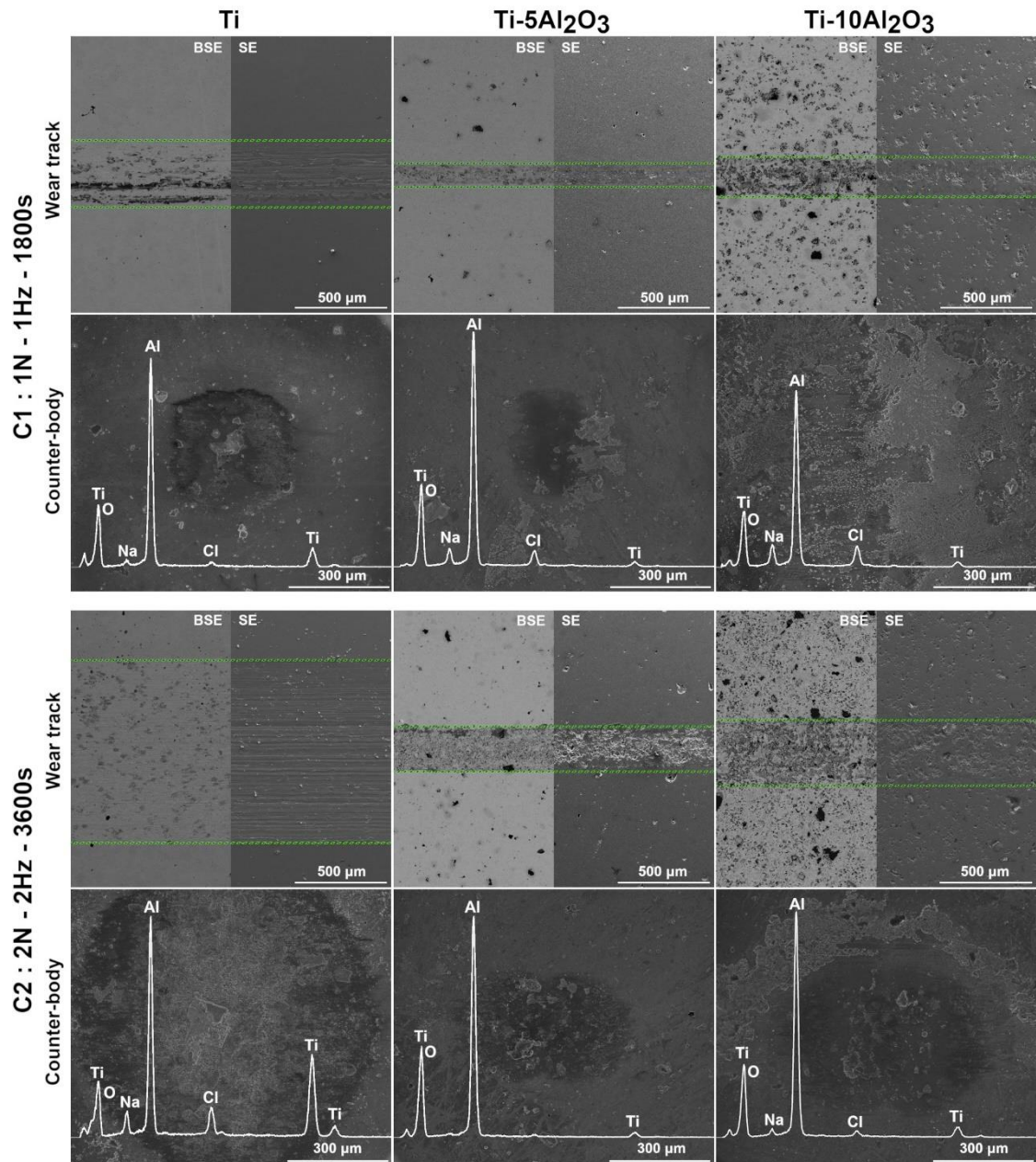


**Figure 3.4.** Lower magnification SE and BSE images of the wear tracks taken from Ti, Ti-5Al<sub>2</sub>O<sub>3</sub> and Ti-10Al<sub>2</sub>O<sub>3</sub> under C1 and C2 conditions, respectively, together with the corresponding EDS spectra taken from the counter-body.

Representative 2D wear profiles together with wear volume loss can be seen in Fig. 3.5. Both composites presented significantly less wear volume loss compared to the unreinforced Ti on both tested conditions. Under C1 condition, no significant differences were observed between the two composites, and in general, wear volume loss was found to be very low. Under C2 conditions, both unreinforced Ti and composites showed an increase in wear volume loss compared to C1 condition. Besides, it was observed that an increase on



reinforcement content led to an increase in wear volume loss. Nonetheless, these groups still presented drastically less wear volume loss compared to Ti.

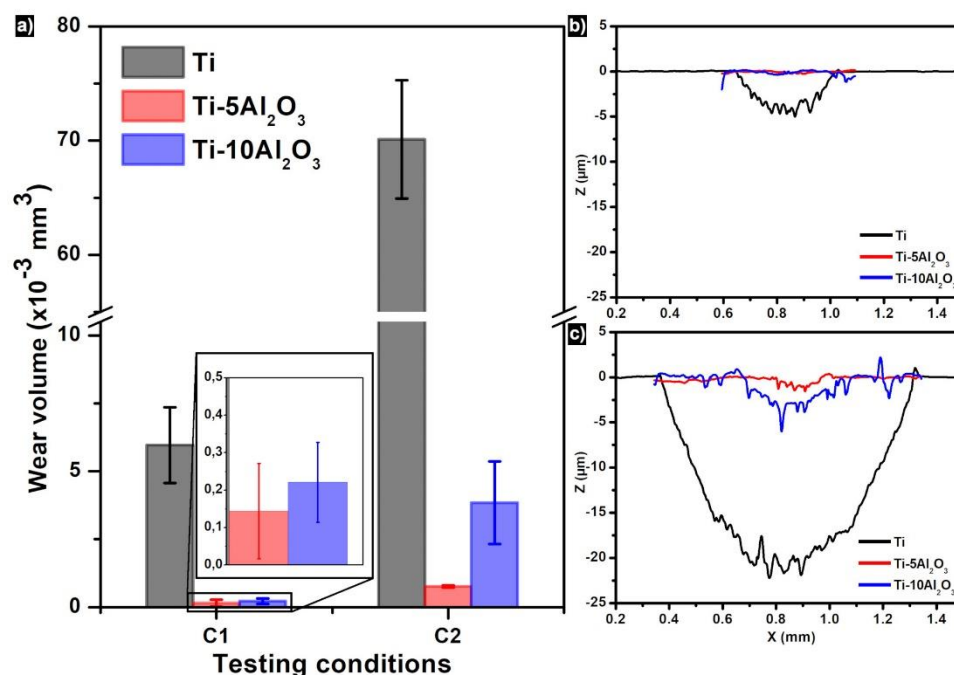


**Figure 3.5.** a) Wear volume loss values and representative wear track profiles for b) C1 and c) C2 condition.

Fig. 3.6 presents higher magnification SE and BSE SEM images of the wear tracks, where the topography and tribological features can be seen in detail. In order to better compare the difference between C1 and C2 condition, the evolution of OCP and COF for the first 1800 s of sliding were plotted together for each group. Clear differences were observed on the overall microstructure of the worn surfaces between Ti and composites. For Ti groups, the worn surfaces consisted of compacted oxide patches (discontinuous tribolayer) and parallel grooves to the sliding direction. Compacted oxide patches originate from the continuous oxidation and compaction of material being transferred between the two mating surfaces. These oxides can play a beneficial and/or detrimental role during tribocorrosion. Loose oxide particles within the wear track can act as a third-body abrasive and increase the mechanical wear. On the other hand, if these debris are compacted on the wear track, they can have a protective role by reducing electrochemical active zones within the wear track, that have been reported before for Ti and TMCs tested under similar conditions to C1 [20,32,33]. This behavior could be seen on the Ti group tested under C1 condition, where substantial increases in OCP and COF values could be seen during sliding

(Fig. 3.6). The formation and consequent thickening of the oxidized patches during sliding resulted in increased roughness, leading to higher COF values. Due to the protective nature of these oxide patches, a consequent increase in OCP was also observed, leading to a decrease on the corrosion susceptibility. With time, these oxide patches may reach a critical thickness and break, leading to a consequent decrease in both OCP and COF values. During the sliding action, this process may be repeated several times [34]. For Ti tested under C2 condition, such behavior was not observed. For this condition, OCP values tended to steadily increase with time, and no sudden variations were observed. COF values were lower than the ones observed on C1 condition and were relatively stable during the entire time of sliding. Silva et al. [27] studied the tribocorrosion behavior of Ti and Ti-TiB-TiN<sub>x</sub> composites processed by hot-pressing using a similar tribocorrosion setup and reported similar results for Ti. In that study, under harsher conditions (1N - 2 Hz), Ti tended to present lower COF values, which were attributed to high frequency sliding, where wear debris may present a more granular structure and consequently, may act as rolling balls (solid lubricant). Recently, Oliveira and Toptan [20] also reported that under harsher conditions (conditions similar to C2), wear debris tended to be pushed outside of the wear track and in this way, did not contribute to the formation of oxide patches. Based on the obtained results, a similar scenario may be considered. Although, some oxide patches could be seen on the worn surfaces for C2 condition, that may explain the slowly increase in OCP values during sliding. Apparently, these patches did not give enough protection to obtain the rather large increases in OCP and COF values observed in C1 condition. Since the wear damage was much lower, and the reinforcing particles played a load-carrying role, the influence of the oxide patches was not so noticeable on the composites.

Parallel grooves to the sliding direction were observed for Ti under both conditions, which were not observed for composite groups. These grooves known as ploughing grooves, are a typical feature of a combination of adhesive and abrasive wear and are usually observed in worn surfaces for Ti and Ti based alloys [35]. Under the same conditions, wear tracks from both composites presented similar features. Besides the oxide patches that were also observed on Ti surfaces, perpendicular cracks to the sliding direction and material

detachments reflect a brittle surface. During sliding, primary cracks can originate at weak points and, with time, the propagation of such cracks as well as the formations of new ones can lead to material detachment [36]. The susceptibility to crack initiation is dependent on several factors. Inclusions and imperfections at the surface can act as nuclei for crack initiation under plastic deformation [36]. On the other hand, high COF values are also a crack driving force since they lead to high shear loads between the two mating surfaces [35]. Additionally, the intrinsic properties of the materials in tribological contact also play a significant role [37]. In this work, the presence of such wear mechanism may be mostly associated by the overall lower fracture toughness of the composite surfaces.

In addition to the Al<sub>2</sub>O<sub>3</sub> particles and porosity, the reaction zones observed around these reinforcement particles may also have acted as nuclei for crack formation as these intermetallic TiAl and Ti<sub>3</sub>Al phases are reported to present very low ductility at room temperature. Furthermore, their compressive yield strength ranging from 350 to 500 MPa [38–41] are in the range of the initial Hertzian contact pressures that were applied in the tribocorrosion tests. High COF values together with the low fracture toughness of composites facilitated the propagation of cracks and consequently material detachment from the surface [42].

As can be observed on the evolution of OCP under sliding presented in Fig. 3.6, both composites presented overall lower OCP values under C2 condition, albeit a small difference, that can be explained by the higher surface damage (i. e. higher wear volume loss). Even though, the detachments on the wear tracks were not enough to cause a significant shift in OCP, as the worn damage was still much lower than the one observed on Ti. Regarding COF evolution, the run-in period that was observed for both composites suggests that initially, the tribological contact was mostly between the reinforcement particles and the counter-body, as suggested by the lower COF values. As sliding continued, the surface was damaged due to material detachment. Consequently, wear debris were oxidized and compacted on the wear track and/or acted as third-body abrasive, which led to a consequent increase of COF values. Under C2 condition, COF values were significantly higher at the onset of sliding compared to C1 condition pointing that a considerable wear damage was done right at the onset of sliding, as suggested by the decrease on OCP values.

Ti-10Al<sub>2</sub>O<sub>3</sub> composites presented considerably more visible material detachment than Ti-5Al<sub>2</sub>O<sub>3</sub> composites. Nevertheless, due to the considerable amount of porosity presented in the Ti-10Al<sub>2</sub>O<sub>3</sub> composites, it was hard to distinguish that porosity from the material that was detached during sliding.

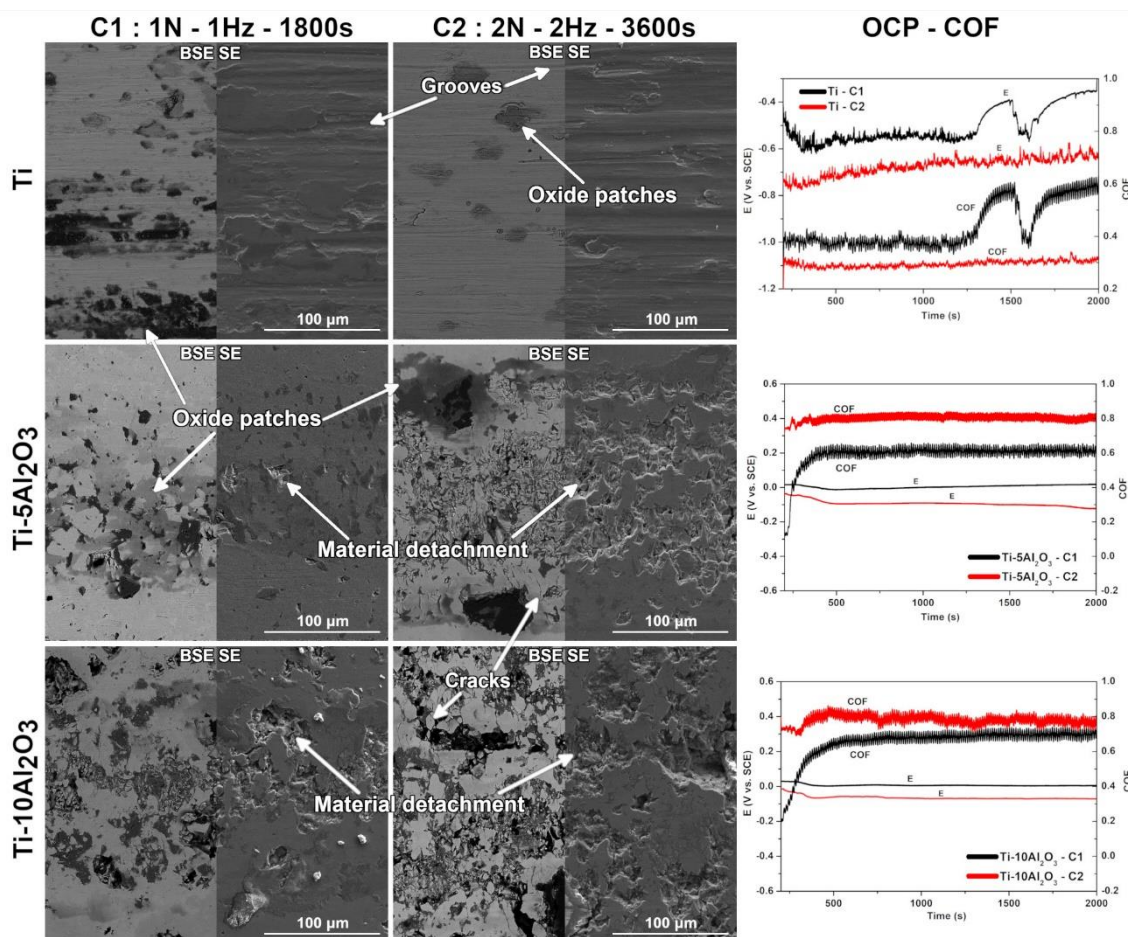


**Figure 3.6.** Higher magnification SE and BSE SEM images of wear tracks from Ti, Ti-5Al<sub>2</sub>O<sub>3</sub>, and Ti-10Al<sub>2</sub>O<sub>3</sub> composites under C1 and C2, respectively, together with the evolution of OCP and COF during sliding.

The proposed wear mechanisms for Ti and composites groups are shown in Fig. 3.7. For Ti groups, the general wear behavior can be described as the typical behavior observed for Ti and its alloys. Ti is highly susceptible to adhesive wear and thus material tends to be transferred from the worn surfaces to the counter material. As sliding continues, transferred material can adhere to the counter body and abrade the surface, leading to the formation of grooves. During the repetitive transfer and mechanical action, this material tends to get oxidized and consequently harder, which can then easily abrade the testing metal. In addition, material can also be compacted on the wear track, leading to the formation of oxide patches, act as a third-body abrasive and/or ejected out of the wear track. For harsher conditions, the amount of material ejected out of the wear

track probably tended to be higher and thus less formation of oxide patches occurred and eventually drastic variations on OCP and COF values were not observed.

Composite surfaces presented considerably lower wear volume loss, especially for harsher conditions. However, due to lower fracture toughness and high contact pressures, cracks formed and propagated on the wear track. As sliding proceeded, cracks started to connect to each other and thus material was detached from the worn surfaces, albeit not enough to observe substantial differences on OCP and COF values. Due to lower fracture toughness and overall, more heterogeneities (i.e. Al<sub>2</sub>O<sub>3</sub> particles, reaction zones and pores) where cracks may originate, Ti-10Al<sub>2</sub>O<sub>3</sub> composites tended to present more cracks and thus material detachments, which were more evident on the harsher C2 condition. Similar to Ti, these detachments may adhere to the counter-body, be compacted and/or ejected on the wear track and/or act as third-body abrasive.

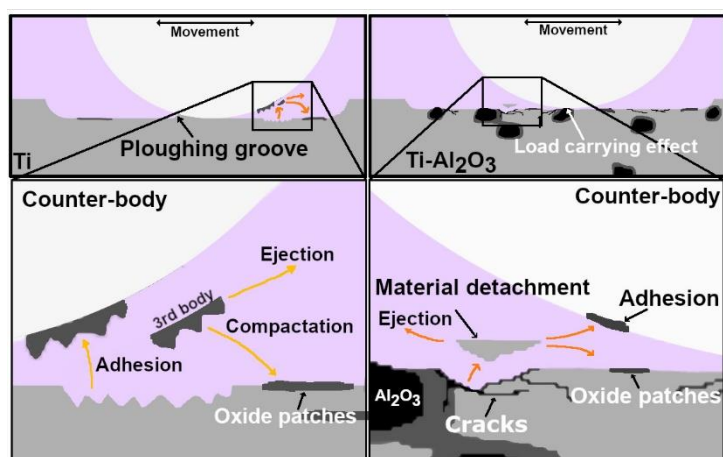


Figure 3.7. Proposed wear mechanisms for Ti and Ti-Al<sub>2</sub>O<sub>3</sub> composites.

### 3.4. Conclusions

TMCs reinforced with different volume fraction of Al<sub>2</sub>O<sub>3</sub> particles were processed by conventional powder metallurgy. Results suggested that the intermetallic TiAl and Ti<sub>3</sub>Al phases formed due to reaction of Ti with reinforcement particles had a substantial impact on the properties of Ti-Al<sub>2</sub>O<sub>3</sub> composites. These intermetallic phases had a detrimental effect on the corrosion behavior of the composites. Moreover, the composites showed a significant decrease in tendency to corrosion under sliding together with a significant reduction on the wear volume loss. The presence of cracks and material detachments from the

composite surfaces indicated that efforts must be made to optimize the processing conditions in order to address the low fracture toughness. Thus, it is suggested that in further studies, microstructure should be improved, mainly to control the excess formation of intermetallic phases.

## References

- [1] S. Affatato, D. Brando, Introduction to wear phenomena of orthopaedic implants, in: S. Affatato (Ed.), *Wear Orthop. Implant. Artif. Joints*, 1st ed., Woodhead, 2012: pp. 3–26.
- [2] G.G. de Lima, G.B. de Souza, C.M. Lepienski, N.K. Kuromoto, Mechanical properties of anodic titanium films containing ions of Ca and P submitted to heat and hydrothermal treatment, *J. Mech. Behav. Biomed. Mater.* 64 (2016) 18–30.
- [3] N. Diomidis, S. Mischler, N.S. More, M. Roy, Tribo-electrochemical characterization of metallic biomaterials for total joint replacement, *Acta Biomater.* 8 (2012) 852–859.
- [4] S. Mischler, Triboelectrochemical techniques and interpretation methods in tribocorrosion: A comparative evaluation, *Tribol. Int.* 41 (2008) 573–583.
- [5] M. Geetha, A.K. Singh, R. Asokamani, A.K. Gogia, Ti based biomaterials, the ultimate choice for orthopaedic implants - A review, *Prog. Mater. Sci.* 54 (2009) 397–425.
- [6] A. Amanov, I.S. Cho, D.E. Kim, Y.S. Pyun, Fretting wear and friction reduction of CP titanium and Ti-6Al-4V alloy by ultrasonic nanocrystalline surface modification, *Surf. Coatings Technol.* 207 (2012) 135–142.
- [7] H. Gülerüüz, H. Çimenoğlu, Effect of thermal oxidation on corrosion and corrosion-wear behaviour of a Ti-6Al-4V alloy, *Biomaterials.* 25 (2004) 3325–3333.
- [8] Y.L. Yang, D. Zhang, W. Yan, Y. Zheng, Microstructure and wear properties of TiCN/Ti coatings on titanium alloy by laser cladding, *Opt. Lasers Eng.* 48 (2010) 119–124.
- [9] B.S. Yilbas, S.Z. Shuja, Laser treatment and PVD TiN coating of Ti6Al4V alloy, *Surf. Coat. Technol.* 130 (2000) 152–157.
- [10] F. Toptan, A. Rego, A.C. Alves, A. Guedes, Corrosion and tribocorrosion behavior of Ti-B<sub>4</sub>C composite intended for orthopaedic implants, *J. Mech. Behav. Biomed. Mater.* 61 (2016) 152–163.
- [11] J.-S. Kim, K.-M. Lee, D.-H. Cho, Y.-Z. Lee, Fretting wear characteristics of titanium matrix composites reinforced by titanium boride and titanium carbide particulates, *Wear.* 301 (2013) 562–568.
- [12] G.C. Lee, R.H. Kim, Incidence of Modern Alumina Ceramic and Alumina Matrix Composite Femoral Head Failures in Nearly 6 Million Hip Implants, *J. Arthroplasty.* 32 (2017) 546–551.
- [13] S. Affatato, E. Modena, A. Toni, P. Taddei, Retrieval analysis of three generations of BioloX® femoral heads: Spectroscopic and SEM characterisation, *J. Mech. Behav. Biomed. Mater.* 13 (2012) 118–128.
- [14] D. Hannouche, M. Zingg, H. Miozzari, R. Nizard, A. Lübbecke, Third-generation pure alumina and alumina matrix composites in total hip arthroplasty, *EFORT Open Rev.* 3 (2018) 7–14.
- [15] M. Liu, Z. Wang, J. Wu, Q. Li, Effects of Nd<sub>2</sub>O<sub>3</sub> on the mechanical properties and oxidation behavior of Ti/Al<sub>2</sub>O<sub>3</sub> composites by vacuum hot pressing sintering, *J. Alloys Compd.* 648 (2015) 116–121.
- [16] Girish P. Kelkar, A.H. Carim, Phase Equilibria in the Ti-Al-O system at 945°C and Analysis of Ti/Al<sub>2</sub>O<sub>3</sub> reactions, *J. Am. Ceram. Soc.* 3 (1995) 572–573.
- [17] L. Rocha, E. Ariza, A. Costa, F. Oliveira, R. Silva, Electrochemical Behavior of Ti/ Al<sub>2</sub>O<sub>3</sub> Interfaces Produced by Diffusion Bonding, *Mater. Res.* 6 (2003) 439–444.
- [18] L.E. Karkina, L.I. Yakovenkova, Dislocation core structure and deformation behavior of Ti<sub>3</sub>Al, *Model. Simul. Mater. Sci. Eng.* 20 (2012) 065003.
- [19] E. Gordo, R.G. das Neves, B. Ferrari, A. Jimenez-Morales, A. Lima, A.C. Alves, A.M. Pinto, F. Toptan, Corrosion and tribocorrosion behavior of Ti-Alumina composites, *Key Eng. Mater.* 704 (2016) 28–37.

- [20] A. Oliveira, F. Toptan, Wear Behavior of Ti-Al<sub>2</sub>O<sub>3</sub> Biocomposites in 9 g/L NaCl Solution, *J. Mater. Eng. Perform.* 28 (2019) 6000–6010.
- [21] Z. Doni, A.C. Alves, F. Toptan, J.R. Gomes, A. Ramalho, M. Buciumeanu, L. Palaghian, F.S. Silva, Dry sliding and tribocorrosion behaviour of hot pressed CoCrMo biomedical alloy as compared with the cast CoCrMo and Ti6Al4V alloys, *Mater. Des.* 52 (2013) 47–57.
- [22] Z. Oksiuta, J.R. Dabrowski, A. Olszyna, Co–Cr–Mo-based composite reinforced with bioactive glass, *J. Mater. Process. Technol.* 9 (2008) 978–985.
- [23] A.M. Kliauga, M. Ferrante, Interface compounds formed during the diffusion bonding of Al<sub>2</sub>O<sub>3</sub> to Ti, *J. Mater. Sci.* 35 (2000) 4243–4249.
- [24] M. Liu, Z. Wang, J. Wu, Q. Li, Ti/Al<sub>2</sub>O<sub>3</sub> interfacial diffusion: Kinetic equation for growth of reaction layer and formation mechanism, *J. Alloys Compd.* 652 (2015) 260–265.
- [25] S. Meir, S. Kalabukhov, N. Frage, S. Hayun, Mechanical properties of Al<sub>2</sub>O<sub>3</sub>/Ti composites fabricated by spark plasma sintering, *Ceram. Int.* 41 (2014) 4637–4643.
- [26] M. Bahraminasab, S. Ghaffari, H. Eslami-Shahed, Al<sub>2</sub>O<sub>3</sub>-Ti functionally graded material prepared by spark plasma sintering for orthopaedic applications, *J. Mech. Behav. Biomed. Mater.* 72 (2017) 82–89.
- [27] J.I. Silva, A.C. Alves, A.M. Pinto, F. Toptan, Corrosion and tribocorrosion behavior of Ti–TiB–TiN<sub>x</sub> in-situ hybrid composite synthesized by reactive hot pressing, *J. Mech. Behav. Biomed. Mater.* 74 (2017) 195–203.
- [28] Y. Chen, J. Zhang, N. Dai, P. Qin, H. Attar, L.-C. Zhang, Corrosion Behaviour of Selective Laser Melted Ti–TiB Biocomposite in Simulated Body Fluid, *Electrochim. Acta.* 232 (2017) 89–97.
- [29] M. Bahraminasab, M. Bozorg, S. Ghaffari, F. Kavakebian, Corrosion of Al<sub>2</sub>O<sub>3</sub>-Ti composites under inflammatory condition in simulated physiological solution, *Mater. Sci. Eng. C.* 102 (2019) 200–211.
- [30] M. Bahraminasab, M. Bozorg, S. Ghaffari, F. Kavakebian, Electrochemical corrosion of Ti-Al<sub>2</sub>O<sub>3</sub> biocomposites in Ringer’s solution, *J. Alloys Compd.* 777 (2019) 34–43.
- [31] H.M. Saffarian, Q. Gan, R. Hadkar, G.W. Warren, Corrosion Behavior of Binary Titanium Aluminide Intermetallics, *Corros. Sci.* 52 (1996) 626–633.
- [32] J.I. Silva, A.C. Alves, A.M. Pinto, F.S. Silva, F. Toptan, Dry sliding wear behaviour of Ti–TiB–TiN<sub>x</sub> in-situ composite synthesised by reactive hot pressing, *Int. J. Surf. Sci. Eng.* 10 (2016) 317–329.
- [33] F. Toptan, A.C. Alves, Ó. Carvalho, F. Bartolomeu, A.M.P. Pinto, F. Silva, G. Miranda, Corrosion and tribocorrosion behaviour of Ti6Al4V produced by selective laser melting and hot pressing in comparison with the commercial alloy, *J. Mater. Process. Tech.* 266 (2019) 239–245.
- [34] I. Çaha, A.C. Alves, L.J. Affonço, P.N.L. Filho, J.H.D. da Silva, L.A. Rocha, A.M.P. Pinto, F. Toptan, Corrosion and tribocorrosion behaviour of titanium nitride thin films grown on titanium under different deposition times, *Surf. Coat. Technol.* 374 (2019) 878–888.
- [35] H. Dong, Tribological properties of titanium-based alloys, in: Hanshan Dong (Ed.), *Surf. Eng. Light Alloy.*, 1st ed., Woodhead Publishing Limited, 2010: pp. 58–80.
- [36] G. Stachowiak, A. Batchlor, Fatigue Wear, in: G.B.S. Gwidon W. Stachowiak, Andrew W. Batchelor (Ed.), *Exp. Methods Tribol.*, 1st ed., Elsevier, 2004: pp. 1–304.
- [37] F. Toptan, L.A. Rocha, Tribocorrosion in Metal Matrix Composites, in: R. Tyagi, J.P. Davim (Eds.), *Process. Tech. Tribol. Behav. Compos. Mater.*, IGI Global, 2015: pp. 149–167.
- [38] M. Nakamura, Y. Kaieda, Microstructure and mechanical properties of sintered TiAl, *Powder Metall.* 31 (1988) 201–209.



- [39] R. Ramaseshan, A. Kakitsuji, S.K. Seshadri, N.G. Nair, H. Mabuchi, Microstructure and some properties of TiAl-Ti<sub>2</sub>AlC composites produced by reactive processing, *Intermetallics*. 7 (1999) 571–577.
- [40] F. Qiu, Y. He, L. Zhu, S.L. Shu, W. Hu, C.H. Zhan, Q.C. Jiang, Microstructure and compression properties of *in situ* dual phase nanosized (TiB<sub>2</sub> – Ti<sub>5</sub>Si<sub>3</sub>)/TiAl matrix composites fabricated by combustion synthesis and hot press consolidation, *Powder Metall.* 58 (2015) 235–240.
- [41] Y. Umakoshi, T. Nakano, T. Takenaka, K. Sumimoto, T. Yamane, Orientation and temperature dependence of yield stress and slip geometry of Ti<sub>3</sub>Al and Ti<sub>3</sub>Al-V single crystals, *Acta Metall. Mater.* 41 (1993) 1149–1154.
- [42] S. Meir, S. Kalabukhov, N. Frage, S. Hayun, Mechanical properties of Al<sub>2</sub>O<sub>3</sub>/Ti composites fabricated by spark plasma sintering, *Ceram. Int.* 41 (2015) 4637–4643.
- [43] M. Niinomi, Mechanical properties of biomedical titanium alloys, *Mater. Sci. Eng. A*. 243 (1998) 231–236.



## Chapter 4

### **Corrosion and tribocorrosion behaviour of Ti-B<sub>4</sub>C composites processed by conventional sintering and hot-pressing technique**

*Published in Journal of Alloys and Compounds*  
*doi.org/10.1016/j.jallcom.2021.161109*

---

**L. Sousa<sup>a,b\*</sup>, A.C. Alves<sup>a</sup>, A. Guedes<sup>a,c</sup>, F. Toptan<sup>a,d,e</sup>**

<sup>a</sup> CMEMS-UMinho – Center of MicroElectroMechanical Systems – Universidade Minho, Campus de Azurém, Guimarães, Portugal

<sup>b</sup> DEMM – Department of Metallurgical and Materials Engineering – Faculdade de Engenharia da Universidade do Porto, Porto, Portugal

<sup>c</sup> DEM-UMinho – Department of Mechanical Engineering – University of Minho, Campus de Azurém, Guimarães, Portugal

<sup>d</sup> IBTN/Euro – European Branch of the Institute of Biomaterials, Tribocorrosion and Nanomedicine, Dept. Eng. Mecânica, Universidade do Minho, Azurém, 4800-058 Guimarães, Portugal

<sup>e</sup> Department of Materials Science and Engineering, Izmir Institute of Technology, 35430, Urla, Izmir, Turkey



## **Abstract**

In this work, low volume reinforcement *ex-situ* Ti-B<sub>4</sub>C composites were produced using two different routes: conventional powder metallurgy (PM) and hot-pressing (HP). The effect of reinforcement phases and processing method on corrosion and tribocorrosion behaviour were studied. Composites processed by PM lost the typical passive behaviour of Ti matrix, while composites processed by HP presented similar behaviour to unreinforced Ti. Tribocorrosion tests showed that both composite groups presented two times decrease in corrosion kinetics under sliding compared to pure titanium. An antagonistic effect between wear and corrosion was observed for composites with at least two times decrease in wear volume compared to titanium.

### **4.1. Introduction**

Titanium (Ti) and its alloys are still among the most used materials in the fabrication of hip implants owing to their good corrosion resistance, biocompatibility and satisfactory mechanical strength [1,2]. However, the high susceptibility to the combined action of wear and corrosion (tribocorrosion) under the physiological environment is still a major concern. The release of Ti wear products together with the release of metallic ions to the surrounding tissue and blood can lead to a vast number of adverse effects including inflammations, cytotoxicity, genotoxicity, carcinogenicity, among other issues, all of which can lead to implant failure [3].

In the last years, titanium matrix composites (TMCs) intended for orthopaedic implants have started to receive attention. By introducing hard ceramic phases into a Ti matrix, it is possible to improve the wear resistance due to a combination of several factors such as the load carrying effect given by the reinforcement phases and by modifications in the microstructure of the matrix yielding with grain refinement, induced dislocations and Orowan strengthening mechanisms [4]. By introduction of such reinforcements, there is a general increase in Young's modulus [5,6], which is the one of the main concern for load bearing biomedical implants. In addition, high volume of reinforcement phases, may also lead to other problems such as porosity, which not only degrade the

mechanical properties but also may jeopardize the corrosion behaviour due to localized corrosion [7].

Boron carbide (B<sub>4</sub>C) is among the most used reactants to produce *in-situ* TMCs, since the Ti+B<sub>4</sub>C reaction leads to the formation of TiC and TiB and/or TiB<sub>2</sub> reinforcement phases, thus it has been considered as excellent reinforcement for TMCs, mainly due to their compatibility and strong interfacial bonding with titanium together with similar coefficients of thermal expansion (CTEs), being  $8.2 \times 10^{-6}/^{\circ}\text{C}$  for Ti,  $7.2 \times 10^{-6}/^{\circ}\text{C}$  for TiB, and  $7.9 \times 10^{-6}/^{\circ}\text{C}$  for TiC [8–10]. Due to its intrinsic properties such as high hardness, wear resistance, high thermal as well as high chemical stability, B<sub>4</sub>C can also be used directly as a reinforcement, which has been widely used in the fabrication of Al-B<sub>4</sub>C composites [11–14].

In a study by some of the present authors [15], Ti-24 %vol. B<sub>4</sub>C composites processed by hot-pressing showed promising results regarding tribocorrosion behaviour. Ti-B<sub>4</sub>C composite not only showed significantly reduced wear volume loss compared to unreinforced Ti, but also presented lower susceptibility to corrosion as well as lower corrosion rates under sliding. However, due to high volume of reinforcement, bridging of reinforcement phases during processing lead to some porosity which than lead to discontinuities in the passive oxide film and a consequent reduction on the corrosion behaviour under static conditions.

Several processing techniques are used to process metal matrix composites (MMCs), which can be mostly divided in two distinct methods as solid- and liquid-phase processing routes. Solid-phase techniques offer several advantages compared to liquid-phase ones as lower processing temperatures, minimizing the undesirable chemical reactions, better matrix/reinforcement interfaces and excellent control over microstructure. Solid-state routes include techniques such as diffusion bonding, hot-rolling, extrusion and powder metallurgy (PM) [16,17].

PM based routes are attractive for the fabrication of both whisker and particle-reinforced MMCs, mainly due to its simplicity when compared to other manufacturing processes as well as the possibility to produce intricate shapes with high accuracy [17,18]. Press-and-sintering approach or pressureless sintering can be considered as the simplest and cost-effective conventional PM technique. Conventional PM processing route is divided in three main steps,

namely, blending and mixing the powders, cold compaction and sintering [19]. However, these methods may have limited success due to poor densification of the resulting composites. In order to obtain composites with higher densification, more advanced techniques, such as HP and spark plasma sintering, can be used. In these methods, pressure and temperature are applied simultaneously, allowing better densifications, but also reduced processing times, thus finer grained microstructures and consequently better mechanical properties, although these techniques are associated with higher costs [17].

In recent years, extensive research has been made on additive manufacturing (AM) routes, which are based on 3D printing layer-upon-layer of the chosen material. The main advantage of AM techniques resides in the fact that they can produce complex and near net shape components with minimal material loss and minimal post processing. When it comes fabrication of TMCs, AM techniques still face some challenges, such as the high melting point of Ti, which complicates processing, poor densification of composites with high volume of reinforcement and limitation on the size of reinforcement particles [20].

From conventional to the recent processing methods, the role of the processing route on the tribocorrosion behaviour of TMCs should be clearly understood before selecting the processing route for load-bearing biomedical implants. In this context, the main objective of this work was to do a comparative study between two different conventional powder technology techniques (pressureless sintering and hot-pressing) on the synergism between wear and tribocorrosion for low volume reinforcement Ti-B<sub>4</sub>C composites.

## **4.2. Experimental**

### *4.2.1. Materials and methods*

Ti composites reinforced with 3% volume of B<sub>4</sub>C particles were produced by two distinct routes by mixing c.p. titanium (grade 2) and B<sub>4</sub>C powders, both with irregular shapes and average particle sizes of 25 and 30 μm. Particle size distributions were obtained by laser particle analyzer (Malvern Series 2600 and Mastersizer 2000) and the results are shown in Figure 4.1. For samples produced by conventional PM (∅ 12 mm, 3 mm thickness), the powders and 0.4 vol.% of binder (PVA from Sigma Aldrich, Mowiol 8-88), were mixed in a ball mill containing Al<sub>2</sub>O<sub>3</sub> balls (∅ 10 mm) and operating at 120 rpm for 4 h under Ar

atmosphere. The mixture was then cold compacted with a uniaxial pressure of 350 MPa during 2 min in a steel die (previously lubricated with zinc stearate). The green compacts were placed in a tubular furnace under Ar atmosphere and heated to 450 °C, at a rate of 5 °C.min<sup>-1</sup>, for the binder elimination. After a 3h stage at this temperature the green compacts were cooled down to room temperature at 5 °C.min<sup>-1</sup>. Samples were then pressureless-sintered at 1100 °C for 3 h under high vacuum atmosphere (<10<sup>-5</sup> mbar) with heating and cooling rates set at 5 °C.min<sup>-1</sup>.

HP samples (∅ 10 mm, 3 mm thickness) were produced by mixing the powders under the same conditions without the addition of binder. After mixing, the powder blends were poured into a graphite die. In order to avoid chemical reactions between Ti and graphite, the die walls were previously coated with zirconia paste. HP was then performed under high vacuum atmosphere (<10<sup>-5</sup> mbar) and under an applied pressure of 40 MPa. The sintering stage was performed at 1100 °C for 30 min, with heating and cooling rates set to 5 °C.min<sup>-1</sup> and 10 °C.min<sup>-1</sup> respectively. For both processing techniques, Ti samples were also produced and were used as control groups.

Prior to each test, samples were ground down to 2400 mesh with SiC papers and then polished down to 0.04 µm with colloidal silica suspension (Struers). Afterwards, samples were cleaned in an ultrasonic bath with propanol and distilled water for 10 and 5 min respectively and finally dried with warm air. Before each corrosion and tribocorrosion test, the samples were kept in a desiccator for a period of 24 h to assure similar surface conditions. In this paper, samples processed by conventionally powder metallurgy are designated as Ti\_PM and Ti-3B<sub>4</sub>C\_PM, whereas samples processed by hot-pressing are designated as Ti\_HP and Ti-3B<sub>4</sub>C\_HP.



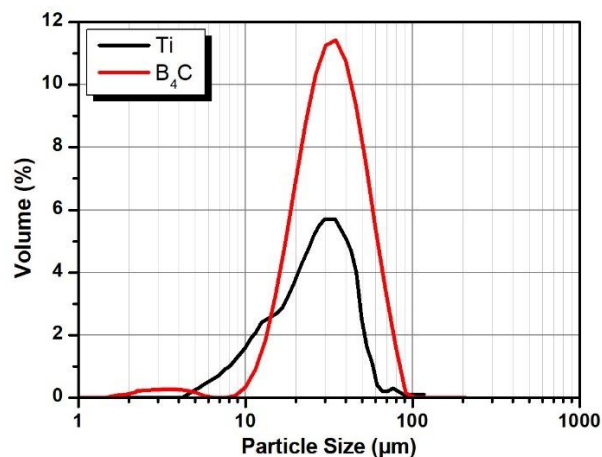


**Figure 4.1.** Particle size distribution for Ti and B<sub>4</sub>C powders.

#### 4.2.2. Electrochemical tests

Electrochemical tests were performed in a conventional three electrodes electrochemical cell (adapted from ASTM: G3-89) containing 0.9 wt.% NaCl solution at body temperature ( $37 \pm 2$  °C) as one of the main constituents of physiological solutions [21–23]. The samples were connected as working electrode (WE), with an exposed area of 0.38 cm<sup>2</sup>, while a saturated calomel electrode (SCE) and a Pt wire were used as reference electrode (RE) and counter electrode, respectively. The electrochemical tests consisted in OCP measurements until stabilization ( $\Delta E < 60$  mV.h<sup>-1</sup>), followed by EIS measurements performed at OCP and finally by potentiodynamic polarization tests. A Gamry Potentiostat/Galvanostat/ZRA (model Referece-600+) was used in all the tests. EIS data were obtained by scanning a frequency range starting from 10<sup>5</sup> until 10<sup>-2</sup> Hz, with 10 points per frequency decade and an amplitude of the sinusoidal signal of 10 mV. Impedance data was fitted using Gamry Echem Analyst software (version 5.61) to the electric equivalent circuits (EEC) and its quality of fitting was evaluated through the values of goodness of fitting. After EIS measurements, potentiodynamic polarization scans were performed in the anodic direction with a rate of 1mV.s<sup>-1</sup>, from -0.9 up to 1 V<sub>SCE</sub>.

#### 4.2.3. Tribocorrosion tests

Tribocorrosion tests were performed in the same NaCl solution at body temperature, placed inside a tribo-electrochemical cell. The samples slid against an alumina ball ( $\varnothing$  10 mm- Cerasec) in a tribometer (CETR-UMT-2) with a

reciprocating ball-on-plate setup. Tribocorrosion tests were then carried out under three different conditions, namely, at OCP and under two distinct applied potentials: +0.5 V<sub>SCE</sub> (anodic potential - AP) and -0.75 V<sub>SCE</sub> (cathodic potential - CP). These potentials were chosen based on the results from potentiodynamic polarization tests in order to study the synergism between wear and corrosion. In this way, applying a potential in the cathodic domain only the mechanical response from the system is given considering the lubricant effect of the electrolyte. On the other hand, applying a potential in the passive region (anodic potential) response from mechanical wear and chemical wear can be accessed.

In order to access the susceptibility to corrosion under sliding, OCP values were measured before, during and after sliding using a two-electrode setup (SCE as RE and samples as WE). For potentiostatic tribocorrosion tests, current evolution was followed before, during and after sliding using three-electrodes setup as previously described. All electrochemical measurements were performed in a Gamry Potentiostat/Galvanostat/ZRA (model Referece-600). All tribocorrosion tests were performed under 1 N normal load (corresponding to a maximum Hertzian contact pressure of 0.41 GPa for c.p. Ti) during 30 min, with a stroke length of 3 mm and 1 Hz of frequency where coefficient of friction (COF) values during sliding were also followed. Before characterization, the worn surfaces were cleaned using the same procedure described previously.

#### *4.2.4. Characterization*

Microstructure was evaluated by field emission gun scanning electron microscope (FEI Nova 200), equipped with EDAX energy dispersive X-ray spectroscopy (EDS). Vickers macro-hardness tests were performed on an Officine Galileo Mod. D200 tester under 30 kgf of load during 15 s in order to calculate the overall hardness of the composites through 5 indentations made per sample (3 samples per condition). After tribocorrosion tests, the worn surfaces were characterized by using the same FEG-SEM/EDS and the wear track profiles were obtained by profilometry (Veeco, Dektak 150). The wear volume calculations followed the same procedure given elsewhere [24]. All the tests were at least triplicated to assure reproducibility and all the values are presented as average  $\pm$  standard deviation. Phase analysis was determined by X-ray diffraction (XRD) on a Bruker AXS D8 Discover with Cu-K $\alpha$  radiation ( $\lambda=1.54060\text{\AA}$ ),

scanning from 15° to 80° at a speed of 0.04°/2s. Once that the amount of reinforcement phases was under the XRD detection, Ti-24 %vol. B<sub>4</sub>C composites were processed by PM under identical conditions for structural analysis purposes. The porosity for composite groups was estimated by image analysis using ImageJ software (version 1.51j8) by considering a total area of 56 mm<sup>2</sup> for each group.

### **4.3. Results**

#### **4.3.1. Microstructure**

The overall microstructure together with the EDS spectra obtained for both composites is shown in Fig. 4.2. The microstructure is composed of three distinct zones: black reinforcement particles (B<sub>4</sub>C), light grey Ti matrix and dark grey reaction zone formed in between the B<sub>4</sub>C particles and the Ti matrix. EDS spectra taken from these zones showed that the reinforcement particles were essentially composed of B and C; the Ti matrix was consisted essentially of Ti and the reaction zone of Ti, B and C elements. Composites processed by PM presented much thicker reaction zones, and consequently smaller B<sub>4</sub>C particles, compared to composites processed by HP, with some porosity between the reaction zone and the Ti matrix, while the same defects were hardly observed on the composites processed by HP. In fact, composites processed by PM presented much more porosity than composites processed by HP, i. e.  $2.65 \pm 0.80$  for PM and  $0.06 \pm 0.02$  % porosity for HP composites. Fig. 4.3 shows the XRD patterns obtained from Ti-24B<sub>4</sub>C\_PM, besides Ti (ICDD 00-044-1294) and B<sub>4</sub>C (ICDD 00-035-0798) peaks, peaks related to TiC (ICDD 00-031-1400) and TiB (ICDD 01-073-2148) phases were also detected. Table 4.1 shows the overall hardness for all groups. Comparing both Ti groups, Ti processed by PM presented significantly higher hardness than Ti processed by HP. Composites processed by PM presented similar hardness values to Ti processed by PM, while composites processed by HP presented higher hardness values compared to Ti processed by HP. Comparing composites groups, similar hardness values were observed.

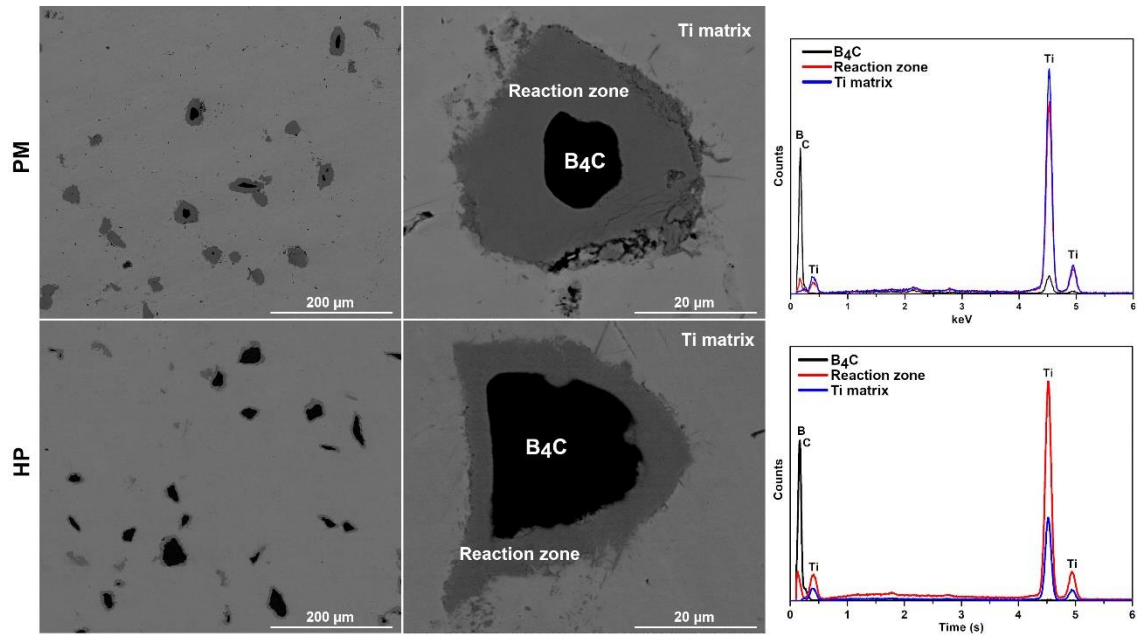


Figure 4.2. Back-scattered electron (BSE) SEM images of the composites processed by PM and HP, together with EDS spectra taken from the B<sub>4</sub>C particles, reaction zone and Ti matrix.

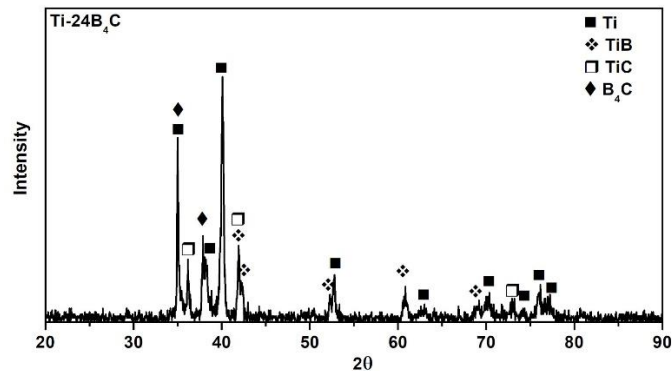


Figure 4.3. XRD spectra obtained from a Ti-24 %vol. B<sub>4</sub>C composite processed under the same PM conditions.

Table 4.1. Hardness values obtained for both Ti and Ti-B<sub>4</sub>C groups.

	Ti_PM	Ti_HP	Ti-3B <sub>4</sub> C_PM	Ti-3B <sub>4</sub> C_HP
HV <sub>30</sub>	387 ± 18	285 ± 8	388 ± 25	401 ± 19

#### 4.3.2. Electrochemical behaviour

Representative potentiodynamic polarization curves for each group are presented in Fig. 4.4a and the average corrosion potential ( $E_{(i=0)}$ ), open circuit potential ( $E_{OCP}$ ) values (average values of the last 10 min of immersion) and passivation current density ( $i_{pass}$ ), taken at 0.5 V are given in Table 4.2. Unreinforced Ti groups presented a well-defined passivation plateau due to the formation of the characteristic passive oxide film. On the other hand, while Ti-B<sub>4</sub>C\_HP presented very similar behaviour to unreinforced Ti with the

passivation plateau starting at around 0.30 V<sub>SCE</sub>, on Ti-B<sub>4</sub>C\_PM, a passivation region was observed, characterized by a slow increment on corrosion current density values. In addition, both groups processed by HP presented higher corrosion potential values (Table 4.2).

Bode and Nyquist diagrams are presented on Figs. 4.4b and 4.4c. On Bode diagrams, constant  $|Z|$  values and phase angles near 0° were observed in all groups for high frequency range (1 kHz to 10 kHz), corresponding to the electrolyte resistance. For both unreinforced Ti and Ti-B<sub>4</sub>C\_HP groups, phase angles near -90° were observed between low and middle frequency range indicating the formation of a compact passive oxide film. On the other hand, Ti-B<sub>4</sub>C\_PM composites presented phase angles near -70°, indicating lower quality of the passive oxide film. The total impedance of the system is given by the values of  $|Z|_{f \rightarrow 0}$ , showing the corrosion resistance of the system. Unreinforced Ti groups and Ti-B<sub>4</sub>C\_HP composites presented very similar values (c.a.  $4 \times 10^5 \Omega \cdot \text{cm}^2$ ) while Ti-B<sub>4</sub>C\_PM composites showed values close to  $10^4 \Omega \cdot \text{cm}^2$ . On Nyquist diagrams, larger diameters correspond to higher overall corrosion resistance. When compared to unreinforced Ti groups, Ti-B<sub>4</sub>C\_HP composites presented slightly smaller diameter while Ti-B<sub>4</sub>C\_PM composites presented noticeably reduced corrosion resistance.

The EECs used to fit the EIS data are shown in Figs. 4.4d and Fig 4.4e. For both unreinforced Ti groups and Ti-B<sub>4</sub>C\_HP, the EEC consists of an electrolyte resistance ( $R_e$ ), and a pair ( $R_{ox}/Q_{ox}$ ) corresponding to the resistance ( $R_{ox}$ ) and CPE (constant phase element,  $Q_{ox}$ ) of the native passive oxide film, respectively. For Ti-B<sub>4</sub>C\_PM composites, the EEC consists of an electrolyte resistance ( $R_e$ ), the resistance and CPE of the oxide film ( $R_{ox}$  and  $Q_{ox}$ ) and the processes taking place inside the pores consisting of an additional electrolyte resistance ( $R_e'$ ), the charge transfer reaction due to localized corrosion ( $R_{ct}$ ) and the capacitance of the double layer ( $Q_{dl}$ ).  $R_{ox}$  was removed from the EEC due to its extremely high value and it does not allow the conduction of electrons inside the passive film.

In both EECs, a CPE was used to account for the deviation of an ideal capacitor, where the capacitance of the CPE is defined by  $Z_{CPE} = [Y_0(j\omega)^n]^{-1}$ , with  $-1 \leq n \leq 1$  and  $n = -1$  corresponding to an inductor,  $n = 0$  to a resistor,

$n = 1$  to a capacitor and,  $n$  values close to 1 representing a non-ideal capacitor. The quality of fitting was evaluated by their goodness of fitting values, where all values were below  $10^{-4}$  indicating that the proposed EECs described adequately the behaviour of all the tested groups (fitting results are given on Table 4.3). Ti-B<sub>4</sub>C\_PM composites presented considerably higher  $Q_{ox}$  values compared to the other groups, indicating the lower quality of the oxide film. Comparing  $R_{ox}$  values, Ti-B<sub>4</sub>C\_HP composites presented lower values compared to unreinforced Ti groups, suggesting a relatively lower resistance of the passive layer formed on the composite surface.

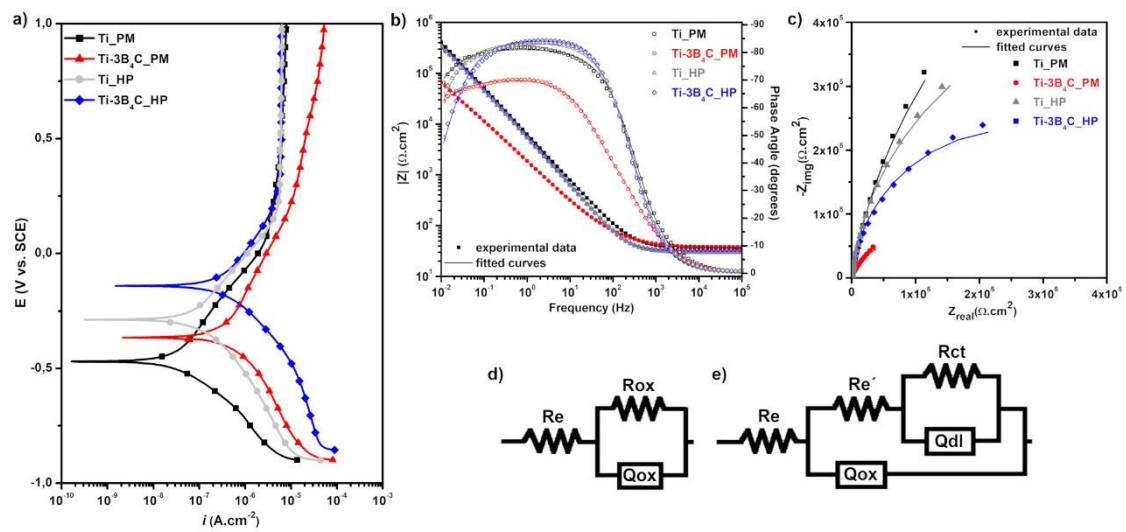


**Figure 4.4.** Corrosion results: a) Representative potentiodynamic polarization curves, b) Bode diagrams, c) Nyquist diagrams, and EECs used for d) Ti\_PM, Ti\_HP and Ti-3B<sub>4</sub>C\_HP groups and for e) Ti-3B<sub>4</sub>C\_PM group.

**Table 4.2.** Corrosion potential ( $E_{(i=0)}$ ), open circuit potential ( $E_{ocp}$ ) and passivation current density ( $i_{pass}$ ) values.

	Ti_PM	Ti_HP	Ti-B <sub>4</sub> C_PM	Ti-B <sub>4</sub> C_HP
$i_{pass}$ ( $\mu\text{A cm}^{-2}$ )	$5.34 \pm 0.70$	$5.86 \pm 0.17$	$34.63 \pm 5.40$	$6.05 \pm 0.17$
$E_{ocp}$	$-0.36 \pm 0.01$	$-0.24 \pm 0.01$	$-0.15 \pm 0.07$	$-0.19 \pm 0.03$
$E_{(i=0)}$ (V)	$-0.44 \pm 0.04$	$-0.28 \pm 0.01$	$-0.25 \pm 0.02$	$-0.14 \pm 0.02$

**Table 4.3.** EEC parameters obtained from EIS data.

	$Q_{ox}$ ( $\times 10^{-5} \text{ s}^n \Omega^{-1} \text{ cm}^{-2}$ )	$n_{ox}$	$Q_{dl}$ ( $\times 10^{-6} \text{ s}^n \Omega^{-1} \text{ cm}^{-2}$ )	$n_{dl}$	$R_{ox}$ ( $\times 10^6 \Omega \text{ cm}^2$ )	$R_{ct}$ ( $\times 10^6 \Omega \text{ cm}^2$ )
Ti_PM	$16.32 \pm 1.00$	$0.90 \pm 0.01$	–	–	$1.47 \pm 0.74$	–
Ti_HP	$21.99 \pm 1.07$	$0.93 \pm 0.01$	–	–	$0.76 \pm 0.18$	–
Ti-3B <sub>4</sub> C_PM	$38.65 \pm 11.99$	$0.76 \pm 0.04$	$12.61 \pm 0.97$	$0.92 \pm 0.06$	–	$0.73 \pm 0.37$
Ti-3B <sub>4</sub> C_HP	$20.84 \pm 1.33$	$0.94 \pm 0.01$	–	–	$0.47 \pm 0.03$	–

### 4.3.3. Tribocorrosion behaviour

The evolution of OCP before, during and after sliding together with the respective evolution of coefficient of friction during sliding is given in Fig. 4.5a. All the groups presented stable OCP values before sliding due to a stable passive film. Immediately after sliding started, a sharp decrease in OCP values towards cathodic direction was observed for all the groups, as a result of the mechanical damage given to the passive film and consequent formation of active zones leading to an increase in susceptibility to corrosion under the mechanical action. For unreinforced Ti groups, Ti\_HP samples presented a sharp OCP drop of around  $-0.73 \pm 0.03$  V, while Ti\_PM presented an initial drop of  $-0.38 \pm 0.02$  V and then a gradual decrease to values around  $-0.65 \pm 0.02$  V.

Compared to unreinforced Ti groups, both composites presented lower OCP drops on the onset of sliding where Ti-B<sub>4</sub>C\_PM presented the lowest OCP drop of  $-0.18 \pm 0.05$  V against the  $-0.45 \pm 0.03$  V observed for Ti-B<sub>4</sub>C\_HP. During sliding, OCP values for Ti-B<sub>4</sub>C\_PM composites increased up to almost the starting potential during the first 600 s of sliding, remaining around the same values until the end of sliding. On the other hand, Ti-B<sub>4</sub>C\_HP composites presented significant fluctuations on OCP during sliding. Nonetheless, OCP values were still nobler than both unreinforced Ti groups. Immediately after sliding stopped, all the groups except Ti-3B<sub>4</sub>C\_PM, which already presented OCP values close to the starting ones, presented a gradual increase in OCP, reaching values close to the ones recorded before sliding started, due to repassivation of the worn area.

Regarding COF values, distinct behaviours were observed between samples processed by PM and HP. Unreinforced Ti\_PM oscillated around similar values until the 500 - 600 s of sliding (around  $0.45 \pm 0.01$ ), after that, COF values increased to around  $0.71 \pm 0.01$ , remaining close to this value until the end of sliding. For unreinforced Ti\_HP, COF values also started at around  $0.39 \pm 0.01$ , however, after a few seconds (between 10 to 100 s), COF values increased to around  $0.58 \pm 0.02$  and oscillated around these values during almost the entire period of sliding, although a few drops were observed. Ti-B<sub>4</sub>C\_PM composites presented a run-in period of around 200 s, where COF values increased from  $0.34 \pm 0.02$  to  $0.59 \pm 0.02$ . After that, COF values slowly increased to around 0.70

and remained around these values until the end of sliding. Ti-B<sub>4</sub>C\_HP composites did not show any distinct run-in period, instead, a gradual increase in COF values was observed during the first 1500 s, after that COF values stayed at around  $0.52 \pm 0.05$ .

Figure 4.5b shows the representative evolution of anodic current at a constant applied potential before, during and after sliding together with the respective evolution of COF. Before sliding, all the groups presented stable current density values due to presence of a stable passive oxide film. While Ti\_PM, Ti\_HP and Ti-3B<sub>4</sub>C\_HP groups presented similar current density values before sliding started, Ti-3B<sub>4</sub>C\_PM group presented higher values, which is in accordance to what was observed on the potentiodynamic polarization curves. Between all the conditions, unreinforced Ti groups presented higher increase in current density values on the onset of sliding where Ti\_HP samples showed the highest increase. On the other hand, both composite groups increased to similar current density values c.a.  $0.30 \mu\text{A}\cdot\text{cm}^2$ . The anodic charge, Q, was calculated by integrating the current density values obtained during sliding, using the average current density before sliding as baseline, and the values were found as  $(5.65 \pm 0.92) \times 10^{-5}$ ,  $(6.81 \pm 1.33) \times 10^{-5}$ ,  $(3.02 \pm 0.53) \times 10^{-5}$ , and  $(3.67 \pm 0.37) \times 10^{-5}$  coulomb/cm<sup>2</sup> for Ti\_PM, Ti\_HP, Ti-3B<sub>4</sub>C\_PM, and Ti-3B<sub>4</sub>C\_HP respectively. Composite groups presented very similar values independently of processing method, while Ti\_PM presented slightly lower Q values compared to Ti\_HP. Overall, composites presented approximately 2 times decrease in Q values suggesting decreased corrosion kinetics under sliding coming from the wear track.

As it can be seen, under these conditions, all the groups presented a run-in period where COF values increased in the approximately first 200 s of sliding. During roughly the same period, all the groups also showed a significant decrease in current density values. Overall, Ti-B<sub>4</sub>C\_PM presented the highest corrosion current density values during sliding. Despite the higher increase in current density values that were observed for both Ti samples after sliding started, after some time, current density values dropped down to values close to the ones registered before sliding, remaining relatively stable until the end of sliding. Ti-3B<sub>4</sub>C\_HP composites presented current density values between both unreinforced Ti groups and Ti-3B<sub>4</sub>C\_PM composites.



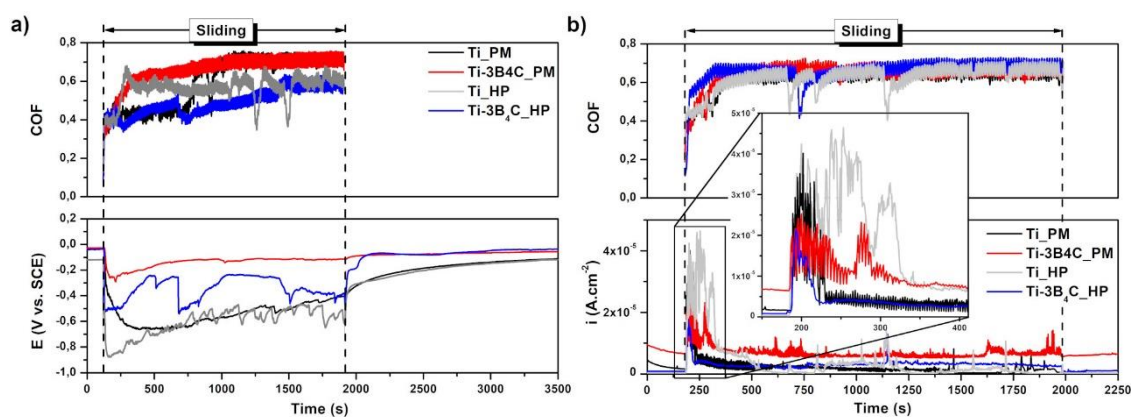
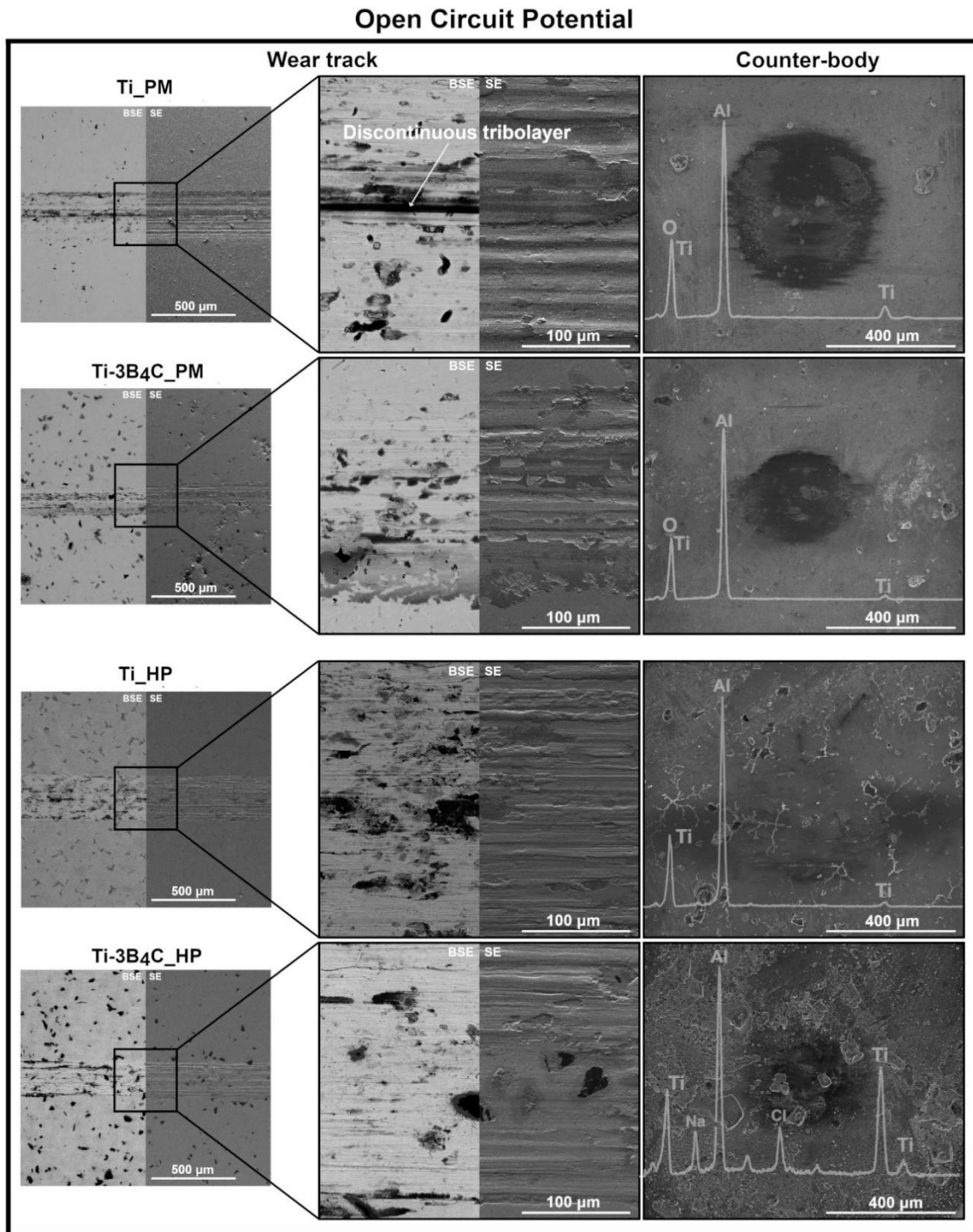


Figure 4.5. Evolution of a) OCP and b) anodic current density before, during and after sliding together with the corresponding evolution of COF during sliding.

Representative secondary and backscattered electron SE/BSE SEM images of the worn surfaces together with SE/SEM images and EDS spectra of the counter-body for all the groups after tribocorrosion tests performed under OCP can be seen on Fig. 4.6. For both unreinforced Ti groups tested under OCP, wear tracks presented ploughing grooves parallel to the sliding direction, which are an indication of an abrasive action of the transferred material to the counter-body due to adhesive wear. Discontinuous tribolayers were also observed within the wear tracks due to continuous oxidation and compaction of material being transferred between the two mating surfaces. In addition, scratch marks due to abrasion action of loose wear debris within the wear track were also observed for both Ti groups. Both composites presented similar features, with SE/SEM images suggesting less wear damage and no evidence of reinforcement particle pull-out was observed under these conditions. EDS spectra taken from the counter-body surfaces confirmed the transference of Ti between the two mating surfaces for all the tested groups, thus confirming the presence of adhesive wear. However, wear scars were relatively larger for unreinforced Ti samples, suggesting increased wear compared to composites.

Similar to what was observed for tribocorrosion tests performed under OCP, under the anodic domain, Fig. 4.7, all the groups also presented discontinuous tribolayers within the wear track. Ploughing grooves, on the other hand, were less pronounced for these conditions. In addition, the visible wear damage on the composite surfaces were significantly less on the low magnification SE images. EDS spectra from the counter-body also confirmed the presence of adhesive wear, however, the wear scars for all the groups were also considerably smaller

than the ones observed under OCP, suggesting reduced wear. For tribocorrosion tests performed on the cathodic domain, Fig. 4.8, ploughing wear grooves were the more prevalent wear feature and discontinuous tribolayers were still present, hence, EDS spectra revealed that material transfer (adhesion) between the two sliding surfaces also occurred.



**Figure 4.6.** SE/BSE SEM images of the wear tracks and respective counter-bodies for tribocorrosion tests performed under OCP.

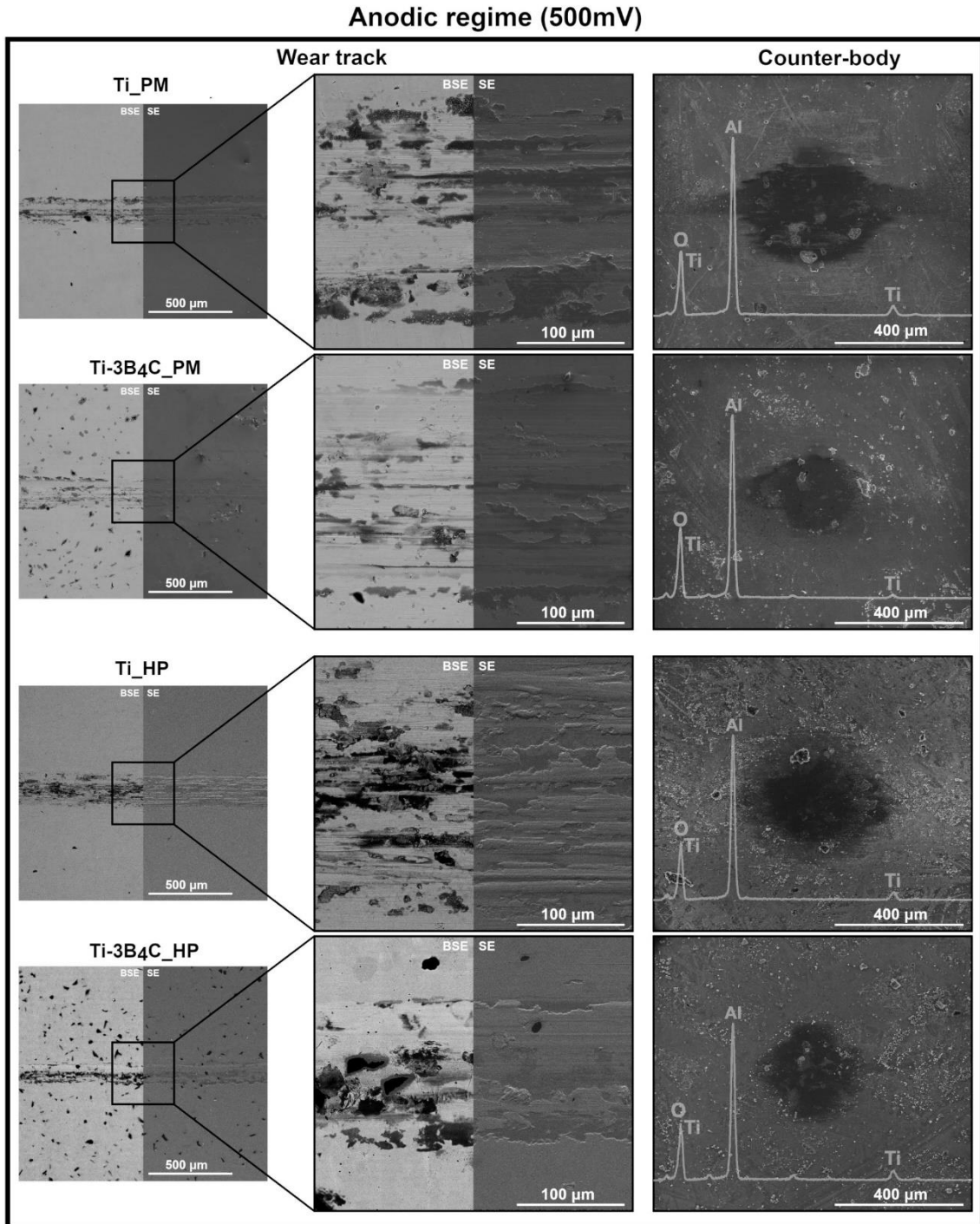
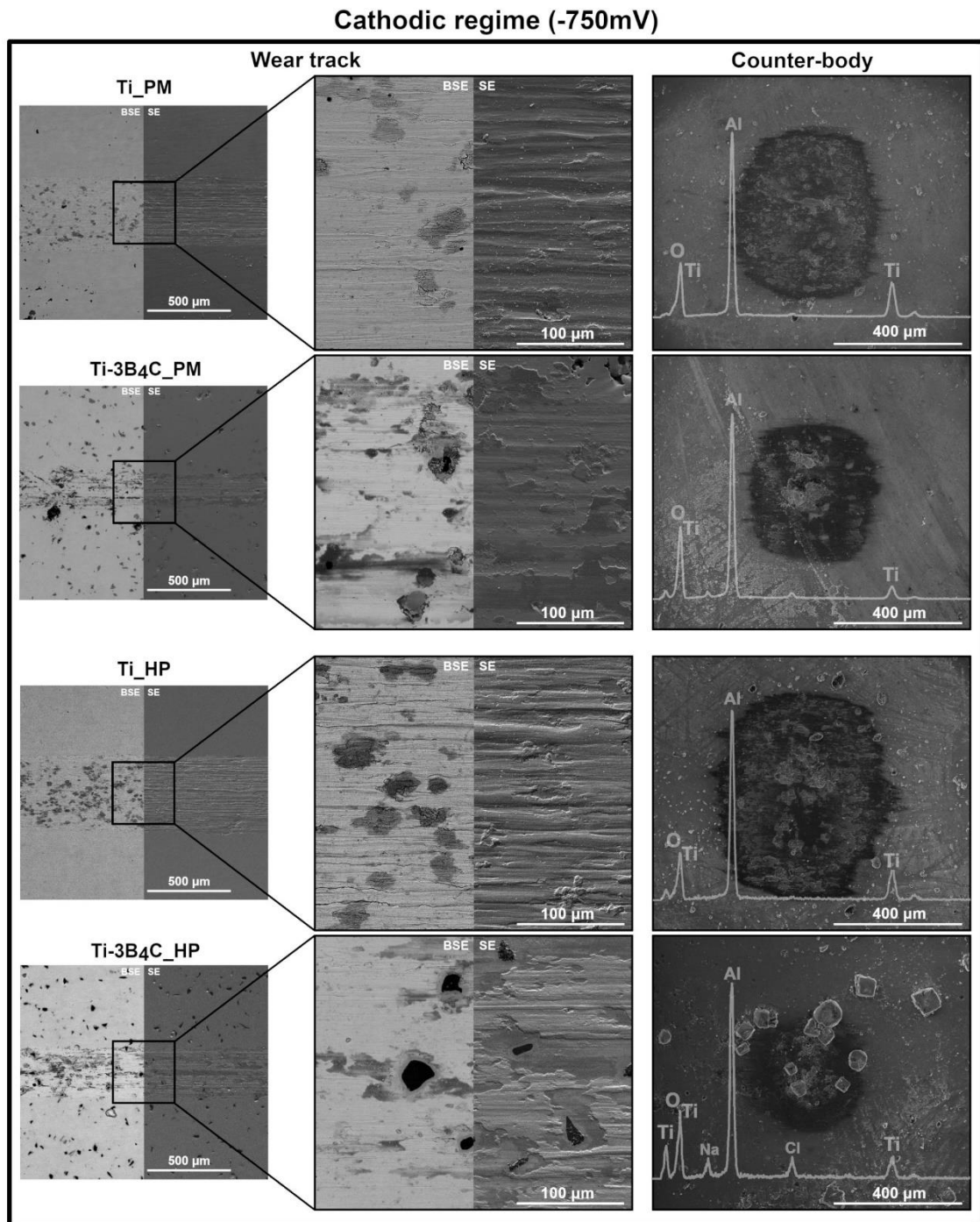


Figure 4.7. SE/BSE SEM images of the wear tracks and respective counter-bodies for tribocorrosion tests performed under 500 mV (anodic regime).



**Figure 4.8.** SE/BSE SEM images of the wear tracks and respective counter-bodies for tribocorrosion tests performed under -750 mV (cathodic regime).

Representative 2D profiles taken from the worn surfaces and wear volume values are presented in Fig. 4.9. All the tested groups presented the same trend in wear volume loss under the different applied potentials, where higher wear volume losses were obtained under the anodic domain, whereas the lowest values were obtained under the cathodic domain. For all the conditions, composites presented lower wear volume losses compared to unreinforced Ti. Regarding

processing methods, no clear trend was observed. Composite groups presented similar wear volume loss values under the different applied potentials. Comparing both Ti groups, particular differences were observed for the tribocorrosion tests performed under the cathodic domain, where Ti\_HP presented considerably higher wear volume loss.

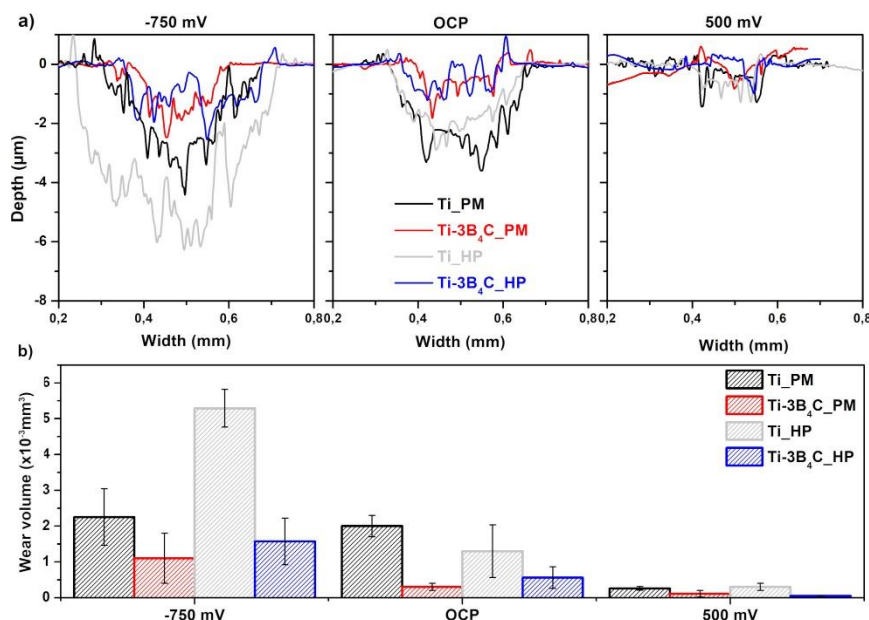


Figure 4.9. a) Representative wear profiles for all the testes groups and tribocorrosion conditions together with b) average wear volume loss values calculated from wear profiles.

#### 4.4. Discussion

The reaction between Ti and B<sub>4</sub>C powders in both composites produced by PM and HP routes revealed a reaction zone around the B<sub>4</sub>C reinforcements particles, containing Ti, B and C elements. XRD analysis on Ti-24B<sub>4</sub>C\_PM composites revealed the formation of TiB and TiC phases. The formation of TiB and TiC phases on Ti-24 %vol. B<sub>4</sub>C composites by HP was also reported previously by some of the present authors [15]. The Ti-B<sub>4</sub>C system is characterized by the formation of TiB<sub>2</sub>, TiB and TiC phases, which belong to the Ti-B-C system [25,26]. Due to its lower Gibbs free energy ( $\Delta G$ ) and enthalpy ( $\Delta H$ ), TiB<sub>2</sub> is more likely to be formed in preference of TiB, however, due to limited mass transport rate in solid-state sintering, the main products of Ti-B<sub>4</sub>C reaction are almost always TiC and TiB [26]. In this way, in addition to the mechanical entrapment of the B<sub>4</sub>C reinforcement particles into the Ti matrix, a chemical bond was also formed. The reaction zones formed on the PM composites were much thicker than the ones observed on the HP composites, that may be explained by

the increased sintering time (3 h for PM vs 30 min for HP) and consequently more time for the reaction between Ti and B<sub>4</sub>C to take place. Once B<sub>4</sub>C is consumed in the reaction, B<sub>4</sub>C reinforcement particles tended to be smaller on the PM composites.

In MMCs, interfacial reactions between the matrix and reinforcement phases play an crucial role on the final mechanical properties of the composite and may have a beneficial or detrimental effect [27,28]. Currently, the main motivation of the Ti-B<sub>4</sub>C system is to use B<sub>4</sub>C as a reactant to produce *in-situ* TMCs, where the reaction products of the Ti + B<sub>4</sub>C system (TiB, TiC and TiB<sub>2</sub>) act as reinforcement phases [8–10,29,30]. In this way, the role of these reaction zones on the mechanical properties of ex-situ Ti-B<sub>4</sub>C composites is still not completely understood. Nonetheless, the mechanical properties of TMCs reinforced with either TiB or TiC or even both phases is widely reported. Both TiB whiskers and TiC particles are reported to improve several mechanical properties, such as yield strength [31,32], ultimate compressive strength [32,33], tensile strength, creep resistance [8,34–36]. Furthermore synergistic effects between TiB and TiC have also been reported, meaning that TMCs reinforced by both TiB and TiC exhibit better mechanical behaviour over sole TiB or sole TiC reinforced TMCs [5].

Hardness values obtained for Ti\_PM were considerably higher than the ones observed for Ti\_HP. Ti and Ti alloys processed by different processing routes can present different hardness values [37]. Due to high affinity of Ti with oxygen, interstitial oxygen contamination is present in almost every step of processing, including mixing and debinding [38]. In this way, the increased hardness obtained on PM samples may be explained by the additional processing steps involved, including pressing and handling of the green compact, the use of binder and the debinding cycle.

By introducing the reinforcement particles, it would be expected that composites would present significantly higher hardness than their Ti counterparts, however this was not the case for composites processed by PM, where composites presented similar hardness values to unreinforced Ti. During the sintering stage, ceramic particles may hinder the sintering process and consequently reduce the densification of the composite, leading to higher amount of residual porosity [39]. Furthermore, it has also been reported that the volume



reduction from the conversion of B<sub>4</sub>C to TiB and TiC phases [40] may also lead to porosity and thus lower overall hardness values. In this way, the hardness values obtained for Ti-3B<sub>4</sub>C\_PM group is most probably related with the antagonistic effect between the introduction of reinforcement particles and porosity observed in these composites. The drawback of pressureless sintering approach was clearly observed in this work since composites presented similar hardness values to Ti due to considerable amount of porosity. Higher porosity for TMCs processed by pressureless sintering was also reported by Patel et al. [41] where the authors compared the microstructure of Ti-TiB<sub>2</sub> composites processed by pressureless and pressure assisted PM routes and reported increased porosity for the pressureless route. The authors also reported that by increasing sintering temperature porosity could be reduced. Due to applied pressure on HP technique, the negative effect of porosity was reduced and consequently composites showed a significant increase in hardness compared to Ti.

In MMCs, galvanic coupling between matrix and reinforcement or interfacial reaction layer may lead to a significant decrease on corrosion resistance. In addition to gaps at the matrix/reinforcement interface, microstructural defects may also have a substantial impact on the corrosion resistance of the base material, due to formation of discontinuities or heterogeneities on the protective passive film [42,43]. However, literature shows that MMCs may also present increased corrosion resistance since reinforcement phases may act as inert physical barriers against corrosion [44]. Additionally, it has also been reported that the introduction of reinforcement phases cause grain refinement leading to higher stability of the passive film [45].

In this work, it was possible to observe that Ti-B<sub>4</sub>C composites processed by different routes had distinct behaviours. Composites processed by HP presented very similar corrosion behaviour to that of Ti, while composites processed by pressureless sintering showed notably reduced corrosion resistance, not only compared to the same composite processed by HP but also to Ti processed by the same route. Consequently, an alternative EEC had to be used to fit EIS data. Regarding the reaction products that were obtained for both composites (TiB and TiC), some studies reported that these phases do not have a negative effect on the corrosion resistance of Ti. In a study by Silva et al. [46], it was reported that the corrosion behaviour of *in-situ* Ti-TiB-TiN<sub>x</sub> composites

processed by HP was slightly better than unreinforced Ti due to the barrier role given by the reinforcement phases. Chen et al. [45] reported that Ti-TiB composites processed by selective laser melting (SLM) presented improved corrosion behaviour compared to Ti processed by the same method. The authors attributed the improved corrosion behaviour to the fact that TiB reinforcements acted as a micro-cathode during corrosion, which facilitated and accelerated the formation of the passive oxide film on the surface of the composites. Regarding TiC, some studies showed that Ti-TiC composites have very similar corrosion behaviour to unreinforced Ti [47,48].

In a previous study by a part of the present authors [49], the electrochemical behaviour of Ti-24 %vol. B<sub>4</sub>C composites processed by hot-pressing was evaluated. It was reported that composites presented slightly reduced corrosion resistance compared to unreinforced Ti that was attributed to the porosity formed due to bridging of the agglomerated reinforcement particles, that consequently induced localized corrosion. In addition, interfacial gaps at the matrix/reinforcement interface, as well as pore sites, may lead to discontinuities on the passive film and/or different states of the passive film. Processing parameters as well as amount of reinforcement phases may also significantly change the corrosion behaviour of composites since they may lead to different densification rates and microstructures.

In this study, it was clear that Ti-B<sub>4</sub>C\_PM presented lower corrosion resistance compared to other tested groups. Considering that the corrosion behaviour of Ti-3B<sub>4</sub>C\_HP composites was very close to that of Ti, it is reasonable to assume that the reduced corrosion behaviour observed on Ti-B<sub>4</sub>C\_PM composites may be due to a combination of different factors, being the porosity associated with PM processing technique and/or the increased thickness of the reaction layers, which may be the cause for the overall lower quality of native oxide film. In a previous study by some of the present authors [50], the corrosion behaviour of Ti-B<sub>4</sub>C composite processed by pressureless sintering using identical processing conditions was also reported, where the authors tested the composites by cyclic polarization scan and observed reduced corrosion current density in the reverse scan indicated that no susceptibility to localized corrosion was present in the system. However, the increased corrosion kinetics was due to microstructural defects between the matrix and the reaction zone, which



compromised the integrity of the passive oxide film. Nonetheless, in order to make a definitive conclusion, further studies by local electrochemical techniques are needed to link better the microstructure with the electrochemical response.

Tribocorrosion tests showed that the introduction of B<sub>4</sub>C reinforcement particles had a significant effect on the tribocorrosion behaviour of Ti. Both composites showed a decrease in tendency to corrosion under sliding, which may be mainly attributed to the load carrying effect given by the reinforcement phases. The fluctuations in COF and OCP values can be attributed to the formation, thickening, and breaking of discontinuous tribolayers during sliding. The presence of tribolayers within the wear tracks can lead to increased roughness and consequently higher COF values during sliding. When these tribolayers eventually reach a critical point and break, exposing new fresh metallic area to the electrolyte, a consequent decrease in OCP and COF is observed [46,51–53]. As it could be observed in the OCP evolution, this phenomenon was more prevalent on Ti-3B<sub>4</sub>C\_HP composites, whereas OCP and COF values were more stable for Ti-3B<sub>4</sub>C\_PM composites.

The evolution of anodic current density under sliding showed that, despite the current density peaks observed on the onset of sliding, after a few minutes, current density values decreased and stabilized at almost the same current density values observed before sliding. Under the anodic applied potential, the formation of tribolayers was promoted since the growth of the native passive oxide film was accelerated. As a result, the overall COF values were higher, possibly due to increased formation of the discontinuous tribolayers and consequently increased roughness. In addition, COF values were also more stable during sliding, in other words, after a run-in period, oscillated around similar values till the end of sliding since the growth and stability of these tribolayers was promoted under the anodic potentiostatic control. It is known that these tribolayers can either play a beneficial and/or detrimental role during tribocorrosion. Due to higher hardness of these layers, they may play a limited protective role owing to load bearing effect and consequently reducing electrochemical active zones within the wear track. On the other hand, if these oxides break and roll freely on the wear track, they may act as a third-body abrasives and increase the mechanical wear [37,39,49,54]. In tribocorrosion, the total wear volume loss due to wear and corrosion cannot be simply calculated by

the sum of material lost due to wear and material lost due to corrosion, since synergetic or antagonist effect may occur. The effect of corrosion on wear and the effect of wear on corrosion should also be considered, as these can significantly change the total wear volume loss. In the synergetic approach the total wear volume loss due to tribocorrosion can be described as the sum between material lost due to wear, material lost due to corrosion and the material lost due to the interplay between wear and corrosion. In most cases, a synergetic effect is observed, meaning that wear increases material lost to corrosion and vice-versa [55]. Based on the tribo-electrochemical and wear volume loss results, it is reasonable to state that under the tested conditions, an antagonistic effect was observed since the oxide layers formed during sliding had a beneficial role on the tribocorrosion behaviour of both Ti and composite groups. All the tested groups presented considerably higher wear volume loss under the cathodic potentials. Under cathodic potentials, the corrosion processes are inhibited, thus, the native oxide film is not allowed to growth, limiting the formation of load carrying tribolayers during sliding.

In fact, comparing the wear volume loss values against the ones observed for tribocorrosion tests under OCP and the cathodic domain, considerably less wear volume loss was observed on the anodic domain. The considerable higher wear volume loss observed for Ti\_HP compared with Ti\_PM under the cathodic domain can be explained by the lower hardness values, since mechanical wear is the main response of the system under these conditions. Under OCP and anodic potential, such differences were not observed, suggesting that the formation of tribolayers played a considerable role in wear resistance. Overall, composites presented considerably lower wear volume losses in all the conditions compared to Ti, independently of processing method. Within the composite groups, wear volume values were in range of the standard deviation of each other, which is in accordance with the hardness values.

#### **4.5. Conclusions**

Within the scope of this study, it was possible to conclude that the introduction of low amount of B<sub>4</sub>C reinforcement particles into a Ti matrix can improve the overall tribocorrosion behaviour of Ti through reduced wear volumes, reduced tendency to corrosion, as well as reduced corrosion kinetics under

sliding. Based on the results, it was possible to see that independently of processing method, under these conditions, Ti and composites showed an antagonistic effect between corrosion and wear, evidenced by the lower wear volume values obtained under the anodic domain. Additionally, it was possible to see that the overall microstructure of these composites played an important role on the corrosion behaviour, that was evidenced by the considerably lower corrosion resistance of the composites processed by PM.



## References

- [1] X. Liu, P.K. Chu, C. Ding, Surface modification of titanium, titanium alloys, and related materials for biomedical applications, *Mater. Sci. Eng. R Reports*. 47 (2004) 49–121.
- [2] S.C. Tjong, Y.W. Mai, Processing-structure-property aspects of particulate- and whisker-reinforced titanium matrix composites, *Compos. Sci. Technol.* 68 (2008) 583–601.
- [3] I. Swiatkowska, N. Martin, A.J. Hart, Blood titanium level as a biomarker of orthopaedic implant wear, *J. Trace Elem. Med. Biol.* 53 (2019) 120–128.
- [4] F. Saba, F. Zhang, S. Liu, T. Liu, Reinforcement size dependence of mechanical properties and strengthening mechanisms in diamond reinforced titanium metal matrix composites, *Compos. Part B*. 167 (2019) 7–19.
- [5] D.R. Ni, L. Geng, J. Zhang, Z.Z. Zheng, Fabrication and tensile properties of *in situ* TiBw and TiCp hybrid-reinforced titanium matrix composites based on Ti-B<sub>4</sub>C-C, *Mater. Sci. Eng. A*. 478 (2008) 291–296.
- [6] S. Gorsse, Y. Le Petitcorps, S. Matar, F. Rebillat, Investigation of the Young ' s modulus of TiB needles *in situ* produced in titanium matrix composite, *Mater. Sci. Eng. A*. 340 (2003) 80–87.
- [7] H. Tanigawa, H. Asoh, T. Ohno, M. Kubota, S. Ono, Electrochemical corrosion and bioactivity of titanium – hydroxyapatite composites prepared by spark plasma sintering, *Corros. Sci.* 70 (2013) 212–220.
- [8] V.S. Balaji, S. Kumaran, Densification and microstructural studies of titanium–boron carbide (B<sub>4</sub>C) powder mixture during spark plasma sintering, *Powder Technol.* 264 (2014) 536–540.
- [9] S. Li, K. Kondoh, H. Imai, B. Chen, L. Jia, J. Umeda, Y. Fu, Strengthening behavior of *in situ*-synthesized (TiC–TiB)/Ti composites by powder metallurgy and hot extrusion, *Mater. Des.* 95 (2016) 127–132.
- [10] S. Li, K. Kondoh, H. Imai, B. Chen, L. Jia, J. Umeda, Microstructure and mechanical properties of P/M titanium matrix composites reinforced by in-situ synthesized TiC–TiB, *Mater. Sci. Eng. A*. 628 (2015) 75–83.
- [11] Q. Bai, L. Zhang, L. Ke, P. Zhu, Y. Ma, S. Xia, B. Zhou, The effects of surface chemical treatment on the corrosion behavior of an Al-B<sub>4</sub>C metal matrix composite in boric acid solutions at different temperatures, *Corros. Sci.* 164 (2020) 108356.
- [12] A. Nirala, S. Soren, N. Kumar, D.R. Kaushal, Materials Today: Proceedings A comprehensive review on mechanical properties of Al-B<sub>4</sub>C stir casting fabricated composite, *Mater. Today Proc.* 21 (2020) 1432–1435.
- [13] R.G. Lakshmikantha, V. Auradi, Materials Today : Proceedings Processing and evaluation of Al/B<sub>4</sub>C particulate MMC's : Tensile strength and wear properties under different elevated temperature test condition, *Mater. Today Proc.* 28 (2020) 504–509.
- [14] D. Patidar, R.S. Rana, ScienceDirect Effect of B<sub>4</sub>C particle reinforcement on the various properties of aluminium matrix composites : a survey paper, *Mater. Today Proc.* 4 (2017) 2981–2988.
- [15] F. Toptan, A. Rego, A.C. Alves, A. Guedes, Corrosion and tribocorrosion behavior of Ti–B<sub>4</sub>C composite intended for orthopaedic implants, *J. Mech. Behav. Biomed. Mater.* 61 (2016) 152–163.
- [16] D. Huda, M.A. El Baradie, M.S.J. Hashmi, Metal-matrix composites: Manufacturing aspects. Part I, *J. Mater. Process. Tech.* 37 (1993) 513–528.
- [17] M.A. Awotunde, A.O. Adegbenjo, B.A. Obadele, M. Okoro, B.M. Shongwe, P.A. Olubambi, Influence of sintering methods on the mechanical properties of aluminium nanocomposites reinforced with carbonaceous compounds: A review, *J. Mater. Res. Technol.* 8 (2019) 2432–2449.

- [18] I. Montealegre Melendez, E. Neubauer, H. Danninger, Consolidation of titanium matrix composites to maximum density by different hot pressing techniques, *Mater. Sci. Eng. A.* 527 (2010) 4466–4473.
- [19] M. Qian, F.H. Froes, *Titanium Powder Metallurgy Science, Technology and Applications*, in: *Int. J. Powder Metall.* (Princeton, New Jersey), 1970: pp. 43–55..
- [20] H. Attar, S. Ehtemam-Haghighi, D. Kent, M.S. Dargusch, Recent developments and opportunities in additive manufacturing of titanium-based matrix composites: A review, *Int. J. Mach. Tools Manuf.* 133 (2018) 85–102.
- [21] M. Bryant, R. Farrar, R. Freeman, K. Brummitt, J. Nolan, A. Neville, Galvanically enhanced fretting-crevice corrosion of cemented femoral stems, *J. Mech. Behav. Biomed. Mater.* 40 (2014) 275–286.
- [22] M. Bryant, R. Farrar, R. Freeman, K. Brummitt, A. Neville, The role of surface pretreatment on the microstructure, corrosion and fretting corrosion of cemented femoral stems, *Biotribology.* 5 (2016) 1–15.
- [23] V. Singh, J.P. Shorez, N.J. Hallab, J.L. Gilbert, Material dependent fretting corrosion in spinal fusion devices : Evaluation of onset and long-term response, *J. Biomed. Mater. Res.* 106 (2018) 2858–2868.
- [24] Z. Doni, A.C. Alves, F. Toptan, J.R. Gomes, A. Ramalho, M. Buciumeanu, L. Palaghian, F.S. Silva, Dry sliding and tribocorrosion behaviour of hot pressed CoCrMo biomedical alloy as compared with the cast CoCrMo and Ti6Al4V alloys, *Mater. Des.* 52 (2013) 47–57.
- [25] X. Zhang, W. Lu, D. Zhang, R. Wu, *In Situ* Technique for synthesizing (TiB+TiC)/Ti composites, *Scr. Mater.* 41 (1999) 39–46.
- [26] L. Jia, S.F. Li, H. Imai, B. Chen, K. Kondoh, Size effect of B<sub>4</sub>C powders on metallurgical reaction and resulting tensile properties of Ti matrix composites by in-situ reaction from Ti-B<sub>4</sub>C system under a relatively low temperature, *Mater. Sci. Eng. A.* 614 (2014) 129–135.
- [27] Z.X. GUO, B. DERBY, B. CANTOR, Comparison of interfaces in Ti composites reinforced with uncoated and TiB<sub>2</sub>/C-coated SiC fibres, *J. Microsc.* 169 (1993) 279–287.
- [28] Y.Q. Yang, H.J. Dudek, J. Kumpfert, TEM investigations of the fibre / matrix interface in SCS-6 SiC / Ti – 25Al – 10Nb – 3V – 1Mo, *Interfaces* (Providence). (2000) 1235–1241.
- [29] B. Choi, I.-Y. Kim, Y. Lee, Y. Kim, Microstructure and friction/wear behavior of (TiB+TiC) particulate-reinforced titanium matrix composites, *Wear.* 318 (2014) 68–77.
- [30] T. Wang, B. Gwalani, S. Shukla, M. Frank, R.S. Mishra, Development of *in situ* composites via reactive friction stir processing of Ti–B<sub>4</sub>C system, *Compos. Part B.* 172 (2019) 54–60.
- [31] H.T. Tsang, C.G. Chao, C.Y. Ma, Effects of volume fraction of reinforcement on tensile and creep properties of in-situ TiB/Ti MMC, *Acta Metall.* 37 (1997) 1359–1365.
- [32] H. Attar, M. Bonisch, M. Calin, L. Zhang, S. Scudino, J. Eckert, Selective laser melting of *in situ* titanium–titanium boride composites: Processing , microstructure and mechanical properties, *Acta Mater.* 76 (2014) 13–22.
- [33] M.H. Loretto, D.G. Konitzer, The effect of matrix reinforcement reaction on fracture in Ti-6Al-4V-base composites, *Metall. Trans. A.* 21 (1990) 1579–1587.
- [34] H.K.S. Rahoma, Y.Y. Chen, X.P. Wang, S.L. Xiao, Influence of (TiC+TiB) on the microstructure and tensile properties of Ti-B<sub>20</sub> matrix alloy, *J. Alloys Compd.* 627 (2015) 415–422.
- [35] J. Wang, X. Guo, J. Qin, D. Zhang, W. Lu, Microstructure and mechanical properties of investment casted titanium matrix composites with B<sub>4</sub>C additions, *Mater. Sci. Eng. A.* 628 (2015) 366–373.

- [36] C. Cai, S. He, L. Li, Q. Teng, B. Song, C. Yan, Q. Wei, Y. Shi, In-situ TiB / Ti-6Al-4V composites with a tailored architecture produced by hot isostatic pressing : Microstructure evolution , enhanced tensile properties and strengthening mechanisms, *Compos. Part B.* 164 (2019) 546–558.
- [37] F. Toptan, A.C. Alves, Ó. Carvalho, F. Bartolomeu, A.M.P. Pinto, F. Silva, G. Miranda, Corrosion and tribocorrosion behaviour of Ti6Al4V produced by selective laser melting and hot pressing in comparison with the commercial alloy, *J. Mater. Process. Tech.* 266 (2019) 239–245.
- [38] E. Baril, L.P. Lefebvre, Y. Thomas, Interstitial elements in titanium powder metallurgy: Sources and control, *Powder Metall.* 54 (2011) 183–187.
- [39] A. Oliveira, F. Toptan, Wear Behavior of Ti-Al<sub>2</sub>O<sub>3</sub> Biocomposites in 9 g/L NaCl Solution, *J. Mater. Eng. Perform.* 28 (2019) 6000–6010.
- [40] A. Jimoh, I. Sigalas, M. Hermann, *In Situ* Synthesis of Titanium Matrix Composite (Ti-TiB-TiC) through Sintering of TiH<sub>2</sub> -B<sub>4</sub>C, *Mater. Sci. Appl.* 3 (2012) 30–35.
- [41] V. V. Patel, a. El-Desouky, J.E. Garay, K. Morsi, Pressure-less and current-activated pressure-assisted sintering of titanium dual matrix composites: Effect of reinforcement particle size, *Mater. Sci. Eng. A.* 507 (2009) 161–166.
- [42] B. Bobić, S. Mitrović, M. Babić, I. Bobić, Corrosion of Metal-Matrix composites with aluminium alloy substrate, *Tribol. Ind.* 32 (2010) 3–11.
- [43] S.C. Ferreira, L.A. Rocha, E. Ariza, P.D. Sequeira, Y. Watanabe, J.C.S. Fernandes, Corrosion behaviour of Al/Al<sub>3</sub>Ti and Al/Al<sub>3</sub>Zr functionally graded materials produced by centrifugal solid-particle method: Influence of the intermetallics volume fraction, *Corros. Sci.* 53 (2011) 2058–2065.
- [44] Q. Feng, T. Li, H. Teng, X. Zhang, Y. Zhang, C. Liu, J. Jin, Investigation on the corrosion and oxidation resistance of Ni-Al<sub>2</sub>O<sub>3</sub> nano-composite coatings prepared by sediment co-deposition, *Surf. Coatings Technol.* 202 (2008) 4137–4144.
- [45] Y. Chen, J. Zhang, N. Dai, P. Qin, H. Attar, L.-C. Zhang, Corrosion Behaviour of Selective Laser Melted Ti-TiB Biocomposite in Simulated Body Fluid, *Electrochim. Acta.* 232 (2017) 89–97.
- [46] J.I. Silva, A.C. Alves, A.M. Pinto, F. Toptan, Corrosion and tribocorrosion behavior of Ti-TiB-TiN<sub>x</sub> in-situ hybrid composite synthesized by reactive hot pressing, *J. Mech. Behav. Biomed. Mater.* 74 (2017) 195–203.
- [47] J. Bernard S. Covino, D.E. Alman, Corrosion of Titanium Matrix Composites, Albany Res. Center, U.S. Dep. Energy, Albany, OR USA. (2002) 1–7.
- [48] P. Figiel, A. Biedunkiewicz, W. Biedunkiewicz, D. Grzesiak, Evaluation of the Effect of Surface Preparation on Corrosion Properties of Cerametallic Composites in Titanium Matrix, 2 (2016) 121–125.
- [49] F. Toptan, A. Rego, A.C. Alves, A. Guedes, Corrosion and tribocorrosion behavior of Ti-B<sub>4</sub>C composite intended for orthopaedic implants, *J. Mech. Behav. Biomed. Mater.* 61 (2016) 152–163.
- [50] J.M. Sousa, A.C. Alves, F. Toptan, E. Ariza, A. Guedes, Corrosion and Tribocorrosion Behavior of Ti-B<sub>4</sub>C Composites Joined with TiCuNi Brazing Alloy, *J. Mater. Eng. Perform.* (2019)..
- [51] I. Çaha, A.C. Alves, L.J. Affonço, P.N.L. Filho, J.H.D. da Silva, L.A. Rocha, A.M.P. Pinto, F. Toptan, Corrosion and tribocorrosion behaviour of titanium nitride thin films grown on titanium under different deposition times, *Surf. Coat. Technol.* 374 (2019) 878–888.
- [52] A. Velhinho, J.D. Botas, E. Ariza, J.R. Gomes, L.A. Rocha, Tribocorrosion Studies in Centrifugally Cast Al-matrix SiCp-reinforced Functionally Graded Composites, 456 (2004) 871–875.
- [53] I. Çaha, A. Alves, C. Caterina, A. Pinto, S. Tsipas, E. Gordo, F. Toptan, Corrosion and Tribocorrosion Behavior of Ti-40Nb and Ti-25Nb-5Fe Alloys Processed by Powder Metallurgy, *Met. Mater Trans A.* 51 (2020) 3256–3267.

- [54] J.I. Silva, A.C. Alves, A.M. Pinto, F.S. Silva, F. Toptan, Dry sliding wear behaviour of Ti-TiB-TiN x in-situ composite synthesised by reactive hot pressing, *Int. J. Surf. Sci. Eng.* 10 (2016) 317–329.
- [55] R. Tyagi, J.P. Davim, L. Johnston, K. Wolfe, E.O. Dea, J. Mull, *Processing Techniques and Tribological Behavior of Composite Materials*, IGI Global, 2015.



## Chapter 5

### **Preliminary tribo-electrochemical and biological responses of the Ti-TiB-TiC<sub>x</sub> *in-situ* composites intended for load-bearing biomedical implants**

*Submitted to Journal of Alloys and Compounds*

---

**L. Sousa<sup>a,b,\*</sup>, A.C. Alves<sup>a,c</sup>, N. A. Costa<sup>d,e</sup>, S. Gemini Piperni<sup>f,g</sup>, A. L. Rossi<sup>f</sup>, A. R. Ribeiro<sup>c,g</sup>, S. Simões<sup>b,h</sup>, F. Toptan<sup>a,c,i,\*</sup>**

<sup>a</sup> CMEMS-UMinho – Center of MicroElectroMechanical Systems – Universidade do Minho, Campus de Azurém, Guimarães, Portugal

<sup>b</sup> DEMM – Department of Metallurgical and Materials Engineering – Faculdade de Engenharia da Universidade do Porto, Porto, Portugal

<sup>c</sup> IBTN/Euro – European Branch of the Institute of Biomaterials, Tribocorrosion and Nanomedicine, Dept. Eng. Mecânica, Universidade do Minho, Azurém, 4800-058 Guimarães, Portugal

<sup>d</sup> UNESP – Universidade Estadual Paulista, Faculdade de Ciências, 17033-360 Bauru, SP, Brazil

<sup>e</sup> IBTN/Br – Brazilian Branch of the Institute of Biomaterials, Tribocorrosion and Nanomedicine, 17033-360 Bauru, SP, Brazil

<sup>f</sup> Centro Brasileiro de Pesquisas Físicas (CBPF), R. Dr. Xavier Sigaud, 150 - Urca, Rio de Janeiro, RJ, Brazil

<sup>g</sup> Universidade do Grande Rio Rua Professor José de Souza Herdy, 1160, Duque de Caxias, RJ, Brazil

<sup>h</sup> LAETA/INEGI, Institute of Science and Innovation in Mechanical and Industrial Engineering, R. Dr. Roberto Frias, Porto, 4200-465, Portugal

<sup>i</sup> Department of Materials Science and Engineering, Izmir Institute of Technology, 35430, Urla, Izmir, Turkey



## **Abstract**

Poor tribocorrosion resistance of Ti and its alloys remains as a concern for load-bearing biomedical implants. Despite being an effective method to improve tribocorrosion resistance, titanium matrix composites (TMCs) have yet to be used in this type of applications. *In-situ* TiB (titanium boride) and TiC (titanium carbide) reinforcement phases have been considered as one of the best options to produce TMCs once these phases present high compatibility and strong interfacial bonding with Ti. Although the effect of these phases on the mechanical properties of Ti has been thoroughly researched in the last years, their effect on corrosion, tribocorrosion and biocompatibility of Ti is yet to be fully understood. In this work, *in-situ* Ti-TiB-TiC<sub>x</sub> composites obtained by reactive hot pressing showed identical corrosion response compared to the unreinforced Ti but displayed improved tribocorrosion behaviour. Early biological tests showed promising results, as composites were biocompatible and induced osteoblasts spreading and possibly proliferation most probably due to composite chemistry and surface hardness.

### **5.1. Introduction**

Poor tribocorrosion resistance of Ti and its alloys remains a concern affecting load-bearing biomedical implants. In the case of orthopaedic implants, it is known that micro-motions occur at fixed points of contact either the interface between the implant and the bone/cement, or between different components of the implant in the case of modular implants, namely at neck/stem and neck/femoral head interfaces [1]. Adverse local tissue reactions (ALTRs), that may include osteolysis, bone, muscle, tendon and capsular necrosis, capsular thickening, cystic lesions, excessive fluid collection(s), aseptic lymphocyte-dominated vasculitis-associated lesions, and soft tissue masses, are one of the main causes of hip implant failure being linked with tribocorrosion processes taking place on the implant. ALTRs are caused by the interaction of body proteins and wear debris leading to the growth of cystic and fibrotic masses, previously known as a pseudotumor. Simply put, the immune system has a stronger reaction than what it should have and consequently, it leads to the dysregulation of the expected biological behaviour at these zones [2]. In fact, a considerable number

of studies regarding hip implant failure due to ALTRs have been published throughout the years [3–8]. Once implant failure occurs, revision surgery is needed which is much more complex procedure than the first implantation. In the case of revision surgery, the damaged implant needs to be removed, along with the cement (in the case of cemented implants) and the surrounding bone and tissue. Thus, complications such as bone loss and bone fracture are more likely to happen. In addition, significant economical burdens are also put on both patients and healthcare infrastructures [9–12].

The incorporation of hard ceramic particles into a Ti matrix to produce TMCs has been reported to be an effective method to improve the tribocorrosion behaviour of Ti. Hard ceramic reinforcement particles may improve the wear resistance through different strengthening mechanisms. Load transfer is the one that has a higher contribution, while other mechanisms such as strain hardening, Orowan strengthening and/or grain size refinement can act simultaneously promoting an improvement in the mechanical properties of the composites [13]. Despite being an effective method of improving the tribocorrosion behaviour of Ti, these classes of materials have not yet sufficiently attracted the attention of the biomaterials industry.

Among all the reinforcement phases that can be successfully used to produce these composites, *in-situ* TiB whiskers (TiB<sub>w</sub>) and TiC particles (TiC<sub>p</sub>) have been recognized as excellent options due to their compatibility and strong interfacial bonding with Ti and similar coefficients of thermal expansion (CTEs), being  $8.2 \times 10^{-6}/^{\circ}\text{C}$  for Ti,  $7.2 \times 10^{-6}/^{\circ}\text{C}$  for TiB, and  $7.9 \times 10^{-6}/^{\circ}\text{C}$  for TiC. Despite *ex-situ* composites also showing superior tribocorrosion resistance compared to unreinforced Ti, these still present some disadvantages, such as particle fragmentation and pull out during sliding, which can lead to third-body wear and consequently an increase in wear volume [14,15]. Another advantage of *in-situ* Ti-TiB-TiC composites resides in the fact that they can be efficiently and economically processed by a mixture of Ti and B<sub>4</sub>C powders using powder metallurgy (P/M) based techniques [16–19].

The effect of TiB and/or TiC phases on the mechanical properties of Ti and Ti alloys have been thoroughly researched. TiB<sub>w</sub> phases can be used to improve yield strength [20,21], ultimate compressive strength [21] as well as tensile strength and creep resistance since TiB<sub>w</sub> phases can undertake higher stress

than the Ti matrix due to different elastic modulus [22–24]. TiC<sub>p</sub> phases are reported to prevent crack nucleation and propagation [23,25] as well as improve yield strength and ultimate tensile strength [26]. TMCs reinforced by both TiB<sub>w</sub> and TiC<sub>p</sub> phases are reported to have improved ultimate tensile strength and yield strength [27]. Studies have also shown synergistic effects between TiB<sub>w</sub> and TiC<sub>p</sub> phases on ultimate tensile strength. TMCs reinforced by both phases exhibit superior mechanical behaviour over TMCs reinforced with either TiB<sub>w</sub> or TiC<sub>p</sub> reinforcements [28].

Currently, very few studies report on the corrosion and biological response of TiB and/or TiC reinforced TMCs. Regarding the biological behaviour, TiB phase dispersed in a Ti matrix has been reported to have good cytocompatibility [29]. In contrast, TiC coatings have been reported to improve the biocompatibility of titanium, as well as being able to stimulate osteoblast proliferation, adhesion and differentiation by creation a microrough surface and the formation of Ti<sub>2</sub>O<sub>3</sub>, TiO<sub>2</sub> and TiO oxides [30].

In TMCs, the introduction of secondary phases into a Ti matrix may improve, reduce, or not significantly change the corrosion behaviour of the matrix Ti or Ti alloy. Problems related to processing may lead to the formation of porosity, which may lead to localized corrosion. In addition, galvanic coupling between reinforcement phases and the Ti matrix may also lead to a decrease in corrosion resistance. On the other hand, reinforcement phases may also act as inert barriers against corrosion and improve corrosion resistance [31]. Literature regarding the effect of both TiB and TiC phases on the corrosion resistance of titanium is also very limited. Diao et al. [32] studied the corrosion resistance of a Ti alloy by laser cladding with Ti/TiC/TiB<sub>2</sub> powders and reported an increase in open circuit potential (OCP) and decrease in corrosion kinetics due to grain refinement and higher corrosion resistance of TiC and TiB<sub>2</sub> phases. Chen et al. [33] studied the corrosion behaviour of Ti-TiB composites processed by selective laser melting (SLM) and obtained favourable results. Ti-TiB composites showed increased corrosion resistance, which was attributed to the presence of TiB<sub>2</sub> and TiB particles. During corrosion process, these particles acted as a micro-cathode, facilitating the anodic dissolution of Ti and consequently accelerating the formation of the protective passive film.

The effect of both TiC and TiB reinforcements on the tribocorrosion behaviour of titanium is still poorly understood as most studies only evaluate the wear resistance under dry conditions. Nonetheless, these studies have shown that TMCs reinforced with TiC and TiB reinforcement phases have decreased wear loss under dry sliding and fretting conditions when compared with unreinforced titanium [34–36].

TMCs reinforced with TiB and TiC phases may be a good candidate for load-bearing implants owing to their both mechanical properties and wear resistance; however, their corrosion, tribocorrosion and biological response should be further investigated. Thus, the main goal of this study was to evaluate the corrosion and tribocorrosion behaviour of *in-situ* Ti-TiB-TiC composites, as well as to give an early insight into the biocompatibility of such composites.

## **5.2. Materials and methods**

### *5.2.1. Processing*

*In-situ* Ti-TiB-TiC<sub>x</sub> composites were obtained using Ti grade 2 and B<sub>4</sub>C powders as raw materials, with average particle sizes of 25 and 9 μm, respectively. In order to produce the composites with 10 %vol. (TiB + TiC), 1.9 mass % of B<sub>4</sub>C was used according to eq. (5.1) [37]. Powders were mixed through ball milling for 4 h at 120 rpm with the help of Al<sub>2</sub>O<sub>3</sub> balls (ø 10 mm) under Ar atmosphere to reduce oxidation. After mixing, the blended powders were placed in a zirconia coated graphite mould to process samples with 10 mm diameter and 3 mm of thickness. Hot pressing (HP) occurred under high vacuum ( $\leq 10^{-5}$  mbar) for 2 h at 1100 °C with heating and cooling rates of 5°C/min and 10°C/min, respectively. A pressure of 40 MPa was applied during the whole duration of the thermal cycle. After processing, samples were ground down to # 2400 SiC papers and mirror finished with colloidal silica suspension (0.04 μm). Afterwards, samples were ultrasonically cleaned in propanol and distilled water for 10 and 5 min, respectively. Similar surface conditions were obtained by keeping the samples in a desiccator for 24 h prior to both electrochemical and tribocorrosion tests.



### 5.2.2. Electrochemical tests

Electrochemical tests were carried out in an electrochemical cell containing phosphate-buffered saline solution (PBS: 0.24 g/l  $\text{KH}_2\text{PO}_4$ , 0.2 g/l  $\text{KCl}$ , 1.44 g/l  $\text{Na}_2\text{HPO}_4$  8 g/l  $\text{NaCl}$ ) with an adjusted pH at 7.4 at body temperature ( $37 \pm 1$  °C). OCP was first monitored until stabilization of the system ( $\Delta E < 60$  mV/h), followed by electrochemical impedance spectroscopy (EIS) measurements. EIS data acquisition was performed in a frequency range from  $10^5$  Hz until  $10^{-2}$  Hz at 7 points per decade, an amplitude of the sinusoidal signal of 10 mV was set. After EIS, potentiodynamic polarization tests were performed from  $-0.2 V_{\text{OCP}}$  to  $1.5 V_{\text{Ag/AgCl}}$  at 1mV/s. All electrochemical tests were performed using a standard three-electrode setup with a saturated Ag/AgCl reference electrode, a Pt counter electrode, and the sample as a working electrode with an exposed area of  $0.1 \text{ cm}^2$ . All the electrochemical tests were carried out in a Gamry Potentiostat/Galvanostat/ZRA (model Referece-600+).

### 5.2.3. Tribocorrosion tests

Tribocorrosion tests were performed in a tribometer (CETR-UMT2) with a ball-on-plate configuration and reciprocating stage, using the same PBS solution at body temperature. The sliding action was performed under two distinct normal loads of 0.5 and 10 N, corresponding to a maximum Hertzian contact pressure of 342 and 930 GPa, respectively, for the unreinforced titanium.

OCP was continuously recorded before stabilization ( $\Delta E < 60$  mV/h), under sliding for 3600 s and also after sliding for 3600 s. Coefficient of friction (COF) values were also recorded during sliding. Sliding time, frequency and stroke length were set as 60 min, 1 Hz and 3 mm, respectively, for both conditions. The electrochemical measurements were performed using a Gamry Potentiostat/Galvanostat/ZRA (model Referece-600) with a two-electrode set-up, the samples were set as working electrode and saturated Ag/AgCl as reference electrode. The same cleaning procedure described previously was used after tribocorrosion tests.

#### 5.2.4. Osteoblasts viability

Ti and composite surfaces were sterilized in ethanol (70%) for 2 h followed by UV light irradiation for 2 h on each surface. Human-like osteoblast-like cells (MG-63) were cultured in a growth medium consisting of Dulbecco's modified Eagle's medium (DMEM) supplemented with 10 % fetal bovine serum (FBS) and 1 % of an antibiotic (penicillin-streptomycin). For live and dead assay, MG-63 cells were seeded ( $2 \times 10^4$  cells/cm<sup>2</sup>) on the samples surfaces in a 24 well plate and incubated at 37 °C in a humidified atmosphere (5 % CO<sub>2</sub>) for 24 h. After that, LIVE/DEAD® assay was performed according to manufacturer's instruction (Thermo Fisher, LIVE/DEAD® Viability/Cytotoxicity Kit). Images were taken with an inverted fluorescence microscope equipped with a digital camera, and the total number of live (green) and dead (red) cells in each field (12 images of 1,5 mm<sup>2</sup> for each condition) were counted. After 24 h, cells were fixed with Karnovsky for 1 h and then post-fixed with osmium tetroxide, dehydrated through a series of ethanol (50, 60, 70, 80, 90, 95 and 100 %) and dried with hexamethyldisilazane (HDMS). Finally, samples were gold-sputtered and then observed by field emission gun scanning electron microscope (FEG-SEM, Tescan Lyra 3).

#### 5.2.5. Characterization

The microstructure of the as-processed composites was analysed by FEG-SEM (Tescan Lyra 3). In order to investigate the microstructure in more detail, lamella for transmission electron microscope (TEM) observation was obtained by focused ion beam (FIB, Tescan-Lyra 3 dual beam) with gallium (Ga) ion source attached to the same FEG-SEM equipment. Afterwards, TEM analysis was performed in a TEM (JEOL 2100F) operating at 200 kV equipped with CCD camera (GATAN Orius) and an energy dispersive X-ray spectroscopy detector (EDS - Noran Seven). XRD analysis was conducted in a diffractometer (X'pert PANalytical) with Cu-K $\alpha$  radiation ( $\lambda = 1.54056 \text{ \AA}$ ) at 40 kV and 40 mA. In An Officine Galileo Mod. D200 tester was used to obtain Vickers macro-hardness by applying a 30 kgf load during 15 s through a total of 15 indentations (in 3 independent samples) for both groups. The worn surfaces obtained after tribocorrosion were observed by FEG-SEM (FEI Nova 200) and the chemical composition was evaluated through EDS (EDAX). A non-contact profilometry (Veeco, Dektak 150)

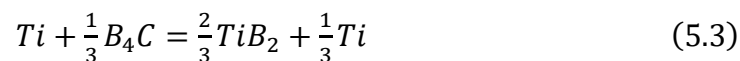
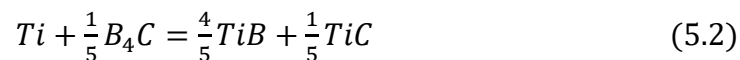


was used to acquire the 2D wear track profiles, which were used to estimate wear volume loss values using a procedure described elsewhere [38].

### 5.3. Results and discussion

#### 5.3.1. Composite microstructures

The overall microstructure and composition of the as-processed composites can be seen on the SEM image obtained with back scattered electron (BSE) detector in Fig. 5.1a. The composite microstructure was constituted by a Ti matrix with well dispersed reinforcement phases, which resulted from the reaction of Ti and B<sub>4</sub>C powders. No significant amount of unreacted B<sub>4</sub>C particles was observed. Fig. 5.1b shows the secondary electron (SE) SEM image of the composite surface over-etched with Kroll's reagent and the EDS elemental maps. The reinforcement phase is composed of TiB needles or clusters dispersed into the Ti matrix. A more detailed characterization was performed by TEM that is present in Fig. 5.1c. A thin cross-section of the sample, prepared by FIB revealed that the reinforcement phases were constituted by clusters of small grains of TiB and TiC<sub>x</sub> phases. Selected area electron diffraction (SAED) from an individual grain revealed the presence of the TiC<sub>x</sub>. In addition, it was observed that long TiB needles grew from these clusters into the Ti matrix. Similar structures were reported by Ni et al. [17], where Ti-(TiB+TiC) composites were processed by hot pressing Ti and B<sub>4</sub>C powders at 1200 °C for 30 min. The authors reported the formation of TiB clusters and small TiC particles as well as the formation of long TiB needles into the Ti matrix. They also reported that by using smaller B<sub>4</sub>C particles, the formation of these clusters could be avoided, and in this way, the overall structure was composed by TiB needles and TiC particles. The Ti-B<sub>4</sub>C system is characterized by the formation of TiB, TiB<sub>2</sub> and TiC phases. When Ti reacts with B<sub>4</sub>C two potential reactions can occur [37,39]:



These reaction products belong to the Ti-B-C system. According to Gibbs free energy ( $\Delta G$ ) and enthalpy ( $\Delta H$ ), the formation TiB<sub>2</sub> is more susceptible to than TiB. However, TiC and TiB phases are usually the main reaction products

due to TiB<sub>2</sub> limited mass transport rate in solid-state sintering [39]. Several studies have shown that reaction of Ti and B<sub>4</sub>C lead mainly to TiB and TiC phases as main reaction products [13,22,23,34,37,40,41]. Due to presence of these reinforcement phases, the overall hardness increased from 286 ± 8 to 431 ± 11 HV<sub>30</sub> from unreinforced Ti to the composites, respectively.

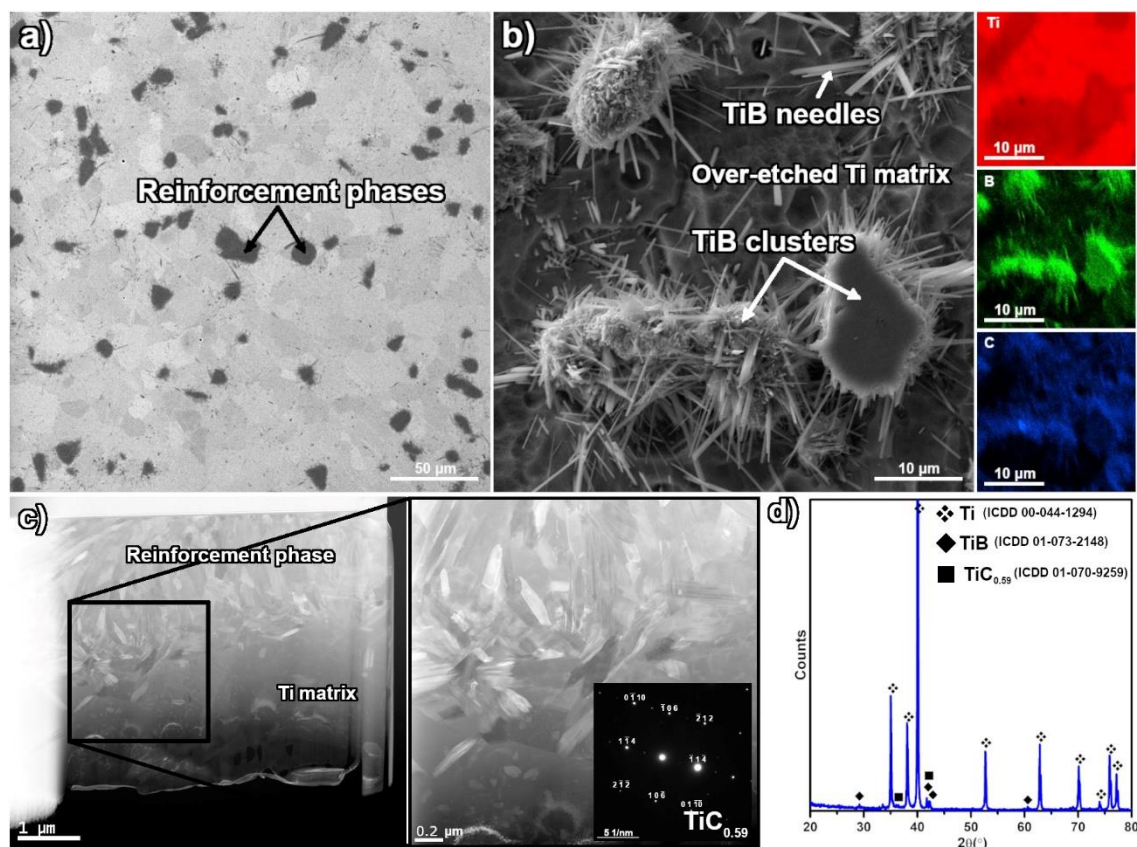


**Figure 5.1.** Characterization after processing: a) BSE SEM image of as-processed composite, b) SE (secondary electron) SEM image and EDS elemental distribution maps of an over-etched composite surface, c) dark-field STEM image of the composite with a higher magnification of the reinforcement phase. The insert shows a selected area electron diffraction pattern (SAED). The diffraction pattern could be indexed in [6 10 1] direction of the TiC<sub>0.59</sub> phase, and d) XRD pattern of the composite showing the presence of TiB and TiC phases.

### 5.3.2. Electrochemical behaviour

Representative potentiodynamic polarization curves for Ti and its composite are presented in Fig. 5.2a. Both Ti and composite presented the typical behaviour of a passive metal with a well-defined passivation plateau, attributed to the formation of a stable passive film. The  $i_{\text{pass}}$  values were extrapolated from potentiodynamic polarization curves as  $5.36 \pm 1.14$  and  $4.65 \pm 0.6 \mu\text{A}\cdot\text{cm}^{-2}$  for Ti and composite, respectively. The slightly lower  $i_{\text{pass}}$  values obtained for composite groups are probably related to the reduced exposed Ti metallic area due to the

presence of reinforcement phases. The composites showed slightly lower  $E_{(i=0)}$  values compared with unreinforced Ti being  $-0.14 \pm 0.06$  and  $-0.27 \pm 0.03$  V for Ti and composite, respectively.

Representative EIS Nyquist and Bode diagrams are presented in Figs. 5.2b and 5.2c. On Bode diagrams, when constant  $|Z|$  values and phase angles near  $0^\circ$  in higher frequencies ranges (higher than 1 kHz) corresponds to the electrolyte resistance. For lower and middle frequencies range, phase angles approaching  $-90^\circ$  were noticed for both groups, indicating a compact passive film formation. The total impedance of the system ( $|Z|_{f \rightarrow 0}$ ) represents the overall corrosion resistance, was very similar for both groups (c.a.  $0.3 \text{ M}\Omega \cdot \text{cm}^2$ ). Considering the Nyquist diagrams where the corrosion resistance is given by the diameter of the semi-circle, composites seem to present slightly smaller diameters compared to Ti, that can indicate slightly reduced corrosion resistance although this difference was very small. In order to better access the results, EIS data was fitted with modified Randels' electrical equivalent circuit (EEC) presented in Fig. 5.2d, consisting of an electrolyte resistance ( $R_e$ ) in series with the  $R_{ox}/CPE_{ox}$  pair, being the resistance and constant phase element ( $Q_{ox}$ ) of the native oxide film. For both groups, a CPE due to the deviation of an ideal capacitor, where the capacitance of the CPE is defined by  $Z_{CPE} = [Y_0(j\omega)^n]^{-1}$ , with  $-1 \leq n \leq 1$  when  $n = -1$  corresponds to an inductor,  $n = 0$  to a resistor,  $n = 1$  to a capacitor and  $n$  values close to 1 representing a non-ideal capacitor. Fitting results can be seen on Table 5.1, where the quality of fitting was determined by the goodness of fitting values, being always under  $10^{-4}$  for both groups indicated that the equivalent circuit described the behaviour of Ti and composite groups adequately. The obtained electrochemical results were very similar between Ti and composite groups, indicating that the *in-situ* phases did not significantly alter the corrosion behaviour of unreinforced Ti.

The effect of TiB and TiC phases on the corrosion behaviour of TMCs have been reported, however, for systems with some key differences from the one studied in this work. Toptan et al. [13] investigated the corrosion response of *ex-situ* Ti-B<sub>4</sub>C composites processed by HP. The overall microstructure of the composites consisted of dispersed B<sub>4</sub>C reinforcement particles within the Ti matrix with a reaction zone surrounding the B<sub>4</sub>C particles composed of TiB and TiC phases due to the reaction of B<sub>4</sub>C with Ti. The authors reported reduced

corrosion resistance under static conditions, which was attributed to the porosity formed due to bridging of B<sub>4</sub>C during processing. Diao et al. [32] studied the corrosion behaviour of Ti-TiC-TiB<sub>2</sub> (weight ration 1:1:2) composite coatings and reported a significant improvement in corrosion behaviour due to the grain refining of Ti and barrier role given by the reinforcement phases.

Chen et al. [33] investigated the corrosion behaviour of Ti-TiB composites processed by SLM, and reported an increase in corrosion resistance, as TiB phases acted as micro-cathodes and accelerated the formation of the passive film on Ti matrix. Thulasiram et al. [42] studied the corrosion performance of Ti-TiB composites obtained by conventional P/M, spark plasma sintering (SPS) and HP. The authors reported that hot-pressed composites presented superior corrosion behaviour due to the formation of finer TiB needles compared to the other processing methods. The authors also reported that higher amount of TiB phases led to an increase in corrosion resistance of the composites. Regarding TiC phases, Covino et al. [43] investigated the effect of TiC reinforcement volume fraction (2.5, 5, 10 and 25 vol. %) on the corrosion behaviour of Ti-TiC composites processed by conventional sintering. The authors reported similar behaviour to that of the unreinforced Ti for all the groups and found no evidence of TiC phases changing the corrosion behaviour of Ti in any significant way. Other *in-situ* composites based on Ti-B-N system, such as Ti-TiB-TiN<sub>x</sub> composites have also been reported to have similar behaviour to the unreinforced Ti [31,44]. In the present work, composites presented rather similar behaviour to that of Ti, however, EIS results suggested that the passive film formed on the surface may have slightly less quality. This behaviour was most probably related to the presence of the rather large TiB clusters, which may compromise the continuity of the passive oxide film.

**Table 5.1.** EEC parameters obtained from EIS data.

	$R_e$	$R_{ox} (x10^6 \Omega.cm^2)$	$Q_{ox} (x10^{-5} S*s^a cm^2)$	$n_{ox}$	$\chi^2$
<b>Ti</b>	34 ± 4	1.13 ± 0.80	2.75 ± 0.51	0.90 ± 0.04	<10 <sup>-4</sup>
<b>Ti-TiB-TiC</b>	35 ± 1	0.43 ± 0.08	2.66 ± 0.21	0.91 ± 0.02	<10 <sup>-4</sup>

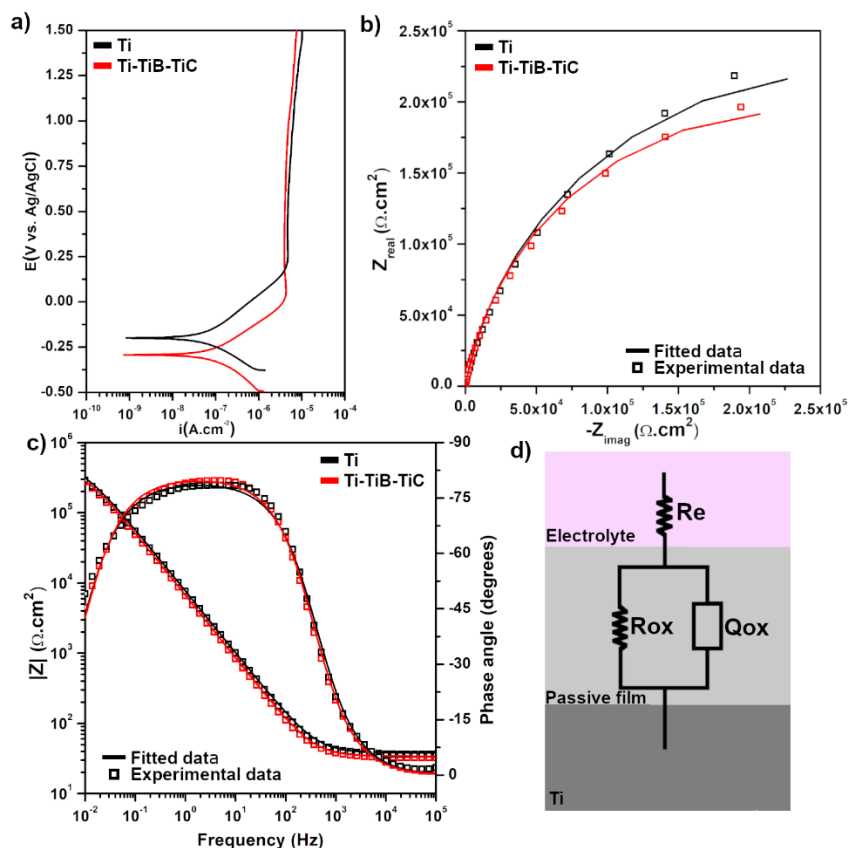


**Figure 5.2.** Electrochemical behaviour: a) Representative potentiodynamic polarization curves for Ti and its composites, b) Nyquist diagrams, c) Bode diagrams and EEC used to fit EIS data.

### 5.3.3. Tribocorrosion behaviour

The evolution of OCP before, during and after sliding, and COF evolution during sliding for Ti and its composite for both loading conditions are presented in Fig. 5.3. Before sliding, Ti and composite groups the stable OCP values were reached due to the formation of a stable passive oxide film. As soon as sliding started, a sudden decrease in OCP values was noticed for all groups and conditions due to removal of the passive oxide film and consequent exposure of fresh metallic area to the PBS. Overall, for 0.5 N applied load, the behaviour of Ti and composite was rather similar. As soon as sliding started, OCP values dropped around  $-0.47 \pm 0.12$  V for composites and  $-0.51 \pm 0.05$  V for Ti in the cathodic direction. Within a brief period of sliding, OCP values increased for nobler values, after that, OCP values for composite groups tended to slowly increase until the end of sliding, while the OCP values for Ti group followed a relatively horizontal course. Periodic drops in OCP values were observed for both groups under sliding that were also corresponded by drops in COF values. This behaviour was reported before for Ti under similar conditions and it was attributed

to the repeatedly formation and breakdown of tribolayers, which give limited protection against corrosion [44,45]. Consequently, a comparable effect was also observed in COF values, as the formation of these tribolayer leads to an increase in the overall roughness of the worn surfaces. Overall, OCP values under sliding were slightly more positive and COF values were slightly lower for composite group.

On the other hand, when the applied load was 10 N, significant differences were observed between the groups. At the onset of sliding, both presented similar drops in OCP values ( $-0.58 \pm 0.05$  V for Ti and  $-0.64 \pm 0.11$  V for composites); however, different behaviours were observed after a few minutes of sliding. After around 20 min, OCP values for Ti group dropped and evolved horizontally around  $-0.79 \pm 0.05$  V till the sliding stopped. Composite groups on the other hand, showed a rapid increase in OCP values after roughly 5 min of sliding, to values around  $-0.55 \pm 0.03$  V, which then tended to slowly increase until the end of the sliding to values close to  $-0.49 \pm 0.06$  V. Contrary to 0.5 N, under these conditions, composites presented slightly higher COF values compared to Ti, suggesting higher roughness of the worn surfaces under these conditions.

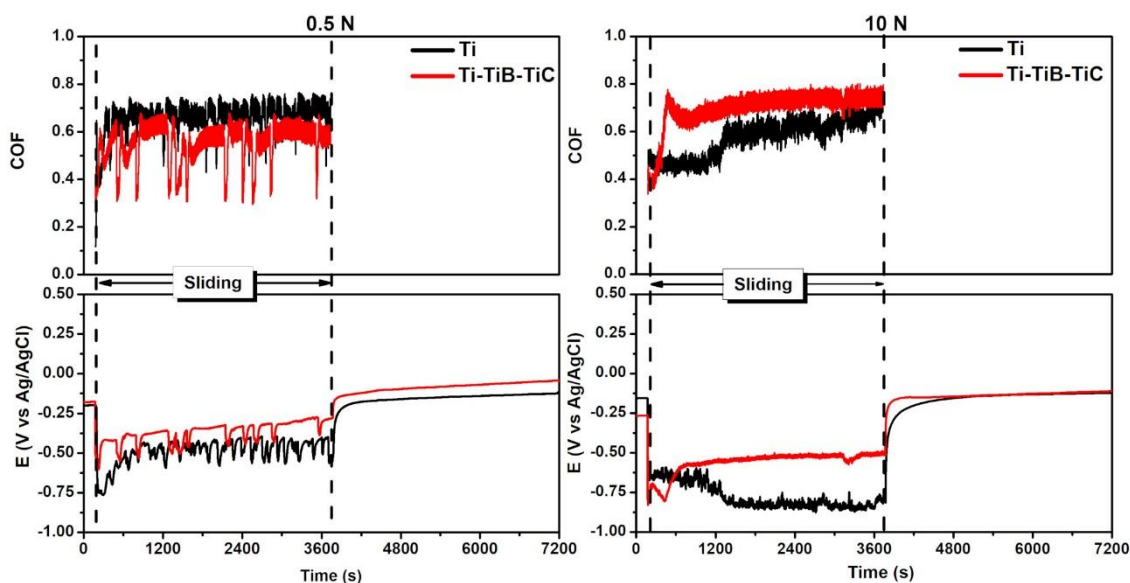


**Figure 5.3.** Evolution of OCP before, during and after sliding together with the evolution of COF during sliding for both conditions and groups.

Fig. 5.4 shows BSE and SE SEM images of the worn sample and counter-material surfaces, together with the respective EDS spectra taken from the worn counter-material surfaces. For 0.5 N condition, similar features were detected on the worn surfaces of Ti and composites, being the formation of parallel grooves

to the sliding direction and discontinuous tribolayers. Grooves originate from abrasion mechanisms caused by the protrusions on the counter-body surfaces, originated from the transference of material from the worn sample surfaces to the counter-body due to adhesion (as confirmed by the Ti peaks observed on EDS spectra in Fig. 5.4). Transferred material can also be compacted on the worn surfaces and result in the formation of discontinuous tribolayers, leading to the oscillations in OCP and COF values as mentioned before. This mechanism can be repeated several times during sliding, making transferred material harder due to work hardening. Additionally, loose oxide wear debris can act as a third-body abrasive and lead to the formation of scratches parallel to the sliding direction.

For 10 N condition, considerably wider wear tracks were observed for Ti. While grooves were observed for both groups, tribolayers were much less predominant on the unreinforced Ti surfaces, contributing to the lower OCP values under sliding. Under this condition, wear debris tends to be pushed out of the wear track and thus, the formation of tribolayers is limited [14,44]. On the other hand, SEM images revealed elevated amount of tribolayer formation for the composites, which extend to almost the entire wear zone and is most probably the cause for the rapid increase on OCP values, as well as COF values after a few minutes of sliding action. The results suggested that under this condition, reinforcement phases served as anchorage points for the elevated formation of the tribolayers.

Due to overall higher hardness and load carrying effect given by the reinforcement phases, together with the formation of an extensive protective tribolayer, OCP values under sliding were considerably higher than the ones registered for unreinforced Ti.

The wear volume loss values are shown on Fig. 5.5. Overall, composite group presented significantly reduced wear volume loss than the unreinforced Ti, especially under the 10 N applied load. A reduction in wear volume loss for Ti or Ti alloys reinforced with TiB and/or TiC phases has been reported before. Kim et al. [35] researched the wear behaviour of Ti-(TiB+TiC) composites produced by vacuum induction melting using Ti and B<sub>4</sub>C powders and reported a decrease in wear volume loss with increasing reinforcement content. The authors attributed this behaviour to the increased hardness of composites and the load carrying effect given by the reinforcement phases, which reduced wear damage on the Ti

matrix and reduced crack propagation during sliding and thus the formation of large wear debris was avoided/reduced. Choi et al. [34] also reported similar behaviour for Ti-(TiB+TiC) composites processed by casting. The authors stated that the formation of protective tribolayers during sliding also leads to additional protection against wear. Singh et al. [46] studied the tribocorrosion response of Ti-(TiB+TiC) composites processed by SPS. The authors reported higher OCP values during sliding compared to Ti-6Al-4V alloy due to improved load distribution, once reinforcement phases reduced the deformation of the matrix alloy. In addition, the authors also attributed improved tribocorrosion behaviour to grain refinement and dispersion strengthening after the introduction of the reinforcement phases.

The results obtained in this work support previous literature, being that an increase in the overall hardness, as well as the load carrying effect given by the reinforcement phases are the main reasons for considerably reduced wear volume loss. Additionally, it was shown in the present work that under high loads, tribolayers were formed on the composite surfaces that gave limited protection against wear and corrosion.



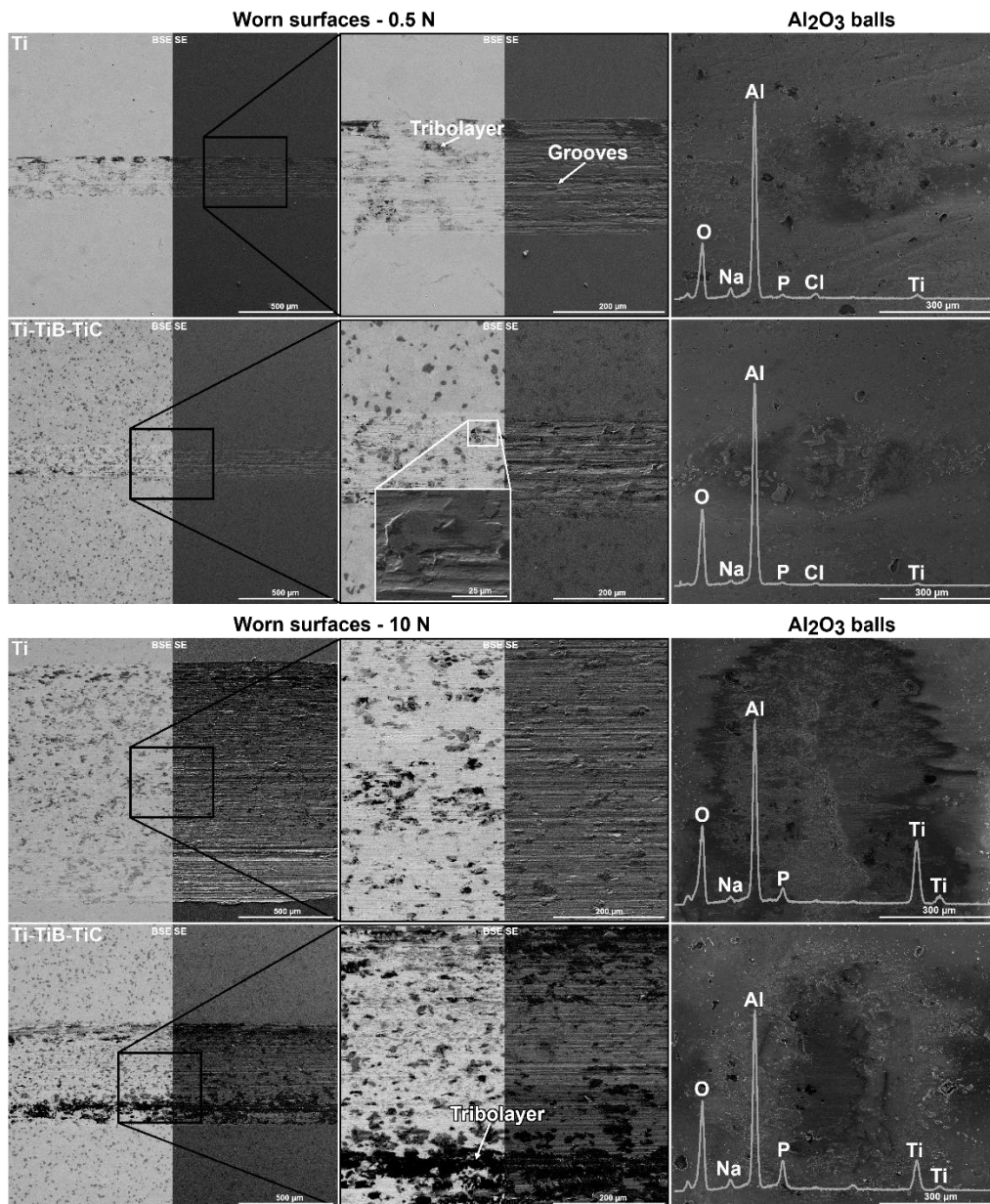


**Figure 5.4.** BSE/SE SEM images of the worn surfaces and SE SEM images of the Al<sub>2</sub>O<sub>3</sub> balls used as counter-body with respective EDS analysis.

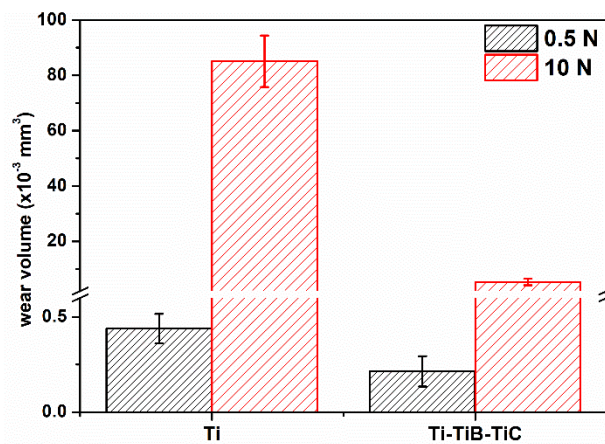


**Figure 5.5.** Wear volume loss values calculated from wear profiles.

#### 5.3.4. Biological behaviour

The MG-63 cell viability was evaluated by Live and Dead assay following 24 h contact with the surfaces (Fig. 5.6a and Fig. 5.6b). Results showed no significant difference between viability of osteoblast-like cells plated on the composite surfaces compared with the ones seeded on control Ti surfaces. An increase of 33% in cell number was observed with cells seeded on the composite surfaces compared with Ti control surfaces possibly suggesting that composites are inducing osteoblasts proliferation, however further studies are underway to confirm this behaviour. Very limited information is available in literature regarding cytocompatibility of TiB and TiC phases. Miklaszewski et al. [29] studied the cytocompatibility of *in-situ* Ti-TiB composites processed by boride microplasma surface *in vitro*, using human osteoblast (NHOst) cells. The results showed similar cytocompatibility of Ti-TiB composites compared to microcrystalline Ti after 1 and 5 days. On the other hand, Balázsi et al. [47] studied the cytocompatibility of TiC and TiCN nanocomposite films obtained by DC magnetron sputtering. The authors reported improvement of osteoblast-like MG-63 cell viability on nanocomposite films possibly due to the formation of a TiO<sub>2</sub> film with anti-bacterial properties. The presence of reinforcement phases led to increment of hardness (from 286 to 431 HV<sub>30</sub>). Harder surfaces have been reported to promote material-cell interactions [48,49].

SEM analysis was performed after 24 h cell direct contact on the surfaces (Fig. 5.6c) to assess osteoblasts morphology. It was possible to observe that osteoblasts adhered to composite surfaces exhibiting an intact and well-defined osteoblastic phenotypic morphology. In all the conditions it was possible to observe that osteoblasts started to spread and developed well defined lamellipodia and filopodia. Interestingly, osteoblasts adhered to composites showing a more flattened cell morphology while in the control group (Ti) cells kept more hemispheroidal. Osteoblasts cultured on composites were larger comparing to cells grown on Ti, indicating that composite surfaces enhanced cell spreading. All together, these results showed that the composites developed in this work are a promising material for biomedical applications since they improve cell viability, induce an enhancement on spreading and possibly affect also proliferation.

This improvement is most likely related to a change in surface chemistry and hardness.

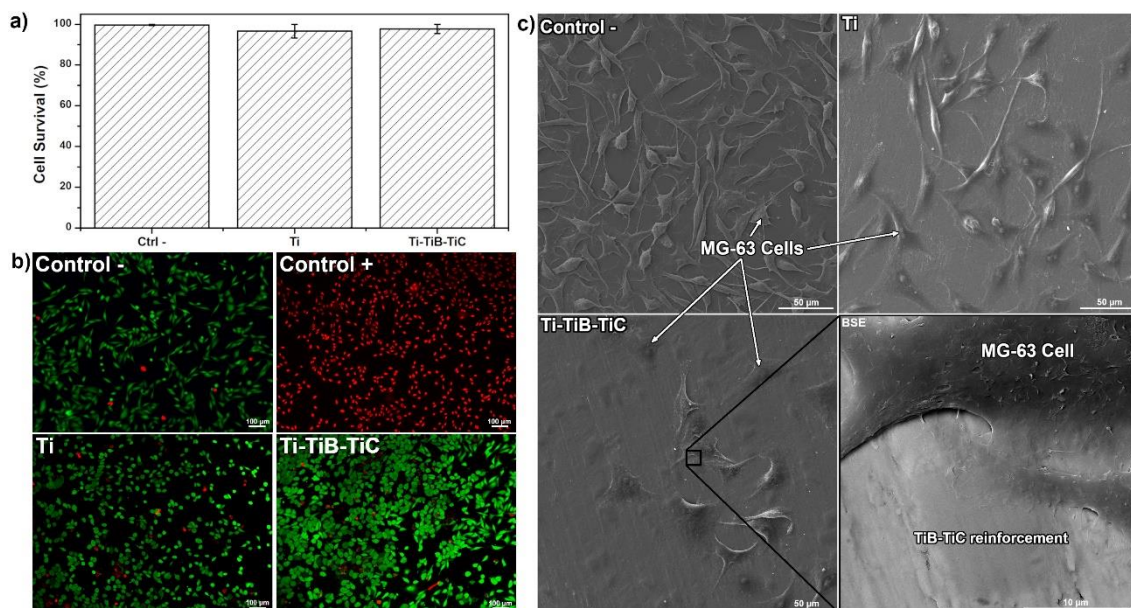


**Figure 5.6.** Biological behaviour: a) Cell survival (%), b) fluorescence micrography of MG-63 cells cultured 24 h on control Ti surfaces and Ti-TiB-TiC composites (green represents live cells and red represents dead cells) and c) SEM images of MG-63 cells attached Ti surfaces and Ti-TiB-TiC composites surfaces for 24 h.

#### 5.4. Conclusions

*In-situ* TMCs reinforced with TiB and TiC phases were synthesised by reactive hot-pressing through the reaction of Ti and B<sub>4</sub>C powders. Composites maintained the good corrosion behaviour of Ti. Due to the load carrying effect given by the reinforcement phases, as well as higher overall hardness of the composite surfaces, a significant decrease in wear volume loss and reduced tendency to corrosion under sliding was observed, being more prominent under harsher conditions. The composite surfaces were biocompatible and modulated cell spreading and possibly proliferation probably due to the combination of specific surface chemistry and hardness. Therefore, within the limitations of this work, it was shown that *in-situ* Ti-TiB-TiC<sub>x</sub> composites may have potential for load bearing hip implants.



## References

- [1] N. Diomidis, S. Mischler, N.S. More, M. Roy, Tribo-electrochemical characterization of metallic biomaterials for total joint replacement, *Acta Biomater.* 8 (2012) 852–859.
- [2] F. Eltit, Q. Wang, R. Wang, Mechanisms of Adverse Local Tissue Reactions to Hip Implants, *Front. Bioeng. Biotechnol.* 7 (2019) 1–17.
- [3] R.B. Cook, B.J.R.F. Bolland, J.A. Wharton, S. Tilley, J.M. Latham, R.J.K. Wood, Pseudotumour Formation Due to Tribocorrosion at the Taper Interface of Large Diameter Metal on Polymer Modular Total Hip Replacements, *J. Arthroplasty.* 28 (2013) 1430–1436.
- [4] H.J. Cooper, R.M. Urban, R.L. Wixson, R.M. Meneghini, J.J. Jacobs, Adverse Local Tissue Reaction Arising from Corrosion at the Femoral Neck-Body Junction in a Dual-Taper Stem with a Cobalt-Chromium Modular Neck, *J. Bone Jt. Surg. Inc.* (2013) 865–872.
- [5] H.J. Cooper, C.J. Della Valle, R.A. Berger, M. Tetreault, W.G. Paprosky, S.M. Sporer, J.J. Jacobs, Corrosion at the Head-Neck Taper as a Cause for Adverse Local Tissue Reaction After Total Hip Arthroplasty, *J. Bone Jt. Surgery, Inc.* (2012) 1655–1661.
- [6] A. Charles, H. Ho, Metal-on-Metal Hip Arthroplasty Does Early Clinical Outcome Justify the Chance of an Adverse Local Tissue Reaction?, *Clin. Orthop. Relat. Res.* (2010) 406–412.
- [7] I. Antoniac, M. Negrusoiu, M. Mardare, C. Socoliuc, M. Niculescu, Adverse local tissue reaction after 2 revision hip replacements for ceramic liner fracture A case report, *Medicine (Baltimore).* 96 (2017) p e6687.
- [8] M.R. Whitehouse, M. Endo, B.A. Masri, Adverse Local Tissue Reaction Associated With a Modular Hip Hemiarthroplasty, *Clin Orthop Relat Res.* 471 (2013) 4082–4086.
- [9] C. Kenney, S. Dick, J. Lea, J. Liu, N.A. Ebraheim, A systematic review of the causes of failure of Revision Total Hip Arthroplasty, *J. Orthop.* 16 (2019) 393–395.
- [10] A. Bottle, S.P. Id, P. Aylin, M. Loeffler, Risk factors for early revision after total hip and knee arthroplasty: National observational study from a surgeon and population perspective, *PLoS ONE* 1. 14 (2019) e0214855.
- [11] M. Weber, T. Renkawitz, F. Voellner, B. Craiovan, F. Greimel, M. Worlicek, J. Grifka, A. Benditz, Revision Surgery in Total Joint Replacement Is Cost-Intensive, *Biomed Res. Int.* 25 (2018) 8987104.
- [12] J. Parvizi, P.F. Sharkey, Revision total hip arthroplasty for instability: Surgical techniques and principles, *J. Bone Jt. Surg.* 58 (2008) 1134–1142.
- [13] F. Toptan, A. Rego, A.C. Alves, A. Guedes, Corrosion and tribocorrosion behavior of Ti-B4C composite intended for orthopaedic implants, *J. Mech. Behav. Biomed. Mater.* 61 (2016) 152–163.
- [14] A. Oliveira, F. Toptan, Wear Behavior of Ti-Al<sub>2</sub>O<sub>3</sub> Biocomposites in 9 g/L NaCl Solution, *J. Mater. Eng. Perform.* 28 (2019) 6000–6010.
- [15] Z. Doni, A.C. Alves, F. Toptan, L.A. Rocha, M. Buciumeanu, L. Palaghian, F.S. Silva, Tribocorrosion behaviour of hot pressed CoCrMo-HAP biocomposites, *Tribol. Int.* 8 (2014) 201–208.
- [16] L. Geng, D.R. Ni, J. Zhang, Z.Z. Zheng, Hybrid effect of TiBw and TiCp on tensile properties of *in situ* titanium matrix composites, *J. Alloys Compd.* 463 (2008) 488–492.
- [17] D.R. Ni, L. Geng, J. Zhang, Z.Z. Zheng, Effect of B4C particle size on microstructure of *in situ* titanium matrix composites prepared by reactive processing of Ti-B4C system, *Scr. Mater.* 55 (2006) 429–432.
- [18] B. V. Radhakrishna Bhat, J. Subramanyam, V. V. Bhanu Prasad, Preparation of Ti-TiB-TiC & Ti-TiB composites by in-situ reaction hot processing, *Mater. Sci. Eng. A.* 325 (2002) 126–130.



- [19] D.R. Ni, L. Geng, J. Zhang, Z.Z. Zheng, TEM characterization of symbiosis structure of *in situ* TiC and TiB prepared by reactive processing of Ti-B4C, *Mater. Lett.* 62 (2008) 686–688.
- [20] H.T. Tsang, C.G. Chao, C.Y. Ma, Effects of volume fraction of reinforcement on tensile and creep properties of in-situ TiB/Ti MMC, *Acta Metall.* 37 (1997) 1359–1365.
- [21] H. Attar, M. Bonisch, M. Calin, L. Zhang, S. Scudino, J. Eckert, Selective laser melting of *in situ* titanium–titanium boride composites: Processing, microstructure and mechanical properties, *Acta Mater.* 76 (2014) 13–22.
- [22] H.K.S. Rahoma, Y.Y. Chen, X.P. Wang, S.L. Xiao, Influence of (TiC+TiB) on the microstructure and tensile properties of Ti-B20 matrix alloy, *J. Alloys Compd.* 627 (2015) 415–422.
- [23] V.S. Balaji, S. Kumaran, Densification and microstructural studies of titanium–boron carbide (B4C) powder mixture during spark plasma sintering, *Powder Technol.* 264 (2014) 536–540.
- [24] J. Wang, X. Guo, J. Qin, D. Zhang, W. Lu, Microstructure and mechanical properties of investment casted titanium matrix composites with B4C additions, *Mater. Sci. Eng. A.* 628 (2015) 366–373.
- [25] S. Li, K. Kondoh, H. Imai, B. Chen, L. Jia, J. Umeda, Y. Fu, Strengthening behavior of *in situ* -synthesized (TiC–TiB)/Ti composites by powder metallurgy and hot extrusion, *Jmade.* 95 (2016) 127–132.
- [26] M.H. Loretto, D.G. Konitzer, The effect of matrix reinforcement reaction on fracture in Ti-6Al-4V-base composites, *Metall. Trans. A.* 21 (1990) 1579–1587.
- [27] C.J. Zhang, F.T. Kong, S.L. Xiao, E.T. Zhao, L.J. Xu, Y.Y. Chen, Evolution of microstructure and tensile properties of *in situ* titanium matrix composites with volume fraction of (TiB and TiC) reinforcements, *Mater. Sci. Eng. A.* 548 (2012) 152–160.
- [28] D.R. Ni, L. Geng, J. Zhang, Z.Z. Zheng, Fabrication and tensile properties of *in situ* TiBw and TiCp hybrid-reinforced titanium matrix composites based on Ti-B4C-C, *Mater. Sci. Eng. A.* 478 (2008) 291–296.
- [29] A. Miklaszewski, M.U. Jurczyk, K. Jurczyk, M. Jurczyk, Plasma surface modification of titanium by TiB precipitation for biomedical applications, *Surf. Coatings Technol.* 206 (2011) 330–337.
- [30] M. Brama, N. Rhodes, J. Hunt, A. Ricci, R. Teghil, S. Migliaccio, C. Della Rocca, S. Leccisotti, A. Lioi, M. Scandurra, G. De Maria, D. Ferro, F. Pu, G. Panzini, L. Politi, R. Scandurra, Effect of titanium carbide coating on the osseointegration response in vitro and in vivo, *Biomaterials.* 28 (2007) 595–608.
- [31] F. Toptan, Corrosion and wear behaviour of highly porous Ti-TiB-TiNx *in situ* composites, *Turkish J. Chem.* 44 (2020) 805–816.
- [32] Y. Diao, K. Zhang, Microstructure and corrosion resistance of TC2 Ti alloy by laser cladding with Ti/TiC/TiB2 powders, *Appl. Surf. Sci.* 352 (2015) 163–168.
- [33] Y. Chen, J. Zhang, N. Dai, P. Qin, H. Attar, L.-C. Zhang, Corrosion Behaviour of Selective Laser Melted Ti-TiB Biocomposite in Simulated Body Fluid, *Electrochim. Acta.* 232 (2017) 89–97.
- [34] B. Choi, I.-Y. Kim, Y. Lee, Y. Kim, Microstructure and friction/wear behavior of (TiB+TiC) particulate-reinforced titanium matrix composites, *Wear.* 318 (2014) 68–77.
- [35] I.Y. Kim, B.J. Choi, Y.J. Kim, Y.Z. Lee, Friction and wear behavior of titanium matrix (TiB+TiC) composites, *Wear.* 271 (2011) 1962–1965.
- [36] J.-S. Kim, K.-M. Lee, D.-H. Cho, Y.-Z. Lee, Fretting wear characteristics of titanium matrix composites reinforced by titanium boride and titanium carbide particulates, *Wear.* 301 (2013) 562–568.
- [37] X. Zhang, W. Lu, D. Zhang, R. Wu, *In Situ* Technique for synthesizing (TiB+TiC)/Ti composites, *Scr. Mater.* 41 (1999) 39–46.

- [38] Z. Doni, A.C. Alves, F. Toptan, J.R. Gomes, A. Ramalho, M. Buciumeanu, L. Palaghian, F.S. Silva, Dry sliding and tribocorrosion behaviour of hot pressed CoCrMo biomedical alloy as compared with the cast CoCrMo and Ti6Al4V alloys, *Mater. Des.* 52 (2013) 47–57.
- [39] L. Jia, S.F. Li, H. Imai, B. Chen, K. Kondoh, Size effect of B4C powders on metallurgical reaction and resulting tensile properties of Ti matrix composites by in-situ reaction from Ti-B4C system under a relatively low temperature, *Mater. Sci. Eng. A.* 614 (2014) 129–135.
- [40] Y. Qin, W. Lu, D. Xu, D. Zhang, High-temperature OM investigation of the early stage of (TiC+TiB)/Ti oxidation, *J. Mater. Sci.* 40 (2005) 687–692.
- [41] S. Ghesmati Tabrizi, S.A. Sajjadi, A. Babakhani, W. Lu, Influence of spark plasma sintering and subsequent hot rolling on microstructure and flexural behavior of in-situ TiB and TiC reinforced Ti6Al4V composite, *Mater. Sci. Eng. A.* 624 (2015) 271–278.
- [42] R. Thulasiram, S. Mani, M. Murugesan, C. Palanisamy, G.S. Kalaraj, Effect of TiB Addition on Corrosion Behavior of Titanium Composites under Neutral Chloride Solution, *Trans. Indian Ceram. Soc.* 78 (2019) 155–160.
- [43] J. Bernard S. Covino, D.E. Alman, Corrosion of Titanium Matrix Composites, Albany Res. Center, U.S. Dep. Energy, Albany, OR USA. (2002) 1–7.
- [44] J.I. Silva, A.C. Alves, A.M. Pinto, F. Toptan, Corrosion and tribocorrosion behavior of Ti-TiB-TiNx in-situ hybrid composite synthesized by reactive hot pressing, *J. Mech. Behav. Biomed. Mater.* 74 (2017) 195–203.
- [45] A.I. Costa, L. Sousa, A.C. Alves, F. Toptan, Tribocorrosion behaviour of bio-functionalized porous Ti surfaces obtained by two-step anodic treatment, *Corros. Sci.* 166 (2020) 108467.
- [46] N. Singh, R. Ummethala, P.S. Karamched, R. Sokkalingam, V. Gopal, G. Manivasagam, K.G. Prashanth, ., *J. Alloys Compd.* 865 (2021) 158875.
- [47] K. Balázs, I.E. Lukács, S. Gurbán, M. Menyhárd, L. Bacáková, M. Vandrovcová, C. Balázs, Structural , mechanical and biological comparison of TiC and TiCN nanocomposites films, *J. Eur. Ceram. Soc.* 33 (2013) 2217–2221.
- [48] M. Kopernik, M. Surmiak, R. Major, M. Gawlikowski, K. Trembecka-w, Effect of the mechanical properties of carbon-based coatings on the mechanics of cell – material interactions, *Colloids Surfaces B Biointerfaces.* 197 (2021) 111359..
- [49] D.M.D. Ehrenfest, P.G. Coelho, B. Kang, Y. Sul, T. Albrektsson, Classification of osseointegrated implant surfaces: materials , chemistry and topography, *Trends Biotechnol.* 28 (2010) 198–206.





## Chapter 6

### Tribocorrosion behaviour of bio-functionalized porous Ti surfaces obtained by two-step anodic treatment

*Published in Corrosion Science (2020) doi.org/10.1016/j.corsci.2020.108467*

---

A.I. Costa<sup>a,b</sup>, **L. Sousa**<sup>a,b,\*</sup>, A.C. Alves<sup>a</sup>, F. Toptan<sup>a,c,d</sup>

<sup>a</sup>CMEMS-UMinho – Center of MicroElectroMechanical Systems – Universidade do Minho, Campus de Azurém, Guimarães, Portugal

<sup>b</sup>DEMM – Department of Metallurgical and Materials Engineering – Faculdade de Engenharia da Universidade do Porto, Porto, Portugal

<sup>c</sup>DEM – Department of Mechanical Engineering – Universidade do Minho, Campus de Azurém, Guimarães, Portugal

<sup>d</sup>IBTN/Br – Brazilian Branch of the Institute of Biomaterials, Tribocorrosion and Nanomedicine, UNESP, Campus de Bauru, Bauru, SP, Brazil



## Abstract

A bio-functionalized porous surface was obtained on Ti by a two-step anodic treatment and its corrosion and tribocorrosion behaviour were evaluated. The first-step provided macro-porosity while the second-step, a bio-functionalization process by micro-arc oxidation (MAO), provided an oxide layer (anatase + rutile) with micro-pores and bio-active elements (Ca + P). Corrosion and tribocorrosion behaviour were improved due to the protective role given by the oxide layer formed on the second-step. Tribocorrosion mechanisms for the bio-functionalized porous structures are presented.

### 6.1. Introduction

Chronic diseases such as osteoarthritis, cardiovascular diseases and old age-related traumas together with the ageing population worldwide are set to increase the demand for medical implants in the next following years. By 2022, the medical implants market is expected to garner 116 billion USD [1]. Several types of materials are used to fulfil the needs of the implants market, and among the metallic materials, Ti is widely used mainly due to its high strength, lower Young's modulus compared to Co-Cr alloys and stainless steel, lower density, and a good combination of mechanical properties and outstanding corrosion resistance [2–4]. However, Ti presents three major concerns as an implant material, such as (i) poor wear resistance, (ii) bio-inertness and (iii) higher Young's modulus compared to bone, that can result in stress shielding effect [5].

A multiscale (macro-, micro- and nano-scale) porosity on the surface could be beneficial for mechanical interlocking, as well, for promoting cell adhesion and proliferation [6]. By varying the parameters of two or more steps of anodic treatment, it is possible to obtain hierarchical porous surfaces on the macro-, micro- or nano-scale. In order to give bio-functions, a specific anodic treatment, micro-arc oxidation (MAO), can be applied. MAO has shown tremendous potential as a process to improve the surface characteristics of materials intended for biomedical applications since it can improve the roughness, create better wettability and promote bio-activity. Consequently, these modifications bring better results regarding adhesion, proliferation, and differentiation of cells, blood compatibility, reduction of the haemolysis rate, extended dynamic coagulation

time, reduction of the amount of platelet adhesion and degree of deformation, among other properties [7–10]. In addition to improved bioactivity, the tailored MAO layer also improves the corrosion [11–16] and tribocorrosion [17–21] behaviour by acting as a physical barrier against corrosion and wear. Moreover, it is also possible to have a further increase on tribocorrosion resistance by optimizing the electrolyte concentrations or compositions in a way to increase the rutile to anatase ratio [17–19].

Hierarchical porous surfaces have already been reported in the literature [6,22–24]. Through a one-step anodic treatment process, Xie et al. [22] obtained a multi-level porous structure with craters sized from 2 to 20  $\mu\text{m}$  that were covered by pores with 50 to 500 nm. Zhou et al. [23] obtained macro-pores in the range of 50 to 1000  $\mu\text{m}$  and micro-pores from 0.6 to 2  $\mu\text{m}$  on the surface through a two-step anodic treatment. Then some of the same authors, by a three-step anodic treatment, obtained pores with 80 to 200  $\mu\text{m}$  and with 0.6 to 2  $\mu\text{m}$  with the incorporation of bioactive elements, such as Ca, P, Si, and Na [24]. More recently, Li et al. [6] obtained surfaces with macro-pores in the range of 100 to 300  $\mu\text{m}$ , micro-pores with 3 to 10  $\mu\text{m}$ , and also submicron/nanopores in the range of 80 to 200 nm by a two-step anodic treatment.

Although macro-porous structures present many advantages as biomaterial, studies regarding their tribocorrosion performance are very scarce [21] and their wear mechanisms are yet to be fully understood. Wear studies on porous materials showed that porosity may play a beneficial role by reduced contact area, reduced third-body abrasive wear after ejection of wear debris to the pores [25], or in an aqueous environment, by promoting a self-lubricant effect [26]. However, porosity may also play a disadvantageous role due to higher effective stresses applied to the outmost surfaces [25], or due to cracks that are originated from pores [25,27].

Bio-functionalized multi-scale porous surfaces may be a promising cost-effective solution to improve bioactivity as well as corrosion and tribocorrosion resistance of Ti. Thus, the present work aimed to study the corrosion and tribocorrosion behaviour of bio-functionalized hierarchical porous surfaces obtained by a two-step anodic treatment. In the first-step, superficial macro-porosity was created and in the second-step, by MAO, a micro-porous oxide layer

was obtained with the incorporation of bio-active elements (Ca and P), in order to bio-functionalize the macro-porous surface obtained on the first-step.

## 6.2. Materials and methods

### 6.2.1. First-step anodic treatment

Prior to the anodic treatments, Ti (Grade 2) plates (20x20x2 mm) were ground down to 800 mesh with SiC papers and etched in a dilute acid mixture ( $V_{\text{HF}}:V_{\text{HNO}_3}:V_{\text{H}_2\text{O}} = 1:1:18$ ) for 5 min in an ultrasonic bath, to remove all impurities, grinding marks and the native oxide film. Cleaning was performed with propanol and distilled water in an ultrasonic bath for 10 and 5 min, respectively.

All anodic treatments were performed using a DC power supply (Agilent technologies N5772A), under agitation in a turbulent regime by using a magnetic stirrer rotating at 200 rpm in an acrylic electrochemical cell. The exposed anodic area was 1.50 cm<sup>2</sup> and a platinum sheet with an exposed area of 7 cm<sup>2</sup> was used as a cathode, positioned 8 cm away from the sample. The first-step was carried out at room temperature using 200 ml of an electrolyte mixture (pH=14) of 0.50 M sodium hydroxide (NaOH, Eka) and 0.10 M sodium nitrate (NaNO<sub>3</sub>, Sigma-Aldrich) under a constant voltage of 45 V with a limiting current of 2.60 A for 1, 2, 3, 4, and 5 minutes (Table 6.1). In order to remove the oxide products formed in the first-step and to reveal the macro-pores, the samples were etched with a dilute acid mixture ( $V_{\text{HF}}:V_{\text{HNO}_3}:V_{\text{H}_2\text{O}} = 1:1:18$ ) in ultrasonic bath for 10 min. After, the samples were ultrasonically cleaned in propanol for 10 min followed by distilled water for 5 min, and then dried with warm air.

**Table 6.1.** Groupings of samples after the first- and the second-step anodic treatment.

Duration of the first-step anodic treatment (min)	0	1	2	3	4	5
Grouping after the first-step anodic treatment	Ti	Ti_1	Ti_2	Ti_3	Ti_4	Ti_5
Grouping after the second-step anodic treatment	Ti_MAO	Ti_1MAO	-	Ti_3MAO	-	-

Pore size distribution was obtained by measuring the diameters of the pores on 9 images of 1.14 x 0.86 mm frames captured from each 3 different samples per each group. Considering the pores size distribution and morphology, just the groups treated for one and three minutes were chosen for the second-step anodic treatment.

Superficial area (the area exposed to electrolyte on corrosion tests) was calculated on optical microscope (OM, Leica DM2500) images using

ImageJ 1.51j8 software through 3 combined cross-sections images per group with a total area of 0.20 cm<sup>2</sup>. The superficial area obtained for Ti\_1 was 0.47 cm<sup>2</sup> and for Ti\_3 was 0.51 cm<sup>2</sup>. These areas were used for normalizing electrochemical data.

### 6.2.2. Second-step anodic treatment under MAO regime

The second-step anodic treatment was performed under MAO regime using 200 ml of a mixture of 0.02 M of  $\beta$ -glycerophosphate disodium salt pentahydrate ( $\beta$ -GP, Alfa Aesar) and 0.35 M of calcium acetate monohydrate (CA, Sigma-Aldrich) electrolyte. This electrolyte was chosen in order to incorporate bio-active species, namely P (from  $\beta$ -GP) and Ca (from CA). The treatment was performed at room temperature under a constant voltage of 300 V with a limiting current of 2.60 A during 1 min. The setup was the same as the one used on the first-step, including the electrochemical cell, cathode, exposed areas, and power supply. Finally, the samples were ultrasonically cleaned in distilled water for 5 min and then dried with warm air. This second-step was identified by MAO on sample grouping presented on Table 1.

The topography, microstructure and chemical composition of the modified surfaces were analysed by FEI Nova 200 field emission gun scanning electron microscope (FEG-SEM) equipped with energy dispersive X-ray spectroscopy (EDS). EDS analysis was performed at an accelerating voltage of 15 keV, using conventional ZAF correction procedure included in the EDAXPegasus software. Crystalline structure was characterized by XRD (Cu K $\alpha$  radiation, Bruker D8 Discover) with a scanning range ( $2\theta$ ) of 20° to 100°. The phase percentage of the oxide layer obtained by MAO was calculated by following Equation (6.1):

$$\% phase_{\alpha} = \frac{\sum I_{\alpha peaks}}{\sum I_{all peaks}} \times 100 \quad (6.1)$$

In order to obtain cross-section images by OM, the samples were embedded in a hard-resin, cut with a diamond disc, ground with 1200 mesh SiC papers, and polished with a colloidal silica suspension (Struers, OP-S) down to 0.04 mm. Surface roughness measurements were carried out by a non-contact profilometer (Veeco Dektak 150). In total, 10 profiles (2 mm in length) were taken per each condition, on different samples to calculate the average roughness

values ( $R_a$ ). In the case of macro-porous samples, the roughness values were taken from the outermost surfaces.

### 6.2.3. Wettability

Hydrophilicity of each group was examined by contact angle measurements through a sessile drop method using an optical tensiometer Theta Lite controlled by OneAttension software. C.a. 5  $\mu$ l droplet of ultra-pure water was dropped on the surface and the contact angle was considered after 10 s. The evaluation was performed at room temperature in air. Five different samples per group were analysed with three valid measurements per sample. One-way analysis of the variance (ANOVA) followed by Tuckey test was used in order to access the differences in the variance within the groups after the first- and the second-step anodic treatments, using a significance level of  $p < 0.05$ .

### 6.2.4. Corrosion tests

Corrosion tests consisted of open circuit potential (OCP) measurement and potentiodynamic polarization were performed using a three-electrode setup at body temperature ( $37 \pm 2$  °C) in 200 ml NaCl solution (9 g/l). Samples with geometric exposed area of 0.38 cm<sup>2</sup> were used as working electrode (WE), a Pt electrode was used as a counter electrode (CE), while a saturated Ag/AgCl electrode was used as a reference electrode (RE). All the potentials were given with respect to saturated Ag/AgCl electrode. Corrosion tests were performed with a Reference 600+ potentiostat/galvanostat/ZRA from Gamry Instruments. OCP was monitored for a period of 180 minutes to evaluate the corrosion potential of the material in contact with the electrolyte and to stabilize the system. The system was considered stable if OCP values did not present a variation higher than 60 mV in the last hour of measurement. Potentiodynamic polarization tests were performed from -0.25 V to 1.50 V using a scanning rate of 0.50 mV/s. At least three samples were evaluated per group in order to assure the reproducibility.

### 6.2.5. Tribocorrosion tests

Tribocorrosion tests were carried out in a tribo-electrochemical cell, containing 25 ml of NaCl solution (9 g/l) at  $37 \pm 2$  °C. The cell was installed in a tribometer with a reciprocating ball-on-disk configuration (CETR-UMT-2), against

an alumina ball with 10 mm of diameter (Ceratec). A three-electrode configuration (RE-Ag/AgCl, CE-Pt, and WE-samples) connected to a Reference 600 potentiostat/galvanostat/ZRA from Gamry Instruments was used for the tribo-electrochemical measurements. Before sliding, the samples were immersed for 180 minutes in the electrolyte in order to stabilize the system. OCP values were monitored before, during, and after sliding. Coefficient of friction (COF) values were also monitored during sliding. Tribocorrosion tests were performed with a total stroke length of 3 mm, frequency of 1 Hz, normal load of 0.50 N (corresponding to a maximum Hertzian contact pressure of 330 MPa for Ti) and total sliding time of 60 min. All groups had at least three tests in order to assure the reproducibility. After each tribocorrosion test, the electrolyte was collected, stored in 2 ml plastic container and kept at 4 °C for posterior analyses. The released ions of Ti, Ca and P was quantified by inductively coupled plasma-atomic emission spectrometer (ICP-AES, Horiba Jobin-Yvon Ultima). Three measurements were performed for each group, however for Ti quantification, in the groups after the second-step, only two numeric ion concentration values were obtained due to a detection limit of 1 µg/l.

### 6.3. Results and discussion

#### 6.3.1. First-step anodic treatment

Figure 6.1a presents a macro-pore formed after 2 minutes of the first-step anodic treatment. The formation of macro-pores covered by oxides (corrosion products) may be explained by the pitting mechanism that Ti suffers randomly across the surface, as a result of the corrosion capacity of  $NO_3^-$  and its predisposition to react with bulk Ti [6,28]. Previously, Zhou et al. [23] suggested that  $OH^-$  promotes the reaction of  $NO_3^-$  with Ti, in this way, a higher amount of  $OH^-$  leads to higher amount of macro-pores due to the formation of more pitting sites on the surface. The first-step anodic treatment was only applied to form macro-pores, and this treatment is known to not to affect the outmost surface [6]. The oxides or corrosion products formed on the macro-pores were removed after etching in a dilute acid mixture (Figure 6.1b and 6.1c).



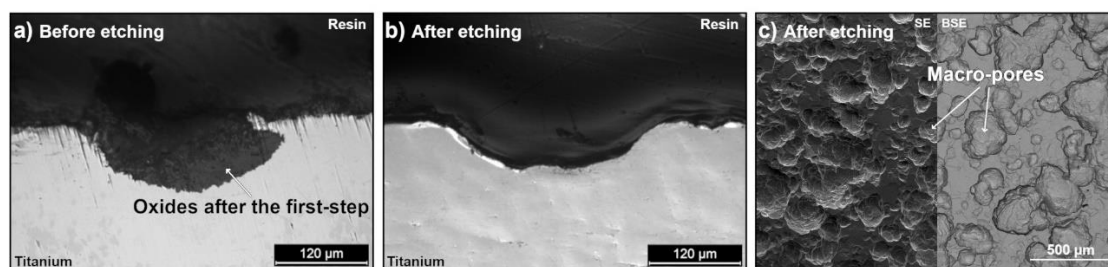


**Figure 6.1.** a) and b) OM images of the cross-sections after first step of anodic treatment before and after etching, respectively and c) secondary electron (SE) and backscattered electron (BSE) SEM images of the porous surface after etching.

The morphology and distribution of the pores can be seen on the OM images given in Figure 6.2 with the respective time of the first-step anodic treatment. The samples shown in Figure 6.2 were slightly polished with 4000 mesh SiC paper to improve the contrast between the macro-pores and the outmost surface in order to reveal the morphology of the macro-pores. With the increasing time, pores grew larger in all directions and became interconnected. All conditions presented a homogeneous distribution of macro-pores through all surface which is in accordance with the literature [6,23,24] stating that a NaOH concentration of 0.50 M in the electrolyte was suitable to obtain a homogeneous distribution of macro-pores.

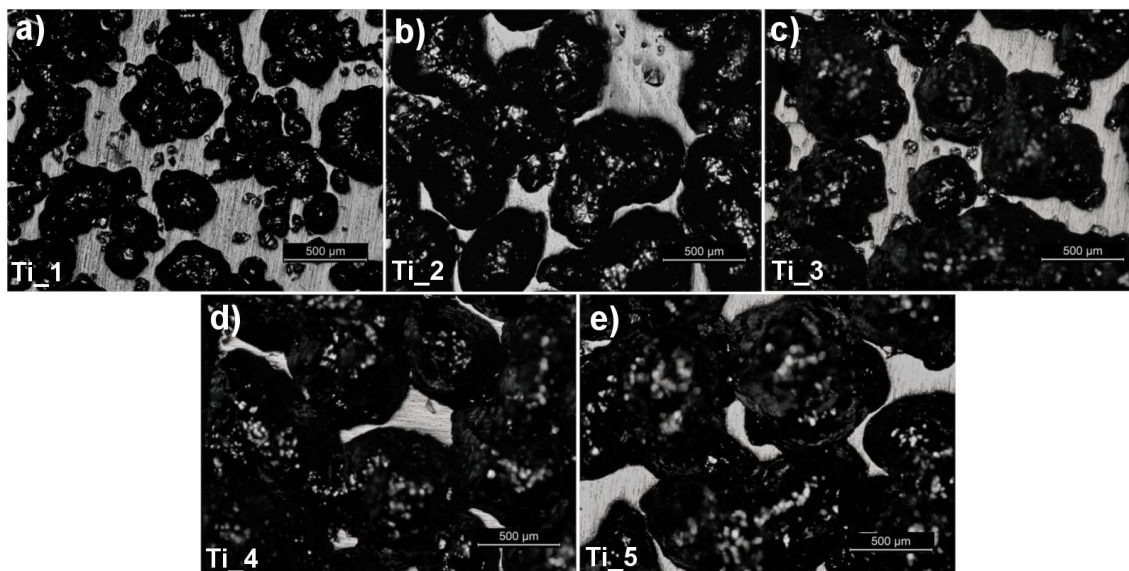


**Figure 6.2.** OM images after the first-step anodic treatment performed for a) 1, b) 2, c) 3, d) 4 and e) 5 minutes.

Pore size distribution after the first-step anodic treatment is presented in Figure 6.3 together with the percentage of superficial macro-porosity and average pore size values. With the increasing time, the pore size distribution was shifted to higher values of pore dimensions due to more time given to the macro-pores

to be enlarged. Consequently, both the average pore size and surface porosity increased with treatment time. An optimum pore size or pore size distribution are still undefined but it is known that if the pores are very small, cells may not migrate inside of the pores and if the pores are too big, cell attachment may be difficult [29]. Pores around 100  $\mu\text{m}$  is reported to facilitate optimal attachment for cell proliferation, differentiation, and bone remodelling [30,31]. On the other hand, macro-pores in the range of 300-600  $\mu\text{m}$  are also required, especially to facilitate the bone formation, bone ingrowth, and vascularization [32–34]. When the first-step was performed for more than three minutes, the favourable range of pores stated before was lost. Thus, Ti\_4 and Ti\_5 were discarded due to the presence of pores with dimensions well above to the ones intended. Within the remaining groups, Ti\_1 and Ti\_3 were selected to carry forward representing the surfaces having mostly isolated round pores and mostly interconnected porosity, respectively. Eventually, the second-step anodic treatment, MAO, was only performed on three groups: Ti as control, Ti\_1, and Ti\_3.

The average depth of the pores for Ti\_1, and Ti\_3 groups was accessed, and the values were  $74 \pm 23 \mu\text{m}$  and  $149 \pm 48 \mu\text{m}$ , respectively. Consequently, the mass loss after Ti\_1 was lower than Ti\_3 ( $11 \pm 3 \%$  and  $16 \pm 3 \%$ , respectively) due to a lower number of pores with smaller dimensions.

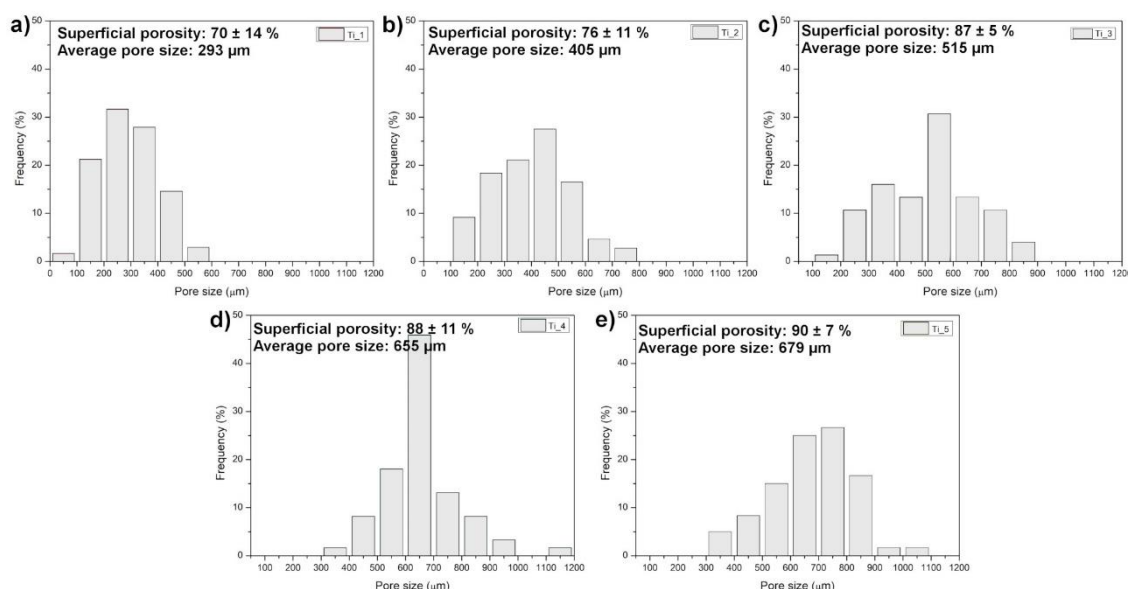
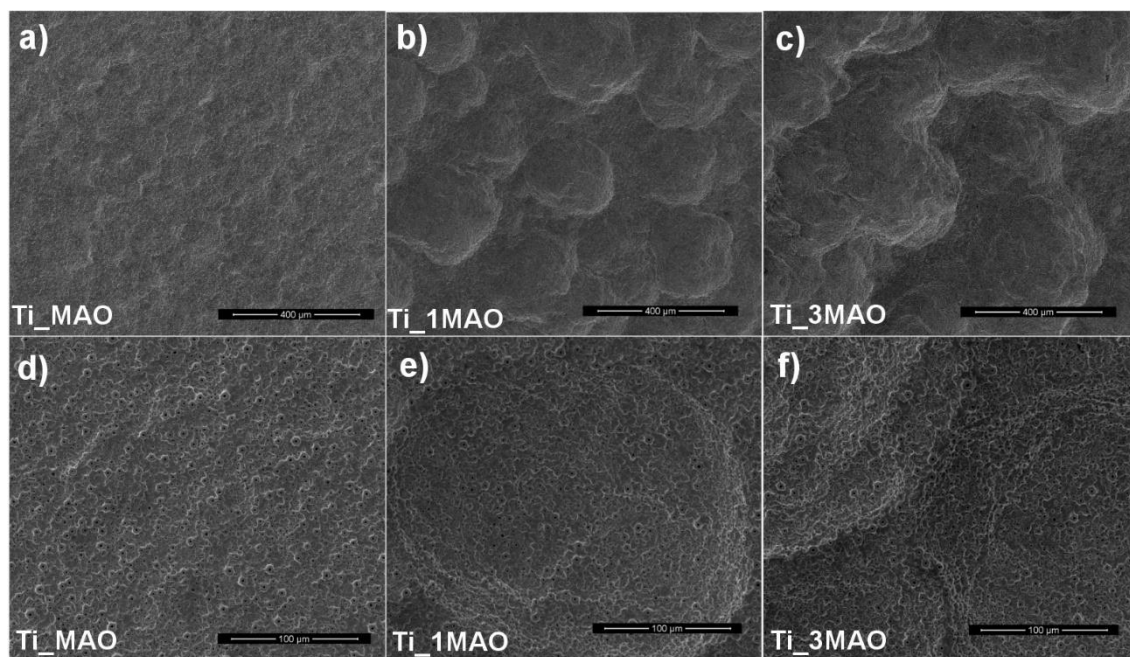


Figure 6.3. Pore size distribution after the first-step anodic treatment for Ti\_1 to Ti\_5 groups, respectively

### 6.3.2. Second-step anodic treatment under MAO regime

After the second-step anodic treatment (MAO), surfaces were covered by a uniform micro-porous anodic layer with the typical volcano-like structure, as shown in the SE SEM images presented in Figure 6.4a to 6.4c, and in more detail in Figure 6.4d to 6.4f. No discontinuities or differences in morphology were observed between the pore surfaces and the outmost surfaces.



**Figure 6.4.** Representative SE-SEM images obtained after the second-step anodic treatment for Ti\_MAO (a and d), Ti\_1MAO (b and e), and Ti\_3MAO (c and f).

The cross-sectional morphology of Ti\_MAO, Ti\_1MAO, and Ti\_3MAO groups are shown in Figure 6.5a, b and c, respectively, revealing a similar oxide layer with a thickness of  $5.20 \pm 1.00 \mu\text{m}$ ,  $5.27 \pm 1.26 \mu\text{m}$ , and  $5.41 \pm 1.06 \mu\text{m}$ , respectively. Alves et al. [35] had previously presented the detailed cross section of a MAO layer obtained with the same processing parameters on a bulk Ti, having a triplex structure composed of a compact and thin layer next to the bulk material followed by an inner porous layer having small pores and an outer porous layer having bigger pores.

During MAO process, the applied voltage exceeded the dielectric breakdown of the oxide layer and a micro-porous structure was formed because of the micro-arc discharges [36]. The initial moments were attributed to the formation of a thin and compact oxide layer. Then, as a result of the higher applied voltage, the oxide layer started to get thicker as a consequence, the measured

current dropped to lower values [6]. The evolution of current during the MAO treatment did not reveal significant differences between the testing groups (Figure 6.5d). These results confirmed that the macro-pores formed at the first-step did not have a noticeable effect on the micro-porous oxide layer formed at the second-step. Furthermore, no significant differences in the cross-section morphology or thickness were observed between the oxide layer inside and out of the pores.

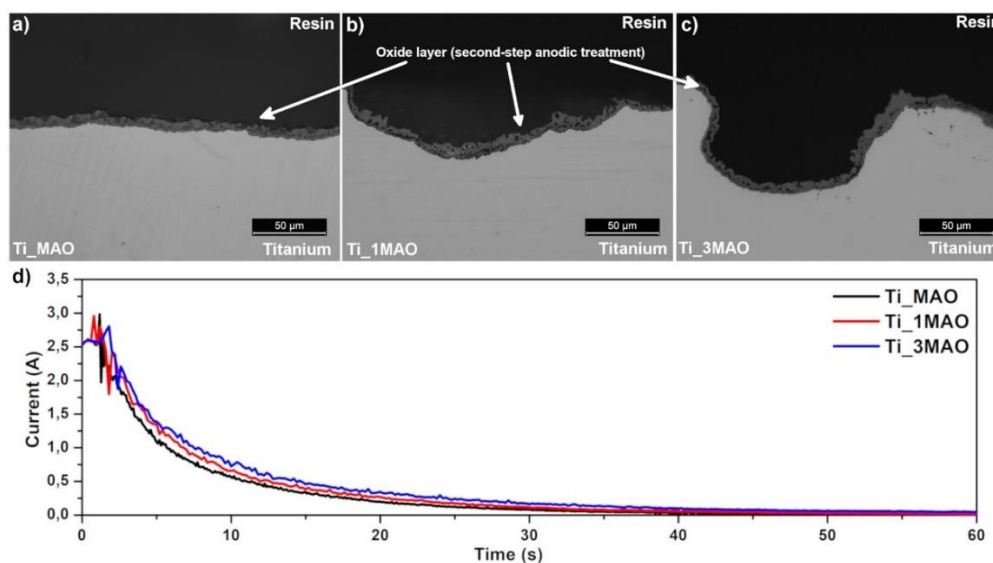


**Figure 6.5.** Cross-sectional OM images of a) Ti\_MAO, b) Ti\_1MAO, and c) Ti\_3MAO, and d) respective current evolution during MAO treatment.

Due to localized melting of the oxide, Ca and P elements presented in the electrolyte were incorporated in the micro-porous anodic layer [19], giving a bio-function since they are the main constituents of bone [37]. Figure 6.6a shows the EDS spectra of MAO treated groups, confirming the incorporation of Ca and P during MAO treatment. The Ca/P as atomic ratio was  $2.91 \pm 0.13$ ,  $2.99 \pm 0.15$ , and  $2.99 \pm 0.11$  for Ti\_MAO, Ti\_1MAO, and Ti\_3MAO, respectively. In the bone, the stoichiometric atomic ratio of Ca/P for hydroxyapatite (HA) is about 1.67 [37]. It was favourable to have Ca/P ratio above the one in HA since Ca presents a faster dissolution than P [38–40].

The XRD patterns of MAO treated groups are shown in Figure 6.6b where characteristic peaks of Ti and TiO<sub>2</sub> (as anatase and rutile) were obtained as in accordance with the literature [17,21,35]. The percentage of anatase and rutile phases were calculated by Equation (6.1) and the results showed around 70 % of anatase and 30 % of rutile for all the conditions. A mixture of anatase and rutile

may play an important role on the tribocorrosion behaviour and biological properties of the implant. It is well reported that MAO treatment improves the wear resistance of Ti, mainly attributed to the increase in hardness due to the presence of mixture of hard anatase and rutile phases [14,17–19]. Hardness of anatase and rutile are around 8 and 17 GPa, respectively [41]. Oliveira et al. [19] studied similar structures on bulk Ti surfaces and reported that anatase was evenly distributed through all the surface while rutile was mostly presented at higher zones around the micro-pores with volcano-like structures. Recently, Alves et al. [7] showed that bio-functionalization process by MAO, with the same parameters used in the second-step anodic treatment described in this work, improved adhesion and proliferation of NIH/3T3 cells when compared to untreated Ti due to chemical composition, nature of the TiO<sub>2</sub> films (a mixture of anatase and rutile), and topography of the anodic layers formed by MAO.

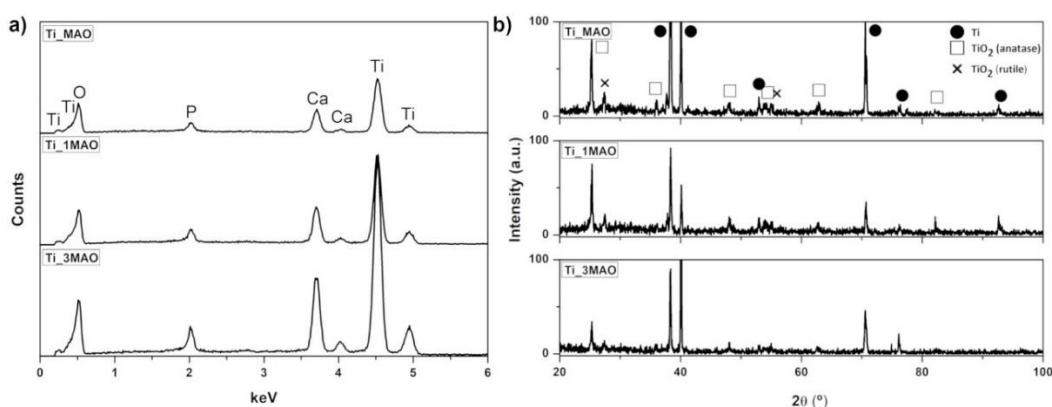


**Figure 6.6.** a) EDS and b) XRD spectra after the two-step anodic treatment.

### 6.3.3. Roughness

Another important surface characteristic influencing the interactions between the implant and the biological material is surface roughness. After the first-step anodic treatment, the acid etched surfaces (just before MAO treatment) presented Ra values of  $1.48 \pm 0.35 \mu\text{m}$ ,  $1.47 \pm 0.78 \mu\text{m}$ , and  $1.41 \pm 0.89 \mu\text{m}$  for Ti, Ti<sub>1</sub>, and Ti<sub>3</sub>, respectively. After the MAO treatment, a slight increase on Ra values was observed, leading to values of  $1.88 \pm 0.49$ ,  $1.85 \pm 0.52 \mu\text{m}$ , and  $1.90 \pm 0.60 \mu\text{m}$  for Ti\_MAO, Ti\_1MAO, and Ti\_3MAO, respectively. These results suggest that the roughness created by etching governed the global roughness after two-step treatment. For biomedical applications, the material response does not necessarily depend on the degree of the surface roughness but rough

surfaces usually presents better biological response [42,43] since cell growth and a better adsorption of proteins can be promoted by an increase in the surface area available for cells [43].

#### 6.3.4. Wettability

Wettability may control four important phenomena between the biological organisms and the surface: adhesion of proteins and other macro-molecules, hard and soft tissue cell interactions, adhesion of bacteria and bio-film formation, and rate of osteointegration [44]. Therefore, wettability of the treated surfaces was defined and the results of the contact angle measurements are presented in Figure 6.7, together with the representative images for each group under water contact angle evaluation test. After the first-step, the average values of contact angle for Ti, Ti\_1, and Ti\_3 were  $71 \pm 9^\circ$ ,  $80 \pm 8^\circ$ , and  $70 \pm 7^\circ$ , respectively. These values pointed a less hydrophilic behaviour after the first-step. Statistical analysis was performed in order to access if the type of porosity influenced the wettability within the groups after the first-step anodic treatment. Results showed statistically significant differences for the values obtained for Ti\_1 as compared to Ti and Ti\_3, indicating that the type of macro-porosity had an effect on the wettability. When the macro-pores were mostly isolated (Ti\_1), the contact angle was higher, and consequently, the wettability decreased when compared with the control group. But, if the interconnected porosity increased, then the wettability increased, and the value was closer to the one found in the control group, Ti. After the second-step, Ti\_MAO, Ti\_1MAO, and Ti\_3MAO presented average contact angles of  $26 \pm 9^\circ$ ,  $27 \pm 8^\circ$ , and  $19 \pm 11^\circ$ , respectively. These values showed that a shift for the hydrophilic regime occurred after the second-step, due to chemical as well as topographical changes on the surface, with the formation of a micro-porous oxide layer. Regarding the MAO groups, there were no statistically significant differences in the average values between the testing groups.

A hydrophilic surface is more prone to interact with the fluids in a biological environment, promoting protein adsorption to the surface, while a hydrophobic one can promote the entrapment of air bubbles that can affect the interaction between the surface and the proteins or the cells, leading to a worse adsorption or adhesion/activation, respectively [44]. Therefore, the second-step anodic



treatment under MAO regime may also promote beneficial interactions in a biological environment by transforming the surfaces from hydrophobic to hydrophilic.

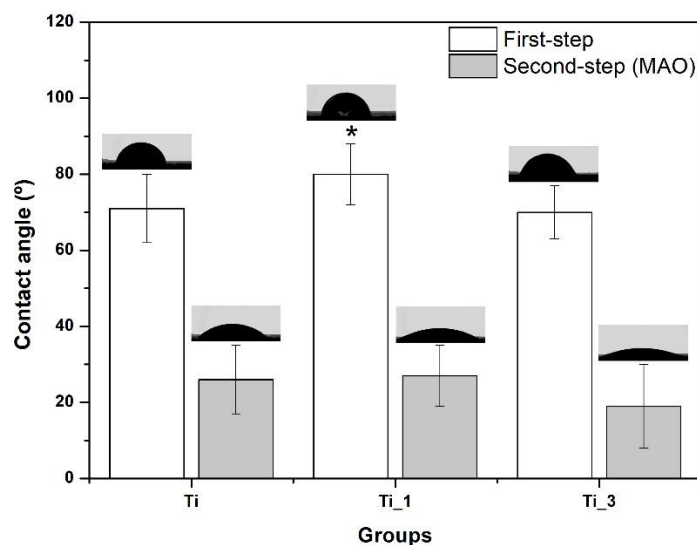


**Figure 6.7.** Contact angle values for each group and the respective representative images (\*Significant difference within the first-step group ( $p < 0.05$ )).

### 6.3.5. Corrosion behaviour

Figure 6.8 shows the representative potentiodynamic polarization curves for all groups and Table 6.2 gives the average values for open circuit potential ( $E_{OCP}$ ), corrosion potential ( $E_{(i=0)}$ ) and passivation current density ( $i_{pass}$ ). All polarization curves exhibited a direct transition from the active region to passive region. It was also possible to see a well-defined passivation plateau for Ti (starting around 0.25 V), that was not lost after the first-step. There was no significant difference between Ti and porous surfaces of Ti<sub>1</sub> and Ti<sub>3</sub> as also can be seen more clearly on  $E_{OCP}$ ,  $E_{(i=0)}$ , and  $i_{pass}$  values presented in Table 6.2, thus, it can be stated that the corrosion behaviour was not affected significantly by the macro-porosity obtained after the first-step. It was clear that the corrosion resistance was improved after the second-step (MAO) since it can be observed that the polarization curves in Figure 6.8 shifted to the left-upper area of the graph, exhibiting lower values of current density as well as higher corrosion potential as it is confirmed in Table 6.2. There were no significant differences between Ti<sub>MAO</sub>, Ti<sub>1MAO</sub>, and Ti<sub>3MAO</sub> on  $i_{pass}$  (values considered at 0.60 V),  $E_{OCP}$ , or  $E_{(i=0)}$ . Improvement of corrosion behaviour after MAO had already been reported in the literature for dense Ti and Ti6Al4V surfaces and it was attributed

to the formation of oxide layers with higher corrosion resistance, mainly by the contribution of the barrier layer that was formed in the MAO treatment [14,19,35].

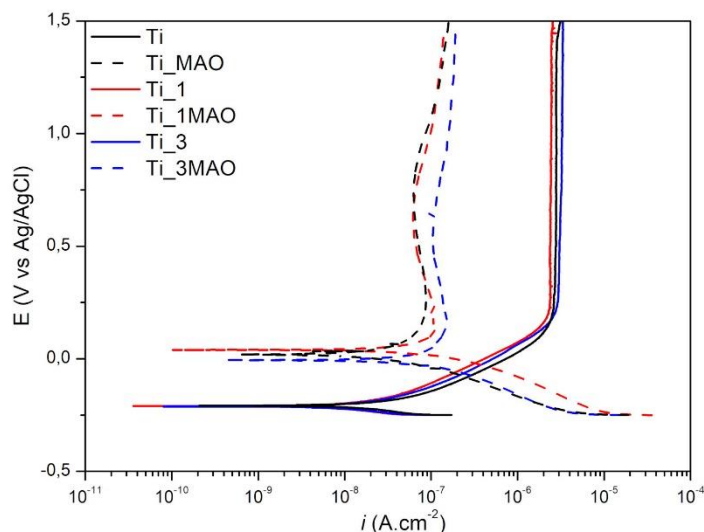


**Figure 6.8.** Potentiodynamic polarization curves before (Ti\_1 and Ti\_3) and after (Ti\_1MAO and Ti\_3MAO) the second-step anodic treatments, in comparison with their control groups (Ti and Ti\_MAO, respectively).

**Table 6.2.** Open circuit potential ( $E_{OCP}$ ), corrosion potential ( $E_{(i=0)}$ ), and passivation current density ( $i_{pass}$ ) values for all testing groups.

	Ti	Ti_1	Ti_3	Ti_M AO	Ti_ 1MAO	Ti_3 MAO
$E_{OCP}$ (V)	-0.16 ± 0.03	-0.20 ± 0.05	-0.17 ± 0.05	0.36 ± 0.05	0.34 ± 0.06	0.38 ± 0.08
$E_{(i=0)}$ (V)	-0.20 ± 0.05	-0.15 ± 0.06	-0.23 ± 0.01	0.01 ± 0.03	0.04 ± 0.02	0.00 ± 0.01
$i_{pass}$ ( $\mu Acm^{-2}$ )	2.97 ± 0.63	2.37 ± 0.34	2.92 ± 0.53	0.06 ± 0.02	0.07 ± 0.02	0.09 ± 0.02

### 6.3.6. Tribocorrosion behaviour

Figure 6.9 presents the representative OM and SEM images of the worn sample and counter-body surfaces, together with the EDS spectra taken from the worn counter-body surfaces after the first- and the second-step anodic treatment. Parallel grooves to the sliding direction were dominant on the samples tested after the first-step anodic treatment, which is a characteristic feature of abrasive wear. MAO treated samples presented smaller worn areas (more evident on the OM images) and less visible wear damage (more evident on the SEM images) compared to samples tested after the first-step anodic treatment. Additionally, SEM images revealed oxidized patches formed due to repetitive transfer of material between the two mating surfaces, as well, loose oxidized wear debris in



the macro-pores. In MAO treated samples, both worn and unworn areas can be seen on the wear tracks since the counter-body was carried by the most protruded surfaces. On the other hand, material transfer from samples to the counter-body (alumina ball) was confirmed for all conditions, evidenced by EDS spectra taken from the worn counter-body surfaces.

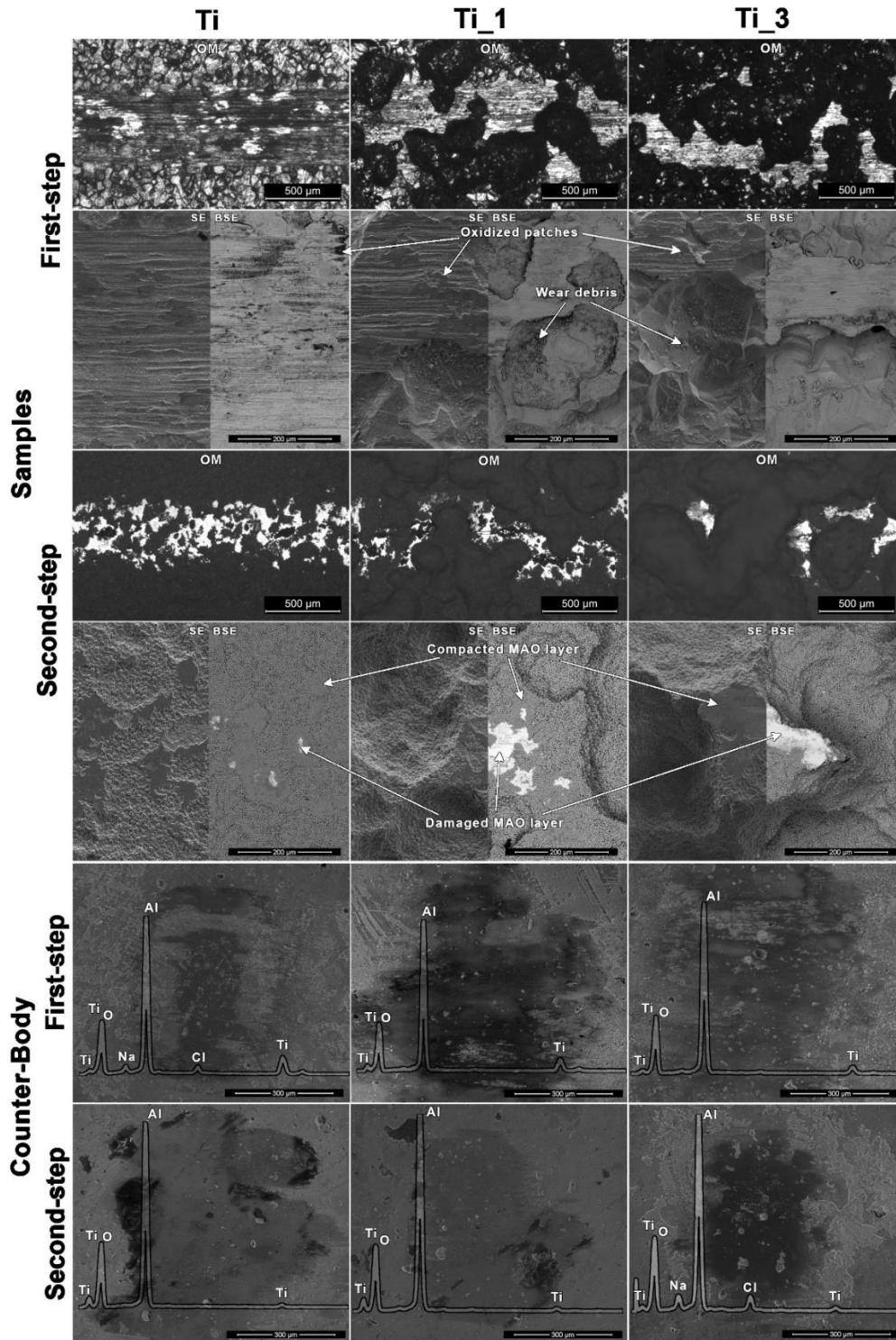


**Figure 6.9.** OM and SEM images of the worn sample surfaces, together with the SEM images and the respective EDS spectra taken from the worn counter-body surfaces after the first- and the second-step anodic treatments.

BSE SEM images taken from Ti\_1MAO sample presented in Figure 6.10 gives a closer look to the worn MAO-treated surfaces, showing some typical key worn surface features observed on all MAO treated surfaces, together with the respective EDS spectra. As it can be seen on Figures 6.10a and 6.10b, the zones

marked as Z1, Z3, and Z6 presented different atomic contrast, pointing severe local damage on the MAO layer, as also evidenced by the EDS spectra where no distinguishable peaks of Ca and/or P were registered. Nevertheless, some differences were observed within these three zones as Z1 and Z6 presented sharp grooves or scratches parallel to the sliding direction, Z3 presented an uneven morphology. In Z2 and Z7 the outmost part of the MAO layer was damaged due to contact with the counter-body and these zones presented a smooth surface with some areas presenting a darker tone that were probably the micro-pores being filled with wear debris. In Z4, the oxide layer was only partially damaged, and Ca and P peaks were still presented in the EDS spectra (Figure 6.10c). The zones marked as Z5 and Z8 represented unaffected areas, where the structure was not changed and therefore similar morphology and similar EDS spectra were observed to the ones already shown in Figure 6.4d and Figure 6.6a, respectively.

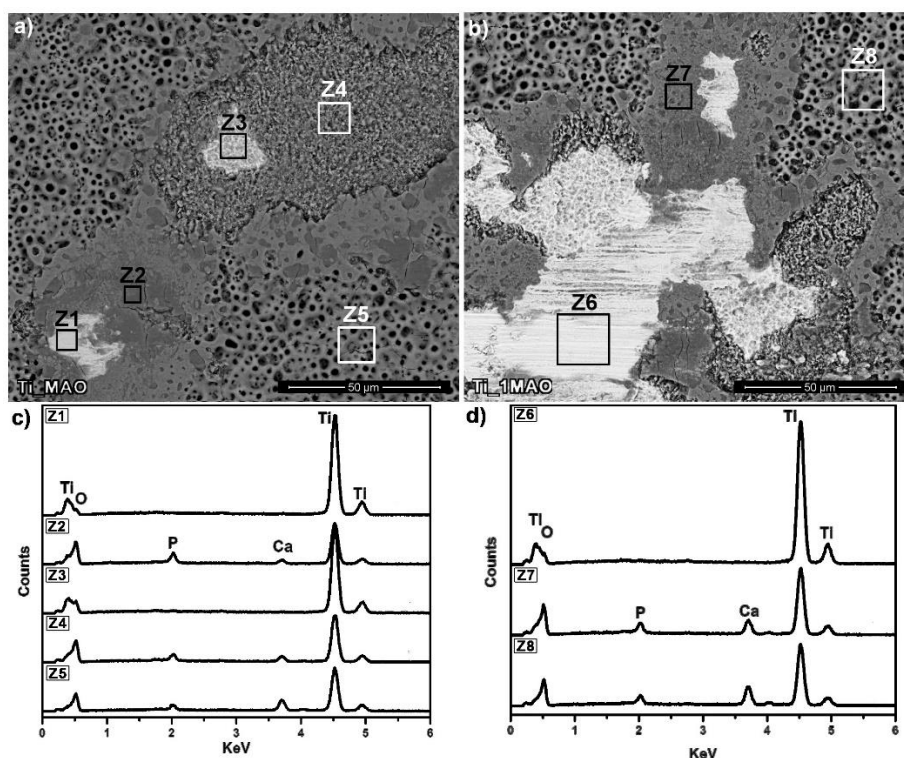


**Figure 6.10.** Higher magnification SEM images of the worn surfaces after the second-step anodic treatment (a and b), together with EDS spectra taken from the marked zones (c and d).

The evolution of OCP before, during, and after sliding together with the evolution of COF during sliding are presented in Figure 6.11. As general, groups before (Figure 6.11a) and after (Figure 6.11b) the second-step anodic treatment exhibited significantly different behaviour. Before sliding Ti, Ti<sub>1</sub>, and Ti<sub>3</sub>

presented stable and very similar potential values due to the presence of the native oxide film. This film was immediately damaged with the starting of sliding as it was evident by a sharp decrease in OCP values. The lowest OCP values were observed on the run-in period and afterwards, OCP values increased and remained relatively stable for the remaining time of sliding. During sliding, simultaneous increases and decreases were observed in both OCP and COF values that were more pronounced on Ti as compared to the porous samples. These variations on OCP and COF can be linked with the adhered oxidized patches. In the presence of macro-pores, some part of the wear debris was ejected into the pores resulting with less dense oxidized patches on the worn Ti<sub>1</sub> and Ti<sub>3</sub> surfaces, as compared to Ti (Figure 6.9). On Ti, on the absence of the macro-pores, it was possible that adhered oxidized patches got denser during sliding time, however, after getting a certain thickness, these wear debris might be broken by the counter-body. As patches were getting thicker, due to their physical barrier role, they can give a limited protection against corrosion, that can explain the local increments on OCP. In the same time, as they were getting thicker, surface roughness was also getting higher, therefore simultaneous increments on COF values were recorded [45].

After the second-step anodic treatment, all groups presented an improvement on the tribocorrosion behaviour, characterized by higher OCP values under sliding, together with more stable COF values (Figure 6.11). It was also observed that within the MAO-treated groups, an increase in macro-porosity led to lower OCP values under sliding, with OCP values slightly decreasing as sliding proceeded. Considering that there were no significant differences in terms of morphology, chemical and phase composition between the MAO layers for each condition, and that there were no significant differences on the corrosion behaviour from potentiodynamic polarization curves, it is reasonable to assume that these differences were related to the distinct tribological contact due to different levels of macro-porosity. As the level of macro-porosity increased, the contact area with the counter-body decreased, leading to higher local contact pressures on the contact zones. In this way, higher contact pressures translated into higher mechanical damage on the contact points with the counter-body. On the other hand, since the contact with the counter-body was only on the protruded

hard oxide zones on the MAO-treated surfaces, more stable evolution of COF values was observed.

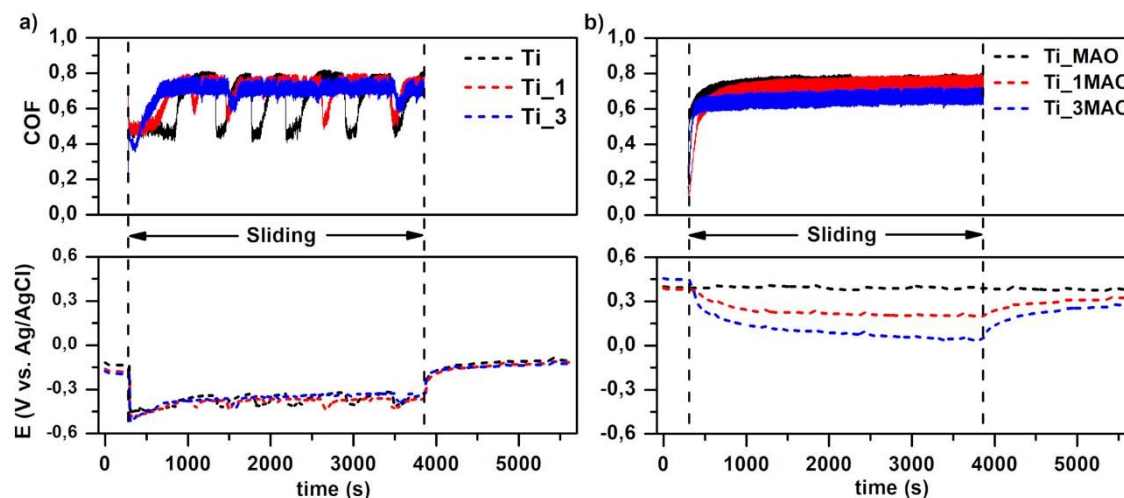


**Figure 6.11.** Evolution of OCP before, during and after sliding on the samples before (a) and after the second-step anodic treatments (b), with the respective COF values.

Metal ion release in the body may significantly alter several biological processes like osteoblastic cell viability and apoptosis as well as regulation of bone resorbing mediators [46]. The average ICP-AES results of the Ti ion concentration in the electrolyte after the tribocorrosion tests for Ti, Ti<sub>1</sub>, and Ti<sub>3</sub> groups were 0.06, 0.10, and 0.11 mg/l, respectively. After the second-step, the results obtained for Ti ion concentration were 0.01, 0.02, and 0.03 mg/l for Ti<sub>MAO</sub>, Ti<sub>1MAO</sub>, and Ti<sub>3MAO</sub>, respectively. Results showed that metal ion release after the second-step anodic treatment was much lower than the one after the first-step. Decreased metal ion release on the bio-functionalized porous surfaces indicated that the oxide layer formed on the second-step protected the metal substrate. ICP-AES results for Ca ion concentration were 1.39, 1.54, and 1.92 mg/l, for Ti<sub>MAO</sub>, Ti<sub>1MAO</sub>, and Ti<sub>3MAO</sub>, respectively, whereas the values obtained for P ion concentration were 0.41, 0.46, and 0.66 mg/l for Ti<sub>MAO</sub>, Ti<sub>1MAO</sub>, and Ti<sub>3MAO</sub>, respectively. These results suggest that as the level of macro-porosity increased, the released amount of ions increased most probably due to the increased damage given at the contact zones due to the higher local contact pressures.

### 6.3.7. Tribocorrosion mechanisms

The tribocorrosion mechanisms proposed based on the microstructural, electrochemical, and tribo-electrochemical analysis of the worn surfaces are illustrated in Figure 6.12. Due to high reactivity of Ti, as well as due to its low tensile and shear strength, during sliding, micro-fractures may occur on the surface and consequently, large amounts of metal may be pulled out (adhesive wear) [47]. As sliding proceeds, pulled-out debris can be work hardened, as well, can be mixed with the oxidized wear debris (third-bodies). Afterwards, these mixed debris can be compacted on the worn surfaces, forming oxidized patches, whereas some of these debris may adhere on counter-body surfaces (Figure 6.9) that can abrade the metal leading to the formation of grooves on the worn surfaces (Figure 6.9), or move freely on the sliding surfaces, acting as third-body particles (Figure 6.12a). As also discussed above, it is suggested that oxidized patches gave a limited protection against corrosion, but as well, led to an increase in COF values. Evolution of COF and OCP values during sliding suggested that thickening and removal of the oxidized patches repeated several times during sliding.

After the first-step anodic treatment, similar mechanisms were also observed on the macro-porous surfaces, however, oxidized patches were less dense and the effect of third-body abrasive wear was reduced due to ejection of wear debris into the macro-pores, but at the same time, higher local contact pressures on the contact surfaces seemed to increase the severity of abrasive wear (Figure 6.12b).

Figure 6.12c presents the proposed wear mechanism for the MAO treated Ti surfaces. As discussed above with the detailed SEM images, local damages were observed on the most pultruded zones of the MAO layer that had direct contact with the counter-body. A similar mechanism was also observed on the samples after two-step anodic treatment (Figure 6.12d). Due to the reduced contact area of the macro-porous surfaces, which was further reduced by the increased roughness of the anodic layer, higher contact pressures were obtained on the contact zones leading to more severe local damage, evidenced mainly by lower OCP under sliding, as compared to Ti\_MAO samples. Ti\_1MAO, and Ti\_3MAO samples presented a gradual decrease in OCP values during sliding,

suggesting a gradual increase on the damage given to the MAO layer, whereas overall lower OCP values were observed on Ti\_3MAO samples. Even though, it is worthy to stress that Ti\_3MAO samples still exhibited better tribocorrosion behaviour as compared to the samples after the first-step anodic treatment in terms of less visible total wear damage, less amount of released metallic ions and more positive OCP values during sliding.

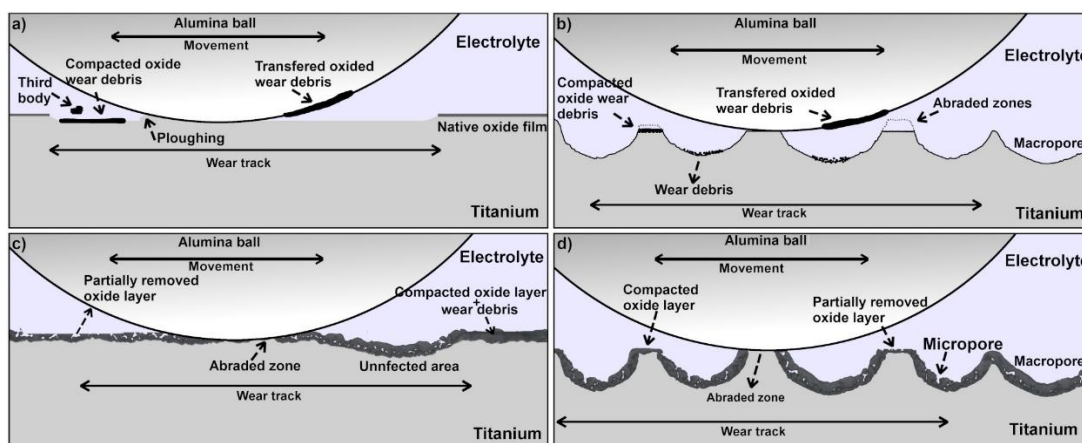


Figure 6.12. Schematic draws of the suggested tribocorrosion mechanisms for a) Ti, b) Ti after the first-step, c) Ti after the second-step, and d) Ti after two-step anodic treatments.

#### 6.4. Conclusions

A fast and simple two-step anodic treatment was used to obtain a macro-porous surface structure covered with a micro-porous Ca- and P-rich anodic layer. By increasing the treatment time of the first-step anodic treatment, bigger and more interconnected macro-porosity was obtained. After the second-step anodic treatment by MAO, multi-scale (micro/macro) porous surfaces exhibited a lower tendency to corrosion and more stable COF values under sliding, together with improved wettability. Therefore, this two-step anodic treatment can be considered as a versatile and low-cost technique to obtain multi-scale porous surfaces having potential of improved bio-activity and mechanical interlocking, along with their improved resistance to tribocorrosion. Nevertheless, before considering this treatment for biomedical implants, biomechanical stability and biological response of these surfaces should be explored.





## References

- [1] Medical Implants Market- Global Opportunity Analysis and Industry Forecast, 2014 - 2022, (2016) 216.
- [2] A. Nouri, Titanium foam scaffolds for dental applications, in: *Met. Foam Bone*, Woodhead Publishing Limited, 2017: pp. 131–160.
- [3] G. Manivasagam, D. Dhinasekaran, A. Rajamanickam, Biomedical Implants: Corrosion and its Prevention - A Review, *Recent Patents Corros. Sci.* 2 (2010) 40–54.
- [4] M. Bruschi, D. Steinmüller-Nethl, W. Goriwoda, M. Rasse, Composition and Modifications of Dental Implant Surfaces, *J. Oral Implant.* (2015) 1–14.
- [5] F.A. España, V.K. Balla, S. Bose, A. Bandyopadhyay, Design and fabrication of CoCrMo alloy based novel structures for load bearing implants using laser engineered net shaping, *Mater. Sci. Eng. C.* 30 (2010) 50–57.
- [6] Y. Li, W. Wang, J. Duan, M. Qi, A super-hydrophilic coating with a macro/micro/nano triple hierarchical structure on titanium by two-step micro-arc oxidation treatment for biomedical applications, *Surf. Coatings Technol.* 311 (2017) 1–9.
- [7] A.C. Alves, R. Thibaux, F. Toptan, A.M.P. Pinto, P. Ponthiaux, B. David, Impact of bio-functionalization on NIH/3T3 adhesion, proliferation and osteogenic differentiation of MC3T3-E1 over highly porous titanium implant material, *J. Biomed. Mater. Res. Part B - Appl. Biomater.* 107 (2019) 73–85.
- [8] L. Xu, K. Zhang, C. Wu, X. Lei, J. Ding, X. Shi, C. Liu, Micro-Arc Oxidation Enhances the Blood Compatibility of Ultrafine-Grained Pure Titanium, *Materials (Basel)*. 10 (2017) 1446.
- [9] A.R. Ribeiro, F. Oliveira, L.C. Boldrini, P.E. Leite, P. Falagan-Lotsch, A.B.R. Linhares, W.F. Zambuzzi, B. Fragneaud, A.P.C. Campos, C.P. Gouvêa, B.S. Archanjo, C.A. Achete, E. Marcantonio, L.A. Rocha, J.M. Granjeiro, Micro-arc oxidation as a tool to develop multifunctional calcium-rich surfaces for dental implant applications, *Mater. Sci. Eng. C.* 54 (2015) 196–206.
- [10] Y. Wang, H. Yu, C. Chen, Z. Zhao, Review of the biocompatibility of micro-arc oxidation coated titanium alloys, *Mater. Des.* 85 (2015) 640–652.
- [11] I.S. Park, T.G. Woo, W.Y. Jeon, H.H. Park, M.H. Lee, T.S. Bae, K.W. Seol, Surface characteristics of titanium anodized in the four different types of electrolyte, *Electrochim. Acta.* 53 (2007) 863–870.
- [12] M.D. Roach, R.S. Williamson, I.P. Blakely, L.M. Didier, Tuning anatase and rutile phase ratios and nanoscale surface features by anodization processing onto titanium substrate surfaces, *Mater. Sci. Eng. C.* 58 (2016) 213–223.
- [13] D. Velten, V. Biehl, F. Aubertin, B. Valeske, W. Possart, J. Breme, Preparation of TiO<sub>2</sub> layers on cp-Ti and Ti6Al4V by thermal and anodic oxidation and by sol-gel coating techniques and their characterization, *J Biomed Mater Res.* 59 (2002) 18–28.
- [14] M. Fazel, H.R. Salimijazi, M.A. Golozar, M.R. Garsivaz jazi, A comparison of corrosion, tribocorrosion and electrochemical impedance properties of pure Ti and Ti6Al4V alloy treated by micro-arc oxidation process, *Appl. Surf. Sci.* 324 (2015) 751–756.
- [15] D. Quintero, O. Galvis, J.A. Calderón, J.G. Castaño, F. Echeverría, Control of the physical properties of anodic coatings obtained by plasma electrolytic oxidation on Ti6Al4V alloy, *Surf. Coatings Technol.* 283 (2015) 210–222.
- [16] L. Benea, E. Mardare-Danaila, M. Mardare, J.-P. Celis, Preparation of titanium oxide and hydroxyapatite on Ti–6Al–4V alloy surface and electrochemical behaviour in bio-simulated fluid solution, *Corros. Sci.* 80 (2014) 331–338.
- [17] A.C. Alves, F. Oliveira, F. Wenger, P. Ponthiaux, J.-P. Celis, L.A. Rocha, Tribocorrosion behaviour of anodic treated titanium surfaces intended for dental implants, *J. Phys. D. Appl. Phys.* 46 (2013) 404001.

- [18] I. da S.V. Marques, M.F. Alfaro, N.C. da Cruz, M.F. Mesquita, C. Sukotjo, M.T. Mathew, V.A.R. Barão, Tribocorrosion behavior of biofunctional titanium oxide films produced by micro-arc oxidation: Synergism and mechanisms, *J. Mech. Behav. Biomed. Mater.* 60 (2016) 8–21.
- [19] F.G. Oliveira, A.R. Ribeiro, G. Perez, B.S. Archanjo, C.P. Gouvea, J.R. Araújo, A.P.C. Campos, A. Kuznetsov, C.M. Almeida, M.M. Maru, C.A. Achete, P. Ponthiaux, J.-P. Celis, L.A. Rocha, Understanding growth mechanisms and tribocorrosion behaviour of porous TiO<sub>2</sub> anodic films containing calcium, phosphorous and magnesium, *Appl. Surf. Sci.* 341 (2015) 1–12.
- [20] L. Benea, E. Danaila, P. Ponthiaux, Effect of titania anodic formation and hydroxyapatite electrodeposition on electrochemical behaviour of Ti-6Al-4V alloy under fretting conditions for biomedical applications, *Corros. Sci.* 91 (2015) 262–271.
- [21] F. Toptan, A.C. Alves, A.M.P. Pinto, P. Ponthiaux, Tribocorrosion behavior of bio-functionalized highly porous titanium, *J. Mech. Behav. Biomed. Mater.* 69 (2017) 144–152.
- [22] L. Xie, X. Liao, H. Xu, G. Yin, Z. Huang, Y. Yao, X. Chen, J. Gu, A facile one-step anodization treatment to prepare multi-level porous titania layer on titanium, *Mater. Lett.* 72 (2012) 141–144.
- [23] R. Zhou, D. Wei, W. Feng, S. Cheng, H. Yang, B. Li, Y. Wang, D. Jia, Y. Zhou, Bioactive coating with hierarchical double porous structure on titanium surface formed by two-step microarc oxidation treatment, *Surf. Coatings Technol.* 252 (2014) 148–156.
- [24] R. Zhou, D. Wei, J. Cao, W. Feng, S. Cheng, Q. Du, B. Li, Y. Wang, D. Jia, Y. Zhou, Conformal coating containing Ca, P, Si and Na with double-level porous surface structure on titanium formed by a three-step microarc oxidation, *RSC Adv.* 5 (2015) 28908–28920.
- [25] D.P. Mondal, S. Das, N. Jha, Dry sliding wear behaviour of aluminum syntactic foam, *Mater. Des.* 30 (2009) 2563–2568.
- [26] M. Gradzka-Dahlke, J.R. Dabrowski, B. Dabrowski, Characteristic of the porous 316 stainless steel for the friction element of prosthetic joint, *Wear.* 263 (2007) 1023–1029.
- [27] M. Gui, S. Bong, J. Moo, Influence of porosity on dry sliding wear behavior in spray deposited Al–6Cu–Mn/SiCp composite, *Mater. Sci. Eng. A.* 293 (2000) 146–156.
- [28] N. Cassillas, S. Charlebois, W. Smyrl, H. White, Pitting Corrosion of Titanium, *Br. Corros. J.* 7 (1972) 59–60.
- [29] C.M. Murphy, F.J. O'Brien, Understanding the effect of mean pore size on cell activity in collagen-glycosaminoglycan scaffolds, *Cell Adhes. Migr.* 4 (2010) 377–381.
- [30] R.F. do Prado, G.C. Esteves, E.L.D.S. Santos, D.A.G. Bueno, C.A.A. Cairo, L.G.O. De Vasconcellos, R.S. Sagnori, F.B.P. Tessarin, F.E. Oliveira, L.D. De Oliveira, M.F.L. Villaça-Carvalho, V.A.R. Henriques, Y.R. Carvalho, L.M.R. De Vasconcellos, In vitro and in vivo biological performance of porous Ti alloys prepared by powder metallurgy, *PLoS One.* 13 (2018) e0196169.
- [31] H.E. Götz, M. Müller, A. Emmel, U. Holzwarth, R.G. Erben, R. Stangl, Effect of surface finish on the osseointegration of laser-treated titanium alloy implants, *Biomaterials.* 25 (2004) 4057–4064.
- [32] G. Li, L. Wang, W. Pan, F. Yang, W. Jiang, X. Wu, X. Kong, K. Dai, Y. Hao, In vitro and in vivo study of additive manufactured porous Ti6Al4V scaffolds for repairing bone defects, *Sci. Rep.* 6 (2016) 34072.
- [33] N. Taniguchi, S. Fujibayashi, M. Takemoto, K. Sasaki, B. Otsuki, T. Nakamura, T. Matsushita, T. Kokubo, S. Matsuda, Effect of pore size on bone ingrowth into porous titanium implants fabricated by additive manufacturing: An in vivo experiment, *Mater. Sci. Eng. C.* 59 (2016) 690–701.
- [34] C.M. Murphy, M.G. Haugh, F.J. O'Brien, The effect of mean pore size on cell attachment, proliferation and migration in collagen-glycosaminoglycan scaffolds for bone tissue engineering, *Biomaterials.* 31 (2010) 461–466.

- [35] A.C. Alves, F. Wenger, P. Ponthiaux, J.-P. Celis, A.M. Pinto, L.A. Rocha, J.C.S. Fernandes, Corrosion mechanisms in titanium oxide-based films produced by anodic treatment, *Electrochim. Acta.* 234 (2017) 16–27.
- [36] A.L. Yerokhin, X. Nie, A. Leyland, A. Matthews, S.J. Dowey, Plasma electrolysis for surface engineering, *Surf. Coatings Technol.* 122 (1999) 73–93.
- [37] N. Eliaz, N. Metoki, N. Eliaz, N. Metoki, Calcium Phosphate Bioceramics: A Review of Their History, Structure, Properties, Coating Technologies and Biomedical Applications, *Materials (Basel)*. 10 (2017) 334.
- [38] O. Banakh, T. Journot, P.A. Gay, J. Matthey, C. Csefalvay, O. Kalinichenko, O. Sereda, M. Moussa, S. Durual, L. Snizhko, Synthesis by anodic-spark deposition of Ca- and P-containing films on pure titanium and their biological response, *Appl. Surf. Sci.* 378 (2016) 207–215.
- [39] L. Wang, G.H. Nancollas, Calcium Orthophosphates: Crystallization and Dissolution, *Chem. Rev.* 108 (2008) 4628–4669.
- [40] S. Kim, H. Ryu, H. Shin, H.S. Jung, K.S. Hong, *In situ* observation of hydroxyapatite nanocrystal formation from amorphous calcium phosphate in calcium-rich solutions, *Mater. Chem. Phys.* 91 (2005) 500–506.
- [41] O. Zywitzki, T. Modes, H. Sahm, P. Frach, K. Goedicke, D. Glöß, Structure and properties of crystalline titanium oxide layers deposited by reactive pulse magnetron sputtering, *Surf. Coatings Technol.* 180–181 (2004) 538–543.
- [42] E. Anitua, R. Prado, G. Orive, R. Tejero, Effects of calcium-modified titanium implant surfaces on platelet activation, clot formation, and osseointegration., *J. Biomed. Mater. Res. A.* 103A (2015) 969–980.
- [43] J.I. Rosales-Leal, M.A. Rodríguez-Valverde, G. Mazzaglia, P.J. Ramón-Torregrosa, L. Díaz-Rodríguez, O. García-Martínez, M. Vallecillo-Capilla, C. Ruiz, M.A. Cabrerizo-Vílchez, Effect of roughness, wettability and morphology of engineered titanium surfaces on osteoblast-like cell adhesion, *Colloids Surfaces A Physicochem. Eng. Asp.* 365 (2010) 222–229.
- [44] R.A. Gittens, L. Scheideler, F. Rupp, S.L. Hyzy, J. Geis-Gerstorfer, Z. Schwartz, B.D. Boyan, A review on the wettability of dental implant surfaces II: Biological and clinical aspects, *Acta Biomater.* 10 (2014) 2907–2918.
- [45] J.I. Silva, A.C. Alves, A.M. Pinto, F. Toptan, Corrosion and tribocorrosion behavior of Ti-TiB-TiNx in-situ hybrid composite synthesized by reactive hot pressing, *J. Mech. Behav. Biomed. Mater.* 74 (2017) 195–203.
- [46] G.O. Alrabeah, P. Brett, J.C. Knowles, H. Petridis, The effect of metal ions released from different dental implant-abutment couples on osteoblast function and secretion of bone resorbing mediators, *J. Dent.* 66 (2017) 91–101.
- [47] B.R. Waterhouse, M.H. Wharton, Titanium and Tribology, *Ind. Lubr. Tribol.* 26 (1974) 20–23.



## Chapter 7

### Tribocorrosion-resistant biofunctionalized Ti-Al<sub>2</sub>O<sub>3</sub> composites

*Published in Surface Coatings and Technology (2021)*  
*doi.org/10.1016/j.surfcoat.2021.127329*

---

**L. Sousa<sup>a,b,\*</sup>, L. Basilio<sup>a</sup>, A.C. Alves<sup>a</sup>, F. Toptan<sup>a,c,d</sup>**

<sup>a</sup> CMEMS-UMinho – Center of MicroElectroMechanical Systems – Universidade Minho, Campus de Azurém, Guimarães, Portugal

<sup>b</sup> DEMM – Department of Metallurgical and Materials Engineering – Faculdade de Engenharia da Universidade do Porto, Porto, Portugal

<sup>c</sup> IBTN/Euro – European Branch of the Institute of Biomaterials, Tribocorrosion and Nanomedicine, Dept. Eng. Mecânica, Universidade do Minho, Azurém, 4800-058 Guimarães, Portugal

<sup>d</sup> Department of Materials Science and Engineering, Izmir Institute of Technology, 35430, Urla,



## Abstract

Recent studies have shown that titanium matrix composites have potential for load-bearing biomedical implants due to their improved tribocorrosion behaviour compared to Ti and its alloys. However, lack of bioactivity remains as a concern due to bioinert Ti matrix and the fact that most reinforcement phases are also bioinert. In this work, biofunctionalized Ti-Al<sub>2</sub>O<sub>3</sub> composites were produced by performing micro-arc oxidation treatment on the Ti-Al<sub>2</sub>O<sub>3</sub> composites processed by hot-pressing technique. The overall microstructure consisted of Al<sub>2</sub>O<sub>3</sub> particles dispersed within a biofunctionalized Ti matrix having a micro-porous structure rich in Ca and P elements. The corrosion behaviour of the composites was greatly improved after MAO treatment, whereas the tribocorrosion behaviour of the composites was also further improved after MAO treatment.

### 7.1. Introduction

Despite being widely used in hip-implants, Ti and its alloys still face some clinical concerns, such as low tribocorrosion resistance and lack of bioactivity. Regarding tribocorrosion resistance, it is well known that the addition of hard ceramic particles into a metal matrix can significantly improve the wear resistance of the metal matrix [1]. For that reason, titanium matrix composites (TMCs) have found several applications in the automotive and aerospace sectors and can also have potential in biomedical field, especially in load bearing orthopaedic implants. In the last few years some studies have reported that TMCs show a significant improvement on tribocorrosion behaviour compared to Ti, through reduced tendency to corrosion as well as reduced corrosion kinetics under a fretting or sliding action. Furthermore, a significant reduction in wear volume was also usually reported [2–4]. Among all the possible reinforcement phases, alumina (Al<sub>2</sub>O<sub>3</sub>), being a well know biomaterial, can be considered as an interesting choice to produce TMCs for biomedical applications. Alumina has been widely used in biomedical implants, being first used to replace the typical metallic femoral head of hip implants and today it is still used together with ultra-high molecular weight polyethylene which is a part of the acetabular component [5].

In total hip replacement, alumina-alumina bearings are known to be one of the most resistant to wear. Furthermore, low rate of osteolysis has also been reported due to exceptional wear resistance and low surface roughness of alumina [6–9]. Similar coefficient of thermal expansion (CTE) with Ti matrix and excellent compressive strength also make alumina a potential candidate for TMCs [10,11]. Ti-Al<sub>2</sub>O<sub>3</sub> composites have shown good mechanical properties [12–14], overall good corrosion behaviour, even under acidic environments [15,16] and improved wear resistance [2], however tribocorrosion behaviour is still poorly understood.

Since most reinforcement phases are bioinert, the bioactivity of such composites continues to be an issue. While Ti-hydroxyapatite or Ti- bioactive glass composites have been reported to improve the bioactivity of Ti [17–20] their tribocorrosion behaviour is still poorly understood.

In order to improve the bioactivity, a range of surface modification techniques can be used, through thermal spraying, physical vapor deposition, chemical vapor deposition, coatings and anodic treatment (AT) [21,22]. AT is a promising technique since it can produce an oxide layer with tailored chemical and mechanical properties, as well with improved bioactivity and osteointegration capabilities [22–29]. Furthermore this technique has also been commercially used in dental implants [30]. Micro-arc oxidation (MAO) is a regime of AT, where several hundreds of volts are used to produce a porous, crystalline, and thick TiO<sub>2</sub> layer that is recognized to improve the bioactivity of Ti [22–26]. Depending on the electrolyte composition, it is possible to incorporate bioactive elements on this layers, such as Ca and/or P. As an example, an electrolyte consisting of mixture of calcium acetate and beta-glycerophosphate disodium salt pentahydrate can be used to incorporate Ca and P and, depending on the processing conditions, Ca/P ratio can be controlled [27,31]. In addition to the improved bioactivity, MAO layers also present other advantages that are of extreme importance for biomedical devices, such as reduced stiffness mismatches and additional corrosion and tribocorrosion resistance [32]. Ti-Al<sub>2</sub>O<sub>3</sub> composites with a biofunctionalized titanium matrix could have potential to improve both the tribocorrosion and bioactivity of Ti. While the advantages of MAO treatment on Ti and Ti alloys have been widely reported in the last years, its effect on TMC surfaces is unknown, not only from a structure standpoint, but



also its effects on the corrosion and tribocorrosion behaviour. One of the most critical aspects of TMCs resides in the interface between the Ti matrix and the reinforcement phases, as these interfaces will play an important role on the final properties of the composite, not only on the mechanical properties but also on the overall corrosion and tribocorrosion behaviour. Studies have shown that TiAl and Ti<sub>3</sub>Al intermetallic phases form between Ti and Al<sub>2</sub>O<sub>3</sub> due to their reaction during processing [2,15,16,33]. Additionally, the extension of this reaction will depend on the processing parameters such as processing temperature. Thus the objective of this work was to introduce biofunctionalized (MAO-treated) Ti-Al<sub>2</sub>O<sub>3</sub> composites processed at two distinct temperatures as an alternative material for load-bearing implants and to study its corrosion and tribocorrosion behaviour.

## **7.2. Materials and methods**

### *7.2.1. Processing*

Ti matrix composites reinforced with 5% vol. of Al<sub>2</sub>O<sub>3</sub> particles were processed by powder metallurgy. Both Ti grade 2 and 99.8% purity Al<sub>2</sub>O<sub>3</sub> powders had irregular shapes (Fig. 7.1) with the particle size distribution presented on Table 7.1. Ball milling was used to mix the powders for 4 h at 120 rpm with the help of Al<sub>2</sub>O<sub>3</sub> balls ( $\varnothing$  10 mm), under Ar atmosphere. Powder blends were placed in a zirconia coated graphite mould (10 mm inner diameter) in order to process samples with 3 mm of thickness. Hot-pressing was then carried out at high vacuum ( $\leq 10^{-5}$  mbar) during 30 min under an applied pressure of 40 MPa. Two different sintering temperatures were used, namely 1000°C and 1100°C, 1100°C was chosen based on a previous work [2], while 1000°C was chosen in order to reduce the degree of reaction between the Al<sub>2</sub>O<sub>3</sub> particles and the Ti matrix and observe its effect on the corrosion and tribocorrosion behaviour of these composites.

Unreinforced Ti samples were also processed under identical conditions and used as control group. Depending on the sintering temperature, samples groups are referred as Ti\_1000C and Ti-5Al<sub>2</sub>O<sub>3</sub>\_1000C, Ti\_1100C and Ti-5Al<sub>2</sub>O<sub>3</sub>\_1100C. Before characterization and testing all samples were ground down to 2400 mesh SiC papers and then mirror finished until 0.04  $\mu$ m with colloidal silica suspension. Samples were then cleaned by propanol and distilled

water in an ultrasonic bath for 10 and 5 min, respectively, and kept in a desiccator for 24 h prior to each test to obtain similar surface conditions.

**Table 7.1.** Particle size distribution for Ti and Al<sub>2</sub>O<sub>3</sub> powders.

	D[v,0.1] (μm)	D[v,0.5] (μm)	D[v,0.9] (μm)
Ti	10	25	44
Al <sub>2</sub> O <sub>3</sub>	17	42	71

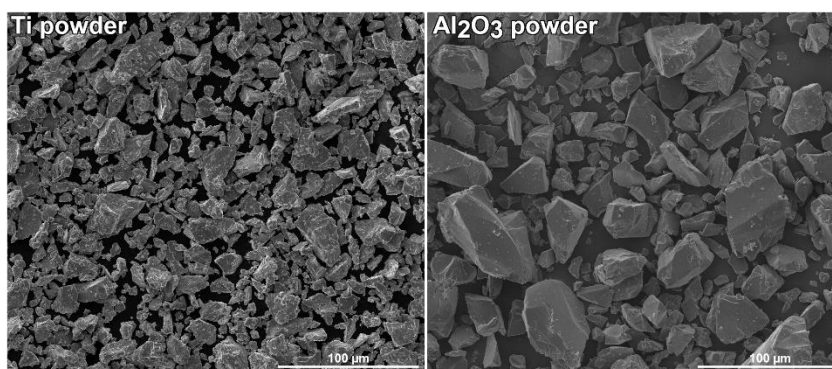


**Figure 7.1.** SE SEM images of the raw Ti and Al<sub>2</sub>O<sub>3</sub> powders.

### 7.2.2. Biofunctionalization

Biofunctionalization was conducted in an electrochemical cell connected to a DC power supply (Agilent technologies N5772A), as shown in detail in Fig. 7.2. MAO treatment was performed under a turbulent regime by means of a magnetic stirrer spinning at 200 rpm. A constant voltage of 300 V was applied for 1 min with an imposed current limit of 2.5 A. A mixture of 0.35 M of calcium acetate monohydrate (CA, Sigma-Aldrich) and 0.02 M of β-glycerophosphate disodium salt pentahydrate (β-GP, Alfa Aesar) was used as electrolyte. Hereafter, ‘\_MAO’ was added to the previous nomenclature in order to identify the biofunctionalized samples.

### 7.2.3. Electrochemical tests

The electrochemical behaviour was evaluated at body temperature (37 ± 2 °C) in phosphate-buffered saline (PBS) solution (0.24 g/l KH<sub>2</sub>PO<sub>4</sub>, 0.2 g/l KCl, 1.44 g/l Na<sub>2</sub>HPO<sub>4</sub> 8 g/l NaCl) having a pH was adjusted to 7.4. Open circuit potential (OCP) was monitored until stabilization (ΔE < 60 mV/h), followed by electrochemical impedance spectroscopy (EIS) measurements, which were scanned with a rate of 7 points per decade starting at 10<sup>5</sup> Hz until 10<sup>-2</sup> Hz with an amplitude of the sinusoidal signal set at 10 mV. Finally, potentiodynamic

polarization tests were performed by scanning at 1 mV/s a potential range from  $-0.2 V_{\text{OCP}}$  to  $1.5 V_{\text{Ag/AgCl}}$ . For all electrochemical tests, a standard three-electrode setup was used consisting in a saturated Ag/AgCl reference electrode, a platinum (Pt) wire as counter electrode and the sample as working electrode. All the electrodes were connected to a Gamry Potentiostat/Galvanostat/ZRA (model Referece-600+). The general setup is described in Fig. 7.2.

#### 7.2.4. Tribocorrosion tests

Tribocorrosion tests were performed in an identical PBS solution at body temperature. A tribo-electrochemical cell, placed in a tribometer (CETR-UMT2) with a ball-on-plate configuration and reciprocating stage, was used for all the tests, where an Al<sub>2</sub>O<sub>3</sub> ball ( $\varnothing$  10 mm) slid against the untreated and MAO treated samples, as described in detail in Fig. 7.2. The OCP values were monitored before sliding until stabilization ( $\Delta E < 60$  mV/h), under sling and after sliding for 1800 s. Coefficient of friction (COF) values were also monitored during sliding. The sliding action was performed under a 1 N of applied normal load (corresponds to a maximum Hertzian contact pressure for CP Ti of 0.41 GPa) during 30 min with 1 Hz frequency and total stroke length of 3 mm. The electrochemical tests were performed using a Gamry Potentiostat/Galvanostat/ZRA (model Referece-600) with a two-electrode set-up, where the samples were connected as working electrode and saturated Ag/AgCl reference electrode.

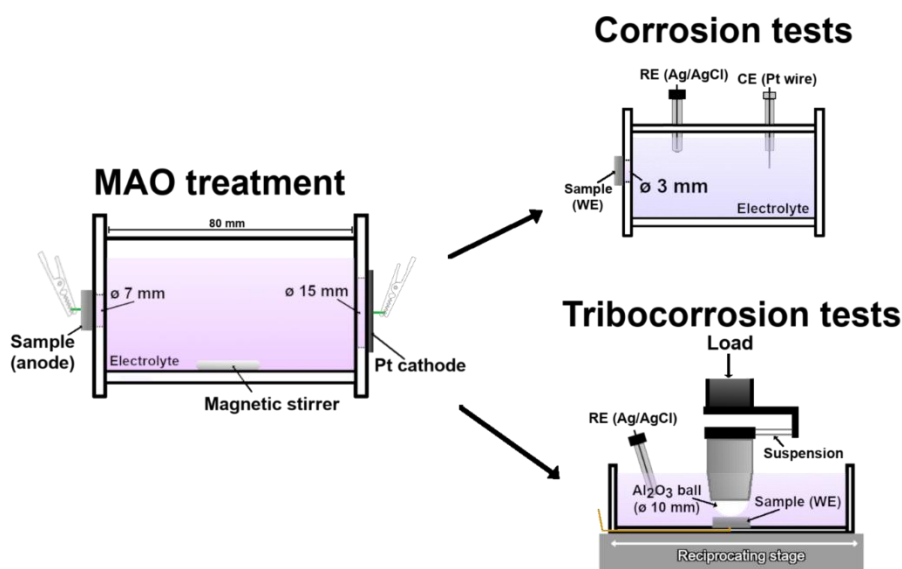


**Figure 7.2.** General setup used in MAO treatments, together with corrosion and tribocorrosion tests.

### 7.2.5. Characterization

The microstructures were analysed by field emission gun scanning electron microscope (FEG-SEM, FEI Nova 200), and the chemical compositions by EDAX energy dispersive X-ray spectroscopy (EDS). The crystalline structures of the MAO layers were evaluated by X-ray diffraction (Bruker D8 Discover diffractometer) at 40 kV with Cu K $\alpha$  radiation. The overall hardness of the untreated samples was evaluated through Vickers macro-hardness tests performed using an Officine Galileo Mod. D200 tester by applying 30 kgf load during 15 s by a mean of 5 indentations per sample, using 3 samples per condition. After tribocorrosion tests, samples were cleaned with the same cleaning procedure used on the metallographic preparation. The microstructures of the worn surfaces were then evaluated parallel to the sliding direction with the same FEG-SEM equipment and the wear track profiles were obtained by profilometry (Veeco, Dektak 150).

## 7.3. Results

### 7.3.1. Characterization

The overall microstructure of the as-processed composites, MAO treated Ti and MAO treated composites can be seen in the back scattered electron (BSE) and secondary electron (SE) SEM images presented in Fig. 7.3. Both Ti-Al<sub>2</sub>O<sub>3</sub> composites presented a uniform distribution of reinforcement phases, with no signs of agglomerations. As it can be seen on the higher magnification images, a reaction zone between the Al<sub>2</sub>O<sub>3</sub> particles and the Ti matrix was formed due to reaction between Ti and Al<sub>2</sub>O<sub>3</sub>. Comparing both processing temperatures, thicker reaction zones were obtained on Ti-Al<sub>2</sub>O<sub>3</sub>\_1100C composites. On average, the thickness of the reaction zones was measured as  $6 \pm 1$  and  $11 \pm 3$   $\mu\text{m}$  for composites processed at 1000 and 1100°C, respectively.

Further inspection revealed that in both groups the reaction zone was formed by two distinct phases, marked in the figures as Z1 and Z2, where Z1 was much more predominant on composites processed at 1100 °C. The area ratio between the reaction zone and the Al<sub>2</sub>O<sub>3</sub> particle increased with the increasing processing temperature, 1.16 and 2.95 for Ti-Al<sub>2</sub>O<sub>3</sub>\_1000C and Ti-Al<sub>2</sub>O<sub>3</sub>\_1100C, respectively.

EDS analysis showed that in both groups, Z1 and Z2 were constituted by a mixture of Ti and Al, with Z1 presenting Ti/Al at% ratios close to 1 and Z2 showing Ti/Al ratios close to 3. The reaction products of Ti + Al<sub>2</sub>O<sub>3</sub> belong to the Ti-Al-O system, where compounds such as Ti<sub>3</sub>Al, TiAl, TiAl<sub>2</sub> and TiAl<sub>3</sub> and titanium oxides such as TiO and TiO<sub>2</sub> can be formed at the interface [34]. However due to limited diffusion capability of oxygen and high instability of TiAl<sub>2</sub> and TiAl<sub>3</sub> compounds at high temperatures [34], the reaction products are almost always TiAl and Ti<sub>3</sub>Al [11,35,36], where the reaction sequence at 1100 °C is Al<sub>2</sub>O<sub>3</sub>/TiAl/Ti<sub>3</sub>Al/Ti [11,35]. The results obtained were highly in accordance with the literature since Z1 corresponded to TiAl (Ti/Al ratio  $\approx$  1) and Z2 corresponded to Ti<sub>3</sub>Al (Ti/Al ratio  $\approx$  3). It has also been reported that Ti<sub>3</sub>Al is the first to be formed and, after Al enrichment, the formation of TiAl occurs. With low residence time and/or low temperature, the formation of TiAl can be reduced or avoided [34,37], that was probably the case on Ti-Al<sub>2</sub>O<sub>3</sub>\_1000C composites, where the reaction zones tended to be smaller and Z1 was much less predominant. Regarding the MAO treated groups, the typical volcano-like structure, usually reported in literature [31,38–40], was obtained for both unreinforced Ti groups, with no discernible differences between them. Ca/P at% ratios were calculated as  $3.02 \pm 0.05$  and  $3.15 \pm 0.12$  for Ti\_1000C\_MAO and Ti\_1100C\_MAO respectively. XRD spectra, Fig. 7.3e, revealed a similar crystalline structure consisting of Ti and TiO<sub>2</sub> in the form of anatase and rutile phases.

For composite groups, MAO treatment led to the formation of the typical volcano-like structure. However, the MAO layer formed on the reaction zone seems to have some differences when compared with the one formed on Ti matrix, namely on the pores size and structure (Figs. 7.3d and 7.3f).

In addition, the cross sections also revealed on Ti matrix the usual MAO layer structure composed of a thin compact film next to the substrate followed by an inner and an outer porous layer [31]. However, the MAO layer formed on the reaction zone seems to be more heterogeneous and it is not possible to distinguish the two porous layers. XRD spectra presented in Fig. 7.3e, revealed the same crystalline structure obtained for Ti, being a mixture of anatase and rutile phases, with no discernible differences between all of the groups. Ca/P at% ratio for composite groups were calculated as  $2.96 \pm 0.28$  and  $3.01 \pm 0.07$  for

Ti-5Al<sub>2</sub>O<sub>3</sub>\_1000C\_MAO and Ti-5Al<sub>2</sub>O<sub>3</sub>\_1100C\_MAO, respectively, which were also in the same value ranges as the ones obtained for Ti groups.

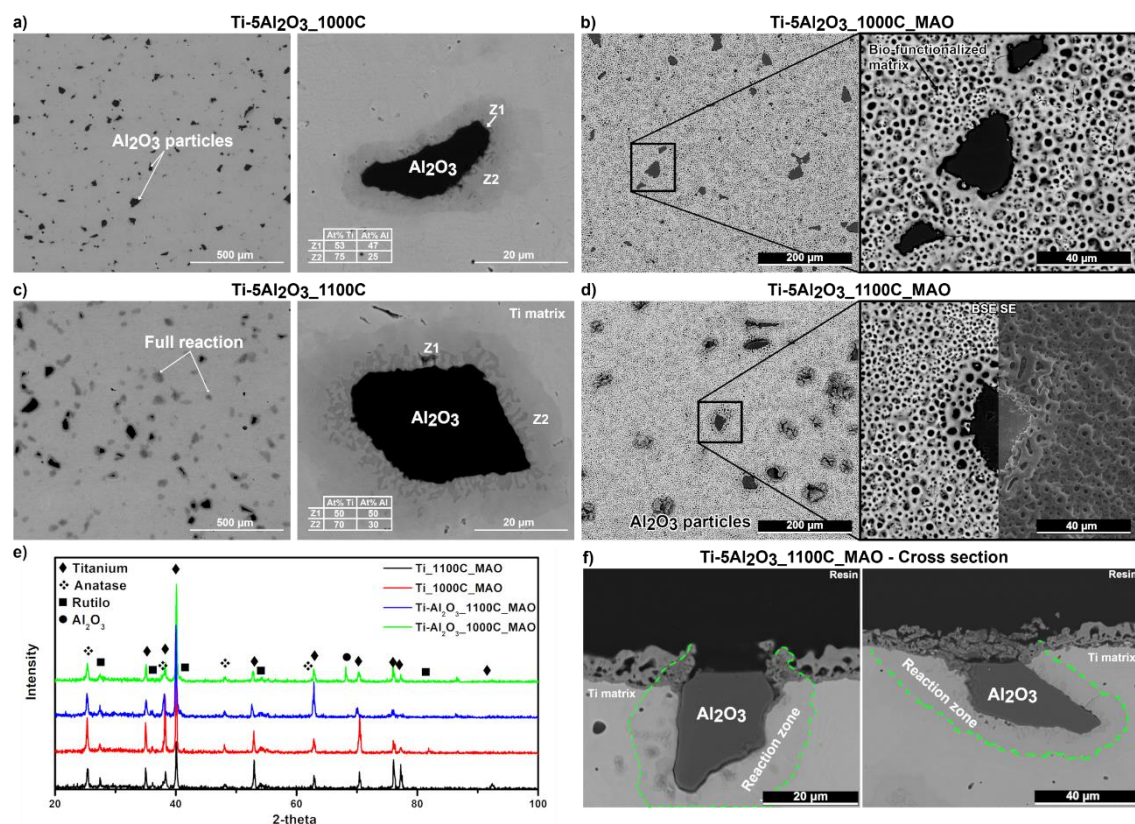


**Figure 7.3.** Overall microstructure of the a,b) as-processed and b,c) biofunctionalized composites, e) XRD spectra for MAO treated groups, and f) cross section BSE images from Ti-Al<sub>2</sub>O<sub>3</sub>\_1100C group.

### 7.3.2. Corrosion behaviour

Representative potentiodynamic polarization curves for untreated and biofunctionalized groups can be seen on Fig. 7.4. The average values obtained for OCP ( $E_{ocp}$ ), corrosion potential ( $E_{(i=0)}$ ) and passive current density ( $i_{pass}$ ) can be seen on Table 7.2. For untreated samples, all the groups presented a well-defined passivation plateau, starting around 0.25 V<sub>Ag/AgCl</sub> for groups processed at 1000 °C and around 0.50 V<sub>Ag/AgCl</sub> for groups processed at 1100 °C. Ti and composites processed at 1100 °C presented slightly lower  $i_{pass}$  and higher  $E_{ocp}$  values while  $E_{(i=0)}$  values were very similar to groups processed at 1000 °C. Comparing the general corrosion behaviour of untreated groups, it was observed that Ti-Al<sub>2</sub>O<sub>3</sub>\_1100C group presented a distinct behaviour, where an abrupt increase in corrosion current density values was observed at  $1.07 \pm 0.19$  as V<sub>Ag/AgCl</sub>. Reinforcement phases may improve the corrosion behaviour of the base material by acting as inert physical barrier to corrosion [3] or by grain refinement

of the metal matrix which may increase the quality of the native oxide film [41]. On the other hand, these reinforcement phases may also jeopardize the corrosion behaviour. Galvanic coupling between different phases including the metal matrix, reinforcement particles and/or phases formed at the reaction zones may lead to dissolution of the metal matrix and/or the reinforcement phases. [42]. On the other hand, the presence of porosity or defects at the interface between reinforcement/reaction zones/matrix interfaces may also lead to decreased corrosion resistance by leading to the formation of heterogeneities on the native oxide film [43,44]. Recent studies by Bahraminasab et al. [15,16] showed that adding Al<sub>2</sub>O<sub>3</sub> particles into a Ti matrix, may have a dual effect on the corrosion behaviour of the composites. On one hand the presence of Al<sub>2</sub>O<sub>3</sub> particles lead to an improvement of the overall corrosion resistance when compared with unreinforced Ti, due to the formation of a higher quality native oxide film, however for higher percentages of reinforcement phases, the authors reported that the corrosion behaviour was lower than unreinforced Ti, probably due to higher percentages of TiAl and Ti<sub>3</sub>Al brittle phases which may have increased susceptibility to corrosion. Rocha et al. [35] showed that the corrosion behaviour of Ti/Al<sub>2</sub>O<sub>3</sub> interfaces was heavily influenced by the presence of TiAl intermetallic phase, as this phase was found to be corrosion susceptible. Accordingly, the corrosion behaviour obtained for Ti-Al<sub>2</sub>O<sub>3</sub>\_1100C group may be explained by the presence of more interfacial zones.

After MAO treatment all the groups presented a considerable increase in corrosion resistance as can be seen by the almost 2 decades decrease in  $i_{pass}$  values. The corrosion behaviour is characterized by a well-defined passivation plateau, where the current density values have a range of variation of about half a decade. A similar increase in corrosion resistance on MAO treated Ti has previously been reported [40,45].

The improvement on the corrosion behaviour is associated to the formation of a triplex layer, having a dense barrier layer between the Ti substrate and the outer porous layers with improved corrosion resistance [31,40]. By analysing the potentiodynamic polarization curves and the values presented on Table 7.2, no discernible differences between the MAO treated groups were observed. The presence of Al<sub>2</sub>O<sub>3</sub> particles and adjacent reaction zones in the Ti matrix did not jeopardize the good corrosion behaviour of these layers, additionally the possible

adverse effect of the reaction zones observed on Ti-Al<sub>2</sub>O<sub>3</sub>\_1100C group was completely avoided, as the Ti-Al<sub>2</sub>O<sub>3</sub>\_1100C\_MAO group presented similar behaviour to the other MAO groups. In addition, the heterogeneities observed on the MAO layer for this groups did not affect the overall corrosion behaviour.

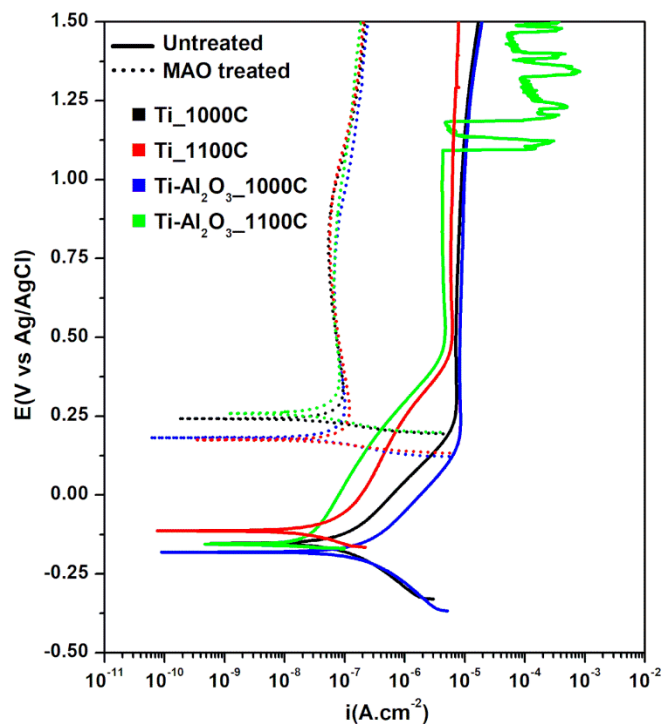


**Figure 7.4.** Potentiodynamic polarization curves for all the conditions.

**Table 7.2.**  $E_{corr}$ ,  $E_{(i=0)}$  and  $i_{pass}$  values for all tested groups.

Group	$E_{corr}$ (V)	$E_{(i=0)}$ (V)	$i_{pass}$ ( $\mu\text{Acm}^2$ )
Ti_1000C	$-0.14 \pm 0.01$	$-0.15 \pm 0.02$	$8.35 \pm 0.70$
Ti_1000C_MAO	$0.39 \pm 0.01$	$0.24 \pm 0.01$	$0.06 \pm 0.01$
Ti-Al <sub>2</sub> O <sub>3</sub> _1000C	$-0.15 \pm 0.04$	$-0.16 \pm 0.01$	$9.64 \pm 1.36$
Ti-Al <sub>2</sub> O <sub>3</sub> _1000C_MAO	$0.33 \pm 0.04$	$0.19 \pm 0.04$	$0.07 \pm 0.01$
Ti_1100C	$-0.03 \pm 0.01$	$-0.12 \pm 0.01$	$6.24 \pm 1.30$
Ti_1100C_MAO	$0.27 \pm 0.10$	$0.11 \pm 0.10$	$0.07 \pm .03$
Ti-Al <sub>2</sub> O <sub>3</sub> _1100C	$0.02 \pm 0.01$	$-0.16 \pm 0.03$	$4.63 \pm 0.40$
Ti-Al <sub>2</sub> O <sub>3</sub> _1100C_MAO	$0.36 \pm 0.03$	$0.21 \pm 0.05$	$0.07 \pm 0.01$

### 7.3.3. Tribocorrosion behaviour

Fig. 7.5 shows the evolution of OCP before, during and after sliding action, as well as the evolution of COF values during sliding for all the groups. Before sliding, all the untreated groups presented stable OCP values due to formation of a stable native oxide film. Immediately after sliding started, all the groups presented a sharp decrease in OCP values due to the mechanical damage given

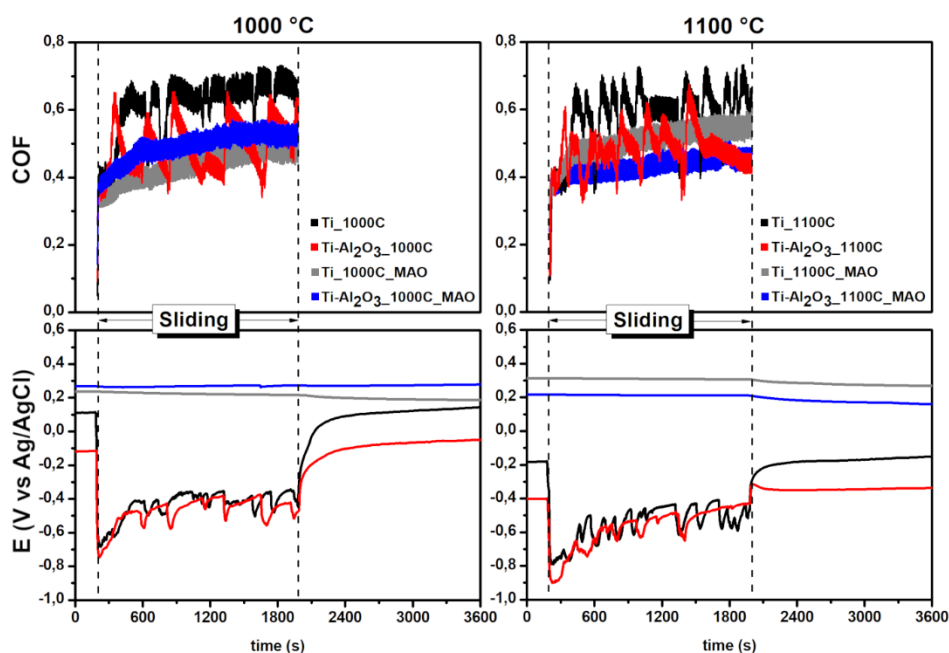


to the native oxide film and consequence exposure of fresh metallic areas to the electrolyte. For Ti groups, OCP values dropped  $670 \pm 90$  and  $837 \pm 50$  mV for Ti\_1100C and Ti\_1000C respectively, while composite groups presented OCP drops of  $490 \pm 17$  and  $527 \pm 81$  mV for Ti-Al<sub>2</sub>O<sub>3</sub>\_1100C and Ti-Al<sub>2</sub>O<sub>3</sub>\_1000C respectively. Overall, no significant differences were observed on OCP evolution between both Ti and composites groups.

During sliding, large fluctuations on OCP and respective COF values were observed for all the untreated groups. This behaviour can be attributed to the continuous formation and breaking of discontinuous tribolayers, which can be seen on BSE SEM images shown in Fig. 7.6. These tribolayers, which were formed due to compaction of wear debris on the wear track, gave limited protection against corrosion, as they protected the metallic area to some extent, and consequently an increase in OCP values was observed. When these tribolayers reached a critical thickness and broke, fresh metallic areas were exposed to the electrolyte and a consequent decrease in OCP values was observed. This behaviour was also reflected on the COF values, where an increase in OCP is accompanied by an increase in COF, which is related with the increase in surface roughness due to formation of these tribolayers. Overall, COF values were lower for both composite groups, which can be attributed to the low COF alumina-alumina tribological contacts happening to some extent on the wear track, as well as the less formation of tribolayers, due to less metallic area being available for material pull-out and also due to overall higher hardness of the composite surfaces. Immediately after sliding, OCP values rapidly recovered to the ones observed before sliding due to repassivation of the worn zones.

All the MAO treated groups presented a substantial improvement on the tribocorrosion behaviour. Before sliding, these groups presented considerably lower tendency to corrosion due to the protective nature of the MAO layers. During the entire time of sliding, no noticeable drops in OCP values were observed, suggesting that not enough mechanical damage was given to reach the bulk material. SE and BSE SEM images of the worn surfaces are given in Fig. 7.7 showing the typical volcano-like structure on the worn areas. The high wear resistance of MAO layers has been attributed to the high hardness of anatase and rutile phases, where rutile is probably more effective since it possesses higher hardness than anatase [38]. COF evolution was very similar

for all MAO treated groups, characterized by a run-in period in the initial 200 - 600 s, and then a slowly increase in COF values were observed until the end of sliding.



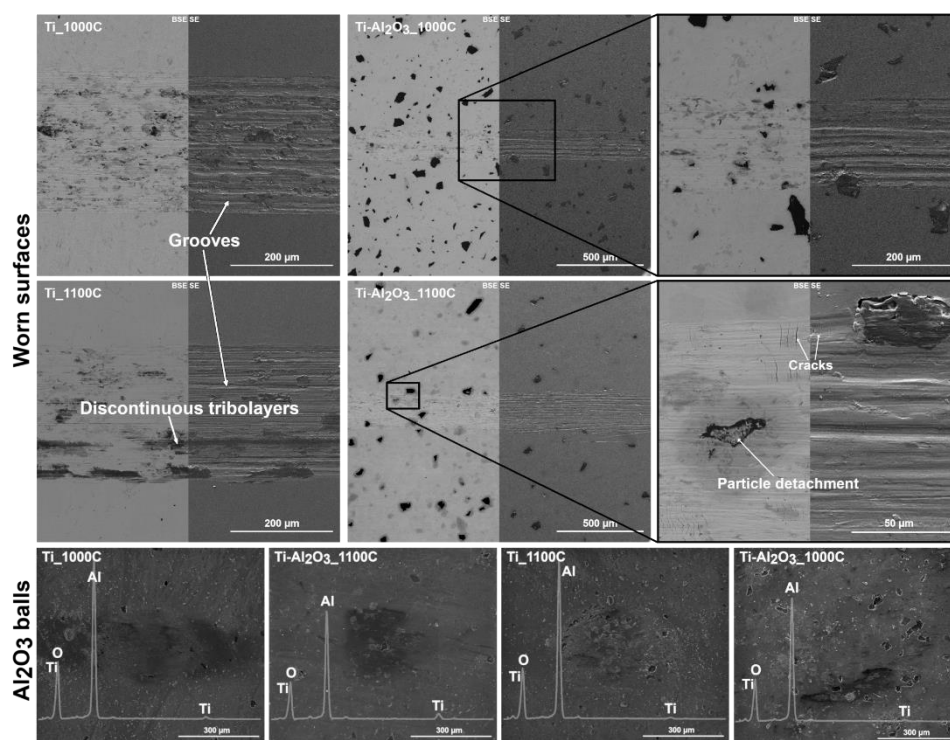
**Figure 7.5.** Evolution of OCP before, during and after sliding, together with the respective COF values registered during sliding.

Fig. 7.6 shows representative BSE SE SEM images of the worn surfaces for untreated groups. Both Ti groups presented similar morphology, where the worn surfaces were composed of discontinuous tribolayers and parallel grooves to the sliding direction. During sliding, a considerable amount of metal may be pulled out from the wear track by the counter-body due to adhesive wear, as confirmed by the chemical analysis performed on the counter-body surfaces (Fig. 7.6). Consequently, this adhered material can transfer repetitively between the sliding surfaces and may be compacted on the wear track, leading to the formation of tribolayers, adhered to the counter-body and/or move freely on the wear track. Due to repetitive transfer of material, this adhered material tends to get harder and act as an abrasive, leading to the formation of grooves on the worn surfaces. Besides, non-adhered, freely moving wear debris can act as an extra abrasive. Composite groups also presented similar features, where discontinuous tribolayers and grooves were observed on the wear tracks. Additionally, it was observed that Ti-Al<sub>2</sub>O<sub>3</sub>\_1100C group presented some Al<sub>2</sub>O<sub>3</sub> particle detachments and small cracks perpendicular to the sliding direction, whereas these features were not observed on Ti-Al<sub>2</sub>O<sub>3</sub>\_1000C group. Fig. 7.8

shows optical microscope images of representative Vickers indentation for each composite group. As can be seen, the indentations performed on Ti-Al<sub>2</sub>O<sub>3</sub>\_1100C group lead to the formation of cracks at the corners of the indentation, which are in accordance with a Palmqvist crack system, also reported by other authors on Ti-Al<sub>2</sub>O<sub>3</sub> systems [12]. The length of these cracks may be used to estimate fracture toughness ( $K_C$ ) by the means of Eq. (7.1), where  $H_V$  is Vickers hardness,  $a$  is half of the diagonal of the Vickers indentation,  $l$  is the length of the crack starting from the corner of the indentation and  $E$  is the Young's modulus. The  $E$  values used in the calculations were estimated by rule of mixtures by taking in consideration reported Young's modulus from CP Ti 2 and Al<sub>2</sub>O<sub>3</sub> (around 120 GPa and 380 GPa, respectively [12]).

$$K_C = 0.0264(H_V a) \left( \frac{E}{H_V} \right)^{0.4} (l^{-0.5}) \quad (7.1)$$

The  $K_C$  values for Ti-Al<sub>2</sub>O<sub>3</sub>\_1100C group were estimated as  $6.6 \pm 0.4$  MPa.m<sup>0.5</sup>, which are considerably lower than the ones usually observed for CP Ti grade 2 ( $\approx 60$  MPa.m<sup>0.5</sup> [46]). Since these cracks were not present on Ti-Al<sub>2</sub>O<sub>3</sub>\_1000C group, it was not possible to estimate  $K_C$  values by this method. However, it is reasonable to assume that this group presented higher fracture toughness by the fact that these cracks around the indentations were not observed. Bahraminasab et al. [14] reported that the low fracture toughness of Ti-Al<sub>2</sub>O<sub>3</sub> composites was often associated with the formation of Ti<sub>3</sub>Al and TiAl intermetallic phases, characterized by their brittle nature. In addition, these phases may also lead to Al<sub>2</sub>O<sub>3</sub> particle pull-out due to low strength ceramic/matrix interface. The morphology observed on the wear tracks for Ti-Al<sub>2</sub>O<sub>3</sub>\_1100C group are most probably related to these factors. Due to higher processing temperature, a higher amount of TiAl and Ti<sub>3</sub>Al intermetallic were obtained, due to higher area of reaction zones. During sliding, even relatively lower contact pressures may induce the formation and propagation of cracks. If these cracks are propagated through the intermetallic phases surrounding the Al<sub>2</sub>O<sub>3</sub> particles, particle pull-out may occur. Thus, due to lower amount of such intermetallic phases on Ti-Al<sub>2</sub>O<sub>3</sub>\_1000C group and consequently higher fracture toughness, no visible cracks were formed during sliding, at least under these conditions.



**Figure 7.6.** BSE and SE SEM images of the worn surfaces for untreated groups after tribocorrosion tests together with SE SEM images of the Al<sub>2</sub>O<sub>3</sub> balls used as counter-body and respective overall chemical composition of these surfaces.

The worn surfaces of MAO treated groups can be seen on Fig. 7.7. Under these conditions, no significant wear was observed for any of the treated groups, hence, BSE images showing no evidence of considerable metallic area being exposed to the electrolyte. The worn surfaces presented a smoother appearance once the outer pores were compacted/abraded by the counter-body. Additionally, the adjacent pores on the lower topographic planes served as wear debris reservoirs, where wear debris compacted inside the pores could be seen. Important to note that for Ti\_1000C\_MAO group, some detachments of the outer porous layer were observed, where the volcano-like structure was lost. Nevertheless, chemical analysis in these zones still showed considerable amount of Ca and P elements, although the Ca/P ratio decreased to about 0.99. SE SEM images and chemical analysis of the counter-body surfaces are also presented in Fig. 7.7. Very small amounts of Ti were found on the counter-body surfaces, probably due to some material transfer from the TiO<sub>2</sub> MAO layer during sliding action.

No considerable differences were observed between the MAO treated composites. As can be seen on the SE SEM images given in Fig. 7.7, the majority of Al<sub>2</sub>O<sub>3</sub> particles were in lower topographic planes than the outer porous layer

and under these testing conditions, no significant wear damage was done on the MAO surfaces exposing the reinforcing particles to the counter-material. Thus, under these tribological testing conditions, on MAO treated composites, direct role of the reinforcing particles on wear resistance by the load-carrying effect was not significantly occurred. Instead, indirect effect of the particle incorporation probably improved the overall wear resistance by strengthening the matrix and increasing the hardness of the base material.

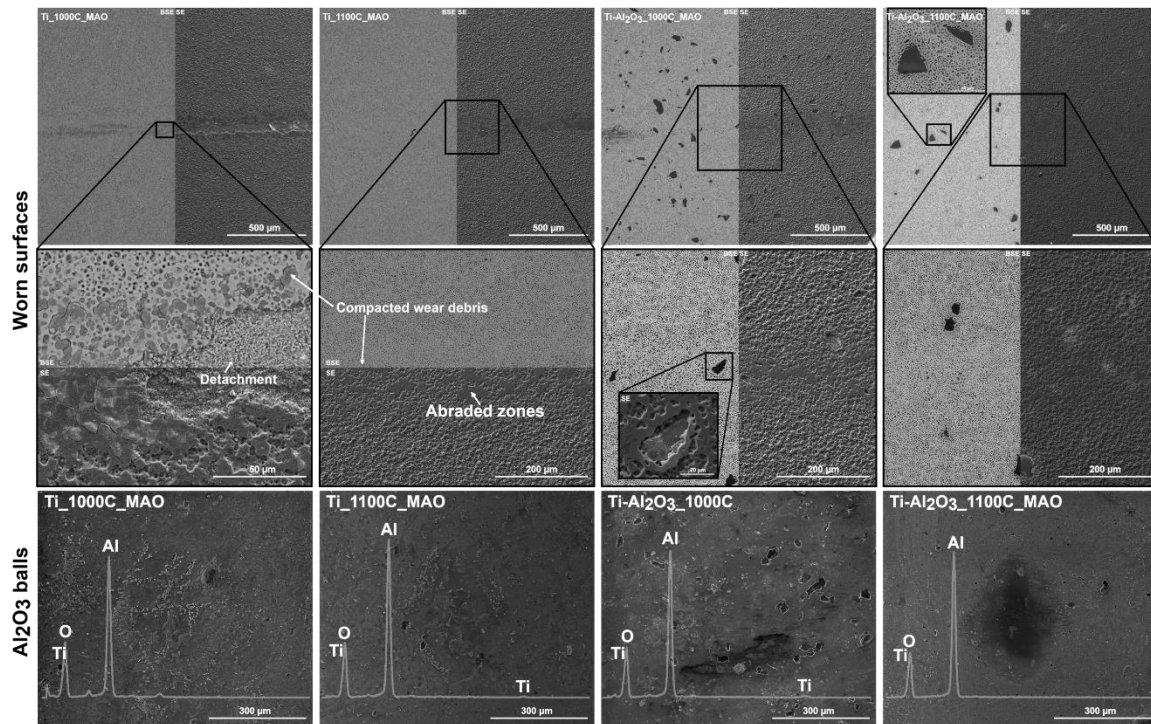


Figure 7.7. BSE and SE SEM images of the worn surfaces for MAO treated groups after tribocorrosion tests.

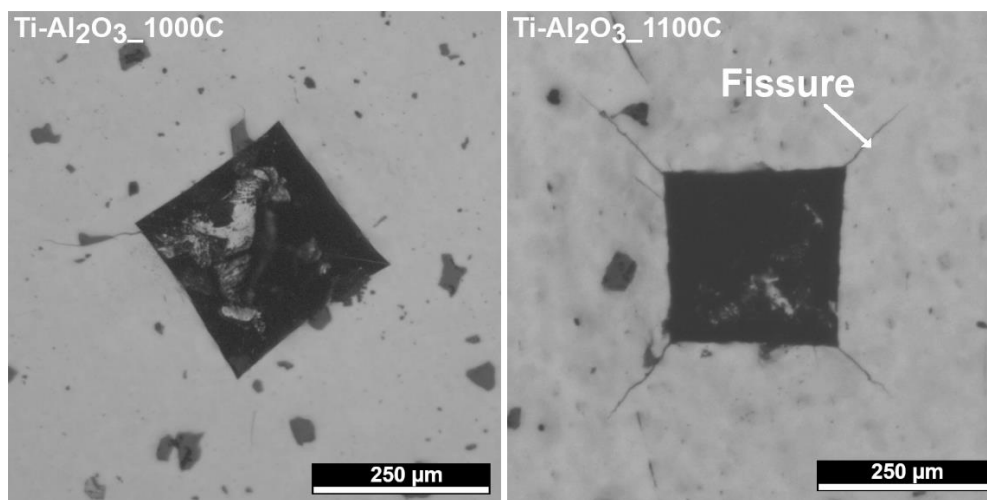
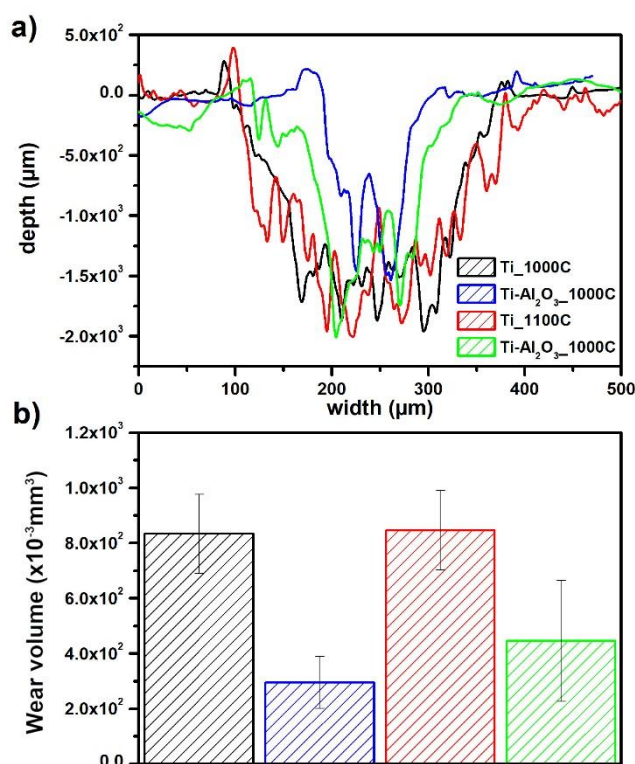


Figure 7.8. Representative optical microscope (OM) images of Vickers indentations for each composite group.

Representative wear track profiles together with the average wear volume values for untreated groups can be seen on Fig. 7.9. Since no significant wear was observed on the MAO treated groups, it was not possible to measure wear volume loss for these groups. Ti groups presented practically the same behaviour with no differences on the average wear volume loss values. Composites presented about 50% reduction in wear volume loss, with Ti-Al<sub>2</sub>O<sub>3</sub>\_1000C group showing the lowest values, which is probably attributed to the increased fracture toughness compared to the other composite group.



**Figure 7.9.** a) Representative wear track profiles and b) average wear volume loss values calculated from wear profiles.

The corrosion and tribocorrosion behaviour of Ti-Al<sub>2</sub>O<sub>3</sub> composites were improved after MAO treatment, with an expected improvement on biological behaviour considering that the overall structure of the MAO layers, in terms of chemical/phase composition as well as morphology, were very similar to the ones already reported on Ti [47]. Even though, before considering these composites for load-bearing implants in contact with bone, the tribological consequences of the relative motions on bones against these composites should be investigated in depth. Afterwards, surface composition and topography should be optimized in order to obtain the optimum tribo-electrochemical and biological performance.

#### 7.4. Conclusions

Ti-Al<sub>2</sub>O<sub>3</sub> composites with a biofunctionalized Ti matrix were successfully produced by performing MAO treatment on Ti-Al<sub>2</sub>O<sub>3</sub> composites. The extension of the reaction zone formed due to Ti and Al<sub>2</sub>O<sub>3</sub> reaction influenced the corrosion and tribocorrosion behaviour of the as processed composites. In addition, these reaction zones lead to some heterogeneities in the structure of the MAO layer.

After MAO treatment, composites presented a significant improvement on the corrosion behaviour, and the possible negative effect of the reaction zone was avoided. Composites showed an improvement on tribocorrosion behaviour compared to unreinforced Ti through reduced overall wear volume losses. After MAO treatment the tribocorrosion behaviour was further improved





## References

- [1] N. Chawla, Y.L. Shen, Mechanical behavior of particle reinforced metal matrix composites, *Adv. Eng. Mater.* 3 (2001) 357–370.
- [2] A. Oliveira, F. Toptan, Wear Behavior of Ti-Al<sub>2</sub>O<sub>3</sub> Biocomposites in 9 g/L NaCl Solution, *J. Mater. Eng. Perform.* 28 (2019) 6000–6010.
- [3] J.I. Silva, A.C. Alves, A.M. Pinto, F. Toptan, Corrosion and tribocorrosion behavior of Ti-TiB-TiN<sub>x</sub> in-situ hybrid composite synthesized by reactive hot pressing, *J. Mech. Behav. Biomed. Mater.* 74 (2017) 195–203.
- [4] F. Toptan, A. Rego, A.C. Alves, A. Guedes, Corrosion and tribocorrosion behavior of Ti-B<sub>4</sub>C composite intended for orthopaedic implants, *J. Mech. Behav. Biomed. Mater.* 61 (2016) 152–163.
- [5] M. Navarro, A. Michiardi, O. Castaño, J.A. Planell, Biomaterials in orthopaedics, *J. R. Soc. Interface.* 5 (2008) 1137–1158.
- [6] S. Affatato, F. Traina, M. De Fine, S. Carmignato, A. Toni, Alumina-on-alumina hip implants: A wear study of retrieved components, *J. Bone Jt. Surg. - Br. Vol.* 94–B (2012) 37–42.
- [7] S. Affatato, F. Traina, A. Toni, Microseparation and stripe wear in alumina-on- alumina hip implants, *Int J Artif Organs.* 34 (2011) 506–512.
- [8] P. Boyer, D. Hutten, P. Loriaut, V. Lestrat, C. Jeanrot, P. Massin, Is alumina-on-alumina ceramic bearings total hip replacement the right choice in patients younger than 50 years of age? A 7 to 15 year follow-up study, *Orthop. Traumatol. Surg. Res.* 96 (2010) 616–622.
- [9] B. Masson, Emergence of the alumina matrix composite in total hip arthroplasty, *Int. Orthop.* 33 (2009) 359–363.
- [10] M. Liu, Z. Wang, J. Wu, Q. Li, Effects of Nd<sub>2</sub>O<sub>3</sub> on the mechanical properties and oxidation behavior of Ti/Al<sub>2</sub>O<sub>3</sub> composites by vacuum hot pressing sintering, *J. Alloys Compd.* 648 (2015) 116–121.
- [11] Girish P. Kelkar, A.H. Carim, Phase Equilibria in the Ti-Al-O system at 945°C and Analysis of Ti/Al<sub>2</sub>O<sub>3</sub> reactions, *J. Am. Ceram. Soc.* 3 (1995) 572–573.
- [12] S. Meir, S. Kalabukhov, N. Frage, S. Hayun, Mechanical properties of Al<sub>2</sub>O<sub>3</sub>/Ti composites fabricated by spark plasma sintering, *Ceram. Int.* 41 (2015) 4637–4643.
- [13] T. Fujii, K. Tohgo, M. Iwao, Y. Shimamura, Fabrication of alumina-titanium composites by spark plasma sintering and their mechanical properties, *J. Alloys Compd.* 744 (2018) 759–768.
- [14] M. Bahraminasab, S. Ghaffari, H. Eslami-Shahed, Al<sub>2</sub>O<sub>3</sub>-Ti functionally graded material prepared by spark plasma sintering for orthopaedic applications, *J. Mech. Behav. Biomed. Mater.* 72 (2017) 82–89.
- [15] M. Bahraminasab, M. Bozorg, S. Ghaffari, F. Kavakebian, Electrochemical corrosion of Ti-Al<sub>2</sub>O<sub>3</sub> biocomposites in Ringer's solution, *J. Alloys Compd.* 777 (2019) 34–43.
- [16] M. Bahraminasab, M. Bozorg, S. Ghaffari, F. Kavakebian, Corrosion of Al<sub>2</sub>O<sub>3</sub>-Ti composites under inflammatory condition in simulated physiological solution, *Mater. Sci. Eng. C.* 102 (2019) 200–211.
- [17] C.Q. Ning, Y. Zhou, In vitro bioactivity of a biocomposite fabricated from HA and Ti powders by powder metallurgy method, *Biomaterials.* 23 (2002) 2909–2915.
- [18] H. Ye, X. Yang, H. Hong, Cladding of titanium/hydroxyapatite composites onto Ti6Al4V for load-bearing implant applications, *Mater. Sci. Eng. C.* 29 (2009) 2036–2044.
- [19] M. Ferraris, A. Ventrella, L. Paracchini, A. Krajewski, E. Verne, Sintering and Plasma Spray Deposition of Bioactive Glass-Matrix Composites for Medical Applications, 18 (1998) 363–372.

- [20] C. Ning, Y. Zhou, Correlations between the in vitro and in vivo bioactivity of the Ti / HA composites fabricated by a powder metallurgy method, *Acta Biomater.* 4 (2008) 1944–1952.
- [21] Y. Wang, H. Yu, C. Chen, Z. Zhao, Review of the biocompatibility of micro-arc oxidation coated titanium alloys, *Mater. Des.* 85 (2015) 640–652.
- [22] C. Chang, X. Huang, Y. Liu, L. Bai, X. Yang, R. Hang, B. Tang, P.K. Chu, High-current anodization : A novel strategy to functionalize titanium-based biomaterials, *Electrochim. Acta.* 173 (2015) 345–353.
- [23] Y. Zhao, T.-Y. Xiong, Formation of bioactive titania films under specific anodisation conditions, *Surf. Eng.* 28 (2012) 371–376.
- [24] B. Yang, M. Uchida, H.M. Kim, X. Zhang, T. Kokubo, Preparation of bioactive titanium metal via anodic oxidation treatment, *Biomaterials.* 25 (2004) 1003–1010.
- [25] Y. Li, B. Li, X. Fu, J. Li, C. Li, H. Li, H. Li, C. Liang, H. Wang, L. Zhou, S. Xin, Anodic Oxidation Modification Improve Bioactivity and Biocompatibility of Titanium Implant Surface, *J. Hard Tissue Biol.* 22 (2013) 351–358.
- [26] M. Tsai, Y. Chang, H. Huang, Y. Wu, T. Shieh, Micro-arc oxidation treatment enhanced the biological performance of human osteosarcoma cell line and human skin fibroblasts cultured on titanium – zirconium films, *Surf. Coat. Technol.* 303 (2016) 268–276.
- [27] G.G. de Lima, G.B. de Souza, C.M. Lepienski, N.K. Kuromoto, Mechanical properties of anodic titanium films containing ions of Ca and P submitted to heat and hydrothermal treatment, *J. Mech. Behav. Biomed. Mater.* 64 (2016) 18–30.
- [28] N.F. Daudt, M. Bram, A.P. Cysne Barbosa, C. Alves, Surface modification of highly porous titanium by plasma treatment, *Mater. Lett.* 141 (2015) 194–197.
- [29] C. Wang, Y. Bai, Y. Bai, J. Gao, W. Ma, Enhancement of corrosion resistance and bioactivity of titanium by Au nanoparticle-loaded TiO<sub>2</sub> nanotube layer, *Surf. Coatings Technol.* 286 (2016) 327–334.
- [30] A. Aalam, H. Nowzari, Clinical Evaluation of Dental Implants with Surfaces Roughened by Anodic Oxidation, Dual Acid-Etched Implants, and Machined Implants, *Int. J. Oral Maxillofac. Implants.* 20 (2005) 793–798.
- [31] A.C. Alves, F. Wenger, P. Ponthiaux, J.P. Celis, A.M. Pinto, L.A. Rocha, J.C.S. Fernandes, Corrosion mechanisms in titanium oxide-based films produced by anodic treatment, *Electrochim. Acta.* 234 (2017) 16–27.
- [32] G. Ryan, A. Pandit, D.P. Apatsidis, Fabrication methods of porous metals for use in orthopaedic applications, *Biomaterials.* 27 (2006) 2651–2670.
- [33] S. Meir, S. Kalabukhov, N. Frage, S. Hayun, Mechanical properties of Al<sub>2</sub>O<sub>3</sub>/Ti composites fabricated by spark plasma sintering, *Ceram. Int.* 41 (2014) 4637–4643.
- [34] M. Liu, Z. Wang, J. Wu, Q. Li, Ti/Al<sub>2</sub>O<sub>3</sub> interfacial diffusion: Kinetic equation for growth of reaction layer and formation mechanism, *J. Alloys Compd.* 652 (2015) 260–265.
- [35] L. Augusto, E. Ariza, A. Maria, Electrochemical Behavior of Ti/ Al<sub>2</sub>O<sub>3</sub> Interfaces Produced by Diffusion Bonding, *Mater. Res.* 6 (2003) 439–444.
- [36] L.E. Karkina, L.I. Yakovenkova, Dislocation core structure and deformation behavior of Ti<sub>3</sub>Al, *Mater. Sci. Eng.* 20 (2012) 0–20.
- [37] A.M. Kliauga, M. Ferrante, Interface compounds formed during the diffusion bonding of Al<sub>2</sub>O<sub>3</sub> to Ti, *J. Mater. Sci.* 35 (2000) 4243–4249.
- [38] A.C. Alves, F. Oliveira, F. Wenger, P. Ponthiaux, J.-P. Celis, L.A. Rocha, Tribocorrosion behaviour of anodic treated titanium surfaces intended for dental implants, *J. Phys. D. Appl. Phys.* 46 (2013) 404001.
- [39] F. Witte, V. Kaese, H. Haferkamp, E. Switzer, A. Meyer-Lindenberg, C.J. Wirth, H. Windhagen, In vivo corrosion of four magnesium alloys and the associated bone response, *Biomaterials.* 26 (2005) 3557–3563.

- [40] A.I. Costa, L. Sousa, A.C. Alves, F. Toptan, Tribocorrosion behaviour of bio-functionalized porous Ti surfaces obtained by two-step anodic treatment, *Corros. Sci.* 166 (2020) 108467.
- [41] Y. Chen, J. Zhang, N. Dai, P. Qin, H. Attar, L.-C. Zhang, Corrosion Behaviour of Selective Laser Melted Ti-TiB Biocomposite in Simulated Body Fluid, *Electrochim. Acta.* 232 (2017) 89–97.
- [42] M. Rani, D. Kim, E. Fleury, Intermetallics dependency of the corrosion properties of in-situ Ti-based BMG matrix composites with the volume fraction of crystalline phase, *Intermetallics.* 22 (2012) 255–259.
- [43] B. Bobić, S. Mitrović, M. Babić, I. Bobić, Corrosion of Metal-Matrix composites with aluminium alloy substrate, *Tribol. Ind.* 32 (2010) 3–11.
- [44] S.C. Ferreira, L.A. Rocha, E. Ariza, P.D. Sequeira, Y. Watanabe, J.C.S. Fernandes, Corrosion behaviour of Al/Al<sub>3</sub>Ti and Al/Al<sub>3</sub>Zr functionally graded materials produced by centrifugal solid-particle method: Influence of the intermetallics volume fraction, *Corros. Sci.* 53 (2011) 2058–2065.
- [45] F.G. Oliveira, A.R. Ribeiro, G. Perez, B.S. Archanjo, C.P. Gouvea, J.R. Araújo, A.P.C. Campos, A. Kuznetsov, C.M. Almeida, M.M. Maru, C.A. Achete, P. Ponthiaux, J.P. Celis, L.A. Rocha, Understanding growth mechanisms and tribocorrosion behaviour of porous TiO<sub>2</sub> anodic films containing calcium, phosphorous and magnesium, *Appl. Surf. Sci.* 341 (2015) 1–12.
- [46] M. Niinomi, Mechanical properties of biomedical titanium alloys, *Mater. Sci. Eng. A.* 243 (1998) 231–236.
- [47] A.C. Alves, R. Thibeaux, F. Toptan, A.M.P. Pinto, P. Ponthiaux, B. David, Influence of macroporosity on NIH/3T3 adhesion, proliferation, and osteogenic differentiation of MC3T3-E1 over bio-functionalized highly porous titanium implant material, *J. Biomed. Mater. Res. Part B - Appl. Biomater.* (2018) 1–13.



## Chapter 8

### Effect of micro-arc oxidation and thermal oxidation treatments on Ti-B<sub>4</sub>C composite surfaces intended for biomedical applications

*To be submitted*

---

**L. Sousa**<sup>a,b,\*</sup>, N. A. Costa<sup>c</sup>, A. Rossi<sup>c</sup>, S. Simões<sup>b,d</sup>, F. Toptan<sup>a,e,f,\*</sup>, A.C. Alves<sup>a,e</sup>

<sup>a</sup>*CMEMS-UMinho – Center of MicroElectroMechanical Systems – Universidade Minho, Campus de Azurém, Guimarães, Portugal.*

<sup>b</sup>*DEMM, Department of Metallurgical and Materials Engineering, University of Porto, Rua Dr. Roberto Frias, Porto, 4200-465, Portugal*

<sup>c</sup>*Centro Brasileiro de Pesquisa Física (CBPF), R. Dr. Xavier Sigaud, 150 - Urca, Rio de Janeiro – RJ*

<sup>d</sup>*LAETA/INEGI, Institute of Science and Innovation in Mechanical and Industrial Engineering, R. Dr. Roberto Frias, Porto, 4200-465, Portugal*

<sup>e</sup>*IBTN/Euro – European Branch of the Institute of Biomaterials, Tribocorrosion and Nanomedicine, Dept. Eng. Mecânica, Universidade do Minho, Azurém, 4800-058 Guimarães, Portugal*

<sup>f</sup>*Department of Materials Science and Engineering, Izmir Institute of Technology, 35430, Urla, Izmir, Turkey*



## **Abstract**

Titanium matrix composites have improved tribocorrosion resistance compared to Ti, however, biocompatibility for biomedical applications remains an issue. Micro-arc oxidation (MAO) and thermal oxidation (TO) treatments are simple techniques to improve the bioactivity of Ti. However, their effect on composite surfaces, particularly the matrix/reinforcement interface is poorly understood. In this work, MAO and TO treatments were carried out on Ti-B<sub>4</sub>C composites processed by hot-pressing. Treated composites presented improved corrosion and tribocorrosion behaviour compared to the untreated ones. However, both treatments also led to B<sub>4</sub>C particle detachment due to the growth of an oxide layer on the interface between the B<sub>4</sub>C particles and the reaction zones.

### **8.1. Introduction**

Ti and its alloys are among the most used materials for load bearing biomedical implants owing to their biocompatibility, good corrosion resistance and adequate mechanical properties. However, these materials still present poor tribological behaviour and lack the bioactivity to promote adequate osteointegration with adjacent bone [1,2]. Titanium matrix composites (TMCs) provide improved wear resistance over the base Ti or Ti alloy. In addition, low density and high specific strength made these materials find their use in aerospace and automotive applications [3]. These materials may also have potential for load bearing biomedical implants. Over the years, studies have shown that reinforcement phases can effectively improve the tribocorrosion behaviour of Ti and its alloys without jeopardizing the corrosion properties of the base material.

In a previous study by some of the present authors [4], it was shown that TMCs reinforced with a relatively small amount (3% vol.) of B<sub>4</sub>C reinforcement particles have improved tribocorrosion behaviour through reduced tendency to corrosion and corrosion kinetics during sliding action, in addition to considerably reduced wear volume loss. Nevertheless, lack of bioactivity is yet to be overcome once most reinforcement phases are bioinert.

Several techniques can be used to improve the bioactivity of Ti. Among them, MAO and thermal oxidation TO techniques are well known simple techniques to produce thick TiO<sub>2</sub> oxide layers with tailored properties that can improve bioactivity [5,6]. MAO, consists of the application of several hundreds of volts through an electrolyte rich in bioactive elements such as calcium (Ca) and phosphorous (P) to produce a micro-porous oxide layer with improved osteointegration capabilities [7,8] together with increased bioactivity [9–11]. MAO treatment has also been performed on TMCs surfaces with promising results. In a previous study by some of the present authors, the effect of MAO treatment on Ti-Al<sub>2</sub>O<sub>3</sub> composite surfaces was studied. The biofunctionalized composites comprised Al<sub>2</sub>O<sub>3</sub> reinforcement particles dispersed within a biofunctionalized titanium matrix surface with a micro-porous structure. In addition to a considerable improvement in corrosion behaviour, biofunctionalized composites also presented improved tribocorrosion behaviour over the untreated composites. Çaha et al. [12] performed MAO treatment on Ti-TiN composites and reported that both reinforcement phases and the Ti matrix were covered by the typical volcano-like structure obtained by MAO treatment. Overall, the authors reported an improvement in both corrosion and tribocorrosion behaviour for the biofunctionalized composites.

TO treatment is also a cost-effective and straightforward technique that takes advantage of the high reactivity of Ti with air and/or water to promote the growth of the native TiO<sub>2</sub> passive layer and alter its properties in terms of topography, chemical composition and crystal structure, leading to improved bioactivity [13–16].

The effect of these techniques on the properties of Ti and its alloys have been thoroughly researched in the last years, in terms of corrosion, tribocorrosion, and biological properties. However, their effect on TMC surfaces is still relatively unknown. In this work, MAO and TO treatments were carried out on TMCs reinforced with B<sub>4</sub>C particles, and the effect of these treatments on the composite surfaces was studied in terms of morphology, corrosion, and tribocorrosion behaviour.



## 8.2. Materials and methods

### 8.2.1. Processing

Ti-1.9 wt.% B<sub>4</sub>C composites were processed by mixing Ti grade 2 and B<sub>4</sub>C powders with irregular shapes and average particle sizes of 25 and 42 μm, respectively. Samples were processed by hot-pressing at 1100 °C for 30 min, under an applied pressure of 40 MPa and under high vacuum ( $\leq 10^{-5}$  mbar). A more detailed description of the processing method was given previously [4]. Before characterization and testing, untreated composite samples were ground down to 2400 mesh SiC papers and then finished until 0.04 μm with colloidal silica suspension. Samples were then cleaned by propanol and distilled water in an ultrasonic bath for 10 and 5 min, respectively, and kept in a desiccator for 24 h prior to each test to obtain similar surface conditions.

For MAO treatment, mirror finished samples were placed in an electrochemical cell connected to a DC power supply (Agilent technologies N5772A), with an exposed area of 0.38 cm<sup>2</sup>, distanced 80 mm from an Pt cathode having an exposed area of 1.77 cm<sup>2</sup>. MAO treatment was then performed under a turbulent regime using a magnetic stirrer spinning at 200 rpm. A constant voltage of 300 V was applied for 1 min with an imposed current limit of 2.5 A. A mixture of 0.35 M of calcium acetate monohydrate (CA, Sigma-Aldrich) and 0.02 M of β-glycerophosphate disodium salt pentahydrate (β-GP, Alfa Aesar) was used as an electrolyte.

For thermal oxidation treatment, samples were ground down to 600 mesh SiC paper, cleaned as described previously and then placed in a tubular furnace with open atmosphere. The thermal cycle was set to 800 °C for 20 min, with both heating and cooling rates set to 5 °C/min.

### 8.2.2. Electrochemical tests

Electrochemical tests were carried out in phosphate-buffered saline solution (PBS: 0.24 g/l KH<sub>2</sub>PO<sub>4</sub>, 0.2 g/l KCl, 1.44 g/l Na<sub>2</sub>HPO<sub>4</sub>, 8 g/l NaCl) with pH 7.4 at body temperature (37 °C). The electrochemical cell was placed in a climate chamber to keep the temperature constant and at the same time to act as a Faraday cage in order to avoid any external currents. OCP was first monitored until stabilization of the system ( $\Delta E < 60$  mV/h) and then potentiodynamic polarization tests were performed from a potential of  $-0.2 V_{OCP}$  to  $1.5 V_{Ag/AgCl}$  with

a scanning rate of 1 mV/s. Cyclic polarization scans were also performed on the untreated composites. After the potentiodynamic scan, the sweep direction was reversed at 1.5 V using the same potential range and scanning rate. In addition, potentiostatic tests for 1 h at 1 and 1.4 V were also carried out in the untreated composites (potential values were chosen based on the PD curves obtained). All tests were performed using a standard three-electrode setup consisting of a saturated Ag/AgCl reference electrode, a platinum counter electrode and the sample as working electrode with an exposed area of 0.1 cm<sup>2</sup>. All electrochemical tests were carried out in a Gamry Potentiostat/Galvanostat/ZRA (model Referece-600+).

### 8.2.3. Tribocorrosion tests

Tribocorrosion tests were performed in a tribometer (CETR-UMT2) with a ball-on-plate configuration and reciprocating stage, using an identical PBS solution at body temperature. Two distinct loads, 0.5 and 10 N, corresponding to a maximum Hertzian contact pressure of 342 and 930 GPa, respectively, for Ti, were used. Before sliding, OCP values were monitored until stabilization ( $\Delta E < 60$  mV/h), and following the stabilization, OCP values were monitored under sliding for 3600 s and also after sliding for the same period of time. Coefficient of friction (COF) values were also observed during sliding. Sliding time, frequency and stroke length were set as 60 min, 1Hz and 3 mm, respectively, for both loads. The electrochemical measurements were performed using a Gamry Potentiostat/Galvanostat/ZRA (model Referece-600) with a two-electrode set-up, where the tested material acted as a working electrode and a saturated Ag/AgCl electrode used as reference electrode. All samples after tribocorrosion tests were cleaned with the same cleaning procedure described previously.

### 8.2.4. Characterization

The microstructure of the untreated composites and MAO and TO treated composite surfaces was analysed by FEG-SEM (FEI Nova 200). In order to investigate the microstructure in more detail of the untreated composite more in detail, lamella for transmission electron microscope (TEM) observation was obtained by focused ion beam (FIB, Tescan-Lyra 3 dual beam) with gallium (Ga)

ion source attached to the same FEG-SEM equipment. Afterwards, TEM analysis was performed in a TEM equipment (JEOL 2100F) operating at 200 kV equipped with CCD camera (GATAN Orius) and EDS (Noran Seven). XRD analysis was conducted in a diffractometer (Bruker D8 Discover) with Cu-K $\alpha$  radiation ( $\lambda = 1.54056 \text{ \AA}$ ) at 40 kV and 40 mA scanning from 20 to 80 ° at 0.04°/2 s. Vickers micro-hardness of the cross-section of TO treated composites was accessed to evaluate the hardness of the oxygen diffusion zone (ODZ). An indenter (EMCOTEST Durascan) was used by applying a 25 g load during 15 s (at least 5 indentations were performed in order to assure repeatability of the results). The worn surfaces obtained after tribocorrosion were observed by FEG-SEM (FEI Nova 200) and the chemical composition was evaluated through EDAX energy dispersive X-ray spectroscopy (EDS). 2D wear track profiles were obtained by profilometry (Veeco, Dektak 150), which were used to estimate wear volume loss values using a procedure described elsewhere [17].

### **8.3. Results and discussion**

#### *8.3.1. Microstructure*

The overall microstructure of the as-processed composites was composed of B<sub>4</sub>C particles dispersed within a Ti matrix, with the formation of a reaction zone between reinforcement particles and the Ti matrix (Fig. 8.1a). A similar microstructure was reported in previous work by some of the present authors, where composites were processed under identical conditions [4]. The reaction zone was composed of a mixture of TiB and TiC phases, as suggested by XRD and TEM analysis, which have been widely reported to be the main reaction products resulting from the reaction of Ti and B<sub>4</sub>C powders [18–21]. The B<sub>4</sub>C/reaction zone interface (Fig. 8.1c) was characterized by a gradual decrease in Ti and an increase in B and C elements.

After MAO treatment (Fig. 8.2), the composite surfaces were covered by a micro-porous oxide layer with a volcano-like structure incorporating Ca and P elements from the electrolyte. B and C elements could also be detected, although it is rather possible that these could come from the substrate. Ca/P atomic ratio was calculated as 3.24 and XRD analysis revealed a mixture of anatase and rutile phases (Fig. 8.3), which are in accordance with previous works on CP Ti surfaces using identical MAO parameters [5,22].

B<sub>4</sub>C Particle depleted zones, where the continuity of the MAO layer was interrupted were observed on the surfaces and can be seen in more detail on the cross-section optical microscope image shown in Fig. 8.2b. Images show that some B<sub>4</sub>C particles were pulled out from the surface during MAO treatment, leading to the formation of these particle depleted zones. The MAO layer also covered the zones left behind. Besides these particle depleted zones, some B<sub>4</sub>C particles surrounded by the MAO layer were also observed (Fig. 8.2c), where the MAO layer grew on the reaction zones and trapped the B<sub>4</sub>C particles within the surface.

The overall microstructure for TO treated composites can be seen in Figs. 8.4a and 8.4b, as well as in the cross-section SEM images presented in Figs. 8.4c-e. TO treatment led to the formation of a thick TiO<sub>2</sub> layer on the composite surfaces, which was mostly composed of rutile phase (Fig. 8.3). TO treatments performed at high temperatures (usually above 700 °C) on Ti and Ti alloys are reported to form TiO<sub>2</sub> oxide layers rich in rutile phases [23,24], while at lower temperatures, anatase or a mixture of rutile and anatase phases are usually observed [25]. Similar to MAO treated composites, B<sub>4</sub>C particle depleted zones were also observed within the surfaces. In this case, it was also clear that the reaction zones were still present and only the B<sub>4</sub>C was ejected from the surface. These zones can be seen more clearly on the cross-section SEM images shown in Fig. 8.4c. B<sub>4</sub>C particles surrounded by an oxide layer were also observed (Fig. 8.4e), where B and C elements from the reaction zone were also detected. TO treatment also lead to diffusion of oxygen into the Ti matrix, and thus the formation of an oxygen diffusion zone (ODZ) with an average depth of 12 μm, Fig. 8.4f, which lead to an increase in the overall hardness of the Ti matrix from  $411 \pm 18$  to around  $597 \pm 17$  HV<sub>0.025</sub> in this zone.

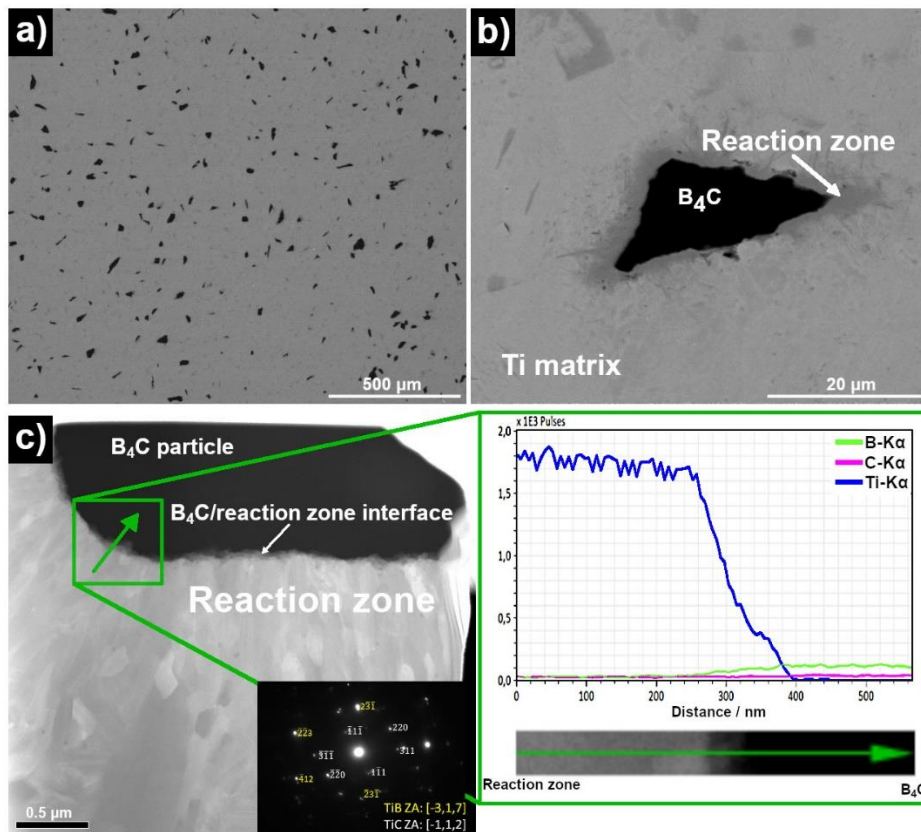


**Figure 8.1.** a and b) Backscattered electron (BSE) SEM images of the untreated composite, c) dark-field TEM image of the B<sub>4</sub>C and reaction zone together with line EDS scan, and diffraction pattern for TiB and TiC phase.

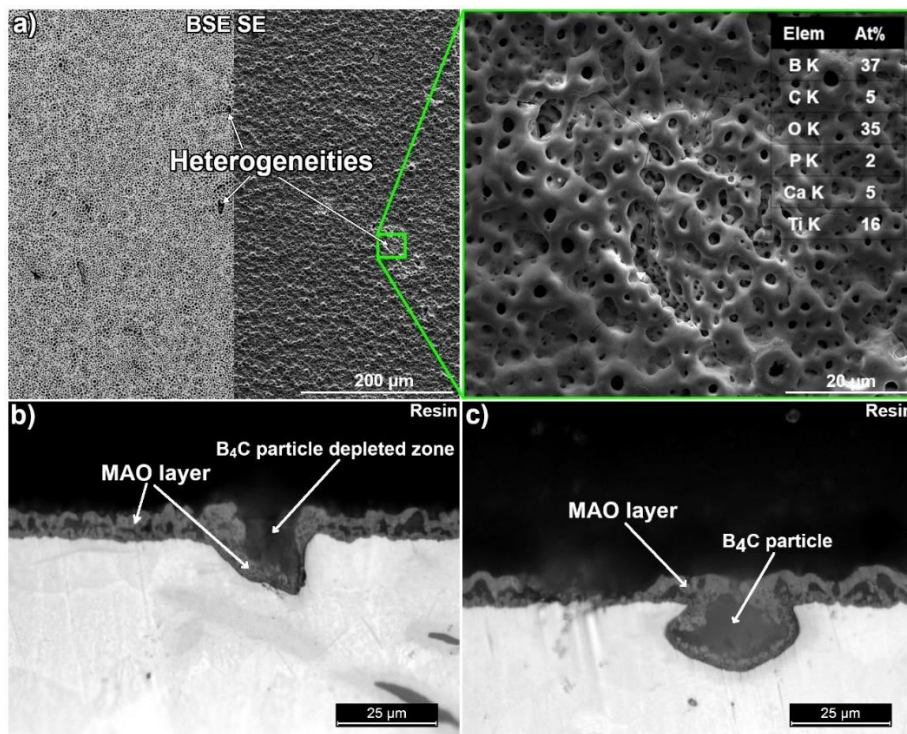


**Figure 8.2.** a) BSE and secondary electron (SE) SEM images of the composite surfaces after MAO treatment, and b) cross-section optical microscope (OM) images of composites after MAO treatment.

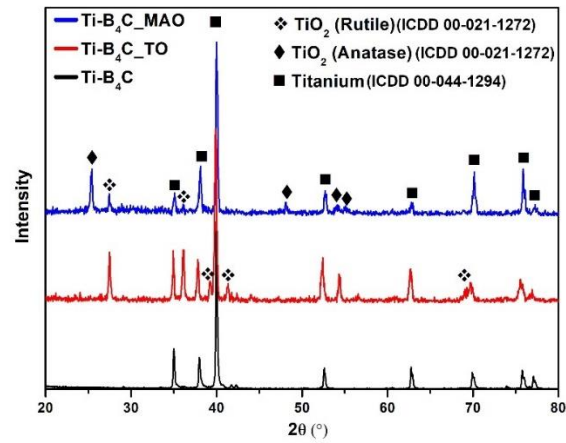


**Figure 8.3.** XRD patterns for untreated, MAO and TO treated Ti-B<sub>4</sub>C composites.

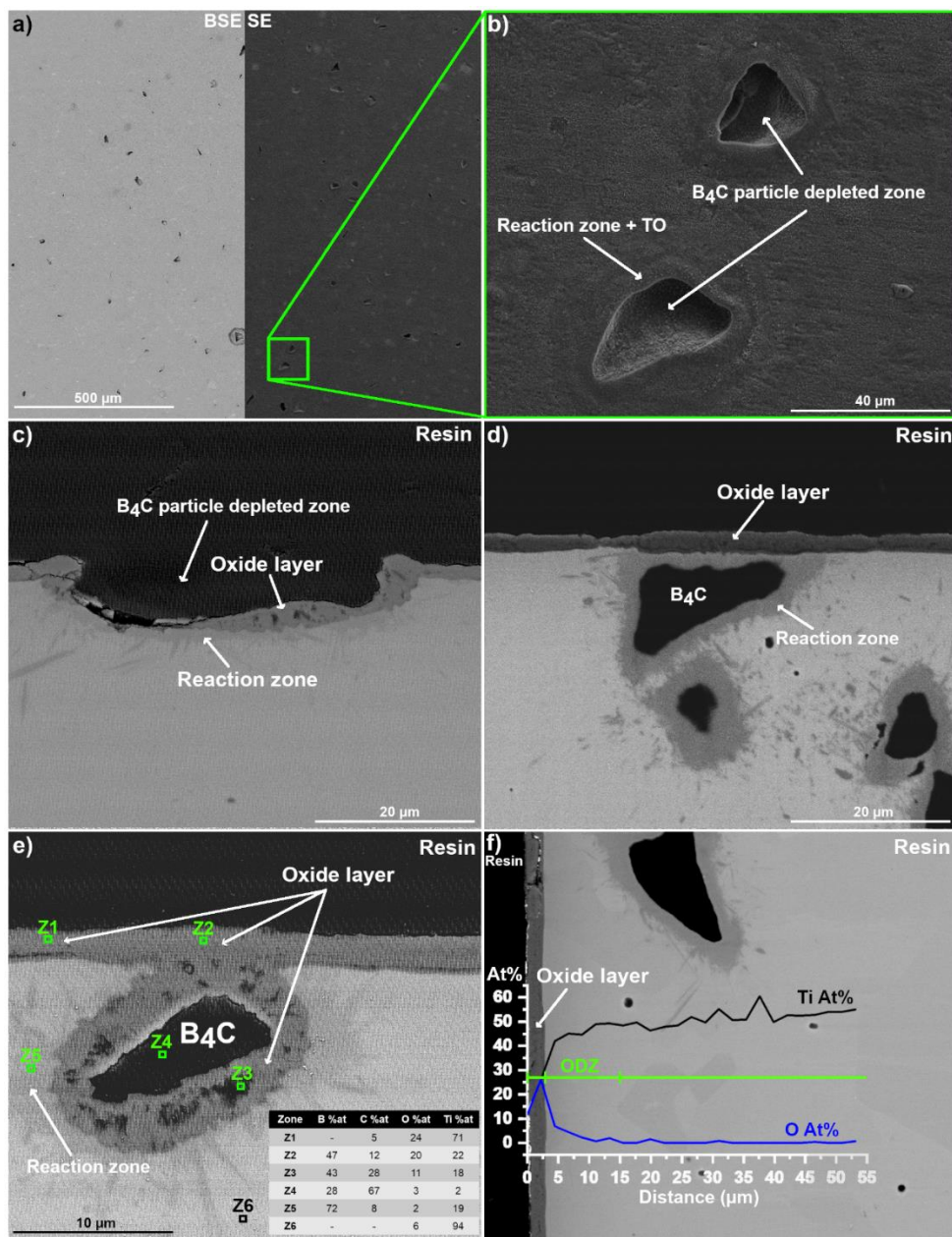
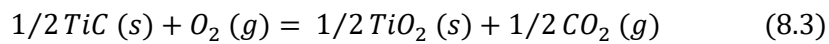
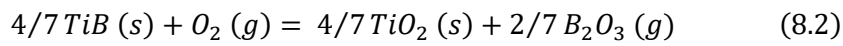


**Figure 8.4.** a,b) BSE and SE SEM images of composite surfaces after TO treatment and c,d,e,f) BSE SEM images of cross-sections obtained for TO treated Ti-B<sub>4</sub>C composites.



Overall, the morphology of the composites after MAO and TO treatments was composed of a functionalized Ti matrix plus reaction zones, with B<sub>4</sub>C particle depleted zones, where these zones were also covered by the MAO and TO oxide layers. All in all, these results suggested for Ti-B<sub>4</sub>C composites that after a specific potential, or temperature in the case of TO treatment, an oxide layer is formed at the B<sub>4</sub>C/reaction zone interface which can result in the detachment of B<sub>4</sub>C particles from the composite surfaces. Either by application of temperature or through an applied potential, the formation of TiO<sub>2</sub> oxide layer on TiB and TiC phases has been reported before [18,26]. At 800 °C the oxidation reactions reported in air are given below [18]:



At these temperature ranges, these reactions have negative values of Gibbs free energy ( $\Delta G$ ) [18], meaning that these reactions are favourable. Moreover reaction 8.2 and 8.3 have higher  $\Delta G$  values than reaction 8.1, thus reinforcement phases have higher oxidation resistance than the Ti matrix. Regarding B<sub>2</sub>O<sub>3</sub>, due to the amorphous structure and the fact that it evaporates easily, these are usually not observed in the composition of the oxide layers [27–29].

The effect of MAO treatment on TiB and TiC phases is still rather unknown, especially on TMCs reinforced with these phases. Zhang et al. [26] studied the effect of MAO treatment on an aluminium matrix composite (AMC) reinforced with 8 wt.% TiB<sub>2</sub> (TiB<sub>2</sub>/A201) by using an aluminate-based electrolyte and a constant current density of 10 A/dm<sup>2</sup>. The authors observed that in an earlier stage of the MAO treatment (150 – 200V) the TiB<sub>2</sub> particles oxidized into TiO<sub>2</sub> and with time these particles tended to be fully transformed into TiO<sub>2</sub>. In a previous study by some of the present authors [22], Ti-Al<sub>2</sub>O<sub>3</sub> composites were also biofunctionalized using identical MAO parameters and a distinct behaviour was observed. The overall morphology of the untreated composites was quite similar, which was composed of Al<sub>2</sub>O<sub>3</sub> particles dispersed within a Ti matrix with the formation of a reaction zone (mixture of TiAl and Ti<sub>3</sub>Al phases) around the Al<sub>2</sub>O<sub>3</sub> particles. After MAO treatment, the resulting microstructure consisted of Al<sub>2</sub>O<sub>3</sub>

particles dispersed within a biofunctionalized Ti matrix with the same volcano-like structure, no detachment of Al<sub>2</sub>O<sub>3</sub> particles was observed.

In the case of the present composites, the proposed mechanism (Fig. 8.5) is as follows. Due to applied potential or temperature, a TiO<sub>2</sub> oxide layer starts to form on the Ti matrix and the adjacent reaction zones (TiB + TiC). With time, the thickness of this layer increases, meanwhile, this layer also propagates through the B<sub>4</sub>C/reaction zone interfaces. The formation of an oxide layer on the (TiB + TiC) reaction zone leads to the detachment of B<sub>4</sub>C particles from the surface once the formation of the oxide layer leads to the breakdown of the B<sub>4</sub>C/reaction zone interface (Fig. 8.2b). In some cases, only the tip of the B<sub>4</sub>C particle stays on the outmost surface. In this way, the oxide layer propagates through the reaction zone around the B<sub>4</sub>C particle. In the end, a B<sub>4</sub>C particle surrounded by an oxide layer is obtained (Fig. 8.2c).

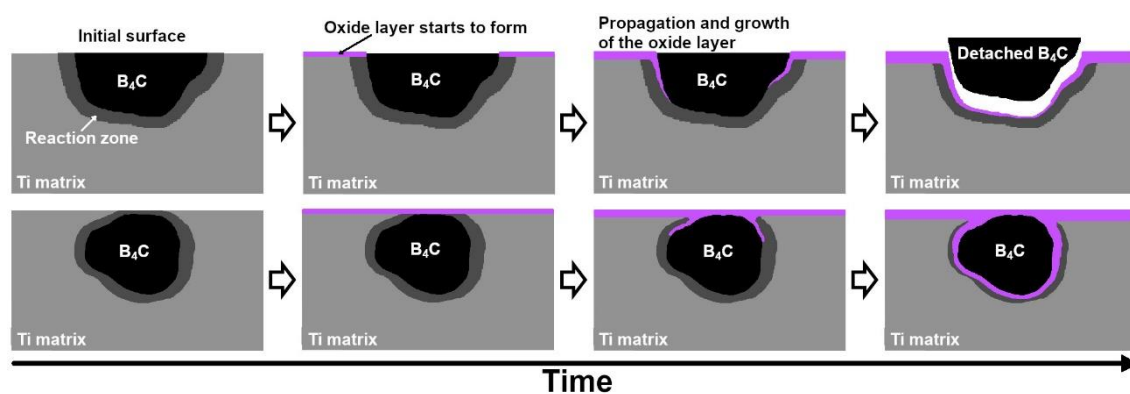


**Figure 8.5.** Proposed mechanism for the oxidation behaviour of Ti-B<sub>4</sub>C composites.

### 8.3.2. Electrochemical behaviour

Representative potentiodynamic polarization curves for all groups can be seen in Fig. 8.6. Untreated composites presented the typical passive behaviour of Ti or its alloys, characterized by a well-defined passivation plateau between 0.25 and 1.1 V due to the formation of a passive oxide film. However, for potentials above 1.1 V a sudden increase in corrosion current density was observed. This behaviour was not observed for unreinforced Ti processed under the identical conditions [22]. After MAO and TO treatments, a considerable reduction in the current density values was observed, due to the protective nature of the MAO and TO oxide layers, which are well reported to improve the corrosion resistance of Ti-based materials [5,30–32]. An increase in current density values for potentials above 1.1 V was still observed for the treated composites. Although



the results could point to localized corrosion, the CP scan for the untreated composites revealed that this was not the case once lower current density values were observed in the reverse scan. To further investigate this behaviour, potentiostatic tests at 1 and 1.4 V were performed on the untreated composites for 60 min. 1 V was chosen to study the behaviour in the passive zone, while 1.4 V was selected to study the corrosion behaviour where the passive film seems to lose its integrity Fig. 8.7 shows the evolution of current density for both applied potentials, as well as OM images of the composites surfaces before and after the potentiostatic tests. Corrosion current densities measured at 1 V applied potential were significantly lower than the ones observed at 1.4 V, as is in accordance with potentiodynamic polarization results. For 1 V, corrosion current densities stabilized shortly after the potential was applied, that was not the case for the tests carried out at 1.4 V, where corrosion current densities tended to decrease during the whole testing period. No considerable changes were observed on the composite surfaces after 1 h at 1 V, however, when 1.4 V was applied, a significant amount of B<sub>4</sub>C particles were detached from the surface. Important to note that after the PD tests, no detachment of B<sub>4</sub>C particles was observed once the time spent at these potentials was relatively short compared to the potentiostatic tests.

The results show increased corrosion kinetics for potentials above 1 V. Considering that Ti composites reinforced with TiB, TiC, and TiB<sub>2</sub> phases do not present this behaviour at these potential ranges [33,34], this response is most probably related to the B<sub>4</sub>C/interface. The results point to the degradation of this interface at these potentials and thus detachment of B<sub>4</sub>C particles from the surface. This behaviour was also observed on the MAO and TO treated composites suggesting that there is still an electrochemical response coming from these interfaces.

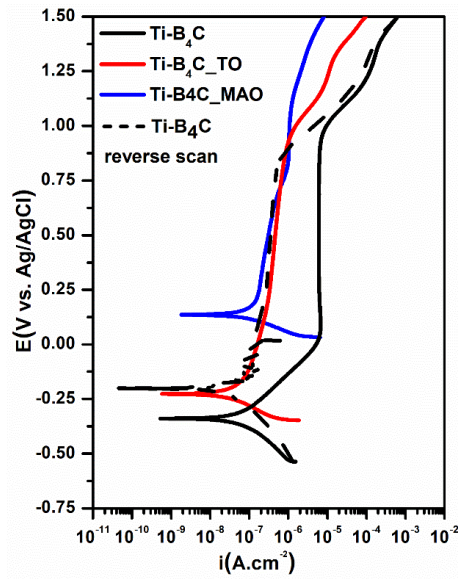


**Figure 8.6.** Potentiodynamic polarization curves for all tested groups together with a CP scan for the untreated composite.

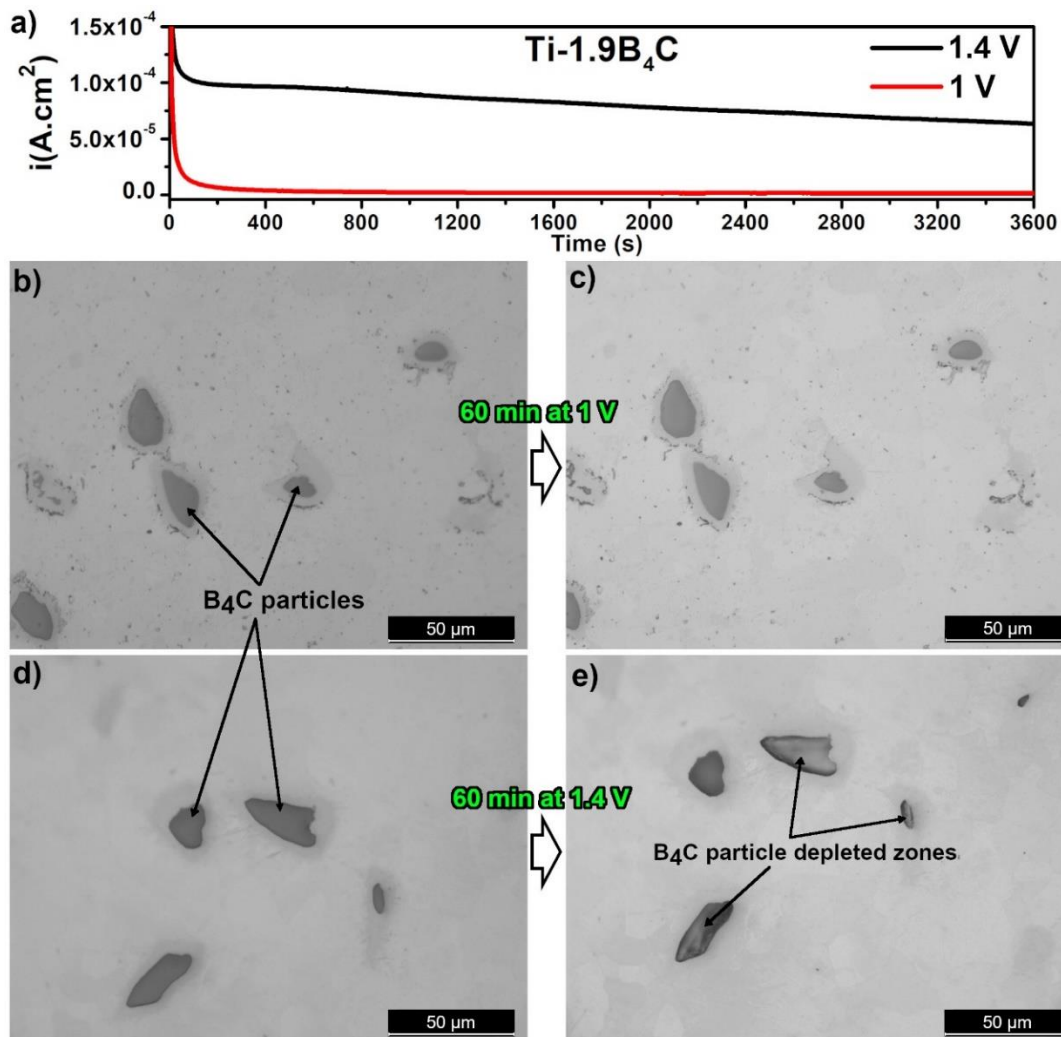


**Figure 8.7.** a) Evolution of current density during potentiostatic tests for the untreated composites; optical microscope (OM) images of composite surfaces b) before and c) after potentiostatic tests at 1 V; and OM images of composite surfaces d) before and e) after potentiostatic tests at 1.4 V.

### 8.3.3. Tribocorrosion behaviour

The evolution of OCP before, during and after sliding, together with evolution of COF during sliding for 0.5 N and 10 N applied loads can be seen in Fig. 8.8. For the untreated composites, after sliding started, a sudden decrease in OCP values was observed for both loads, due to removal of the passive oxide film and exposure of the fresh metallic surface to the electrolyte. For 0.5 N load, soon after sliding started, OCP values partially recovered and displayed a relatively horizontal course except for some occasional drops in OCP, which were accompanied by an increase in COF. In Ti-based materials, sudden changes in OCP and COF values during tribocorrosion tests are usually related to the continuous formation and breaking down of compacted oxide debris, which changes the overall topography of the worn surfaces, and thus COF values, and also give limited protection against corrosion as these oxides protect the metallic substrate.

For 10 N condition, OCP values during sliding were considerably lower, while COF values were higher, due to more significant wear damage on the composite surfaces. In addition, no sudden drops in OCP and COF values were observed. It may be expected that under harsher conditions, stabler OCP and COF values can be observed once most wear debris tends to be pushed outside the wear tracks and thus does not contribute to the formation of compacted oxide debris [35]. Once sliding finished, OCP values also quickly increased to those observed before sliding due to repassivation of the worn zone.

For MAO and TO treated groups tested under 0.5 N load, no changes in OCP values were observed during sliding once no considerable wear damage was given to the functionalized surfaces under these conditions (Fig. 8.9). Accordingly, only a relatively low amount of Ti was transferred to the counter-body surfaces (Fig. 8.9). The overall COF values for TO groups were lower than the ones observed for MAO groups due to smoother and compact nature of the TO oxide layer. Additionally, higher amount of rutile phase can also contribute to lower COF values since rutile has been reported to present a self-lubrication behaviour [36].

Significant differences were observed between the treated groups for 10 N load. TO treated composites presented a sharp OCP drop on the onset of sliding,

suggesting that considerable damage was done to the oxide layer. Nevertheless, the OCP drop was considerably lower than the one observed for the untreated group. After a few minutes of sliding and adjustment of contacting surfaces, OCP and COF values tended to decrease and stabilize towards the end of sliding action. On the other hand, MAO treated composites presented a distinct behaviour, where a gradual decrease in OCP values was observed on the onset of sliding, suggesting a relatively better wear resistance on the MAO layers in an earlier stage. However, the lowest OCP values were registered for this group after some time, which remained until the end of sliding. After sliding, OCP values for TO group reached the values obtained before sliding. In contrast, values for the MAO treated groups only reached similar OCP values as the ones observed for the untreated group. The higher OCP values for TO groups are most probably related to the presence of the ODZ, which is reported to have higher corrosion resistance than Ti due to incorporation of oxygen accelerating the formation of the native oxide passive film [31]. Under these conditions, COF values for TO group were lower and the evolution was smoother than those observed for MAO group. At the same time, the untreated composites also presented a smoother behaviour and COF values between TO and MAO groups.

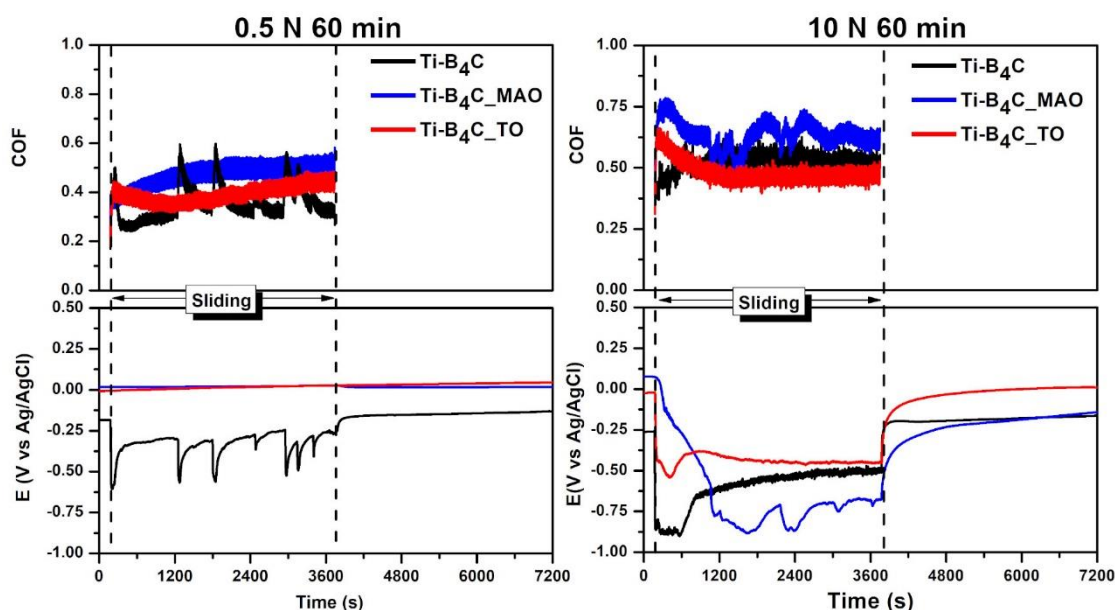
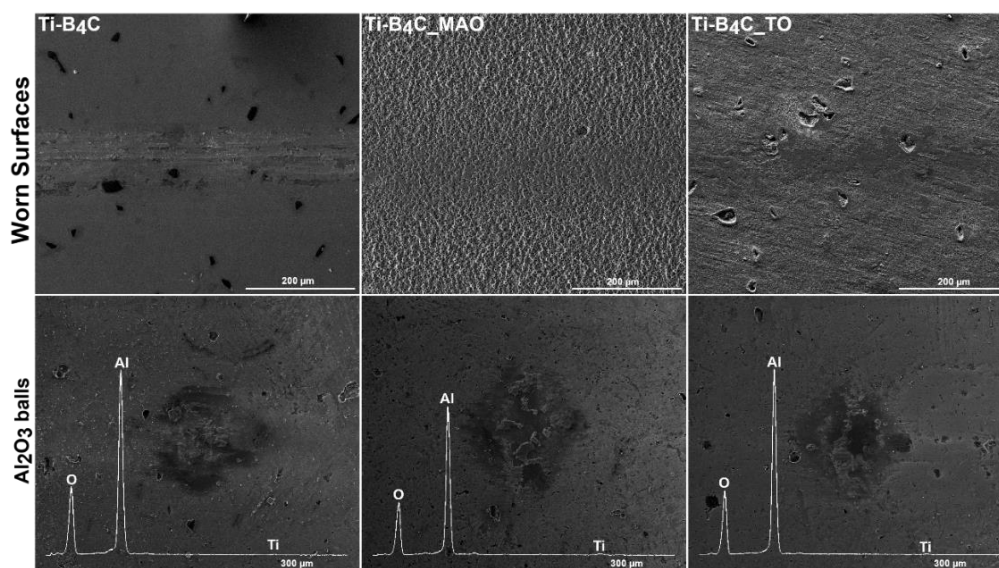


Figure 8.8. OCP evolution before, during and after sliding, together with the evolution of COF during sliding.



**Figure 8.9.** SE SEM images of the worn surfaces together with SE SEM images and EDS analysis of the Al<sub>2</sub>O<sub>3</sub> balls used as counter-body for 0.5 N.

BSE and SE SEM images of the worn surfaces for 10 N condition together with SE SEM images and EDS spectra of the Al<sub>2</sub>O<sub>3</sub> balls used as counter-bodies can be seen in Fig. 8.10. The untreated groups presented scratches and ploughing grooves parallel to the sliding direction due to combination of adhesive and abrasive wear mechanisms, once transferred material from the wear track to the counter-body (adhesion) damaged the surface resulting in grooves. On the other hand, loose wear debris can act as a third-body abrasive and lead to the formation of sharp scratches parallel to the sliding surface. MAO treated groups presented very similar mechanisms in the centre of the wear tracks, where the MAO layer was completely removed, and the counter-body slid against the bare composite. On the edges of the wear track, considerable deposition of wear debris was observed, possibly trapped in the adjacent MAO layer. The MAO layer adjacent to the wear track was also damaged, where the volcano-like structure was not observed. It seems that in these areas, the MAO layer could not follow the deformation of the substrate due to high applied load, leading to detachments in these zones. Even though, as shown by the BSE images, only the outmost porous layer was detached in these zones.

Wear tracks for TO treated composites presented significant differences compared to the other groups, as neither significant number of scratches nor ploughing grooves were observed within the wear tracks. In addition, EDS analysis suggested much less adhered titanium to the counter-body surfaces compared with the untreated and MAO treated groups, as well reduced visible

wear damage on the counter-body surfaces. Representative wear profiles and wear volume loss values for 10 N condition can be seen in Fig. 8.11. MAO treated composites presented the highest wear volume values, which are in accordance with the lower OCP values observed during sliding. Meanwhile, TO treated composites presented the lowest wear volume values. All in all, these results suggest significant reduction in adhesion and abrasion mechanisms for the TO treated groups.

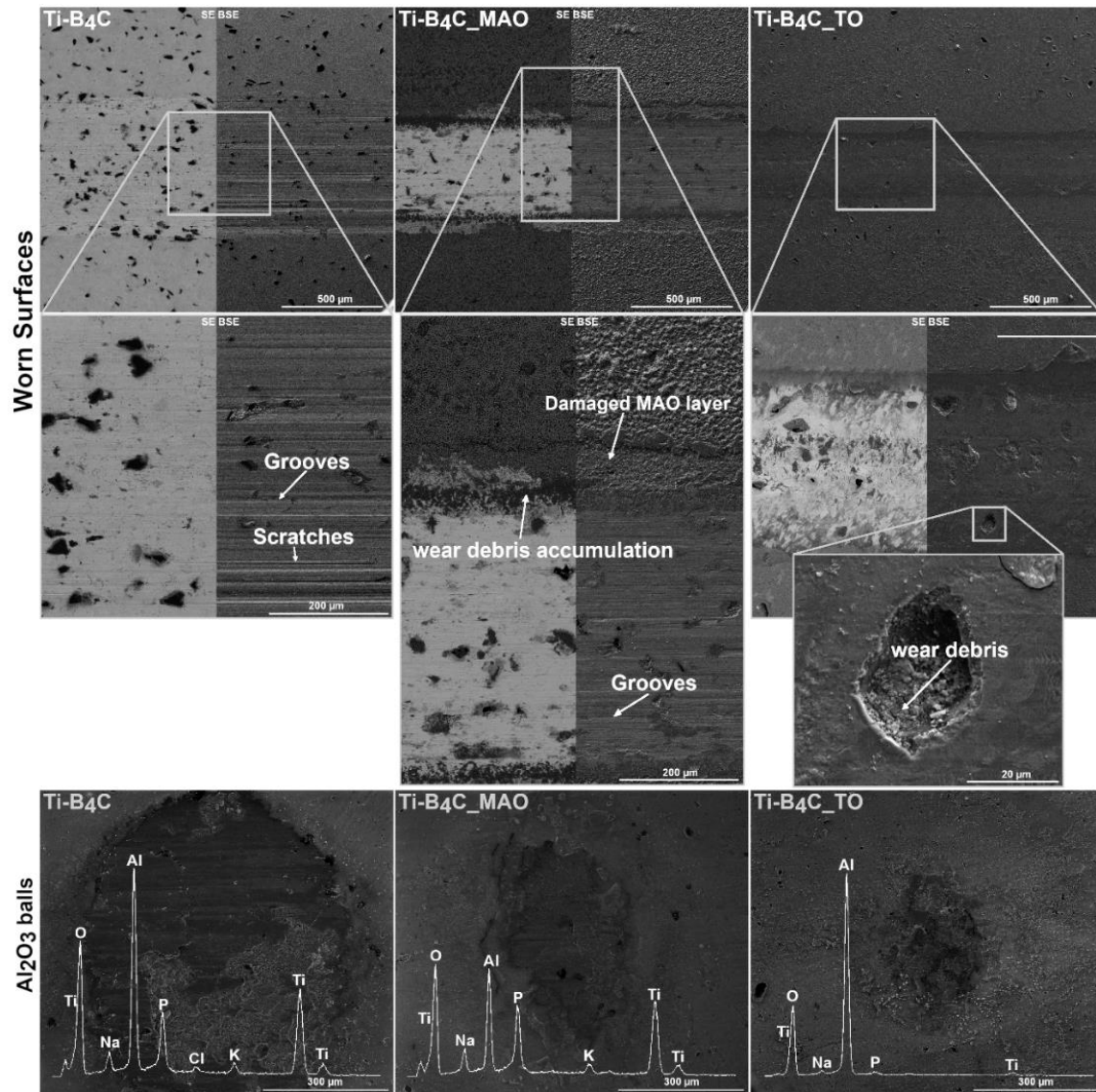


**Figure 8.10.** BSE/SE SEM images of the worn surfaces together with SE SEM images and EDS spectra of the Al<sub>2</sub>O<sub>3</sub> balls used as counter-body for 10 N.

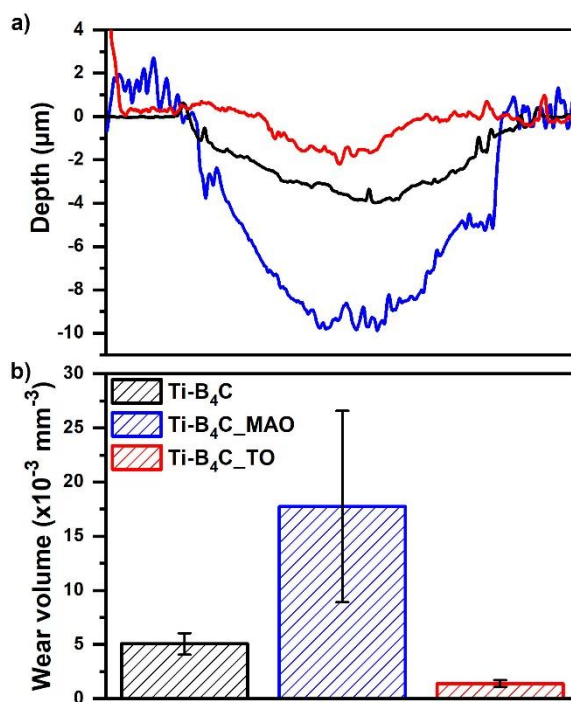


Figure 8.11. a) Representative 2D wear profiles for all the groups together with b) wear volume values estimated from wear profiles.

Overall, MAO and TO treated composites presented considerably improved tribocorrosion behaviour under 0.5 N with no noticeable changes in tendency to corrosion during the sliding action. In addition, no considerable wear volume loss was observed. On the other hand, when 10 N was applied, while TO treated composites presented improved behaviour compared to the untreated composite, the MAO treated composites presented an overall worse behaviour, through both higher tendency to corrosion under sliding as well as higher wear volume losses. The improved tribocorrosion behaviour for TO treated samples under 10 N condition can be attributed the presence of the ODZ below the TO oxide layer, which has improved wear resistance due to higher overall hardness. Once the TO oxide layer was destroyed at the onset of sliding (as suggested by the sharp drop in OCP values) the counter-body slid against a harder substrate, and thus wear damage was lower and OCP values were higher (Fig. 8.12c). Untreated and MAO treated composites presented roughly the same wear mechanisms being a mixture of adhesive and abrasive wear, which lead to the formation of ploughing grooves and scratches parallel to the sliding direction (Fig. 8.12a and 12b). MAO treated composites presented the overall worse tribocorrosion behaviour which can be attributed to increased third-body wear due to freely moving hard oxide wear debris from the MAO oxide layer (Fig. 8.12b). Although MAO treated



composites presented a worse tribocorrosion behaviour under these conditions, the evolution of OCP values may suggest that in the first minutes of sliding, this group showed better behaviour. The slower decay on OCP values on the onset of sliding may suggest better wear resistance than TO layers. However, with time wear debris from the MAO layer led to a significant increase in wear volume loss and thus higher tendency to corrosion under sliding.

The results showed that Ti-B<sub>4</sub>C composites might not be suitable for this functionalization treatment due to the detachment of B<sub>4</sub>C particles during the functionalization process. Nevertheless, it was shown that these treatments might be promising to improve corrosion, tribocorrosion and even biological properties of Ti-based composites for biomedical applications. It is suggested for further studies to fully react B<sub>4</sub>C with Ti matrix to produce *in-situ* Ti-(TiB+TiC) composites to avoid the reaction zone/B<sub>4</sub>C interface.

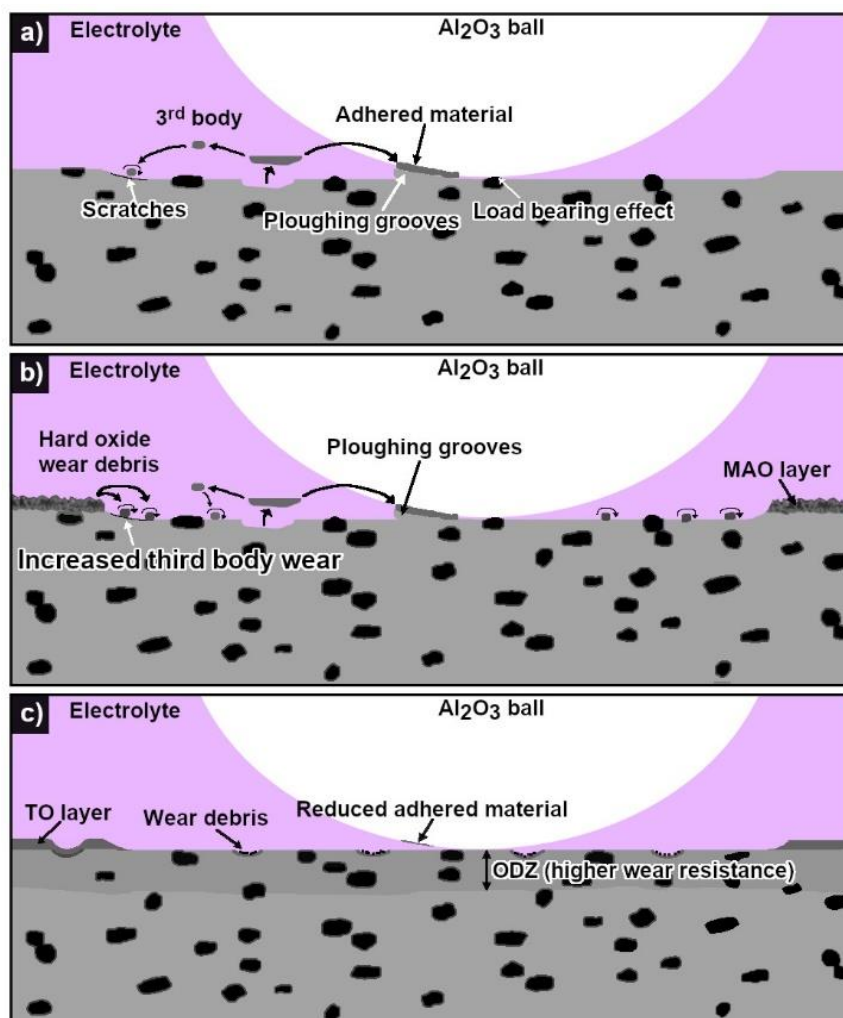


Figure 8.12. Main wear mechanisms observed for a) untreated composites, b) MAO treated composites and c) TO treated composites under 10 N condition.



## 8.4. Conclusions

MAO and TO treatments have the potential to improve both corrosion and tribocorrosion behaviour of TMCs. However, detachments of B<sub>4</sub>C particles from the Ti matrix were observed due to the grow of an oxide layer at the interface between the reaction zone and B<sub>4</sub>C particles. Thus, future research should consider *in-situ* Ti-TiB-TiC composites to avoid the interface with B<sub>4</sub>C particles.



## References

- [1] S. Kaur, K. Ghadirinejad, R.H. Oskouei, An Overview on the Tribological Performance of Titanium Alloys with Surface Modifications for Biomedical Applications, *Lubricants*. 7 (2019) 65.
- [2] D. Apostu, O. Lucaciu, C. Berce, D. Lucaciu, D. Cosma, Current methods of preventing aseptic loosening and improving osseointegration of titanium implants in cementless total hip arthroplasty : a review, *J. Int. Med. Res.* 46 (2018) 2104–2119.
- [3] M.D. Hayat, H. Singh, Z. He, Titanium metal matrix composites: An overview, *Compos. Part A*. 121 (2019) 418–438.
- [4] L. Sousa, A.C. Alves, A. Guedes, F. Toptan, Corrosion and tribocorrosion behaviour of Ti-B<sub>4</sub>C composites processed by conventional sintering and hot-pressing technique, *J. Alloys Compd.* 885 (2021) 161109.
- [5] A.I. Costa, L. Sousa, A.C. Alves, F. Toptan, Tribocorrosion behaviour of bio-functionalized porous Ti surfaces obtained by two-step anodic treatment, *Corros. Sci.* 166 (2020) 108467.
- [6] A.C. Alves, R. Thibaux, F. Toptan, A.M.P. Pinto, P. Ponthiaux, B. David, Influence of macroporosity on NIH/3T3 adhesion, proliferation, and osteogenic differentiation of MC3T3-E1 over bio-functionalized highly porous titanium implant material, *J. Biomed. Mater. Res. Part B - Appl. Biomater.* (2018) 1–13.
- [7] M. Tsai, Y. Chang, H. Huang, Y. Wu, T. Shieh, Micro-arc oxidation treatment enhanced the biological performance of human osteosarcoma cell line and human skin fibroblasts cultured on titanium – zirconium films, *Surf. Coat. Technol.* 303 (2016) 268–276.
- [8] C. Chang, X. Huang, Y. Liu, L. Bai, X. Yang, R. Hang, B. Tang, P.K. Chu, High-current anodization : A novel strategy to functionalize titanium-based biomaterials, *Electrochim. Acta.* 173 (2015) 345–353.
- [9] Y. Zhao, T.-Y. Xiong, Formation of bioactive titania films under specific anodisation conditions, *Surf. Eng.* 28 (2012) 371–376.
- [10] B. Yang, M. Uchida, H.M. Kim, X. Zhang, T. Kokubo, Preparation of bioactive titanium metal via anodic oxidation treatment, *Biomaterials*. 25 (2004) 1003–1010.
- [11] Y. Li, B. Li, X. Fu, J. Li, C. Li, H. Li, H. Li, C. Liang, H. Wang, L. Zhou, S. Xin, Anodic Oxidation Modification Improve Bioactivity and Biocompatibility of Titanium Implant Surface, *J. Hard Tissue Biol.* 22 (2013) 351–358.
- [12] I. Çaha, A.C. Alves, C. Chirico, A. Maria, S. Tsipas, E. Gordo, F. Toptan, Improved tribocorrosion behavior on bio-functionalized  $\beta$ -type titanium alloy by the pillar effect given by TiN reinforcements, *Surf. Coat. Technol.* 415 (2021) 127122.
- [13] P.S. Vanzillotta, M.S. Sader, I.N. Bastos, G. De Almeida, Improvement of in vitro titanium bioactivity by three different surface treatments, *Dent. Mater.* 22 (2006) 275–282.
- [14] Y. Park, H.-J. Song, I. Kim, H. Yang, Surface characteristics and bioactivity of oxide film on titanium metal formed by thermal oxidation, *J. Mater. Sci.* 18 (2007) 565–575.
- [15] G. Wang, J. Li, K. Lv, W. Zhang, X. Ding, G. Yang, Surface thermal oxidation on titanium implants to enhance osteogenic activity and in vivo osseointegration, *Sci. Rep.* 6 (2016) 1–13.
- [16] S. El-hadad, Optimizing the Surface Treatment Processes to Enhance the Bioactivity of Ti–6Al–7Nb Alloy, *Trans. Indian Inst. Met.* 73 (2020) 2727–2738.
- [17] Z. Doni, A.C. Alves, F. Toptan, J.R. Gomes, A. Ramalho, M. Buciumeanu, L. Palaghian, F.S. Silva, Dry sliding and tribocorrosion behaviour of hot pressed CoCrMo biomedical alloy as compared with the cast CoCrMo and Ti6Al4V alloys, *Mater. Des.* 52 (2013) 47–57.

- [18] M. Yi, X. Zhang, C. Ge, G. Liu, D. Zhong, G. Qiao, Oxidation behavior of *in situ* synthesized (TiB+TiC)/Ti-6Al-4V composites from Ti-B<sub>4</sub>C-C and Ti-TiB<sub>2</sub>-TiC systems, *J. Mater. Res.* 34 (2019) 1762–1772.
- [19] B. Choi, I.-Y. Kim, Y. Lee, Y. Kim, Microstructure and friction/wear behavior of (TiB+TiC) particulate-reinforced titanium matrix composites, *Wear.* 318 (2014) 68–77.
- [20] J.M. Sousa, A.C. Alves, F. Toptan, E. Ariza, A. Guedes, Corrosion and Tribocorrosion Behavior of Ti-B<sub>4</sub>C Composites Joined with TiCuNi Brazing Alloy, *J. Mater. Eng. Perform.* 28 (2019) 4972–4982.
- [21] A. Jimoh, I. Sigalas, M. Hermann, *In Situ* Synthesis of Titanium Matrix Composite (Ti-TiB-TiC) through Sintering of TiH<sub>2</sub>-B<sub>4</sub>C, *Mater. Sci. Appl.* 2012 (2012) 30–35.
- [22] L. Sousa, L. Basilio, A.C. Alves, F. Toptan, Tribocorrosion-resistant biofunctionalized Ti-Al<sub>2</sub>O<sub>3</sub> composites, *Surf. Coat. Technol.* 420 (2021) 127329.
- [23] M. Jamesh, T.S.N.S. Narayanan, P.K. Chu, Thermal oxidation of titanium : Evaluation of corrosion resistance as a function of cooling rate, *Mater. Chem. Phys.* 138 (2013) 565–572.
- [24] S. Kumar, T.S.N.S. Narayanan, S.G. Sundara, S.K. Seshadri, Thermal oxidation of CP Ti — An electrochemical and structural characterization, *Mater. Charact.* 61 (2010) 589–597.
- [25] H. Gülerüz, H. Çimenoglu, Effect of thermal oxidation on corrosion and corrosion-wear behaviour of a Ti-6Al-4V alloy, *Biomaterials.* 25 (2004) 3325–3333.
- [26] H. Zhang, J. Geng, X. Li, Z. Chen, M. Wang, N. Ma, H. Wang, The micro-arc oxidation (MAO) behaviors of in-situ TiB<sub>2</sub>/A201 composite, *Appl. Surf. Sci.* 422 (2017) 359–371.
- [27] H. Hu, L. Huang, L. Geng, B. Liu, B. Wang, Oxidation behavior of TiB-whisker-reinforced Ti60 alloy composites with three-dimensional network architecture, *Corros. Sci.* 85 (2014) 7–14.
- [28] E. Zhang, Oxidation behavior of *in situ* TiB short fibre reinforced Ti-6Al-1.2B alloy in air, *J. Mater. Res.* 7 (2002) 4063–4071.
- [29] S.L. Wei, L.J. Huang, X.T. Li, Q. An, L. Geng, Interactive effects of cyclic oxidation and structural evolution for Ti-6Al-4V/(TiC+TiB) alloy composites at elevated temperatures, *J. Alloys Compd.* 752 (2018) 164–178.
- [30] A.C. Alves, F. Wenger, P. Ponthiaux, J.P. Celis, A.M. Pinto, L.A. Rocha, J.C.S. Fernandes, Corrosion mechanisms in titanium oxide-based films produced by anodic treatment, *Electrochim. Acta.* 234 (2017) 16–27.
- [31] R. Bailey, Y. Sun, Corrosion and Tribocorrosion Performance of Thermally Oxidized Commercially Pure Titanium in a 0.9 % NaCl Solution, *J. Mater. Eng. Perform.* 24 (2015) 1669–1678.
- [32] S. Kumar, T.S.N.S. Narayanan, S.G. Sundara, S.K. Seshadri, Thermal oxidation of CP-Ti : Evaluation of characteristics and corrosion resistance as a function of treatment time, *Mater. Sci. Eng. C.* 29 (2009) 1942–1949.
- [33] J.I. Silva, A.C. Alves, A.M. Pinto, F. Toptan, Corrosion and tribocorrosion behavior of Ti-TiB-TiN<sub>x</sub> in-situ hybrid composite synthesized by reactive hot pressing, *J. Mech. Behav. Biomed. Mater.* 74 (2017) 195–203.
- [34] Y. Diao, K. Zhang, Microstructure and corrosion resistance of TC2 Ti alloy by laser cladding with Ti/TiC/TiB<sub>2</sub> powders, *Appl. Surf. Sci.* 352 (2015) 163–168.
- [35] J.I. Silva, A.C. Alves, A.M. Pinto, F.S. Silva, F. Toptan, Dry sliding wear behaviour of Ti-TiB-TiN<sub>x</sub> in-situ composite synthesised by reactive hot pressing, *Int. J. Surf. Sci. Eng.* 10 (2016) 317–329.
- [36] O. Çomakli, T. Yetim, A. Çelik, The effect of calcination temperatures on wear properties of TiO<sub>2</sub> coated CP-Ti, *Surf. Coatings Technol.* 246 (2014) 34–39.

## Chapter 9

### Micro-arc and Thermal oxidation treated *in-situ* Ti composites intended for load-bearing biomedical implants

*To be submitted*

---

**L. Sousa**<sup>a,b\*</sup>, S. Simões<sup>b,c</sup>, F. Toptan<sup>a,d,e\*</sup>, A.C. Alves<sup>a,d</sup>

<sup>a</sup>CMEMS-UMinho – Center of MicroElectroMechanical Systems – Universidade do Minho, Campus de Azurém, Guimarães, Portugal

<sup>b</sup>DEMM – Department of Metallurgical and Materials Engineering – Faculdade de Engenharia da Universidade do Porto, Porto, Portugal

<sup>c</sup>LAETA/INEGI, Institute of Science and Innovation in Mechanical and Industrial Engineering, R. Dr. Roberto Frias, Porto, 4200-465, Portugal

<sup>d</sup>IBTN/Euro – European Branch of the Institute of Biomaterials, Tribocorrosion and Nanomedicine, Dept. Eng. Mecânica, Universidade do Minho, Azurém, 4800-058 Guimarães, Portugal

<sup>e</sup>Department of Materials Science and Engineering, Izmir Institute of Technology, 35430, Urla, Izmir, Turkey



## Abstract

Titanium matrix composites (TMCs) have shown potential for load bearing implants due to their promising mechanical, corrosion and particularly tribocorrosion behaviours. However, the lack of bioactivity remains a problem, once that most reinforcement phases are bioinert. Micro-arc oxidation (MAO) and thermal oxidation treatment (TO) are well-known techniques used to improve the bioactivity of Ti through the formation of a thick TiO<sub>2</sub> oxide layer with tailored properties. In this work, MAO and TO treatments were carried out on *in-situ* Ti-TiB-TiC composite surfaces and compared to MAO and TO treated Ti. Corrosion and tribocorrosion behaviour was studied in phosphate buffered saline solution (PBS) at body temperature. No significant changes were observed in the overall structure of the MAO and TO layers from unreinforced Ti to composite groups. However treated composites presented considerably lower corrosion resistance as compared to the unreinforced treated Ti. Tribocorrosion resistance was higher for the composite groups as they tended to present less tendency to corrosion under mechanical action and a significant decrease in wear volume loss as compared to the treated Ti.

### 9.1. Introduction

Lack of bioactivity and poor tribocorrosion resistance of Ti and its alloys still affect load-bearing biomedical implants. To achieve a lasting implant, these devices must possess good osteointegration with the adjacent bone and an adequate tribocorrosion resistance to reduce implant degradation under the physiological conditions in which they are inserted. In order to improve the tribocorrosion resistance of Ti and its alloys, a variety of techniques can be used, including surface coatings or surface modification techniques [1–4] and incorporation of hard ceramic particles (reinforcements) into a Ti matrix to produce titanium matrix composites (TMCs) [5,6].

In the last years, research has been made on TMCs to be considered for load bearing biomedical implants, showing promising mechanical, corrosion and tribocorrosion behaviours. Among all the reinforcement phases that can be successfully used to produce these composites, *in-situ* TiB whiskers (TiB<sub>w</sub>) and TiC particles (TiC<sub>p</sub>) have been recognized for being excellent options, mainly due

to their compatibility and strong interfacial bonding with Ti. Furthermore, they also possess desirable mechanical and electrochemical properties such as high hardness, low density and good corrosion resistance [7–9]. It is well reported that the addition of these phases can improve the mechanical properties of titanium [10,11], however, studies on corrosion and tribocorrosion are still very limited.

Compared to ex-situ composites, *in-situ* composites generally present cleaner and stronger matrix/reinforcement interfaces in addition to a more homogeneous distribution of reinforcement phases [12,13]. *In-situ* TiB and TiC phases can be easily and economically processed by mixing Ti and B<sub>4</sub>C powders using powder metallurgy-based techniques [14–17]. To obtain a full reaction with the Ti matrix, B<sub>4</sub>C particles with smaller particle size distributions (typically between 1 and 10 μm) are generally used.

Ti implants do not possess the necessary bioactivity to achieve adequate osteointegration with the adjacent bone. Most of the reinforcement phases are bioinert. Therefore, lack of bioactivity may continue to be an issue regarding TMCs for load-bearing biomedical implants [18,19]. Surface modification techniques can be used to tailor the implant surface in terms of topography and chemistry, to allow Ti implants to address the specific requirements necessary to promote positive interaction between the bone and implant surface, leading to improved osteointegration, bone ingrowth, and cell proliferation and differentiation [20–23].

Among the various techniques that can be used, anodic treatment (AT) has an excellent potential to produce implants with adequate topography and chemistry [24–27]. Micro-arc oxidation (MAO) is one of the most known forms of AT, where several hundreds of volts are used to produce a micro-porous, crystalline, and thick TiO<sub>2</sub> layer with improved osteointegration capabilities and improved bioactivity [21,28–31]. On the other hand, thermal oxidation (TO) treatment is a cost-effective and straightforward technique that can also improve the bioactivity of titanium surfaces. This method takes advantage of the high reactivity of Ti with air and/or water to promote the growth of the native TiO<sub>2</sub> passive layer and alter its properties, such as crystal structure, topography, and chemical composition, to improve bioactivity [22,23,32,33].

In addition to improved bioactivity, MAO and TO oxide layers also have improved corrosion and tribocorrosion resistance due to the formation of hard



and wear resistant crystalline phases such as anatase and rutile [34–38]. The effect of MAO and TO treatments on the properties of Ti has been extensively researched; however, their impact on TMCs surfaces is still mostly unknown. Biofunctionalized TMCs may have improved tribocorrosion resistance compared to biofunctionalized Ti and its alloys and enhanced bioactivity. Thus, the objective of this work was to study the effect of MAO and TO treatments on the surface of Ti-TiB-TiC composites and study their corrosion and tribocorrosion behaviour.

## 9.2. Materials and methods

### 9.2.1. Processing

*In-situ* Ti composites reinforced with 10 vol.% of (TiB +TiC) phases were processed by mixing of Ti grade 2 and 1.9 wt.% B<sub>4</sub>C powders according to Eq. (9.1) [39], with average particles sizes of 25 and 9 μm, respectively. Powders were mixed through ball milling for 4 h at 120 rpm with the help of Al<sub>2</sub>O<sub>3</sub> balls (ø 10 mm), under Ar atmosphere to minimize oxidation. After mixing, the powder blends were placed in a zirconia coated graphite mould (10 mm inner diameter) in order to process samples with 3 mm of thickness. Hot-pressing was then carried out at high vacuum (≤10<sup>-5</sup> mbar) for 120 min at 1100 °C with heating and cooling rate of 5°C/min and 10°C/min, respectively. An applied pressure of 40 MPa was applied through all the cycles. Before characterization and testing, untreated samples were ground down to 2400 mesh SiC papers and then mirror finished until 0.04 μm with colloidal silica suspension. Samples were then cleaned by propanol and distilled water in an ultrasonic bath for 10 and 5 min, respectively, and kept in a desiccator for 24 h prior to each test to obtain similar surface conditions. In addition to composites, unreinforced Ti was also processed to be used as the control group.



For MAO treatment, Ti and composite samples were placed in an electrochemical cell connected to a DC power supply (Agilent technologies N5772A). An exposed area of 0.38 cm<sup>2</sup> was distanced 80 cm from an Pt cathode with 1.77 cm<sup>2</sup> of area. MAO treatment was then performed under a turbulent regime through a magnetic stirrer spinning at around 200 rpm. A constant voltage of 300 V was applied for 1 min with an imposed current limit of 2.5 A. A mixture

of 0.35 M of calcium acetate monohydrate (CA) and 0.02 M of  $\beta$ -glycerophosphate disodium salt pentahydrate ( $\beta$ -GP) was used as electrolyte. Hereafter, MAO treated samples will be referred to as Ti\_MAO and Ti-TiB-TiC\_MAO, for Ti and composite groups, respectively.

The samples were ground down to 600 mesh SiC paper for thermal oxidation treatment, cleaned as described previously and then placed in a furnace with an open atmosphere. The thermal cycle was set to 800 °C for 20 min, with both heating and cooling rates set to 5 °C/min. The stage temperature and time were chosen based on a previous work by Dalili et al. [40], where a uniform, wear resistant and well adhered oxide layer was obtained on Ti-6Al-4V/TiC composites by using the same temperature and time. Hereafter, thermally oxidized samples will be referred to as Ti\_TO and Ti-TiB-TiC\_TO for Ti and composites groups, respectively.

### 9.2.2. Electrochemical tests

Electrochemical tests were carried out at body temperature ( $37 \pm 1$  °C) in an electrochemical cell containing phosphate-buffered saline (PBS) solution (0.24 g/l  $\text{KH}_2\text{PO}_4$ , 0.2 g/l KCl, 1.44 g/l  $\text{Na}_2\text{HPO}_4$ , 8 g/l NaCl – pH 7.4). Open circuit potential (OCP) was first monitored until stabilization ( $\Delta E < 60$  mV/h), followed by electrochemical impedance spectroscopy (EIS) measurements, with a scanning rate of 7 points per decade from  $10^5$  Hz until  $10^{-2}$  Hz with an amplitude of the sinusoidal signal of 10 mV. After EIS, potentiodynamic polarization tests were performed by scanning a potential range from  $-0.2 V_{\text{OCP}}$  to  $1.5 V_{\text{Ag/AgCl}}$  at 1mV/s. All the electrochemical tests were performed using a standard three-electrode setup consisting of a saturated Ag/AgCl reference electrode, a platinum (Pt) counter electrode and the sample as a working electrode with an exposed area of  $0.1 \text{ cm}^2$ . All the tests were carried out in a Gamry Potentiostat/Galvanostat/ZRA (model Reference-600+).

### 9.2.3. Tribocorrosion tests

Tribocorrosion tests were performed in a tribometer (CETR-UMT2) with a ball-on-plate configuration and reciprocating stage, using an identical PBS solution at  $37 \pm 1$  °C. Two distinct loads (0.5 and 10 N), each corresponding to a maximum Hertzian contact pressure for c.p. Ti of 342 and 930 GPa, respectively,

were used in the tests. Before sliding, OCP values were continuously monitored until stabilization ( $\Delta E < 60$  mV/h), during sliding for 1 h, and after sliding for an additional 1 h. Coefficient of friction (COF) values were also monitored during sliding. Sliding time, frequency and stroke length were set to 60 min, 1 Hz and 3 mm, respectively, for both conditions. Electrochemical data was monitored using a Gamry Potentiostat/Galvanostat/ZRA (model Referece-600) with a two-electrode set-up, where the samples were connected as working electrode and saturated Ag/AgCl reference electrode.

#### 9.2.4. Characterization

Microstructure and chemical composition of Ti and composites surfaces after MAO and TO treatments was investigated by FEG-SEM (FEI Nova 200) equipped with EDS (EDAX energy dispersive X-ray spectroscopy). Phase identification was performed by XRD (Bruker D8 Discover diffractometer) operating at 40 kV and 40 mA using Cu K $\alpha$  radiation by scanning a range ( $2\theta$ ) from 20° to 80° with a step size of 0.04°/s. After tribocorrosion tests, the worn surfaces were characterized using the same FEG-SEM equipment. Wear track profiles were obtained by profilometry (Veeco, Dektak 150), and were used to estimate wear volume loss values following the procedure described elsewhere [41].

### 9.3. Results and discussion

#### 9.3.1. Microstructure

The overall microstructure of Ti and composite surfaces after MAO and TO treatments can be seen on the secondary electron (SE) SEM images shown in Fig. 9.1. MAO treatment led to the formation of a micro-porous oxide layer with a volcano like structure on both Ti and composite surfaces, with no discernible differences between the two groups. Back-scattered electron (BSE) SEM images of the cross-sections (Fig. 9.2a) revealed that the MAO layer was formed on the top of both Ti matrix and reinforcements phases (mixture of TiB and TiC<sub>0.59</sub> phases according to XRD pattern presented on Fig. 9.2d). This MAO layer formed three distinct zones, an inner and an outer porous layers and a thin and compact oxide layer formed just after the bulk material, as in accordance with previous works by some of the present authors, where MAO treatments were performed

on Ti surfaces using the same parameters [35,37,42]. Ca/P atomic ratios were calculated as  $3.15 \pm 0.14$  and  $3.21 \pm 0.06$  for Ti and composite groups, respectively, above the stoichiometric ratio for hydroxyapatite (HA) present in the bone [43]. A considerable amount of B and C elements ( $33 \pm 3$  at% and  $15 \pm 5$  at% for B and C, respectively) were also detected for the MAO treated composites. Still, XRD analysis revealed a very similar phase composition for both groups, which were composed of a mixture of anatase and rutile phases.

The effect of the B element on the structure of MAO layers has been studied by Sopchenski et al. [44]. The authors produced MAO layers on Ti substrates using an Ca, P, and B-rich electrolyte and reported that the presence of B element did not change the structure of the MAO layer in terms of morphology, roughness, and phase composition. In the same study, the authors also studied the effect of the B element on the biological behaviour of these layers. Compared to the boron-free MAO layer, these layers presented similar cell viability and activity with improved anti-bacterial properties against *S. aureus* and *P. aeruginosa*.

After TO treatment, a homogeneous oxide layer was formed on the surface of both groups, with no evidence of defects such as cracks and/or detachments. Cross-section images for TO treated Ti and composites (Figs. 9.2b and 9.2c) showed a similar oxide layer for both groups, which presenting around  $3.8 \mu\text{m}$  of thickness. Similar to MAO treatment, the TO oxide layer was formed on the top of the Ti matrix and reinforcement phases, with no discernible differences in terms of structure and chemical composition. For both Ti and composite groups, the formation of an oxygen diffusion zone (ODZ) was also observed, which is often reported for TO treatment performed on Ti-based substrates [2,34,45,46]. This ODZ presented considerably higher hardness values compared to the bulk material. For Ti the hardness increased from  $354 \pm 21$  to  $614 \pm 14$   $\text{HV}_{0.025}$ , as for the composite group, the hardness of the Ti matrix increased from  $665 \pm 25$  to  $812 \pm 28$   $\text{HV}_{0.025}$ . Regarding phase composition, only peaks related to the rutile phase were observed for Ti and composite groups, with no significant differences between the two groups.

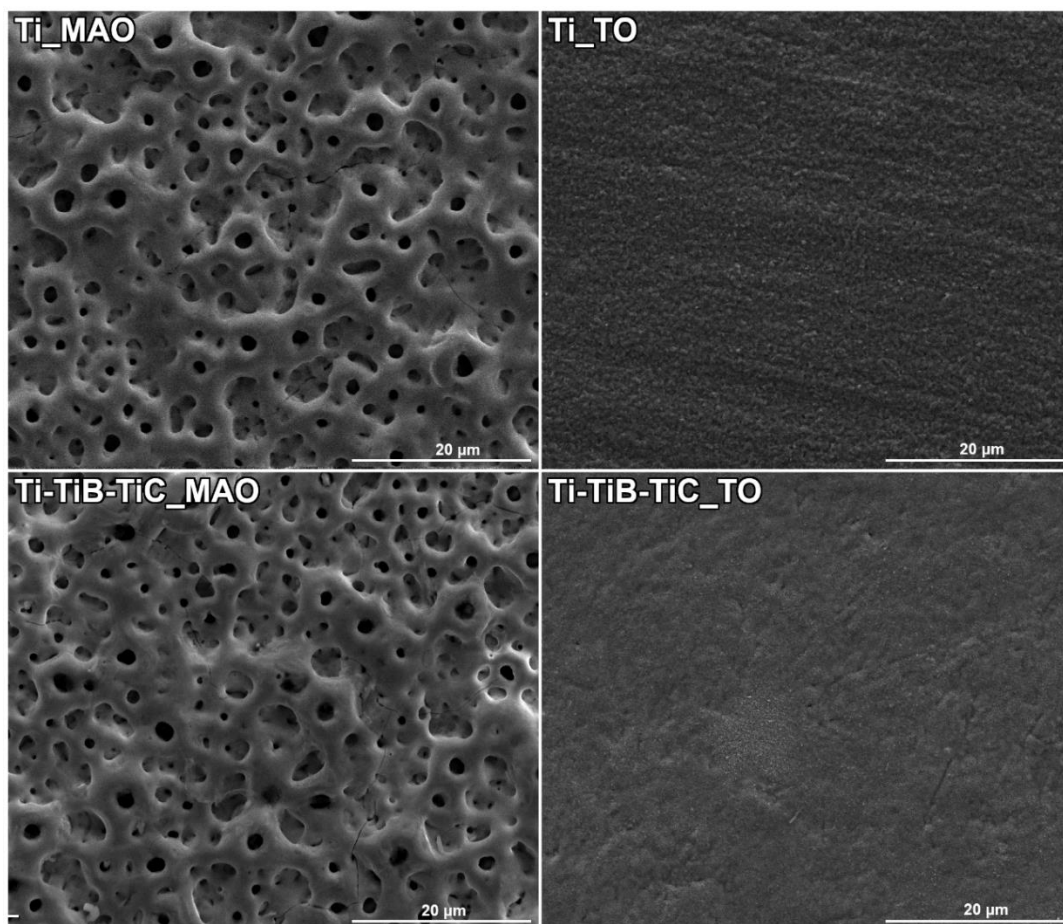


Figure 9.1. Representative SE SEM image of MAO and TO treated Ti and composite groups

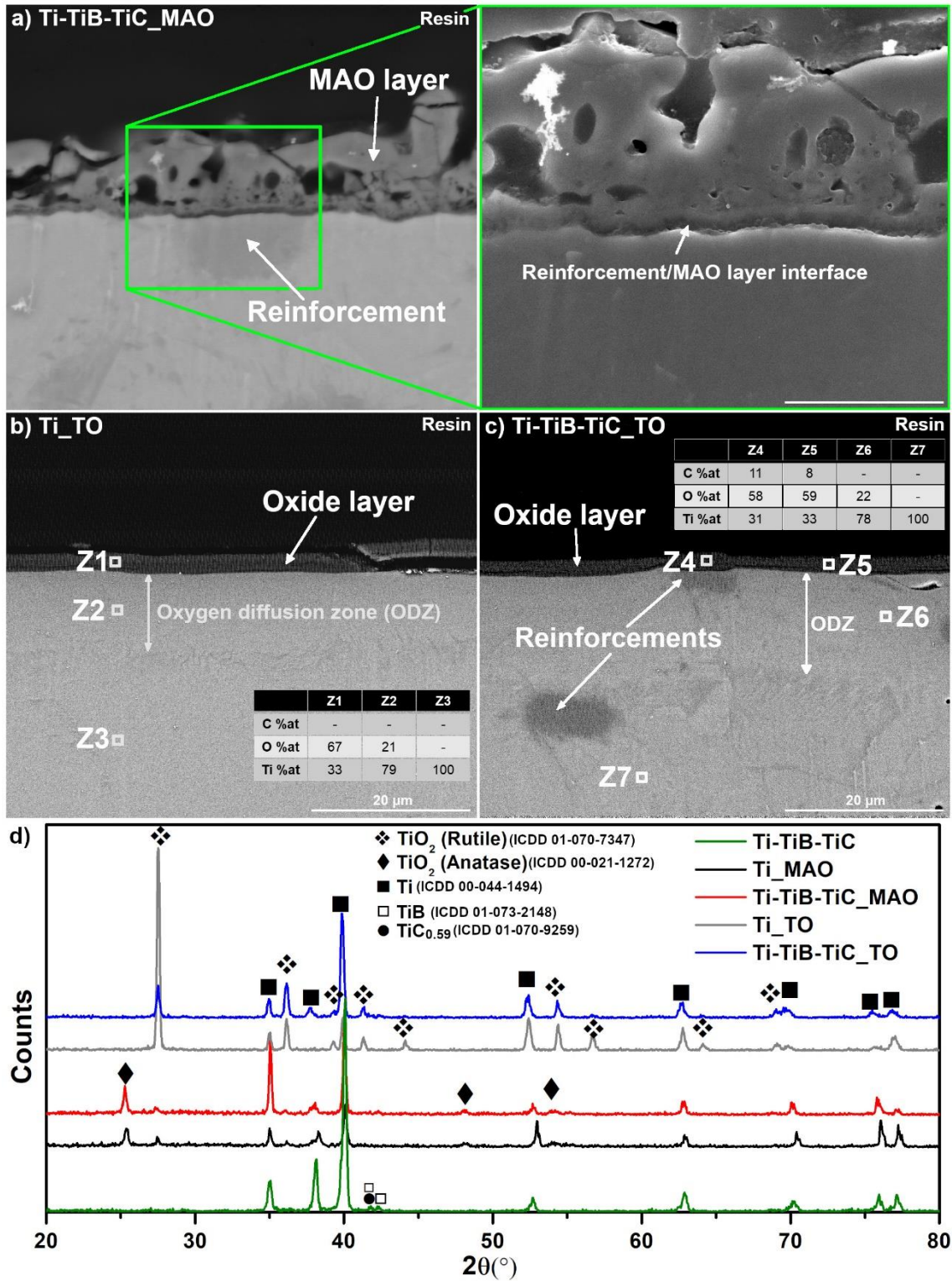


Figure 9.2. a) BSE/SE SEM image of a representative cross-section of MAO treated composite, b and c) BSE SEM image of a representative cross-section of TO treated Ti and composite, respectively, and d) XRD patterns for untreated composite and MAO and TO treated Ti and composite groups.

### 9.3.2. Electrochemical behaviour

Representative potentiodynamic polarization curves for MAO and TO treated Ti, and composite groups are presented in Fig. 9.3. The average values of  $E_{(i=0)}$  and  $i_{pass}$  (taken at 0.75 V<sub>Ag/AgCl</sub>) are given in Table 9.1. Ti\_MAO group presented the typical behaviour expected for MAO layers formed under these conditions, which is characterized by the formation of a passivation plateau, with a substantial increase in  $E_{(i=0)}$  values together with a decrease of around two orders of magnitude for corrosion current density values when compared to commercial titanium. The improvement in corrosion behaviour is attributed to the formation of a TiO<sub>2</sub> layer with overall higher corrosion resistance, mainly attributed to the formation of a barrier layer between the Ti substrate and the inner porous layer. Similar behaviour for MAO treated Ti was reported before by some of the present authors [35,37]. MAO treated composites presented considerable different behaviour, despite  $E_{(i=0)}$  values being similar to those observed for Ti\_MAO,  $i_{pass}$  values were considerably higher. In addition, the evolution of current density with the applied potential is quite different. For Ti\_MAO, the passive plateau starts to form shortly after the  $E_{(i=0)}$  is reached, however there is a significant delay for composite groups. Similar behaviour was observed for TO groups, however the average  $E_{(i=0)}$  values were considerably lower than MAO treated groups, while  $i_{pass}$  values were very similar.

For TO treatment, the improvement in corrosion resistance is also attributed to the formation of thick oxide layer, which separates the metallic substrate from the electrolyte, and thus, serves as a physical barrier against corrosion [47]. Although no significant differences were observed in the morphology of the MAO and TO layers between Ti and composite groups. The  $i_{pass}$  values obtained for composite groups were significantly lower than the ones observed for treated Ti groups. The  $i_{pass}$  values observed for composite groups were slightly higher than those usually observed for untreated CP-Ti, which typically present  $i_{pass}$  values between 3 and 10  $\mu\text{A}\cdot\text{cm}^{-2}$  [35,37]. Once the corrosion behaviour of MAO layers is dependent mainly on the properties of the inner barrier layer [48], the results suggest that for composite groups, this layer is not as protective as the ones formed on the unreinforced Ti groups. This is possibly due to the different state of the barrier layer at the reinforcement/MAO layer interface (Fig. 9.2a). As for

TO treated composites, results show that oxide layers formed on the composite substrates have overall less corrosion resistance.

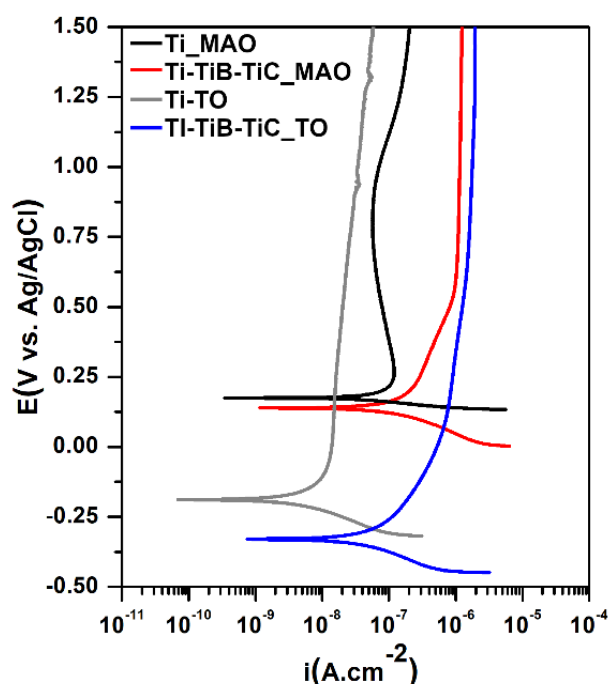


**Figure 9.3.** Representative potentiodynamic polarization curves for all the groups.

**Table 9.1.** Average values of  $E_{(i=0)}$  and  $i_{pass}$  values for all the groups.

	Ti_MAO	Ti-TiB-TiC_MAO	Ti_TO	Ti-TiB-TiC_TO
$E_{(i=0)}$ (V vs Ag/AgCl)	$0.11 \pm 0.07$	$0.11 \pm 0.03$	$-0.16 \pm 0.03$	$-0.34 \pm 0.03$
$i_{pass}$	$(7.26 \pm 2.66) \times 10^{-8}$	$(1.13 \pm 0.03) \times 10^{-6}$	$(5.05 \pm 2.85) \times 10^{-8}$	$(1.56 \pm 0.25) \times 10^{-6}$

### 9.3.3. Tribocorrosion behaviour

The evolution of OCP before, during and after sliding for all the groups can be seen in Fig. 9.4 together with the evolution of COF during sliding. Before sliding, all the groups presented stable OCP values due to presence of the oxide layer formed on MAO and TO treatments. Under 0.5 N condition, no substantial changes in OCP values were observed during sliding action once no considerable wear damage was done to the MAO or TO oxide layers (Fig. 9.5). Moreover, no difference was observed between Ti and composite groups. In fact, under these conditions, the oxide layers only presented a very low amount of abrasion due to the rubbing counter-body. Overall, lower COF values were obtained for TO treated groups, with no differences between Ti and composites. These differences were probably related to the differences in morphology between MAO and TO oxide layers, since the MAO layer usually tends to present rougher



surfaces due to the formation of micro-pores. In addition, a higher amount of rutile phase for the TO oxide layer may contribute to lower COF values once this phase is reported to have low shear strength and thus decreased friction [49].

Under 10 N, the evolution of OCP values for all the groups could be divided into two distinct zones: the first consists in a substantial decrease in OCP values on the onset of sliding. In contrast, the second one corresponds to the evolution of OCP values during the remaining sliding time. For MAO treated groups, the first zone lasted around 700–1200 s, where a gradual decrease in OCP values was observed. On the other hand, TO treated groups presented a sharp decrease in OCP values. Comparing Ti\_MAO and Ti-TiB-TiC\_MAO groups, OCP values decreased at a slower rate for the composite group, suggesting increased wear resistance for this group. On the second zone, the OCP values for both groups were in the range of untreated CP-Ti tested under similar conditions [50], suggesting that considerable damage was done to the MAO layers and the electrochemical response was coming mostly from the Ti and composite substrates. Comparatively, the OCP values in this zone tended to be slightly higher for the composite groups, probably due to the higher wear resistance of the substrate material. Some oscillations in OCP and COF values were also observed in this zone which can be attributed to the formation and breakdown of compacted wear debris zones within the wear tracks, which can be seen on the SEM images of the worn zones (Fig. 9.6). These compacted wear debris gave limited protection against corrosion and, at the same time, led to changes in the overall roughness of the surfaces, leading to a consequent increase or decrease in COF values. After sliding ended, OCP values started to increase, as a native TiO<sub>2</sub> passive oxide film started to grow on the worn zones.

The sharp decrease in OCP values for TO groups suggests that substantial damage was done to the TO oxide layers on the onset of sliding. Ti group presented the highest OCP drop. Afterwards, OCP values stabilized and remained relatively constant until the end of sliding for the Ti\_TO group. In contrast, for the Ti-TiB-TiC\_TO group, a gradual decrease in OCP until the end of sliding was observed. For the most part, OCP values tended to be higher for the composite groups in the second zone suggesting improved tribocorrosion resistance.

Compared to MAO treated groups, more stable and higher OCP values were observed in the second zone for TO treated groups together with more stable COF values. This was probably related to the presence of the ODZ for the TO treated groups. Compared to the base materials, increased wear resistance can be expected on the ODZ due to its higher overall hardness. It has also been reported that the ODZ has superior corrosion resistance than the base Ti or Ti alloy due to higher oxygen content which might accelerate the formation of the native passive film [51].

After sliding ended, OCP values rapidly increased due to repassivation of the worn zones. Interestingly, after roughly 60 min for both Ti and composite groups, OCP values reached the same values observed before sliding, even though the damaged TO oxide layer cannot regenerate. Considering that the potential measured after sliding is a mixed potential between the worn and unworn zones and the fact that the ODZ has superior corrosion resistance, it is quite possible that the extension of wear damage (Fig. 9.6 and 9.7) was not enough to observe significant changes in OCP values, given enough time for the ODZ to repassivate.

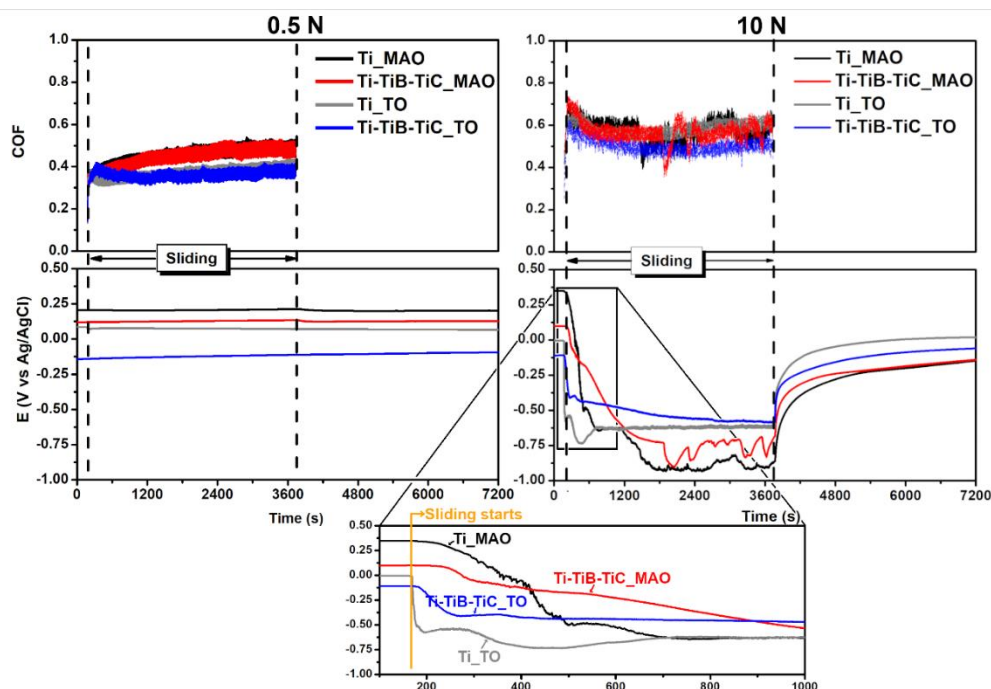


**Figure 9.4.** OCP evolution before, during, and after sliding for both conditions under 0.5 and 10 N, together with the evolution of COF during sliding.

The overall morphology of the wear tracks and  $\text{Al}_2\text{O}_3$  balls used as counter-body for 10 N condition can be seen in Fig. 9.6. For MAO treated groups, the

BSE/SE SEM images of the worn surfaces clearly show that the MAO layer was destroyed and the Ti and composite substrate were exposed to the electrolyte. The formation of grooves and compacted wear debris were observed on the worn substrates for both groups. These features are usually a consequence of adhesive wear. During sliding, Ti can be adhered to the counter-body, as can be seen on the SEM and EDS analysis of the counter-body. In this case, it is also quite possible that part of the MAO layer was mixed with the adhered Ti from the substrate. This transferred material might then abrade to the surface and led to the formation of ploughing grooves. Additionally, removed material from the worn surfaces can also be compacted on the wear track and give limited protection against wear and corrosion. This process is usually repeated several times during sliding, leading to oxidation of the transferred material and an increase in its overall hardness. Some amount of wear debris also tends to be pushed-out of the wear track. In this case, a considerable amount of wear debris was accumulated on the edges of the worn zones, trapped inside the micro-pores of the adjacent MAO layer. In fact, the only considerable differences between Ti and composite groups were observed on the edge of the wear tracks. For Ti\_MAO group, the worn Ti substrate was followed by a zone of compacted wear debris and the MAO oxide layer. However, for Ti-TiB-TiC\_MAO group, the zone with compacted wear debris was followed by a zone where the MAO layer was partially damaged, where the outer porous layer was detached from the surface, once no micro-pores were observed. These detachments hint at a brittle surface due to the higher hardness of the composites.

TO treated groups presented overall less wear damage than MAO treated groups, especially for Ti groups. As suggested by the evolution of OCP, the TO oxide layer was destroyed during sliding and the ODZ was exposed to the electrolyte, as evidenced by the EDS analysis of Z1 (Fig. 9.6). Comparing the worn surfaces between TO and MAO groups, it is possible to observe a key difference, as no ploughing grooves were observed for both TO groups. SEM and EDS analysis of the counter-bodies also revealed considerably less transferred Ti to the counter-body surfaces, meaning that adhesive wear was considerably reduced. This can be explained by the presence of the ODZ for TO groups, which was the main contact surface after the removal of the TO oxide layer. This can be confirmed by the wear track profiles shown in Fig. 9.7, where the depth was

considerably lower than the thickness of the ODZs shown in Fig. 9.2b and 9.2c. Due to the substantial higher hardness of the ODZ compared to the base substrate, wear damage and thus adhesive wear was considerably reduced. Similar to MAO groups, compacted wear debris was also observed within the worn surfaces, mainly on Ti\_TO surfaces, as confirmed by the EDS analysis of Z2 (Fig. 9.6), where there was also incorporation of elements from the PBS electrolyte. Nevertheless, these were not enough to cause significant changes in OCP and COF values. In addition, the higher tribocorrosion resistance of the ODZ may also hide the overall impact of these wear debris on the evolution of OCP and COF values. Comparing Ti\_TO and Ti-TiB-TiC\_TO groups, no significant differences were observed in the morphology of the wear tracks meaning that both groups presented roughly the same wear mechanisms, being a mixture of adhesive and abrasive wear.

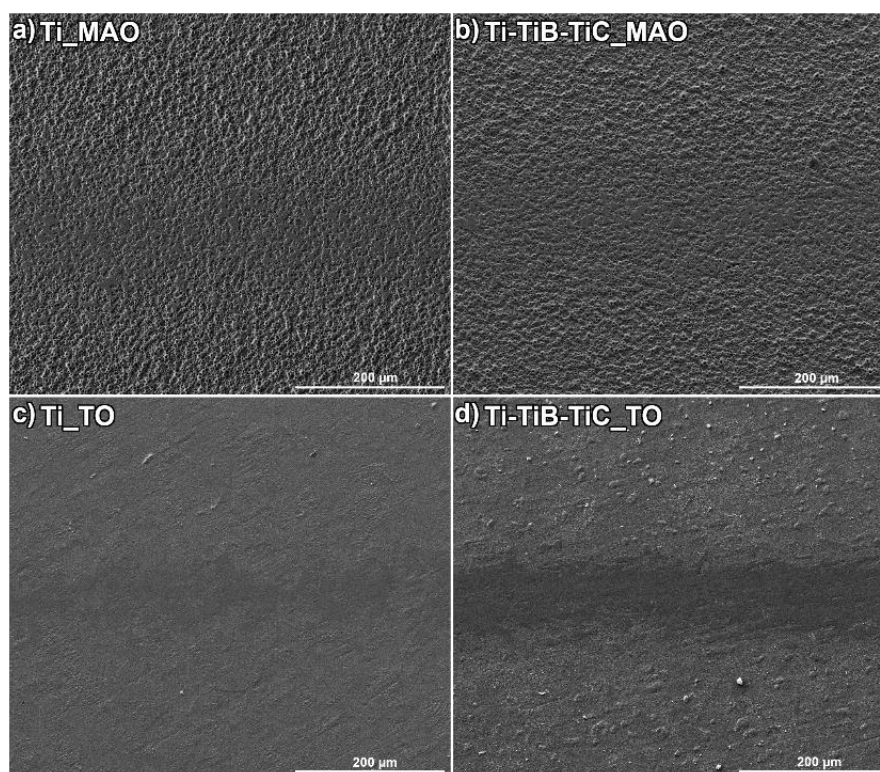


**Figure 9.5.** Worn surfaces for all the groups tested under 0.5 N condition.

Representative wear profiles and the average wear volume loss values for 10 N condition can be seen in Fig. 9.7. Ti-TiB-TiC\_MAO group presented approx. a 70 % reduction in wear volume loss compared to Ti\_MAO, while the Ti-TiB-TiC\_TO group showed approx. a 30 % reduction compared to Ti\_TO.



For the Ti\_MAO group, after the MAO layer was removed, a considerable amount of Ti from the substrate was lost to wear. Due to the higher wear resistance of the composite substrate, the Ti-TiB-TiC\_MAO group presented considerably lower wear volume loss values. The same was observed for TO treated groups. However, due to the formation of an ODZ in both groups, the effect of increased wear resistance of the composite was not as drastic as the MAO groups.

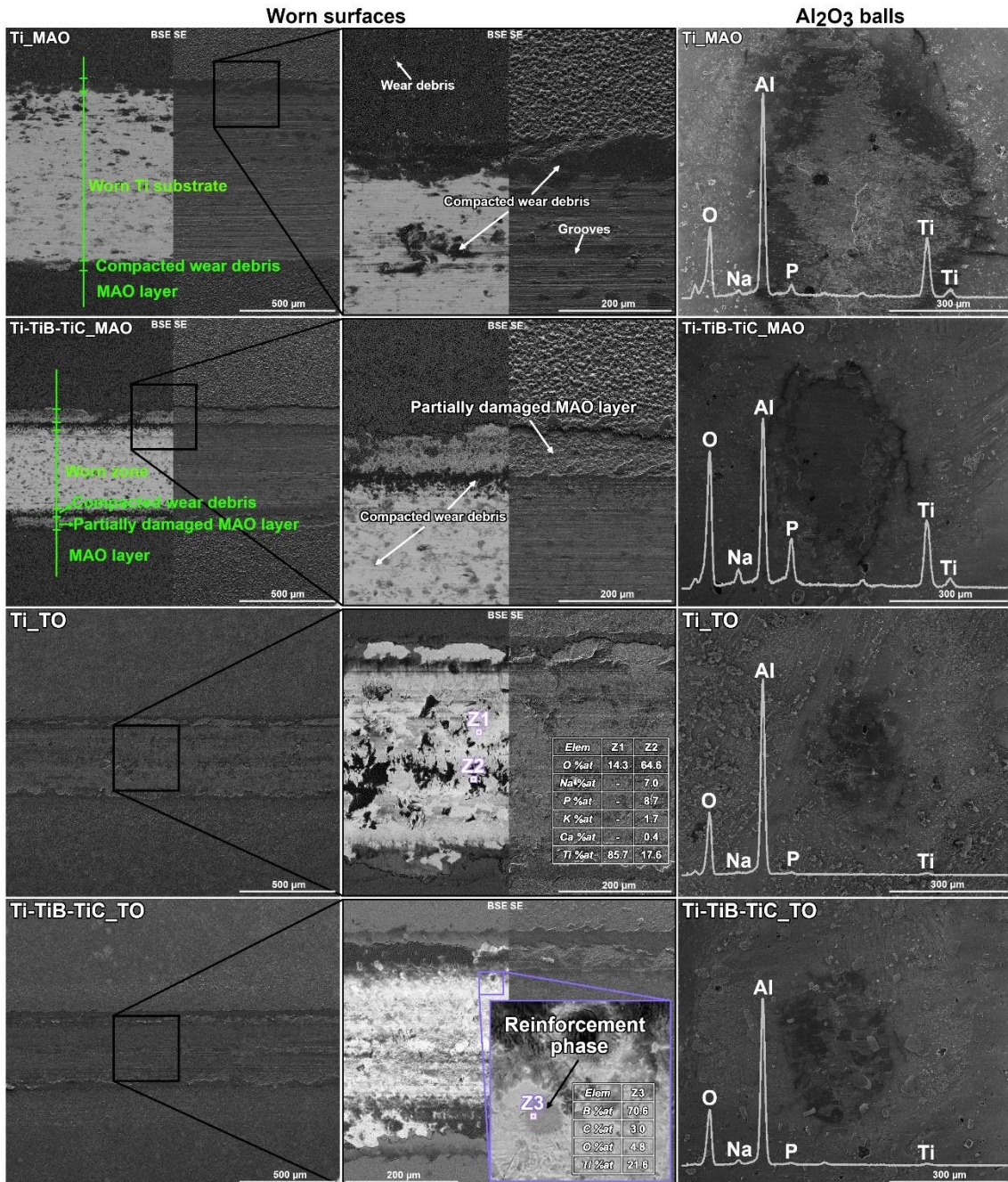
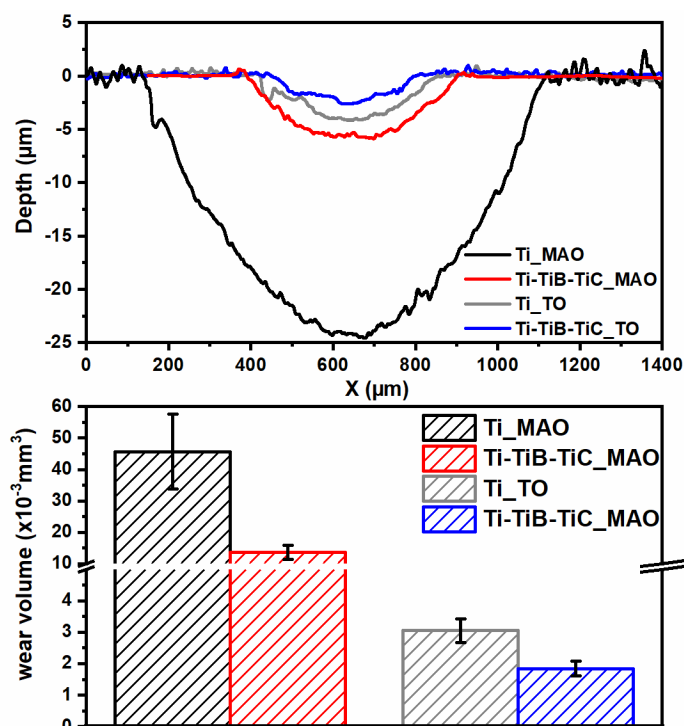


Figure 9.6. SEM images of the worn surfaces and Al<sub>2</sub>O<sub>3</sub> balls together with EDS analysis from Al<sub>2</sub>O<sub>3</sub> balls for 10 N.



**Figure 9.7.** Wear profiles and average wear volume loss for 10 N applied load.

The scope of this work showed that the MAO treated and TO treated Ti-TiB-TiC composites may have the potential for load bearing implants. The overall structure and phase composition of these layers were very similar between Ti and composites groups. After tribocorrosion tests, biofunctionalized composites presented considerably reduced wear damage compared to biofunctionalized Ti. The slighter decrease in OCP values under sliding for MAO and TO treated composite groups also suggests that the harder composite substrate may provide better support for these layers once the transition in mechanical properties between these layers and the substrate is not so sharp as the one observed between MAO and TO layers and the soft Ti substrate. In addition, once these layers are removed, the higher wear resistance of the composite substrate leads to considerably reduced wear damage, especially for MAO groups.

#### 9.4. Conclusions

MAO and TO treated Ti-TiB-TiC composites presented improved tribocorrosion behaviour compared to MAO and TO treated Ti through the reduced tendency to corrosion under mechanical action as well as overall lower

wear volume loss values. Thus, it can be concluded that composites may provide better support for these layers due to increased hardness and wear resistance.





## References

- [1] A. Amanov, I.S. Cho, D.E. Kim, Y.S. Pyun, Fretting wear and friction reduction of CP titanium and Ti-6Al-4V alloy by ultrasonic nanocrystalline surface modification, *Surf. Coatings Technol.* 207 (2012) 135–142.
- [2] H. Güleriyüz, H. Çimenoğlu, Effect of thermal oxidation on corrosion and corrosion-wear behaviour of a Ti-6Al-4V alloy, *Biomaterials.* 25 (2004) 3325–3333.
- [3] Y.L. Yang, D. Zhang, W. Yan, Y. Zheng, Microstructure and wear properties of TiCN/Ti coatings on titanium alloy by laser cladding, *Opt. Lasers Eng.* 48 (2010) 119–124.
- [4] B.S. Yilbas, S.Z. Shuja, Laser treatment and PVD TiN coating of Ti6Al4V alloy, *Surf. Coat. Technol.* 130 (2000) 152–157.
- [5] F. Toptan, A. Rego, A.C. Alves, A. Guedes, Corrosion and tribocorrosion behavior of Ti–B4C composite intended for orthopaedic implants, *J. Mech. Behav. Biomed. Mater.* 61 (2016) 152–163.
- [6] J.-S. Kim, K.-M. Lee, D.-H. Cho, Y.-Z. Lee, Fretting wear characteristics of titanium matrix composites reinforced by titanium boride and titanium carbide particulates, *Wear.* 301 (2013) 562–568.
- [7] V.S. Balaji, S. Kumaran, Densification and microstructural studies of titanium–boron carbide (B4C) powder mixture during spark plasma sintering, *Powder Technol.* 264 (2014) 536–540.
- [8] S. Li, K. Kondoh, H. Imai, B. Chen, L. Jia, J. Umeda, Y. Fu, Strengthening behavior of *in situ*-synthesized (TiC–TiB)/Ti composites by powder metallurgy and hot extrusion, *Mater. Des.* 95 (2016) 127–132.
- [9] S. LI, K. Kondoh, H. Imai, B. Chen, L. Jia, J. Umeda, Microstructure and mechanical properties of P/M titanium matrix composites reinforced by in-situ synthesized TiC–TiB, *Mater. Sci. Eng. A.* 628 (2015) 75–83.
- [10] C.J. Zhang, F.T. Kong, S.L. Xiao, E.T. Zhao, L.J. Xu, Y.Y. Chen, Evolution of microstructure and tensile properties of *in situ* titanium matrix composites with volume fraction of (TiB and TiC) reinforcements, *Mater. Sci. Eng. A.* 548 (2012) 152–160.
- [11] D.R. Ni, L. Geng, J. Zhang, Z.Z. Zheng, Fabrication and tensile properties of *in situ* TiBw and TiCp hybrid-reinforced titanium matrix composites based on Ti-B4C-C, *Mater. Sci. Eng. A.* 478 (2008) 291–296.
- [12] L. Jia, S.F. Li, H. Imai, B. Chen, K. Kondoh, Size effect of B4C powders on metallurgical reaction and resulting tensile properties of Ti matrix composites by in-situ reaction from Ti-B4C system under a relatively low temperature, *Mater. Sci. Eng. A.* 614 (2014) 129–135.
- [13] The Mechanical Properties of In-Situ Composites, *JOM J. Miner. Met. Mater. Soc.* 49 (1997) 35–39.
- [14] L. Geng, D.R. Ni, J. Zhang, Z.Z. Zheng, Hybrid effect of TiBw and TiCp on tensile properties of *in situ* titanium matrix composites, *J. Alloys Compd.* 463 (2008) 488–492.
- [15] D.R. Ni, L. Geng, J. Zhang, Z.Z. Zheng, Effect of B4C particle size on microstructure of *in situ* titanium matrix composites prepared by reactive processing of Ti-B4C system, *Scr. Mater.* 55 (2006) 429–432.
- [16] B. V. Radhakrishna Bhat, J. Subramanyam, V. V. Bhanu Prasad, Preparation of Ti-TiB-TiC & Ti-TiB composites by in-situ reaction hot processing, *Mater. Sci. Eng. A.* 325 (2002) 126–130.
- [17] D.R. Ni, L. Geng, J. Zhang, Z.Z. Zheng, TEM characterization of symbiosis structure of *in situ* TiC and TiB prepared by reactive processing of Ti-B4C, *Mater. Lett.* 62 (2008) 686–688.
- [18] X. Liu, P.K. Chu, C. Ding, Surface modification of titanium, titanium alloys, and related materials for biomedical applications, *Mater. Sci. Eng. R Reports.* 47 (2004) 49–121.

- [19] A. Arifin, A. Bakar, N. Muhamad, J. Syarif, M. Ikram, A.B. Sulong, N. Muhamad, J. Syarif, M.I. Ramli, A. Bakar, M. Ikram, Material processing of hydroxyapatite and titanium alloy (HA/Ti) composite as implant materials using powder metallurgy: A review, *Mater. Des.* 55 (2014) 165–175.
- [20] Y. Wang, H. Yu, C. Chen, Z. Zhao, Review of the biocompatibility of micro-arc oxidation coated titanium alloys, *Mater. Des.* 85 (2015) 640–652.
- [21] C. Chang, X. Huang, Y. Liu, L. Bai, X. Yang, R. Hang, B. Tang, P.K. Chu, High-current anodization: A novel strategy to functionalize titanium-based biomaterials, *Electrochim. Acta.* 173 (2015) 345–353.
- [22] P.S. Vanzillotta, M.S. Sader, I.N. Bastos, G. De Almeida, Improvement of in vitro titanium bioactivity by three different surface treatments, *Dent. Mater.* 22 (2006) 275–282.
- [23] Y. Park, H.-J. Song, I. Kim, H. Yang, Surface characteristics and bioactivity of oxide film on titanium metal formed by thermal oxidation, *J. Mater. Sci.* 18 (2007) 565–575.
- [24] L. Xie, X. Liao, G. Yin, Z. Huang, D. Yan, Y. Yao, W. Liu, X. Chen, J. Gu, Preparation, characterization, in vitro bioactivity, and osteoblast adhesion of multi-level porous titania layer on titanium by two-step anodization treatment, *J. Biomed. Mater. Res. - Part A.* 98 A (2011) 312–320.
- [25] L. Xie, X. Liao, H. Xu, G. Yin, Z. Huang, Y. Yao, X. Chen, J. Gu, A facile one-step anodization treatment to prepare multi-level porous titania layer on titanium, *Mater. Lett.* 72 (2012) 141–144.
- [26] Y. Li, W. Wang, J. Duan, M. Qi, A super-hydrophilic coating with a macro/micro/nano triple hierarchical structure on titanium by two-step micro-arc oxidation treatment for biomedical applications, *Surf. Coatings Technol.* 311 (2017) 1–9.
- [27] R. Zhou, D. Wei, J. Cao, W. Feng, S. Cheng, Q. Du, B. Li, Y. Wang, D. Jia, Y. Zhou, Conformal coating containing Ca, P, Si and Na with double-level porous surface structure on titanium formed by a three-step microarc oxidation, *RSC Adv.* 5 (2015) 28908–28920.
- [28] M. Tsai, Y. Chang, H. Huang, Y. Wu, T. Shieh, Micro-arc oxidation treatment enhanced the biological performance of human osteosarcoma cell line and human skin fibroblasts cultured on titanium – zirconium films, *Surf. Coat. Technol.* 303 (2016) 268–276.
- [29] Y. Zhao, T.-Y. Xiong, Formation of bioactive titania films under specific anodisation conditions, *Surf. Eng.* 28 (2012) 371–376.
- [30] B. Yang, M. Uchida, H.M. Kim, X. Zhang, T. Kokubo, Preparation of bioactive titanium metal via anodic oxidation treatment, *Biomaterials.* 25 (2004) 1003–1010.
- [31] Y. Li, B. Li, X. Fu, J. Li, C. Li, H. Li, H. Li, C. Liang, H. Wang, L. Zhou, S. Xin, Anodic Oxidation Modification Improve Bioactivity and Biocompatibility of Titanium Implant Surface, *J. Hard Tissue Biol.* 22 (2013) 351–358.
- [32] G. Wang, J. Li, K. Lv, W. Zhang, X. Ding, G. Yang, Surface thermal oxidation on titanium implants to enhance osteogenic activity and in vivo osseointegration, *Sci. Rep.* 6 (2016) 1–13.
- [33] S. El-hadad, Optimizing the Surface Treatment Processes to Enhance the Bioactivity of Ti–6Al–7Nb Alloy, *Trans. Indian Inst. Met.* 73 (2020) 2727–2738.
- [34] M. Lou, A.T. Alpas, High temperature wear mechanisms in thermally oxidized titanium alloys for engine valve applications, *Wear.* 426–427 (2019) 443–453.
- [35] A.C. Alves, F. Wenger, P. Ponthiaux, J.P. Celis, A.M. Pinto, L.A. Rocha, J.C.S. Fernandes, Corrosion mechanisms in titanium oxide-based films produced by anodic treatment, *Electrochim. Acta.* 234 (2017) 16–27.
- [36] L. Cao, Y. Wan, S. Yang, J. Pu, The Tribocorrosion and Corrosion Properties of Thermally Oxidized Ti6Al4V Alloy in 0.9 wt.% NaCl Physiological Saline, *Coatings.* 8 (2018) 285.
- [37] A.I. Costa, L. Sousa, A.C. Alves, F. Toptan, Tribocorrosion behaviour of bio-functionalized porous Ti surfaces obtained by two-step anodic treatment, *Corros. Sci.* 166 (2020) 108467.

- [38] A.C. Alves, F. Oliveira, F. Wenger, P. Ponthiaux, J.-P. Celis, L.A. Rocha, Tribocorrosion behaviour of anodic treated titanium surfaces intended for dental implants, *J. Phys. D. Appl. Phys.* 46 (2013) 404001.
- [39] X. Zhang, W. Lu, D. Zhang, R. Wu, *In Situ* Technique for synthesizing (TiB+TiC)/Ti composites, *Scr. Mater.* 41 (1999) 39–46.
- [40] N. Dalili, A. Edrissy, K. Farokhzadeh, J. Li, J. Lo, A.R. Riahi, Improving the wear resistance of Ti–6Al–4V/TiC composites through thermal oxidation (TO), *Wear.* 269 (2010) 590–601.
- [41] Z. Doni, A.C. Alves, F. Toptan, J.R. Gomes, A. Ramalho, M. Buciumeanu, L. Palaghian, F.S. Silva, Dry sliding and tribocorrosion behaviour of hot pressed CoCrMo biomedical alloy as compared with the cast CoCrMo and Ti6Al4V alloys, *Mater. Des.* 52 (2013) 47–57.
- [42] F. Toptan, A.C. Alves, A.M.P. Pinto, P. Ponthiaux, Tribocorrosion behavior of bio-functionalized highly porous titanium, *J. Mech. Behav. Biomed. Mater.* 69 (2017) 144–152.
- [43] N. Eliaz, N. Metoki, Calcium Phosphate Bioceramics: A Review of Their History, Structure, Properties, Coating Technologies and Biomedical Applications, *Materials* (Basel). 10 (2017) 104.
- [44] L. Sopchenski, S. Cogo, S. Eli, K.C. Popat, P. Soares, Bioactive and antibacterial boron doped TiO<sub>2</sub> coating obtained by PEO, *Appl. Surf. Sci.* 458 (2018) 49–58.
- [45] K. Anio, The influence of thermal oxidation parameters on the growth of oxide layers on titanium, *Vacuum.* 144 (2017) 94–100.
- [46] P.A. Dearnley, K.L. Dahm, H. Çimeno, The corrosion–wear behaviour of thermally oxidised CP-Ti and Ti–6Al–4V, *Wear.* 256 (2004) 469–479.
- [47] S. Kumar, T.S.N.S. Narayanan, S.G. Sundara, S.K. Seshadri, Thermal oxidation of CP-Ti: Evaluation of characteristics and corrosion resistance as a function of treatment time, *Mater. Sci. Eng. C.* 29 (2009) 1942–1949.
- [48] M. Fazel, H.R. Salimijazi, M.A. Golozar, M.R. Garsivaz Jazi, A comparison of corrosion, tribocorrosion and electrochemical impedance properties of pure Ti and Ti6Al4V alloy treated by micro-arc oxidation process, *Appl. Surf. Sci.* 324 (2015) 751–756.
- [49] E. Arslan, Y. Totik, E. Demirci, A. Alsaran, Influence of Surface Roughness on Corrosion and Tribological Behavior of CP-Ti After Thermal Oxidation Treatment, *J. Mater. Eng. Perform.* 19 (2010) 428–433.
- [50] J.I. Silva, A.C. Alves, A.M. Pinto, F. Toptan, Corrosion and tribocorrosion behavior of Ti–TiB–TiN<sub>x</sub> in-situ hybrid composite synthesized by reactive hot pressing, *J. Mech. Behav. Biomed. Mater.* 74 (2017) 195–203.
- [51] R. Bailey, Y. Sun, Corrosion and Tribocorrosion Performance of Thermally Oxidized Commercially Pure Titanium in a 0.9 % NaCl Solution, *J. Mater. Eng. Perform.* 24 (2015) 1669–1678.



## Chapter 10

### General discussion, conclusions, and future work

---

#### 10.1. General discussion

Although THR is one of the most successful orthopaedic surgeries, as discussed in the previous chapters, there are still some major problems that must be overcome. To further improve the implant lifespan, the development of new materials with improved mechanical, corrosion, and tribocorrosion properties and enhanced biological response is necessary.

Despite Ti and its alloys being widely used in producing these implants, these still face some concerns such as poor tribocorrosion resistance and lack of bioactivity. From chapters 3 to 5, it was shown that by introducing a relatively small percentage of hard reinforcement phases into a Ti matrix to produce TMCs, it was possible to improve the overall tribocorrosion resistance of Ti. Therefore, with a considerable reduction in wear volume loss and considerably less amount of wear debris released to the surrounding environment. TMCs also tended to present a reduced tendency to corrosion as well as reduced corrosion kinetics during sliding action. However, some considerations still need to be taken into account. The corrosion behaviour of Ti can be significantly affected by the addition of reinforcement phases once these can react with the Ti matrix and form intermetallic compounds that may be more susceptible to corrosion. In the end, the corrosion behaviour can be considerably lower than that of unreinforced Ti. This was specially the case for Ti-Al<sub>2</sub>O<sub>3</sub> composites (chapters 3 and 7), where it was shown that the formation of TiAl and Ti<sub>3</sub>Al intermetallic phases could considerably jeopardize the corrosion behaviour. On the other hand, it was also shown in chapter 7 that by reducing the amount of these intermetallic phases, in

this case by using lower processing temperatures, it was possible almost to avoid this problem.

Besides, it was also shown that choosing an appropriate processing method is essential to produce such composites successfully. Porosity played an essential role in the overall corrosion resistance of the composites. As it was shown in chapter 4, Ti-B<sub>4</sub>C composites processed by hot-pressing presented very similar corrosion behaviour to that of Ti. However, the same composites processed by conventional powder metallurgy showed a higher amount of porosity leading to a significantly reduced corrosion resistance. Besides the increased corrosion kinetics, the typical passivation plateau of Ti was also lost for these composites. Ti-Al<sub>2</sub>O<sub>3</sub> composites processed by conventional powder metallurgy (chapter 3) also presented considerably reduced corrosion resistance when compared with the same composites processed by hot pressing in chapter 7.

Even though, Ti-B<sub>4</sub>C composites processed by hot-pressing (chapter 4) presented similar corrosion behaviour to that of Ti up to a certain potential range. For higher potential values (above 1 V) there was a sudden increase in corrosion kinetics, due to degradation of the interface between B<sub>4</sub>C particles and the reaction zone, which could lead to particle detachment (chapter 8). Nevertheless, the relevant potential region in the human body is lower than 1 V [1], additionally it has been reported that breakdown potentials above 1 V are not a decisive criteria to approve or reject materials for biomedical applications [2]. On the other hand, different processing parameters can also result in different mechanical properties, influencing the overall tribocorrosion behaviour of the composites. In chapter 7, Ti-Al<sub>2</sub>O<sub>3</sub> composites processed at 1100 °C presented considerably lower fracture toughness than the same composites processed at 1000 °C, leading to the crack's formation during tribocorrosion tests and higher wear volume losses.

Overall, the *in-situ* composites processed in chapter 5, obtained by fully reacting Ti and B<sub>4</sub>C powders, presented the overall best corrosion behaviour, where their corrosion resistance was very similar to unreinforced Ti. In addition, the problematic corrosion behaviour observed at higher potentials for Ti-B<sub>4</sub>C composites was not observed. Preliminary biological tests also showed similar biocompatibility to that of Ti and results also hinted at improved bioactivity

probably due to changes in the overall chemical composition and hardness of the composite surfaces.

Anodic treatment is a simple and versatile technique that allows tailoring the surface of Ti-based materials. As shown in chapter 6, it is possible to combine different anodic treatments to obtain both macro and micro-pores in order to improve the bioactivity of Ti. It was shown that the macro-porous surfaces still retain the characteristic passive behaviour of Ti. Through MAO treatment, using an electrolyte rich in bioactive Ca and P elements, it was possible to form a micro-porous oxide layer rich in Ca and P elements as well as hard anatase and rutile phases. Besides improved corrosion resistance, the MAO layers also showed improved tribocorrosion behaviour, wettability, and reduced ion release during sliding action compared with untreated Ti.

In chapter 7, the same MAO treatment was applied to Ti-Al<sub>2</sub>O<sub>3</sub> composite surfaces. After treatment, the overall microstructure consisted of Al<sub>2</sub>O<sub>3</sub> reinforcement particles dispersed within a biofunctionalized matrix, with the same characteristics of the MAO layers processed in chapter 6, in terms of morphology, chemical and phase composition as well as corrosion behaviour. Similar to Ti surfaces, biofunctionalized composites also presented a considerable improvement in corrosion behaviour, which was in the same order of magnitude as the one observed on Ti surfaces. It was also possible to observe that through this treatment, the negative effect of intermetallic TiAl and Ti<sub>3</sub>Al phases on the corrosion behaviour was avoided entirely, once these phases were also covered by the MAO layer. On the other hand, it was observed that these intermetallic phases also affected the microstructure of the biofunctionalized composites where higher amount of these phases can lead to heterogeneities in the micro-porous structure of the MAO layer. Even though no significant effect of those heterogeneities was observed on the results in terms of corrosion and tribocorrosion behaviour. Overall, it was shown that biofunctionalized composites have improved the corrosion and tribocorrosion behaviour.

As could be seen in chapters 8 and 9, performing the same MAO treatment on Ti-B<sub>4</sub>C and Ti-TiB-TiC *in-situ* composite surfaces led to different overall microstructures. After performing MAO treatment on the *in-situ* composites, both reinforcement phases and Ti matrix were covered by the micro-porous oxide layer, which was not the case for Ti-Al<sub>2</sub>O<sub>3</sub> composites where reinforcement

particles were clearly visible. This was most probably related to the different nature of the reinforcement particles, while  $\text{Al}_2\text{O}_3$  is a very stable compound, characterized as chemical inert [3], titanium borides and titanium carbides can oxidize under dry or  $\text{H}_2\text{O}$  environments [4,5].

In the case of *in-situ* Ti composites, no apparent differences were observed in terms of morphology between the MAO layer formed on the top of reinforcement phases and the Ti matrix. Similar behaviour was observed for thermal treatments, where both reinforcement phases and Ti matrix were covered by the oxide film, with no significant differences in terms of overall morphology. Treated composites presented improved corrosion resistance over the untreated composites (chapter 5). However, this improvement was not as significant as the one observed on unreinforced Ti or the Ti- $\text{Al}_2\text{O}_3$  composites studied in chapter 7. The results suggest that the oxide layers formed on these surfaces have overall lower corrosion resistance, possibly due to heterogeneities at the reinforcement/oxide layer interface. Nevertheless, additional characterization is needed to have a definitive answer.

Regarding tribocorrosion behaviour, no significant differences were observed between treated unreinforced Ti and treated composites under low contact pressures. However, at higher contact pressures, treated composites presented improved tribocorrosion behaviour, in addition to a slower drop in OCP values during tribocorrosion tests, as well as considerably lower wear volume loss values compared to treated unreinforced Ti.

MAO and TO treatments carried out on Ti- $\text{B}_4\text{C}$  composite surfaces led detachment of  $\text{B}_4\text{C}$  particles from the composite surfaces. For both treatments, the overall morphology consisted of a functionalized surface, where instead of  $\text{B}_4\text{C}$  particles, a functionalized pore was observed. It was shown that in both cases, the reaction zones were still present, where an oxide layer was also formed. Combining the results of both treatments as well as corrosion tests, it was reasonable to assume that the weak point was located at the interface between  $\text{B}_4\text{C}$  particles and the reaction zone, where after a certain potential or temperature, a degradation of these interfaces and/or oxides can be formed, growth and eventually lead to detachment of the  $\text{B}_4\text{C}$  particles. Still, treated composites presented improved tribocorrosion behaviour compared to treated Ti under the same conditions (chapter 9), as well as compared to the untreated



composite. Comparing both MAO and TO treatments, both presented its advantages and disadvantages. While the improvement in corrosion behaviour was quite similar for both treatments, distinct tribocorrosion behaviours were observed. Under lower normal loads (0.5 and 1 N), no considerable wear damage was observed for both treatments. However, for higher loads (10 N), TO treated groups presented considerably lower wear volume loss values as well as reduced tendency to corrosion under sliding for both unreinforced treated Ti and composites groups. This behaviour was attributed to the formation of an oxygen diffusion zone with increased hardness and thus improved wear resistance. In chapter 8, it was shown that MAO treated composites can in fact presented higher wear volume losses compared to the untreated composites, once wear debris from the MAO layer could act as an extra abrasive. However, it is also important to note that MAO treated composites presented a noticeable delay in OCP drops on the onset of sliding action, which may indicate superior wear resistance, at least in an earlier stage under high loads. It is also important to consider that the contact pressures observed in-vitro after THR are relatively lower (most of the time below 100 MPa [6,7]). Still, the abrasive effect from the wear debris prevented from the MAO layers should not be forgotten in further studies.

Besides corrosion and tribocorrosion behaviour, MAO treatment also has the advantage of providing more tailored surfaces for biomedical applications. In addition to micro-pores, it is also possible to incorporate bioactive elements as well as antibacterial elements into its composition, all of which can be controlled by changing processing parameters, mainly electrolyte composition.



## 10.2. Conclusions

The main hypothesis of this work was that biofunctionalized titanium matrix composites could improve both the tribocorrosion behaviour and bioactivity of Ti. By adding reinforcement particles into a Ti matrix, to produce TMCs, it was possible to improve the tribocorrosion resistance of Ti significantly. However, depending on the reinforcement phase or processing parameters, the corrosion behaviour of Ti can be jeopardized.

The overall structure of biofunctionalized composite surfaces is strongly dependent on the properties of the base composite. The overall nature of the reinforcement phases, reaction products (due to reaction with the Ti matrix) as well the interface between these materials can lead to differences in morphology of the oxide layers obtained for both MAO and TO treatments, all of which may affect the overall corrosion and tribocorrosion behaviour.

Although it was not possible to perform biological tests on the biofunctionalized composites, preliminary tests on the untreated *in-situ* composites showed promising results once they hint at improved bioactivity. Still an improvement in bioactivity is expected for biofunctionalized composites, once the overall structure of the oxide layers is similar to the structures already reported in the literature for an improved biological response on Ti and its alloys.

Thus, within the limitations of this work, the main hypothesis of this thesis can be accepted and therefore it can be concluded that biofunctionalized titanium matrix composites may be promising for load bearing biomedical implants.



### 10.3. Future works

Biofunctionalized TMCs are promising materials for load bearing biomedical implants. However, further studies are still needed, thus the following studies are suggested:

1. The chemical and phase composition of MAO and TO oxide layers should be further investigated, especially for *in-situ* composites, as they may hint to the differences observed in corrosion behaviour. Techniques such as XPS, EBSD and TEM are recommended.
2. Young's modulus is still one of the main concerns of load bearing biomedical implants, once they are directly connected to stress shield effects. On the other hand, fatigue resistance is also of outmost importance once these implants are subject to cyclic loads throughout their life-span. Thus, the investigation of the mechanical behaviour of untreated and biofunctionalized composites, mainly Young's modulus and fatigue resistance should be investigated with techniques such as compression tests or standard stress-strain experiments. For oxide layers, nano-indentation tests could be performed to evaluate the mechanical properties.
3. In real conditions, implants are surrounded by complex environments containing proteins and micro-organisms, all of which can affect the overall corrosion and tribocorrosion behaviour. Thus, in further tests it is suggested to use more complex electrolytes by the addition of proteins and/or micro-organisms.
4. Although there are studies on the biological response of MAO and TO treatments on unreinforced Ti and Ti alloys, the biological response of biofunctionalized composites might be different. Thus, the biological response of biofunctionalized composites needs to be studied.
5. The main goal of reinforcement particles is to improve the tribocorrosion resistance of Ti, thus these are only relevant on the surface of the implant. One of the main concerns of TMCs is the increase in Young's modulus due to incorporation of reinforcement phases. Therefore, it is suggested to process a functional graded

material (FGM) in future works, with a Ti core and a gradual increase in reinforcement content towards the surface.

## References

- [1] E. Gomez-barrena, R. Trebs, Special modes of corrosion under physiological and simulated physiological conditions, *Acta Biomater.* 4 (2008) 468–476.
- [2] R. Schenk, The corrosion properties of titanium and titanium alloys, in: D.M. Brunette, M. Textor, P. Thomsem (Eds.), *Titan. Med. Mater. Sci. Surf. Sci. Eng. Biol. Responses Med. Appl.*, Springer-Verlag Berlin Heidelberg, 2001: pp. 145–170.
- [3] S. Affatato, L. Grillini, Topography in bio-tribocorrosion, in: *Bio-Tribocorrosion Biomater. Med. Implant.*, Woodhead Publishing Limited, 2013: p. 1–22a.
- [4] S. Shimada, T. Onuma, H. Kiyono, M. Desmaison, Oxidation of HIPed TiC Ceramics in Dry O<sub>2</sub>, Wet O<sub>2</sub> and H<sub>2</sub>O Atmospheres, *J. Am. Ceram. Soc.* 1225 (2006) 1218–1225.
- [5] A. Kulpa, T. Troczynski, Oxidation of TiB<sub>2</sub> Powders below 900°C, *J. Am. Ceram. Soc.* 79 (1996) 518–520.
- [6] C. Luo, X. Wu, Y. Wan, J. Liao, Q. Cheng, M. Tian, Femoral Stress Changes after Total Hip Arthroplasty with the Ribbed Prosthesis: A Finite Element Analysis, *Biomed Res. Int.* 2020 (2020) 8.
- [7] W. A. Hodge, W.H. Harris, K.L. Carlson, R.G. Burgess, W.H. Harris, R.W. Mann, Contact pressures in the human hip joint measured in vivo, *Proc. Natl. Acad. Sci. U. S. A.* 83 (1986) 2879–2883.